

**Design, Synthesis, and Biological Evaluation of Compounds for DNA Targeted  
Therapy**

by

Ahmed Hamdy Mahmoud Elmenoufy

A thesis submitted in partial fulfillment of the requirements for the degree of

Doctor of Philosophy

Department of Chemistry  
University of Alberta

© Ahmed Hamdy Mahmoud Elmenoufy, 2020

# Abstract

At present, the number of cancer patients who develop resistance to conventional cancer therapeutics, such as DNA damaging chemotherapeutics, or radiotherapy, is increasing. A major reason for developing such resistance is that cancer cells have the ability to repair their DNA damage caused by these therapies through various DNA repair pathways. The most important of these damages are photo adducts produced by the UV component of sunlight, such as cyclobutane pyrimidine dimers (CPD) and cisplatin-DNA products, which cause intra-strand crosslinks (ICL). These bulky, helix distorting lesions are repaired mainly by nucleotide excision repair (NER), a highly versatile repair pathway that can recognize, verify, remove, and correct these damages.

ERCC1–XPF is a 5′-3′ structure-specific endonuclease that is involved in NER and ICL repair pathways in mammalian cells. It plays a central role in NER because it removes CPD and chemically induced helix-distorting lesions by incising the damaged DNA strand 5′ and 3′, respectively. Therefore, ERCC1–XPF has become an interesting therapeutic target to manipulate the DNA repair pathways, and its inhibition has the potential of sensitizing cancer cells towards cytotoxic chemotherapeutic agents and ionizing radiation (IR). One of the potential sites on ERCC–XPF to target for inhibiting its endonuclease activity is the interaction site between ERCC and XPF which is essential for the protein stability and activity. A few groups have developed hits that interfere with the interaction site and inhibit its endonuclease activity successfully. However, the activities of the reported hits to date are suboptimal in terms of clinical properties, including potency and further optimization is required.

In Chapter 2, we used the reported **F06** (compound **1**) as a reference hit that was subjected in docking-based virtual screening. The *in-silico* screening results yielded compounds with a better binding energy and ligand efficiency values using the XPF interaction domain. Synthesis of seven novel analogues of **F06** (**1**) is discussed. Two of the new F06-based derivatives were shown to have a potent inhibitory effect on ERCC1–XPF activity relative to **F06** *in vitro*. The cell-based assays showed that compound **4** significantly inhibited NER by inhibiting the removal of CPDs in UV-irradiated cells. Also, it successfully showed a significant sensitization of colorectal cancer cells to cyclophosphamide and UV radiation.

Chapter 3 describes the use of a multi-step CADD strategy to identify better inhibitors than **F06** (**1**) based on the modification of one site of **F06** (**1**), methoxy-acridine functional group. The *in silico* screening study identified two compounds that showed improved inhibitory effect on the ERCC1–XPF nuclease activity compared to the parent compound **F06** (**1**). The *in vitro* endonuclease assay revealed that **B9** has a better ERCC1–XPF inhibition with an IC<sub>50</sub> of 0.49 μM, showing 3-fold improvement in inhibition activity compared to **1**. Detailed analysis of the predicted binding mode of **B9** to XPF derived from molecular dynamics simulations is discussed. This analysis showed that the hydroxyl group substituting the methoxy in **F06** (**1**) was involved in a new hydrogen bond interaction with side chain of V859, not observed for **F06** (**1**) or our previous inhibitor compound **4**. Therefore, having a polar hydrogen bond donor group in this site is responsible for the better *in vitro* activity of these two compounds in comparison to **F06** (**1**).

Chapter 4 discusses an extensive structure activity relationship analysis that has been conducted based on the previously identified hit compound, **F06 (1)**, as a reference compound. Two different series of generations have been developed by structure-based design and were synthesized through various modifications on two different sites of **F06 (1)**, according to the corresponding pharmacophore model. Unfortunately, lack of piperazine moiety in Gen **C** compounds was accompanied by a lost activity. Also, replacing the acridine moiety with smaller aromatic group such as quinoline (Gen **D** compounds) was responsible for losing the inhibitory effect on ERCC1-XPF. Therefore, **B9** has been selected for carrying out further cell-based/ cell-free assays. **B9** elicit high binding affinity to the ERCC1–XPF complex with a  $K_d$  of 85 nM relative to 140 nM for **1**. **B9** also showed a significant sensitization of lung and colorectal cells towards cisplatin, cyclophosphamide, and Mitomycin C. The proximity ligation assay suggested that the mechanism of inhibition of **B9** is mediated by heterodimerization disruption.

# Preface

Chapter 2 of this thesis has been published as Elmenoufy, A. H.; Gentile, F.; Jay, D.; Karimi-Busheri, F.; Yang, X.; Soueidan, O. M.; Weilbeer, C.; Mani, R. S.; Barakat, K. H.; Tuszynski, J. A.; Weinfeld, M.; West, F. G. Targeting DNA Repair in Tumor Cells via Inhibition of ERCC1–XPF. *Journal of Medicinal Chemistry* **2019**, 62, 7684-7696.

I was responsible for the synthesis and design of all compounds, data collection, and manuscript composition. F.G. designed the computational studies of the compounds and helped in mastering some of the graphs. D.J. expressed and purified ERCC1–XPF, employed the *in vitro* ERCC–XPF1 assay, and conducted microscale thermophoresis measurements. F.K.B and Y.X. carried out cell culture, UV dimer repair assay, and clonogenic survival assay. O.S. helped in mentoring A.E in the synthesis and characterization of the compounds. C.W. was responsible for purification and HPLC analysis of compound 4. R.M. conducted the binding affinity studies of the compounds. F.K.B. and J.T. supervised F.G. in designing VS studies. M.W. and F.W. drafted the manuscript.

Chapter 3 of this thesis has been published as Gentile, F.; Elmenoufy, A. H.; Ciniero, G.; Jay, D.; Karimi-Busheri, F.; Barakat, K. H.; Weinfeld, M.; West, F. G.; Tuszynski, J. A. Computer-aided drug design of small molecule inhibitors of the ERCC1–XPF protein–protein interaction. *Chemical Biology & Drug Design* **2020**, 95, 460-471. F.G. and I contributed equally to this work. We were responsible for data collection, data analysis, and manuscript writing. D.J. expressed and purified ERCC1–XPF and employed the *in vitro* ERCC–XPF1 assay. F.K.B helped in the

manuscript composition. K.B. supervised F.G. in designing the *in silico* studies. M.W., F.G., and J.T. drafted the manuscript.

Chapter 4 of this thesis will be published as Elmenoufy, A. H; Gentile, F; Soueidan, O. M; Karimi-Busheri, F.; Jay, D.; J. Tuszynski; Barakat, K. H.; Weinfeld, M.; West, F. G., “Design, synthesis and *in vitro* cell-free/cell-based biological evaluations of novel ERCC1-XPF inhibitors targeting DNA repair pathway” I was responsible for collecting and analyzing data as well as designing and writing the manuscript. I was also responsible for the synthesis and characterization of all compounds. F.G performed the computational work for predicting the binding mode of Gen B9. D.J. carried out the *in vitro* ERCC–XPF1 endonuclease assay. F.K.B carried out cell culture, UV dimer repair assay, and clonogenic survival assay. O.S. helped in mentoring A.E in the synthesis and characterization of Gen B compounds. R.M. conducted the binding affinity studies of the compounds. F.G. was involved in concept formation and manuscript composition.

# Dedication

*To my amazing wife Alshimaa Nassar, my adorable son Yaseen, my great parents, as well as my whole family for their continuous years of prayers, support and encouragement.*

# Acknowledgements

Firstly, I would like to express my sincere gratitude to my supervisor, Dr. F. G. West, for his continuous support, guidance, as well as his endless mentorship and patience. Also, I am very thankful to you for accommodating me in your laboratory and providing the appropriate atmosphere to manage my project flexibly; the freedom you offered me in choosing a suitable project influenced the way I think and gave me the self-confidence during my PhD studies. I would not be able to defend my thesis and achieve such a milestone without your support and thoughtful advice. Thanks for being always here for me.

Also, I am truly grateful to my Supervisory Committee Members, Dr. Jack Tuszynski and Dr. Robert Campbell, for their support and dedication to help aid my research with their valuable ideas and expertise during my graduate studies. I am also truly thankful to all examiners for the PhD defence exam. I would like to express my deepest sincere appreciation to them for enriching my knowledge in my discipline.

Words cannot express how grateful and thankful I am to my amazing collaborators, Dr. Michael Weinfeld, Dr. Feridoun Karimi-Busheri, Dr. David Jay, Dr. Rajam Mani, and Yang Xiaoyang, for providing me with a rich multi-disciplinary environment. My chemical biology background was enriched through our usual meetings and this knowledge was broadened through the fantastic scientific community I was involved with through several symposiums organized by you. My thesis story would not be significant without your guidance and help.

I would like to thank the past and current members of the West group for creating such an amazing environment to conduct research. I have acquired inevitable research skills from the West group, which broadened my knowledge to reach such a stage. I would like to express my deepest gratitude for Dr. Olivier Soueidan from whom I learnt several things in my lab and life. He was such an amazing mentor for me throughout my graduate studies. Also, I am thankful to Peter Ghaly for his support and help in the lab. I want to thank my best brother, Yaseen Almeahadi, for his presence all the time beside me, not only while working in the lab but also the fun time we share outside the lab. I am grateful for my friends, Ahmed Oraby, Omar Torky and Ahmed Elfaramawy for their support during my studies.

I am also extremely thankful to the staff members of the NMR, IR, Mass Spectroscopy facility labs, and X-ray services. Research would not have been possible without the support you provide. I am also very grateful to Dr. Anna D. Jordan for reading my thesis and providing me with her valuable feedback and comments. This thesis would not be composed in such high quality without your amazing touches on it. Your dedication for lengthy hours editing my thesis is very much appreciated. Thank you very much to every single one of you for being so approachable.

I am also grateful to the Department of Pharmaceutical Chemistry, Misr University for Science and Technology in Egypt for giving me the academic leave to be engaged in such a highly dynamic research environment at one the best universities in North America, University of Alberta. I am greatly indebted to Dr. Soheir El-Ansary, Dr. Mohamed Hussein and Dr. Akram Hifny for their encouragement and strong support during and after my undergraduate studies.

Finally, words cannot express how grateful and thankful I am to my family and relatives, especially to my mother Samia El-boghdady, my father Hamdy Elmenoufy, my beloved brother Mahmoud Elmenoufy, and younger sisters Eman and Aya Elmenoufy, as well as my beloved wife Alshimaa Nassar and son Yaseen Elmenoufy. I would like to thank them for their endless prayers and support to pass stressful moments throughout my studies. Indeed, I cannot thank you enough for the never-ending support, unlimited love, and care.

# Table of Contents

<b>Chapter 1: Introduction .....</b>	<b>1</b>
1.1 Cancer .....	1
1.2 Sources of DNA Damage.....	2
1.3 Major DNA Repair Pathways and Cancer Therapy Resistance.....	5
1.3.1 Mismatch Repair (MMR).....	5
1.3.2 Base Excision Repair (BER).....	6
1.3.3 Double-strand Break Repair (DSB).....	6
1.3.4 Nucleotide Excision Repair (NER).....	7
1.3.4.1 Mechanism of NER.....	9
1.4 ERCC1–XPF and DNA Repair Pathways .....	12
1.5 Patients with NER Deficiency and Mutated ERCC1–XPF.....	13
1.6 The Structure of ERCC1–XPF Endonuclease .....	14
1.6.1 Residues Essential for ERCC1–XPF Dimerization and DNA Binding .....	15
1.7 Small Molecule Targets of the ERCC1–XPF Heterodimer .....	17
1.7.1 ERCC1/XPA Binding Inhibitors.....	17
1.7.2 XPF Endonuclease Inhibitors.....	19
1.7.3 ERCC1–XPF Heterodimerization Inhibitors .....	23
1.8 Conclusion .....	32
1.9 References.....	36
<b>Chapter 2: Targeting DNA Repair in Tumor Cells via Inhibition of ERCC1-XPF</b> <b>.....</b>	<b>44</b>
2.1 Introduction.....	44
2.2 Results and Discussion .....	48
2.2.1 Computer-aided Drug Design of Compound 1 Analogues .....	48
2.3.2 Synthesis of Compound 1-based Analogues.....	56
2.3.3 Inhibition of ERCC1–XPF Endonuclease Activity.....	57
2.3.4 Inhibitor Binding to ERCC1–XPF .....	60
2.3.5 Inhibition of Cellular Repair of Cyclobutane Pyrimidine Dimers .....	64
2.3.6 Increased Sensitization to UV Radiation and Cyclophosphamide.....	65
2.3.7 Pharmacokinetic Properties of Compound 4 and Compound 1 .....	66
2.4 Conclusion .....	68
2.5 Methods and Experimental Section .....	71

2.5.1 General Experimental Procedures for Preparation of The Top Compound 1 Analogues .....	71
2.5.2 Synthesis and Characterization of Inhibitors (1-8) .....	72
2.5.3 Molecular Docking of Compound 1 .....	81
2.5.4 Characterization of The Binding Pocket and Pharmacophore Modeling .....	81
2.5.5 Docking-based Virtual Screening of Compound 1 Analogues .....	82
2.5.6 Molecular Dynamics Simulations and MM/GBSA Rescoring of the Analogues ...	83
2.5.7 ERCC1–XPF Protein Preparation .....	83
2.5.8 Microplate Fluorescence Incision Assay .....	84
2.5.9 Steady-state Fluorescence Assay .....	84
2.5.10 Expression and Purification of Recombinant Truncated Forms of ERCC1 and XPF .....	85
2.5.11 Microscale Thermophoresis (MST) Measurements .....	85
2.5.12 Cell Culture .....	86
2.5.13 Cellular Repair of Cyclobutane Pyrimidine Dimers .....	86
2.5.14 Clonogenic Survival Assay .....	87
2.5.14 PK Assessment of Compound 4 and Compound 1 .....	88
2.10 References .....	89
<b>Chapter 3: Computer-Aided Drug Design of The Second-Generation ERCC1–XPF Inhibitors .....</b>	<b>94</b>
3.1 Introduction .....	94
3.2 Results and Discussion .....	98
3.2.1 Molecular Dynamics Simulations .....	98
3.2.2 Interactions of F06 with The XPF Binding Site .....	102
3.2.3 Virtual Screening of F06 (1) Analogues .....	104
3.2.4 Chemistry .....	105
3.2.5 Inhibitory Effect of Gen B Compounds on ERCC1–XPF Activity .....	108
3.2.6 Predicted Binding Mode of B9 to XPF .....	110
3.3 Conclusion .....	111
3.4 Methods and Experimental Section .....	112
3.4.1 Molecular Dynamics of XPF HhH2 Domain Alone, F06-bound and ERCC1-bound .....	112
3.4.2 Analysis of The Binding Mode of F06 .....	114
3.4.3 Computer-aided Design of F06 Analogues .....	114
3.4.4 Structure-based Virtual Screening .....	115
3.4.5 Preparation of F06-based Analogues (Gen B Compounds) .....	117

3.4.6 ERCC1–XPF Protein Preparation.....	125
3.4.7 Microplate Fluorescence Incision Assay .....	125
3.5 References.....	126
<b>Chapter 4: Design, Synthesis and <i>In vitro</i> Cell-free/Cell-based Biological Evaluations of Novel ERCC1–XPF Inhibitors Targeting DNA Repair Pathway</b> .....	<b>130</b>
4.1 Introduction.....	130
4.2 Results and Discussion .....	134
4.2.1 Chemistry.....	134
4.2.2 Inhibition of ERCC1–XPF Endonuclease Activity .....	137
4.2.2.1 Inhibitory Effect of Gen C Compounds on ERCC1–XPF Activity .....	137
4.2.2.2 Inhibitory Effect of Gen D Compounds on ERCC1-XPF Activity.....	138
4.2.3 Gen B9 Binding to ERCC1–XPF .....	140
4.2.4 Inhibition of DNA Repair by B9.....	143
4.2.5 Cytotoxicity Profile of Inhibitors .....	144
4.2.6 Increased Sensitization to UV Radiation and Cyclophosphamide.....	145
4.2.7 Pharmacokinetic Properties (PK) of B9 and F06 (1) .....	146
4.2.8 Cell Death by a Combination of Compound 4 (Gen A) or B9 with Chemotherapeutic Agents .....	147
4.2.9 Heterodimerization Inhibition of ERCC1–XPF by A4 and B9.....	148
4.3 Conclusion .....	149
4.4 Methods and Experimental Section .....	151
4.4.1 Synthesis of C and D Compounds .....	151
4.4.1.1 Synthesis of Gen C Compounds .....	153
4.4.1.2 Synthesis of Gen D Compounds .....	163
4.4.2 ERCC1–XPF Protein Preparation.....	165
4.4.3 <i>In vitro</i> ERCC1-XPF Endonuclease Assay.....	165
4.4.4 Steady-State Fluorescence Assays .....	166
4.4.5 Cell Culture.....	166
4.4.6 Cellular Repair of Cyclobutane Pyrimidine Dimers .....	166
4.4.7 Rapid Cell Viability Assay .....	167
4.4.8 Clonogenic Survival Assay Following UV Treatment .....	168
4.4.9 Combination Effect of B9 and Cisplatin and MMC .....	168
4.4.10 Partial Pharmacokinetic Profile of Compounds Gen B9 and F06 (1) .....	169
4.4.11 Partial Pharmacokinetic Profile of Compounds B9 and F06 (1).....	169

4.4.12 Proximity Ligation Assay .....	169
4.5 References.....	171
<b>Chapter 5 .....</b>	<b>174</b>
5.1 General Conclusions .....	174
5.2 Future Directions .....	180
5.3 References.....	183
<b>Compiled References .....</b>	<b>184</b>
<b>Appendix I: Selected NMR Spectra .....</b>	<b>204</b>
<b>Appendix II: HPLC chromatogram of Compound 4 .....</b>	<b>221</b>
<b>Appendix III: Selected NMR Spectra .....</b>	<b>223</b>
<b>Appendix IV: HPLC chromatogram of B9 .....</b>	<b>234</b>
<b>Appendix V: Selected NMR Spectra .....</b>	<b>236</b>

# List of Figures

## Chapter 1

<b>Figure 1.1.</b> Endogenous events as sources of DNA damage. ....	3
<b>Figure 1.2.</b> DNA damage and repair pathways. ....	5
<b>Figure 1.3.</b> UV-induced formation of A) a cyclobutane pyrimidine dimer and B) a pyrimidine-pyrimidone 6-4 photoproduct.....	8
<b>Figure 1.4.</b> A simplified model of steps of Nucleotide Excision Repair (NER).....	10
<b>Figure 1.5.</b> Structure of ERCC1–XPF.. ....	14
<b>Figure 1.6.</b> Interaction of ERCC1 and XPF through their HhH2 domains .....	16
<b>Figure 1.7.</b> Structure of UCN-01 as an ERCC1–XPA inhibitor. ....	18
<b>Figure 1.8.</b> The nuclease domain of XPF. Cartoon representation of XPF identifying amino acids and their side chains.....	19
<b>Figure 1.9.</b> Structures of XPF endonuclease active site inhibitors E-X AS5-4 and E-X AS7. ....	20
<b>Figure 1.10.</b> Structures of XPF endonuclease active site inhibitor hydroxypyrimidinone derivative.....	21
<b>Figure 1.11.</b> Metal chelators as ERCC1–XPF nuclease inhibitors. ....	21
<b>Figure 1.12.</b> Structures of ERCC1–XPF nuclease inhibitors procyanidine <b>8</b> and hydroxy-naphthalene derivative <b>9</b> .....	22
<b>Figure 1.13.</b> <i>In silico</i> screening for ERCC1–XPF interaction inhibitors .....	24
<b>Figure 1.14.</b> <i>In silico</i> screened products as potential ERCC1–XPF heterodimerization inhibitors. ....	25
<b>Figure 1.15.</b> Binding energy decomposition identified three interaction sites in ERCC1-XPF .....	27
<b>Figure 1.16.</b> Binding modes of the three hits, F02 (A), F03 (B), and F06 (C) .....	28
<b>Figure 1.17.</b> Sensorgram for interaction between XPF <sup>814-905</sup> and ERCC1. <sup>220-297</sup> .....	29

<b>Figure 1.18.</b> Fluorescence experiments for the interaction between XPF <sup>814-905</sup> and <b>F06 (1)</b> .....	30
--	----

<b>Figure 1.19.</b> Potential modality of NER inactivation through ERCC1–XPF heterodimerization inhibition.....	32
---	----

## Chapter 2

<b>Figure 2.1.</b> The structure of the reference hit, compound <b>1</b> (F06).....	47
---	----

<b>Figure 2.2.</b> Visual analysis of <b>1</b> docking pose. ....	49
---	----

<b>Figure 2.3.</b> Compound <b>1</b> analogues functionalized with different substituents on the piperazine ring .....	51
--	----

<b>Figure 2.4.</b> Analysis of the binding mode of the top hits.....	55
--	----

<b>Figure 2.5.</b> The structure of DNA stem loop substrate. ....	57
---	----

<b>Figure 2.6.</b> <i>In-vitro</i> inhibition of ERCC1–XPF endonuclease activity.....	58
---	----

<b>Figure 2.7.</b> Time-dependent inactivation of ERCC1–XPF by compound <b>4</b> .....	60
--	----

<b>Figure 2.8.</b> Determination of the affinity (dissociation constant, $K_d$ ) between compound <b>4</b> and the ERCC1–XPF complex .....	61
--	----

<b>Figure 2.9.</b> Microscale thermophoresis measurements .....	63
---	----

<b>Figure 2.10.</b> Inhibition of cellular NER by compound <b>4</b> . ....	64
--	----

<b>Figure 2.11.</b> Survival of HCT-116, SW620, and XPF <sup>-/-</sup> cells treated with increasing doses of compound <b>4</b> and compound <b>5</b> .....	65
---	----

<b>Figure 2.12.</b> Sensitization of cells to UV and cyclophosphamide by compound <b>4</b> ....	66
---	----

## Chapter 3

<b>Figure 3.1.</b> Involvement of ERCC1–XPF complex in three major DNA repair pathways .....	96
--	----

<b>Figure 3.2.</b> Chemical structure of <b>1</b> , ERCC1-XPF heterodimerization inhibitor. ....	97
--	----

<b>Figure 3.3.</b> RMSDs analysis of <b>F06 (1)</b> and ERCC1 .....	99
---	----

<b>Figure 3.4.</b> Structural differences between bound and unbound forms of XPF.....	101
<b>Figure 3.5.</b> RMSF for the XPF backbone atoms calculated for the last 100 ns of MD simulation for the unbound (red), F06-bound (blue) and ERCC1-bound (green) XPF structure.....	101
<b>Figure 3.6.</b> Protonated 3D structure of F06 ( <b>1</b> ). Polar atoms are labelled with their names. ....	103
<b>Figure 3.7.</b> Poisson–Boltzmann electrostatic feature maps of the F06 binding site on XPF.. ....	103
<b>Figure 3.8.</b> F06 ( <b>1</b> ) analogues. A) modification sites of F06 ( <b>1</b> ) explored using a CADD strategy. B) structure of compound <b>4</b> , best ERCC1–XPF inhibitor among Gen A compounds. ....	104
<b>Figure 3.9.</b> Pharmacophore model of the scaffold common to all the compounds, including three aromatic features.....	105
<b>Figure 3.10.</b> Structures of <b>Gen B</b> compounds including controls. ....	106
<b>Figure 3.11.</b> <i>In-vitro</i> inhibition of ERCC1–XPF endonuclease activity.....	109
<b>Figure 3.12.</b> Detailed analysis of the predicted binding mode of <b>B9</b> to XPF derived from the 2 ns-long MD simulation.....	110
 <b>Chapter 4</b>	
<b>Figure 4.1.</b> Structure of F06 ( <b>1</b> ) hit and the potential modification sites for hit to lead optimization. ....	134
<b>Figure 4.2.</b> Chemical structures of <b>C</b> analogues. ....	135
<b>Figure 4.3.</b> Chemical structures of <b>D</b> analogues. ....	137
<b>Figure 4.4.</b> <i>In-vitro</i> inhibition of ERCC1–XPF endonuclease activity by <b>C</b> compounds (10 $\mu$ M each). ....	138
<b>Figure 4.5.</b> <i>In-vitro</i> inhibition of ERCC1–XPF endonuclease activity by <b>D</b> compounds (10 $\mu$ M each). The increase of fluorescence signal as a function of time. ....	139
<b>Figure 4.6.</b> Determination of the affinity ( $K_d$ ) between ERCC1–XPF complex and <b>B9</b> (active inhibitor) and <b>B7</b> (negative control).....	140

<b>Figure 4.7.</b> The binding affinity measurement of <b>B7</b> on the stem–loop DNA substrate. ....	142
<b>Figure 4.8.</b> Inhibition of cellular NER by compound <b>B9</b> .....	143
<b>Figure 4.9.</b> Crystal violet-based viability assay to assess the cytotoxicity profile of <b>B9</b> (active inhibitor), <b>B7</b> (negative control), and <b>F06 (1)</b> (hit).....	144
<b>Figure 4.10.</b> Sensitization of HCT 116 cells to UV and cyclophosphamide by <b>B9</b> ..	146
<b>Figure 4.11.</b> Survival of A549 (A) and HCT-116 (B) cells after exposure to alkylating agents and NER inhibitors alone or in combination. ....	148
<b>Figure 4.12.</b> Interaction between endogenous ERCC1 and XPF revealed by a proximity ligation assay (red dots) in A549 cells incubated alone (NT) or in the presence of <b>A4</b> or <b>B9</b> (2 $\mu$ M) or cisplatin (20 $\mu$ M) for 24 h.....	149

## Chapter 5

<b>Figure 5.1.</b> Structural modifications on <b>B9</b> or <b>A4</b> for lead optimization. ....	180
---	-----

# List of Tables

## Chapter 2

<b>Table 2.1.</b> Pharmacophore Features Built from the Docking Pose of <b>1</b> to the XPF Site .....	50
<b>Table 2.2.</b> Computational Results for the Subset of Analogues Chosen for Synthesis .....	52
<b>Table 2.3.</b> Decomposition of Total MM/GBSA Binding Energy in Different Contributions for Compound <b>1</b> and the Two Top Analogues.....	53
<b>Table 2.4.</b> Half-Maximum Inhibitory Concentrations for The Compounds with The Highest Inhibitory Potentials .....	59
<b>Table 2.5.</b> Pharmacokinetic Profile of Compound <b>4</b> and Compound <b>1</b> .....	67

## Chapter 3

<b>Table 3.1.</b> Main Ligand–Receptor and Ligand–Solvent Hydrogen Bonds Detected for the XPF–F06 Complex During the Last 100 ns of MD Simulation <sup>a</sup> .....	102
<b>Table 3.2.</b> Computational Results for the Series of F06 Analogues Selected for Chemical Synthesis <sup>a</sup> .....	108

## Chapter 4

<b>Table 4.1.</b> The Half-maximum Inhibitory Concentrations (IC <sub>50</sub> ) and Binding Constants Values of Inhibitors.....	141
--	-----

# List of Schemes

## Chapter 2

**Scheme 2.1.** Synthetic route of compounds **1–8** A) One-pot sequential addition reaction. B) Main steps and intermediates included in the one-pot sequential addition reaction..... 56

## Chapter 3

**Scheme 3.1.** General synthetic route of **Gen B** compounds..... 107

## Chapter 4

**Scheme 4.1.** General synthetic route for **Gen C** compounds..... 136

# Abbreviations

°C	Celsius
μL	microliter
μM	micromolar
6-4 PPs	pyrimidine- (6-4)-pyrimidone
6-FAM	6-Carboxyfluorescein
Å	angstrom
ADME	absorption, distribution, metabolism and elimination
AP	apurinic
APE	apurinic endonuclease
ATCC	American Type Culture Collection
BER	base excision repair
CADD	computer-aided drug design
CHAPS	3-[(3-cholamidopropyl)dimethylammonio]-1-propanesulfonate
CHK1	human checkpoint kinase
CO <sub>2</sub>	carbon dioxide
CPD	cyclobutene pyrimidine dimer
CSA	Cockayne syndrome
CYP	cytochrome P
d	doublet (spectral)
D	aspartic acid
DCM	dichloromethane
DMEM	Dulbecco's Modified Eagle's Medium
DMSO	dimethyl sulfoxide
DSB	double-strand breaks
E	glutamic acid
EDG	electron donating group
EDTA	ethylenediamine tetraacetic acid
Eq	equivalent

ERCC1	excision repair cross-complementation group 1
Et	ethanol
EWG	electron withdrawing group
FBS	fetal bovine serum
FEN	flap endonuclease
GBVI/WSA	Generalized Born Volume Integral/Weighted Surface Area
Gen	generation
GG-NER	global genome nucleotide excision repair
H	histidine
HA	heavy atom
HBA	hydrogen bond acceptor
HBD	hydrogen bond donor
HCl	hydrochloric acid
HEPES	N-2-hydroxyethylpiperazine-N-ethanesulfonic acid
HhH2	helix-hairpin-helix
HPLC	high performance liquid chromatography
HR	homologous recombination
HRMS	high resolution mass spectrometry
HTS	high throughput screening
Hz	hertz
IC <sub>50</sub>	half maximal inhibitory concentration
ICL	inter-strand crosslink
IgG	immunoglobulin G
<i>in vitro</i>	referring to the studies performed in living organisms
<i>in vivo</i>	referring to the studies performed in cell culture
<i>in silico</i>	computer simulation in reference to biological experiments
<i>i</i> -PrOH	isopropyl alcohol
FTIR	fourier transform infrared
IR	ionizing radiation
J	coupling constant (in NMR)
K	lysine

$K_d$	dissociation constant
LC	liquid chromatography
M	moles per liter
m	multiplet (spectral)
M	methionine
m/z	mass to charge ratio
MD	molecular dynamics
Me	methyl
MeCN	acetonitrile
MeOH	methanol
MHz	megahertz
Min	minute
mL	milliliter
MM/GBSA	Molecular Mechanics-Generalized Born Surface Area
MMC	mitomycin C
MMR	mismatch repair
MOE	molecular operating environment
Mp	melting point
MS	mass spectrometry
MST	microscale thermophoresis
NaCl	sodium chloride
NER	nucleotide excision repair
NHEJ	non-homologous end joining
nm	nanometer(s)
NMA	normal mode analysis
NMR	nuclear magnetic resonance
NSCLC	Non-small cell lung cancer
OMe	methoxy
PBS	phosphate-buffered saline
PDB	protein data bank
PK-C	protein kinase-C

PLA	proximity ligation assay
Polb	polymerase b
Ppm	part per million
q	quartet (spectral)
Q	glutamine
R	arginine
R	generalized alkyl group of substituents
RFU	relative fluorescence units
RMSD	Root-mean-square deviation of atomic positions
ROS	reactive oxygen species
s	singlet (spectral)
SAM	S-adenosylmethionine
SAR	structure activity relationship
SD	standard deviation
SEM	standard error of mean
SNAr	nucleophilic aromatic substitution
SPR	surface plasmon resonance
TC-NER	transcription-coupled nucleotide excision repair
TLC	thin layer chromatography
UV	ultraviolet
VS	virtual screening
WT	wild type
wt.	weight
XP	xeroderma pigmentosum
Y	tyrosine
$\delta$	chemical shift in parts per million downfield from tetramethylsilane
$\lambda$	wavelength

# Chapter 1

## 1. Introduction

### 1.1 Cancer

Cancer is a global public health problem and is the second leading cause of death in the United States.<sup>1</sup> In 2017, of 1.7 million of cancer patients, about 0.6 million patients died from the disease.<sup>1</sup> Drug resistance, which results in ineffectiveness of the drug treatment, is responsible for 90% of the cancer-related deaths.<sup>2-4</sup> Cancer related drug resistance is a widely known phenomenon that results from the tolerance of cancer to the pharmaceutical treatment. Resistance to cancer therapeutics arises from a wide array of factors, such as epigenetic changes and/or genetic mutations, upregulated drug efflux, and several other molecular and cellular pathways. Currently, cancer therapy is managed mainly by radiotherapy, chemotherapy, surgery, and immunotherapy.<sup>5-7</sup> Despite the successful achievements made in treating various cancers during the past decades, a major problematic issue in cancer management arises due to the development of resistance to either conventional chemotherapeutics or novel targeted therapies.<sup>8,9</sup>

Several conventional chemotherapeutic anticancer agents, such as platinum-containing drugs, cyclophosphamide, and mitomycin C elicit cytotoxicity to cancer cells by damaging their DNA directly; however, such therapy lacks specificity and showed a high toxicity to normal cells as well. Although many drugs targeting proliferation of cancer cells provided significant benefit during initial treatment, the majority of cancer patients develop resistance as treatment continues. For example, there is a 30%–55% relapse occurrence in non-small cell lung cancer (NSCLC) patients who eventually die

from the disease.<sup>10</sup> The ovarian adenocarcinomas relapse within the first year after chemotherapy and surgery is 50%–70%.<sup>11</sup> In addition, about 20% of pediatric patients develop a recurrence of acute lymphoblastic leukemia.<sup>12</sup> About 60% of colorectal cancer patients develop relapses after two years of related chemotherapy treatment.<sup>13</sup> Therefore, mechanisms and pathways underlying the drug resistance must be well-understood, and there is an urgent need to facilitate the development of novel therapeutic modalities that lead to better clinical outcomes.

## **1.2 Sources of DNA Damage**

Like most biomolecules, DNA can undergo various chemical reactions; however, such reactions often can lead to changes in the genetic code for various critical cellular proteins (Figure 1.1). Intrinsic or extrinsic agents may cause DNA damage; however, in general, most of the DNA modifications are endogenous in origin and are mediated by spontaneous hydrolysis.<sup>14, 15</sup> The N-glycosidic bond between the deoxyribose and DNA base is especially prone to hydrolytic cleavage under acidic conditions. The products of hydrolytic nucleobase loss from abasic or AP sites (apurinic/apyrimidinic sites) occur at an approximate rate of ~10,000 per cell per day.<sup>15, 16</sup> Moreover, abasic sites are chemically labile and prone to  $\beta$ -elimination that may cause DNA strand scission.<sup>17</sup> Another well known hydrolysis reaction is the deamination of DNA bases bearing exocyclic amino groups.<sup>15, 18</sup> Most of these lesions form uracil from cytosine, which is estimated to occur 100–500 times per cell per day.<sup>19, 20</sup> In addition, hypoxanthine and xanthine could be formed by the spontaneous deamination of the

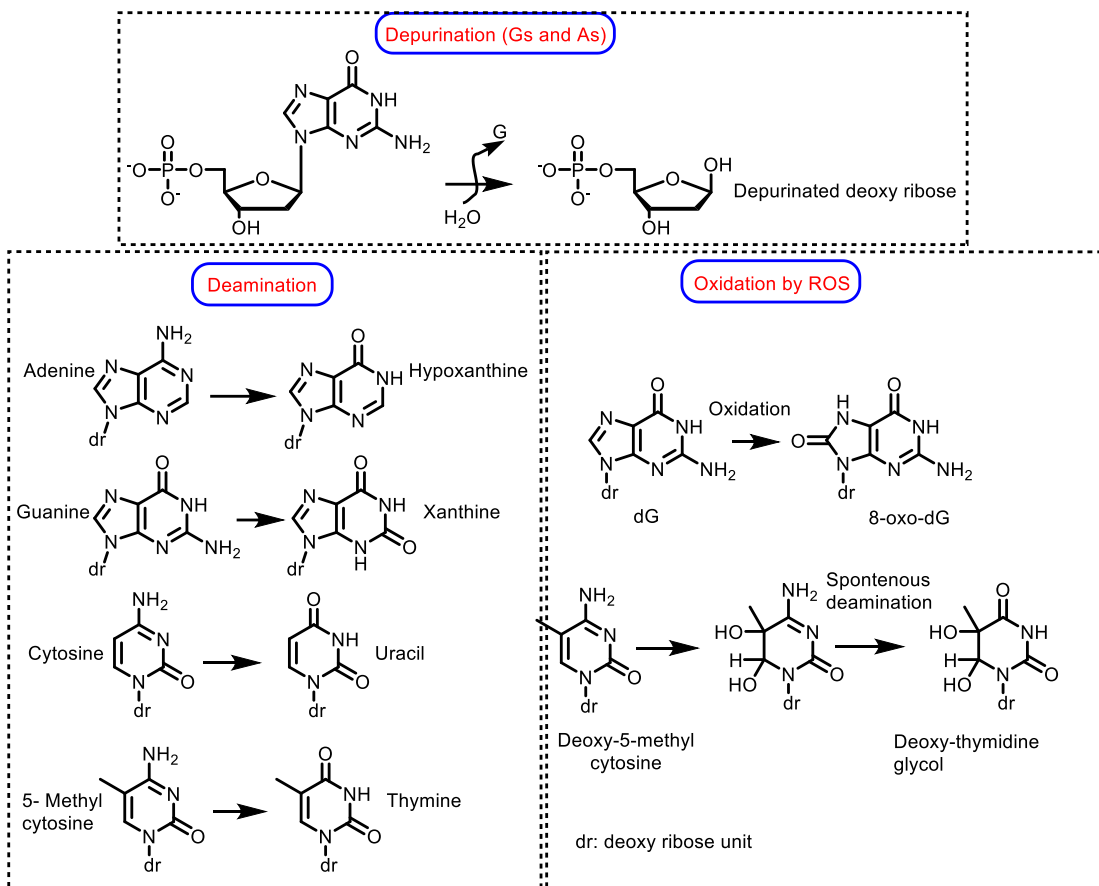


**Figure 1.1.** Endogenous events as sources of DNA damage.

adenine and guanine, respectively.<sup>21</sup> The DNA strand also can be modified chemically by reactive oxygen species (ROS), such as  $O_2^{\cdot-}$ ,  $H_2O_2$ , and  $\cdot OH$  produced during normal cellular metabolic processes.<sup>22, 23</sup> ROS create more than one hundred different oxidative DNA adducts, such as deoxyribose oxidation, base modification, DNA-protein cross-links, and single- or double-strand breakage.<sup>24</sup> Endogenous reactive nitrogen species, such as nitric oxide ( $NO^{\cdot}$ ) and its byproducts, also can create similar oxidative adducts.<sup>25</sup> For example, 8-oxoguanine is the most commonly studied oxidative DNA lesion that is used as a measure of oxidative DNA damage in biological systems.<sup>26</sup> Alkylation, which occurs primarily at O and N atoms of nucleobases, is another example of DNA damage

caused by endogenous reactive molecules, such as S-adenosylmethionine (SAM) and methyl radicals produced by lipid peroxidation.<sup>14, 27</sup>

Cellular DNA also could be insulted by exogenous DNA-damaging agents, such as ionizing radiation (IR) and classical chemotherapeutic agents, which are used widely in cancer therapy because of their capability of forming DNA lesions that resulted from interference with various DNA-associated proteins and/or DNA breaks. These, in turn, might cause disruption to normal cellular processes, such as replication, transcription, and/or recombination, and thus lead to cell death.<sup>28, 29</sup> The outcome of treatment with such cancer therapeutics, whether the cell will survive or die, is dependent on how the cells respond to the damaged DNA by activating DNA repair streams or cell cycle arrest.<sup>30</sup> Normal cells can reverse the DNA damage caused by many chemotherapeutic drugs and IR by inducing appropriate repair mechanisms. Cancerous cells have a similar capacity to recognize DNA lesions effectively and initiate DNA repair pathways; however, this phenomenon leads to treatment resistance to various cancer therapeutics.<sup>31</sup> On the other hand, because of the inherited or somatic mutations in certain DNA repair genes, cancer cells would depend on functioning DNA mechanisms more than the normal cells.<sup>32</sup> Therefore, therapeutics that are able to manipulate the DNA repair pathways have the potential of sensitizing cancer cells to the cytotoxic chemotherapeutic agents and IR. Several reports stated that the activation of DNA repair pathways is responsible for the chemoresistance of cancer cells to DNA-damaging agents and suppressing DNA repair pathways, leading to potentiation to these cytotoxic agents.<sup>33, 34</sup>

## 1.3 Major DNA Repair Pathways and Cancer Therapy

### Resistance

Cells have developed several repair mechanisms to correct lesions caused by DNA damage (Figure 1.2) Mammalian cells have four major DNA repair pathways: mismatch repair (MMR), base excision repair (BER), double-strand break repair, which includes both homologous recombination (HR) and non-homologous end joining (NHEJ), and nucleotide excision repair (NER).

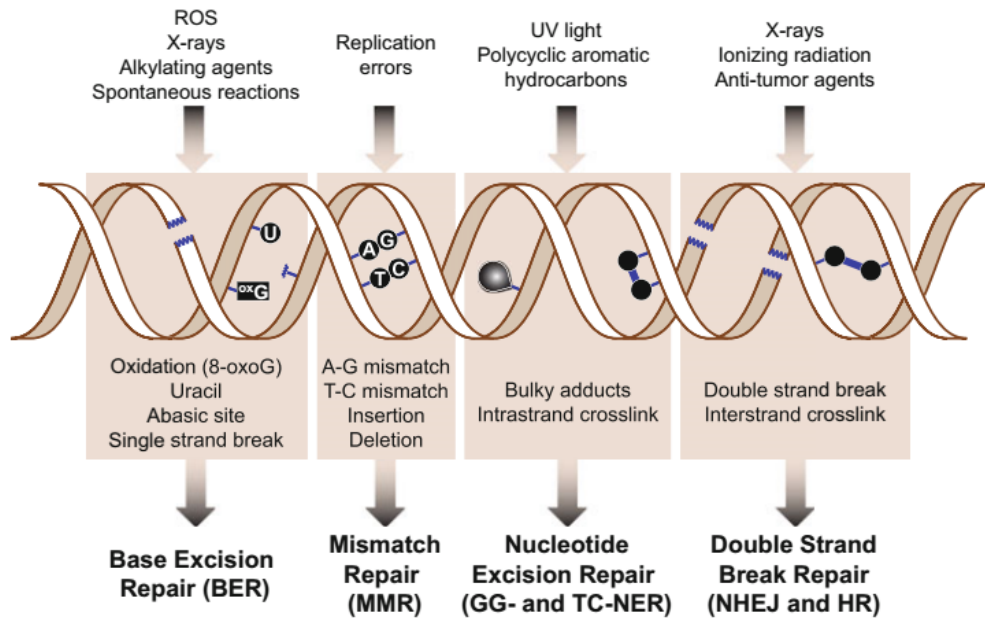


**Figure 1.2.** DNA damage and repair pathways. The diagram shows common DNA damaging agents, examples of DNA lesions caused by these agents, and the relevant DNA repair mechanism responsible for their removal, (figure adapted with permission from Boland et al.<sup>35</sup>).

### 1.3.1 Mismatch Repair (MMR)

The MMR system plays a central role in the repair of mis-incorporated bases that pass by the proofreading step post-replication. In addition, MMR proteins also recognize and correct faulty loops (IDLs) that are inserted or deleted from polymerase slippage during

the replication of repetitive DNA sequences. The importance of this pathway is the fact that MMR deficient cells are reported to display a mutator phenotype, which is characterized by an elevated mutation frequency and a microsatellite instability. Another more important point is that MMR genes that have germline mutations are predisposed to a wide variety of cancers, especially the inherited non-polyposis colon cancer, also known as Lynch syndrome.<sup>36</sup> The MMR mechanism can be categorized into three main steps: 1) a recognition step of mis-paired bases, 2) an excision step where the damaged DNA strand is degraded, resulting in a gap, and 3) a repair synthesis step, where the DNA is re-synthesized to fill the gap.<sup>37-39</sup>

### **1.3.2 Base Excision Repair (BER)**

The base excision repair mechanism recognizes and accurately removes damaged bases that are formed by oxidation, alkylation, ring saturation, or ionizing radiation,<sup>40</sup> and also eliminates the deaminated bases and DNA single strand breaks (SSBs). Base lesions are excised by a damage-specific endonuclease, called DNA glycosylase, resulting in the formation of potentially cytotoxic apyrimidinic or apurinic sites (AP sites) intermediates. Afterwards, the AP sites are processed by an AP endonuclease (APE1), which produces a strand break that is processed further by poly (ADP-ribose) polymerase (PARP), DNA polymerase b (Polb), and ligase III. Subsequent repair steps are followed and completed through further stream events.<sup>41</sup>

### **1.3.3 Double-strand Break Repair (DSB)**

Double-strand breaks (DSBs) are one of the most biologically hazardous kinds of DNA damage. For example, a single unrepaired DSB is often enough to cause cell death.

Moreover, inaccurate repair events can result in chromosomal aberrations or deletions, which are associated with the development of some genomic instability syndromes or cancer. Therefore, the repair of DSBs is vital for both the maintenance of genome integrity and cell survival.<sup>42, 43</sup> The two main pathways by which eukaryotic cells repair DSBs are homologous recombination (HR) and non-homologous end-joining (NHEJ). The difference between these two repair mechanisms is in their fidelity of DSB repair and their requirement for a homologous template DNA. Generally, HR repair is an error-free pathway because it utilizes the undamaged sister chromatid genetic information as a template.<sup>44</sup> On the contrary, NHEJ directed-repair normally is prone to errors, and the elimination of DSBs is mediated by direct ligation of the broken ends.<sup>45</sup> NHEJ is reasoned to be the dominant mechanism in mammalian cells that operate in all phases of the cell cycle, whereas HR is restricted to the G2 and late-S phases.

### **1.3.4 Nucleotide Excision Repair (NER)**

NER is a highly versatile repair mechanism that can recognize, verify, and remove various bulky, helix-distorting lesions from the DNA. The most important of these damages are pyrimidine dimers, such as 6–4 photoproducts and cyclobutane pyrimidine dimers (CPD), which are photoproducts generated by the UV component of sunlight (Figure 1.3).

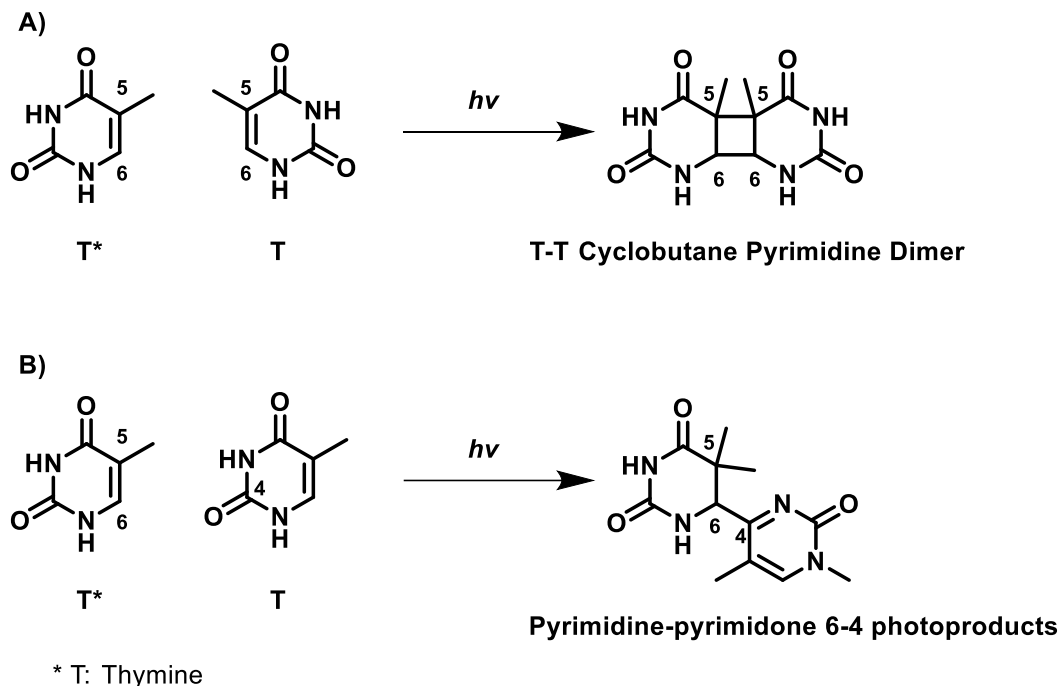


**Figure 1.3.** UV-induced formation of A) a cyclobutane pyrimidine dimer and B) a pyrimidine-pyrimidone 6-4 photoproduct.

Another significant substrate of NER is cisplatin-DNA adducts, which cause intra-strand crosslinks. NER is mediated by a sequence of assembled repair proteins at the site of the DNA damage. Although mechanistically similar to the BER pathway, the NER mechanism is much more complex because it requires about thirty different proteins to carry out a multi-step ‘cut-and-patch’-like pathway. These steps include the recognition of DNA lesion, opening of the DNA double helix around the local lesion, and excision of a short single-strand sequence of DNA spanning the damage, followed by a sequential repair synthesis and strand ligation steps.<sup>46-49</sup> The biological importance of NER is reasoned by the fact that defects in NER cause many human genetic diseases, such as xeroderma pigmentosum, trichothiodystrophy, and Cockayne syndrome; these conditions all cause extreme sun sensitivity. Furthermore, these disorders develop

symptoms that overlap with developmental delay, neurodegeneration, immunological defects, premature aging, and cancer.<sup>50, 51</sup>

### **1.3.4.1 Mechanism of NER**

The NER pathway consists of two related sub-pathways, termed transcription-coupled NER (TC-NER) and global genome NER (GG-NER)<sup>49</sup> (Figure 1.4). As the names imply, TC-NER plays a preferential role in repairing lesions located on the coding strand of genes that are transcribed actively, whereas GG-NER eliminates damaged DNA throughout the genome. Both pathways are the same mechanistically, regardless of the initial damage recognition step. In GG-NER, the main protein complex for damage recognition is XPC/HR23B/CEN2 (XP complementation group C/Rad23 homolog B/Centrin-2).<sup>52</sup> CEN2 and HR23B are accessory proteins that increase both the specificity and affinity of XPC binding to helix-distorting DNA damage. Additionally, the binding affinity of DNA to XPC generally correlates with the extent of helical distortion.<sup>53</sup> For instance, XPC has a low affinity to DNA lesions formed by only minor distortions, such as UV-induced CPDs. Therefore, the UV-damaged DNA binding complex (UV-DDB), an auxiliary damage-recognizing complex that consists of two subunits, XPE (DDB2) and DDB1, initially recognizes and detects these kinds of lesions. The subsequent binding of UV-DDB to lesions result in only minor distortions (i.e., DNA bending), which, in turn, facilitate the recruitment of the XPC complex to the damaged site.<sup>54</sup>

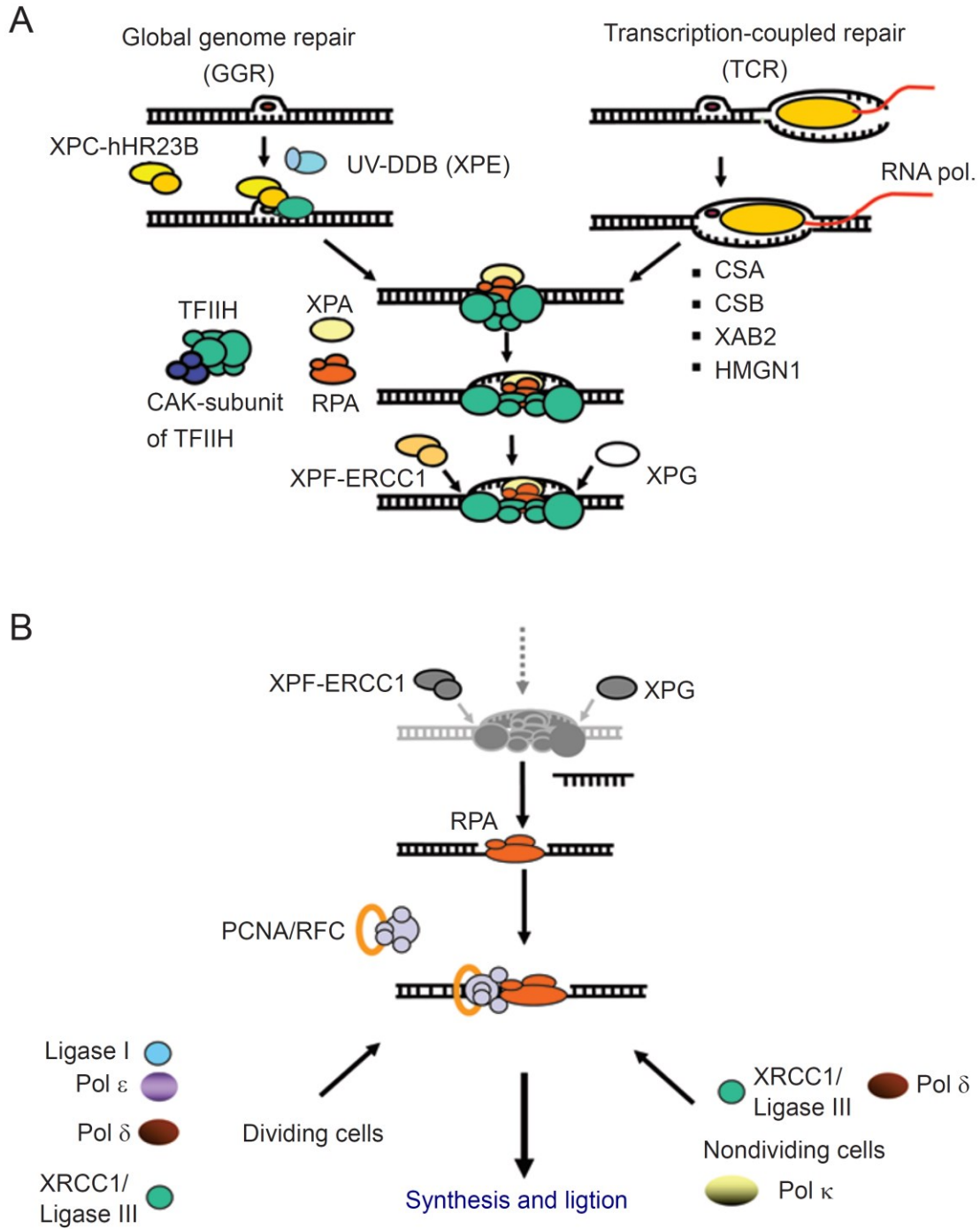


**Figure 1.4.** A simplified model of steps of Nucleotide Excision Repair (NER). A) Recognition of DNA damage that differs between transcription coupled- and global genomic NER (TC-NER and GG-, respectively). B) dual incision of DNA strand, ligation and synthesis of DNA strand. (copied with permission from Fousteri et al.<sup>55</sup>).

On the contrary, in TC-NER, the initial recognition of DNA damage is started when an elongating RNA polymerase II (RNAPII) is arrested upon encountering a site of DNA lesion.<sup>55</sup> Afterwards, Cockayne syndrome A (CSA) and B (CSB), two TC-NER-specific proteins, are believed to replace the stalled RNAPII to facilitate the access of NER proteins to the damage.<sup>56</sup> Subsequently, both TC-NER and GG-NER continue via the common 'core' NER reactions. At first, either the XPC complex in CSB and CSA in TC-NER or GG-NER recruit multi-functional transcription factor TFIIH and a ten protein-complex (multi-subunit) to the lesion site. Next, the asymmetric unwinding of the DNA helix is orchestrated by ATP-dependent helicases, such as XPB and XPD, to produce a bubble consisting of ~30 nucleotides flanking the damaged DNA site.

A second level of damage recognition is activated upon initial DNA unwinding by having access of XPA to the region of the lesion to ensure that unaffected DNA is not subjected to excision repair. Upon XPA binding to the damaged DNA, a heterotrimeric single stranded DNA binding protein, called RPA (replication protein A), is recruited for stabilizing the pre-incision complex and extension completion. In the following step, ERCC1–XPF and XPG, two structure-specific endonucleases, cleave at the 5' position of a deoxyribose phosphodiester and XPG cleaves at the 3' position of a different deoxyribose phosphodiester, respectively, resulting in the excision of about 30 nucleotides from the lesion site. Finally, DNA polymerase  $\delta$  or  $\epsilon$  utilizes the undamaged DNA strand as a template to re-synthesize the produced gap. Then, DNA ligase seals the nick of the repaired strand, thus finalizing the NER process.<sup>49</sup>

## 1.4 ERCC1–XPF and DNA Repair Pathways

The ERCC1–XPF protein complex is a 5′-3′ structure-specific endonuclease that is involved in several DNA repair mechanisms in mammalian cells. It is crucial for nucleotide excision repair (NER) because it removes pyrimidine-(6,4)-pyrimidone photoproducts (6-4PPs) and cyclobutane pyrimidine dimers (CPDs) induced by UV irradiation by having the damaged DNA strand 5′ and 3′ incised, respectively. The ERCC1–XPF heterodimer also plays a central role in the repair of chemically induced helix-distorting and bulky DNA lesions, which are all substrates for the NER pathway. ERCC1–XPF also has a key role in the repair of double-strand breaks (DSBs), induced by free radicals, ionizing radiation, and chemotherapeutics such as the crosslinking agents mitomycin C (MMC) and cisplatin, or the topoisomerase inhibitor etoposide, which can be repaired by non-homologous end-joining (NHEJ) repair or homologous recombination (HR). The role of ERCC1–XPF in DSB repair (DSBR) was shown previously in budding yeast where mutations in RAD1 and RAD10, the yeast orthologues of XPF and ERCC1, suppressed the HR repair pathway.<sup>57</sup> Mammalian cells containing mutant ERCC1–XPF were shown to be sensitive to DSBs,<sup>58</sup> and both the NHEJ and HR streams for DSBR were attenuated.<sup>59, 60</sup> The principle activity of the ERCC1–XPF heterodimer in both types of DSBR is its capability to remove non-homologous 3′ single-stranded flaps at broken ends before their rejoining.<sup>58</sup>

It is also noteworthy to mention that the ERCC1–XPF complex is involved in inter-strand crosslink (ICL) repair. ERCC1-XPF endonuclease operates to remove chemotherapeutic-induced crosslinks caused by psoralen, cisplatin, and MMC<sup>61</sup>. Such damages are particularly toxic because of their ability to prevent helix unwinding and,

in turn, block the transcription and replication phases. The sensitivity of mammalian cells with ERCC1–XPF mutation to ICL DNA-damaging agents was found to be significantly higher than the wild-type cells.<sup>61</sup> In eukaryotes, the pathway of ICL removal is dependent on the cell cycle phase in which the lesion is encountered.<sup>62</sup> Incisions adjacent to an ICL are repaired completely in the G0 or G1 phase, whereas ICL lesions persist into the S stage and will be repaired by the DSB pathway. The ERCC1–XPF-dependent step is required not only in several models for ICL repair<sup>61, 62</sup> to carry out the incision on either side of an ICL<sup>63</sup> but also in the S-phase-dependent and -independent ICL repair pathway.<sup>64, 65</sup>

## **1.5 Patients with NER Deficiency and Mutated ERCC1–XPF**

Inherited defects in human NER genes lead to rare syndromes, such as Cockayne syndrome (CS), xeroderma pigmentosum (XP), and trichothiodystrophy. While XP is considered a repair syndrome, trichothiodystrophy and CS are regarded as transcription syndromes.<sup>66</sup> Diagnostic characteristics of XP are dry skin and abnormal pigmentation that is patterned in areas exposed to sun, developing into severe photosensitivity. This leads to an increase in the risk of developing UV-induced skin cancers by more than 1000-fold. Also, about 20–30% of XP patients have progressive neurological disorders, emphasizing how NER is extremely important in repairing endogenous DNA damage.<sup>66</sup> CS patients are photosensitive as well but do not develop pigmentation abnormalities or an increased risk of having cancer,<sup>66, 67</sup> however, they show neurological and developmental defects.<sup>66</sup>

Mutations in XP patients are characterized by mutated ERCC1<sup>68</sup> and XPF genes.<sup>69,70</sup> Mutations in the XPF or ERCC1 genes can result in a rare XF-E syndrome.<sup>71</sup> XF-E patients exhibit similar characteristics of XP and CS and show additional neurologic, musculoskeletal hepatobiliary and hematopoietic symptoms.<sup>71</sup> XF-E patients not only have a complete loss of GG- and TC-NER but also develop hypersensitivity to ICL agents due to the central role of ERCC1–XPF in the repair of ICL damage.<sup>71</sup> This is what distinguishes XF-E syndrome from either XP or CS.<sup>71</sup>

## 1.6 The Structure of ERCC1–XPF Endonuclease

The ERCC1 domain consists of 297 amino acids, with a central domain that is catalytically inactive but plays a key role in interaction with both the XPA protein and DNA,<sup>72, 73</sup> and a helix-hairpin-helix (HhH2) domain required for heterodimerization with XPF (Figure 1.5).<sup>72, 74, 75</sup>

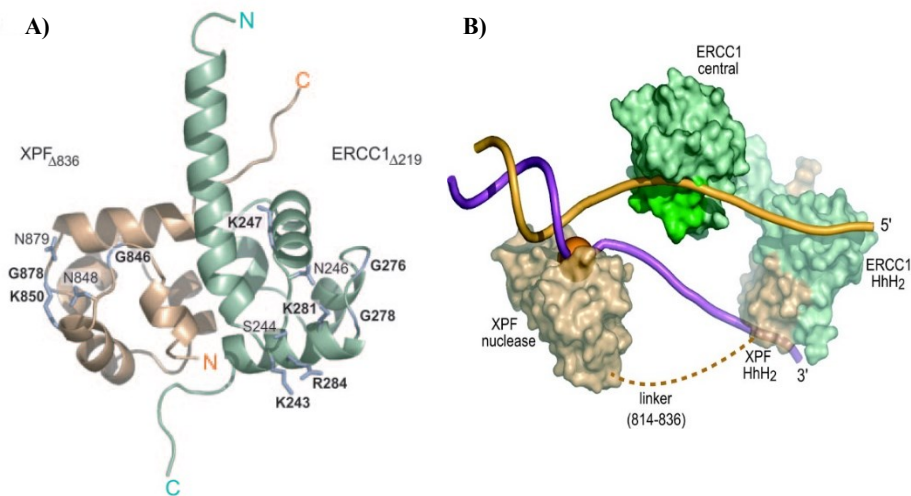


**Figure 1.5.** Structure of ERCC1–XPF copied with permission from Tsodikov et al\*.<sup>72</sup> A) Crystal structure of ERCC1–XPF heterodimeric HhH2 complex, B) A model for XPF<sub>Δ655</sub>–ERCC1<sub>Δ95</sub> binding to a splayed-arm DNA substrate. Light brown indicates XPF, and green indicates ERCC1. The cleavage site is shown by the orange sphere, and the linker between the nuclease and the HhH2 domains of XPF by the dashed line. The XPA binding region of ERCC1 (residues 99–118) is shown in dark green.

\* "Copyright (2005) National Academy of Sciences, U.S.A."

On the other hand, the XPF protein domain has 916 amino acids, with key residues (FANCO) that are comprised of nuclease, helicase-like,<sup>76-78</sup> and helix–hairpin–helix (HhH2) domains.<sup>72, 74, 75</sup> The main protein–protein interaction of ERCC1 and XPF is the heterodimerization formation of their hydrophobic C-terminal domains to form a stable heterodimer complex through the double helix–hairpin–helix motifs in their HhH2 regions.<sup>74</sup> It is believed that XPF acts as a scaffold for ERCC1 during protein folding, and it is thought that ERCC1 lacks the ability to fold correctly *in vitro* without the presence of XPF.<sup>74</sup> It was shown that neither protein was stable in monomeric form and rather forms aggregates after the exposure of their hydrophobic interaction domains, leading to their rapid degradation.<sup>74, 75</sup> It has been proven that without dimerization, the endonuclease activity of the protein complex that came from the catalytic nuclease domain within XPF was lost. In addition, it has been shown that the catalytically inactive ERCC1 fragment remains indispensable for the heterodimer complex activity.<sup>74</sup>

### **1.6.1 Residues Essential for ERCC1–XPF Dimerization and DNA Binding**

The HhH2 domains of ERCC1 and XPF have a predominant hydrophobic interacting surface.<sup>72</sup> XPF Phe905 and ERCC1 Phe293 are two crucial residues essential for dimerization interaction, which allows the two proteins to be anchored together (Figure 1.6). In some of the reported mutational studies, the deletion of ERCC1 Phe293 led to complete loss of catalytic activity, and no evidence of heterodimerization.<sup>69, 79</sup> Therefore, this could explain the decreased levels of ERCC1

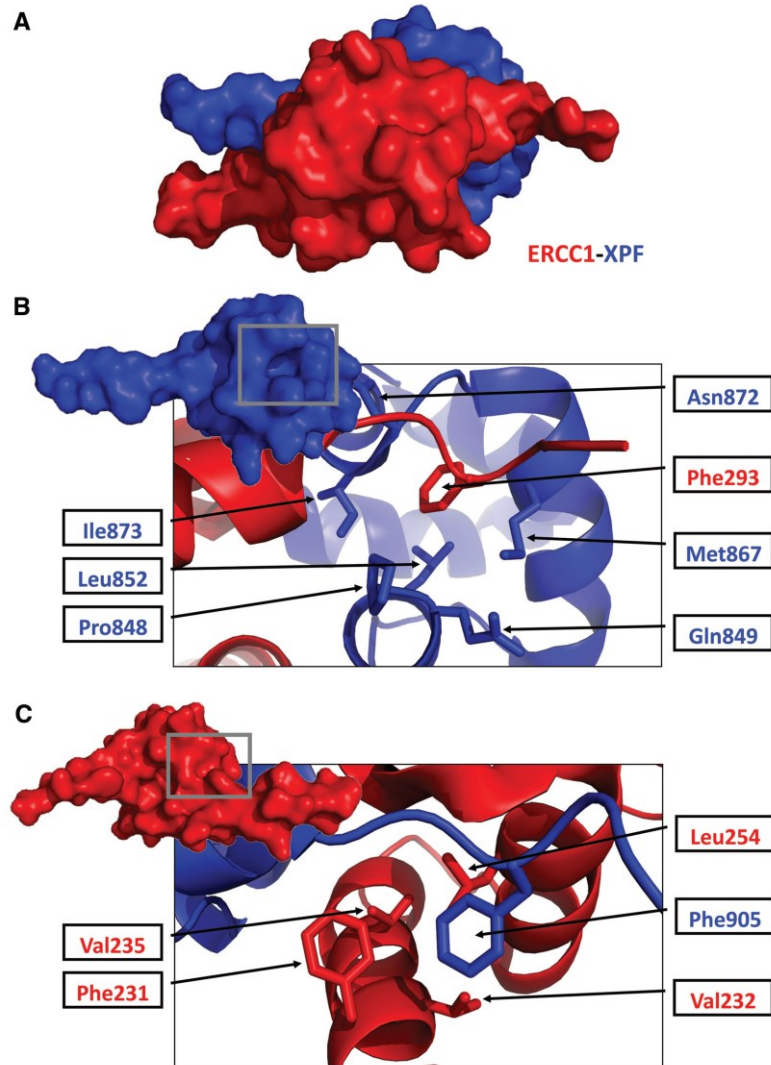


**Figure 1.6.** Interaction of ERCC1 and XPF through their HhH2 domains copied with permission from Tsodikov et al.<sup>72</sup> (A) Heterodimer of the HhH2 domains of ERCC1 (red) and XPF (blue). (B) Expanded cartoon representation of the region boxed on XPF, identifying key interacting residues in the XPF pocket for ERCC1 Phe293. (C) Expanded cartoon representation of the region boxed on ERCC1, identifying key interacting residues in the ERCC1 pocket for XPF Phe905. Figure created using PyMOL v0.99 with the ERCC1–XPF HhH2 domain crystal structure (PDB code 2A1J).

XPF complex and moderate sensitivity to crosslinking agents and UV observed in cells from patients with XPF Phe905 mutations.<sup>80</sup>

It is also important to denote that the binding of the HhH2 fragment to DNA significantly affects the endonuclease activity of the protein complex. It has been reported that the HhH2 domains of ERCC1–XPF form two independent binding sites to

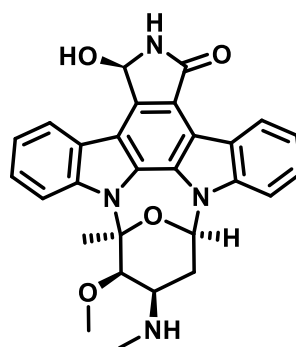
complex with ss-DNA.<sup>72, 74</sup> This interaction is thought to be needed for an appropriate orientation of the ERCC1–XPF complex at the ds- to ss-DNA junction.<sup>81</sup> Tripsianes et al.<sup>74</sup> monitored chemical shift perturbations after DNA binding and observed that both central and hairpin regions of ERCC1 and XPF were in contact with DNA; however, the DNA interaction by XPF could not be detected under their experimental conditions. Tsodikov et al.<sup>72</sup> also observed similar DNA contacts with ERCC1 residues, but noticed that XPF made DNA interactions via Gly857, Lys861, and Gly889 residues. They demonstrated that the HhH2 domain of the recombinant truncated version of ERCC1-XPF complex binds to two ss-DNA strands with a 6-fold preference over ds-DNA and was assessed via the binding affinity measurements.<sup>72</sup>

## **1.7 Small Molecule Targets of the ERCC1–XPF Heterodimer**

Various strategies for inhibition of ERCC1–XPF are described in the following sections. However, the three targets with highest therapeutic potential on the ERCC1–XPF heterodimer are the XPA-binding domain needed for NER complex recruitment, the XPF endonuclease domain that is required for the catalytic activity of the ERCC1–XPF complex, and the ERCC1–XPF interaction domain required for stability and catalytic activity.

### **1.7.1 ERCC1/XPA Binding Inhibitors**

Hong et al. reported that UCN-01 **1** (Figure 1.7), a non-specific human checkpoint kinase (CHK1) and protein kinase-C (PK-C) inhibitor, was able to inhibit the NER pathway by reducing the ERCC1 binding to the XPA domain and showed an activity on lung and colorectal cancer.<sup>82</sup>



**UCN-01 (1)**

**Figure 1.7.** Structure of UCN-01 as an ERCC1–XPA inhibitor.

Barakat et al. observed that upon DNA-lesion formation and UCN-01 treatment, DNA-bound XPA accumulation was noticed; however, DNA-bound ERCC1 was observed to have decreased. The binding energy of UCN-01 to ERCC1 was calculated *in silico* with a value of 4.81 kcal/mol.<sup>83</sup> UCN-01 also was shown to bind into the ERCC1–XPA interaction site, resulting in disruption of the interaction between Tyr145 and Tyr152 in ERCC1 and capturing several hydrogen bond interactions that stabilize the UCN-01/ERCC1 interaction.<sup>83</sup> Potential ERCC1–XPA interaction inhibitors were screened *in silico*, but the *in vitro* or *in vivo* activity of these compounds has not been investigated yet.<sup>83</sup> The *in vitro* and *in vivo* inhibition of this site has been demonstrated by Tsodikov et al. with a synthetic XPA peptide that mimicked the interacting XPA region.<sup>73</sup> Therefore, ERCC1–XPA interaction inhibition is an attractive target for drug design and discovery due to the known inhibitors and the availability of crystal structures. However, an inhibitor of this interaction site would only cause disruption to NER and would not have an effect on the role of ERCC1–XPF in either ICL or DSB repair. Thus, use of an ERCC1/XPA inhibitor synergistically with a DNA crosslinking

agent, such as platinum containing compounds, would be of limited benefit, despite the promising early evidence for inhibition of ERCC1–XPA interaction.

### 1.7.2 XPF Endonuclease Inhibitors

Inhibition of all well-known functions of ERCC1–XPF in DNA repair could be achieved by inhibiting the nuclease catalytic domain of XPF (Figure 1.8). Because of the presence of the divalent metal ion ( $Mg^{2+}$ ) in the active site, it provides a potential target for metal ion chelation, which weakens XPF binding with DNA and thus inhibits its endonuclease activity.

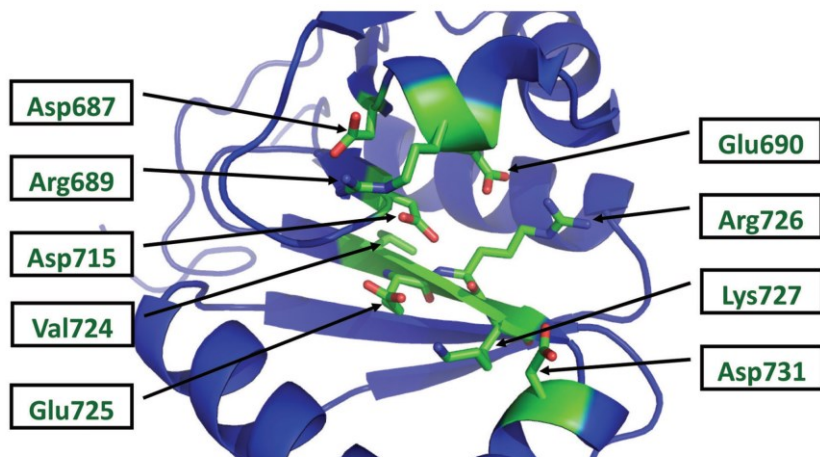


**Figure 1.8.** The nuclease domain of XPF. Cartoon representation of XPF identifying amino acids and their side chains. Residues Asp687, Glu690, Asp715, and Glu725 are implicated in metal binding.<sup>84</sup> No metal ion has been shown. Figure created using PyMOL v0.99 with a homology model of XPF generated using the Protein Homology/ analogy Recognition Engine v2.0 (PHYRE).<sup>85</sup> Although the crystal structure of XPF (PDB code 2BGW) from an archaebacterial strain<sup>86</sup> has been used widely to produce a human homology model to facilitate the development of active site inhibitors, there is no crystal structure reported for the human XPF endonuclease domain to date, (copied with permission from McNeil et al.<sup>87</sup>).

McNeil et al.<sup>88</sup> employed *in silico* and high throughput screening (HTS) to identify inhibitors targeting the XPF catalytic active site. They were the first group to identify nuclease active site inhibitors for ERCC1–XPF and to conduct a fuller series of

biophysical, biochemical, and cancer-related cell-based assays. Their results from cell-free and cell-based assays showed that E-X AS5-4 **2** and E-X AS7 **3** (Figure 1.9) displayed specificity for  $\Delta$ ERCC1- $\Delta$ XPF, truncated versions of XPF (residues 667–916, containing the endonuclease and HhH2 domains) and ERCC1 (residues 96–297, containing the central and HhH2 domains), over two other endonucleases, such as FEN and DNAase enzymes *in vitro*, so that interfering with other signaling pathways involved with these enzymes would be minimized; however, no binding affinity values on ERCC1-XPF were reported for these compounds. The two active site inhibitors, E-X AS5-4 and E-X AS7, were able to block the NER pathway in two independent assays with micromolar  $IC_{50}$  values of 10  $\mu$ M and 2  $\mu$ M, respectively, and moderately sensitized NER-proficient mouse and human cells to cisplatin by 1.2-fold and 1.6-fold folds, respectively.

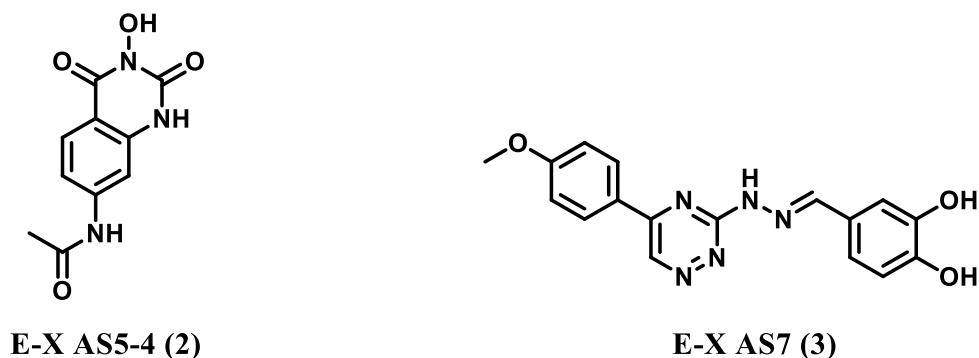


**Figure 1.9.** Structures of XPF endonuclease active site inhibitors E-X AS5-4 (**2**) and E-X AS7 (**3**).

Chapman et al.<sup>89</sup> have shown that a N-hydroxyimide-containing compound **4** (Figure 1.10) with the metal-binding chemotype inhibited the endonuclease activity of  $\Delta$ ERCC1- $\Delta$ XPF; however, they showed that it has a high potency against seminal endonuclease FEN-1. They further explored the structure-activity relationships (SARs)

around this nucleus that resulted in sub-micromolar inhibitors with enhanced selectivity for the  $\Delta$ ERCC1- $\Delta$ XPF over FEN-1.

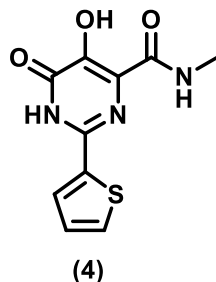


**Figure 1.10.** Structures of XPF endonuclease active site inhibitor hydroxypyrimidinone derivative.

Chapman and his co-workers<sup>90</sup> also identified catechol-based compounds (Figure 1.11) as ERCC1-XPF endonuclease inhibitors from HTS. Exploration of further structure activity relationship studies within this chemotype yielded compound **5**, which hampered NER through  $\Delta$ ERCC1- $\Delta$ XPF inhibition with an  $IC_{50}$  of 0.6  $\mu$ M and sensitized A375 melanoma cells to cisplatin through  $\delta$ H2AX assays. Due to the known toxicity of catechol groups, they screened other alternative fragments to the catechol group. The screening results revealed 3-hydroxypyridones, which were able to inhibit  $\Delta$ ERCC1- $\Delta$ XPF and yielded two compounds **6** and **7**, which showed inhibition of ERCC1-XPF with an  $IC_{50}$  values of <10  $\mu$ M.

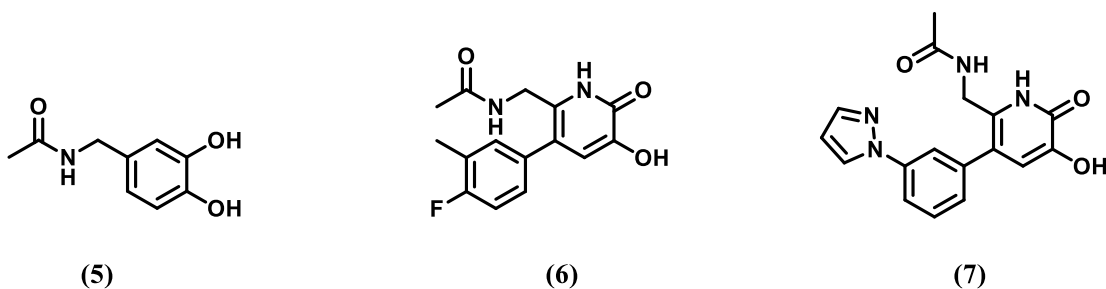


**Figure 1.11.** Metal chelators as ERCC1-XPF nuclease inhibitors.

Further efforts have been conducted for identifying small molecule inhibitors of ERCC1–XPF endonuclease activity. Recently, Arora et al.<sup>91</sup> developed a fluorescence-based assay suitable for HTS to identify ERCC1–XPF endonuclease inhibitors and able to decrease DNA repair function. The screening results yielded two hits (Hit 1: NSC143099 **8** and Hit 2: NSC 16168 **9**) (Figure 1.12), which had a high affinity to the purified  $\Delta$ ERCC1– $\Delta$ XPF enzyme and did not inhibit the DNA binding to it, resulting in inhibiting the nuclease activity of the protein complex. However, in cell culture experiments, Hit 1 lacked potency ( $IC_{50} \sim 15 \mu\text{M}$  for cisplatin efficacy). The authors hypothesized that the weak cellular activity displayed by Hit 1 could be due to significant off-target binding to unknown proteins, preventing the compound from inhibiting the enzyme in a complex cellular environment effectively.

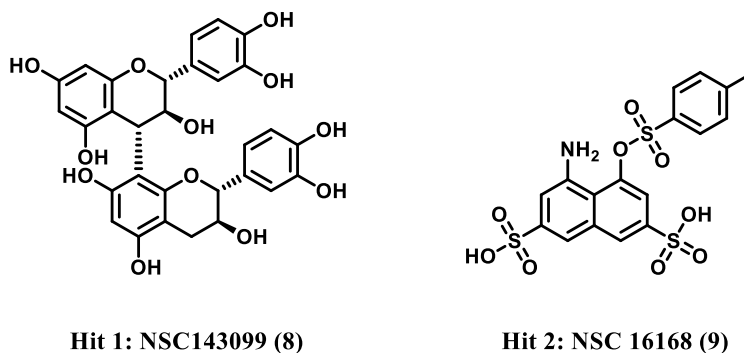


**Figure 1.12.** Structures of ERCC1–XPF nuclease inhibitors procyanidine **8** and hydroxy-naphthalene derivative **9**.

In contrast, **9** targeted the purified  $\Delta$ ERCC1– $\Delta$ XPF enzyme and also sensitized cancer cells towards cisplatin *in vitro*. Furthermore, Arora et al. carried out an *in vivo* experiment as a proof of principle using a xenograft of H460 lung cancer cells. The results showed that cisplatin efficacy was potentiated against these cancer cells.

Although all previous studies were conducted to target the catalytic nuclease active site of ERCC1–XPF, inhibition of such a domain of XPF is problematic due to

mechanistic similarity among several essential cellular endonucleases, such as Flap Endonuclease 1 (FEN1), which is necessary in NER and BER,<sup>92-94</sup> RAD51 recombinase, which is involved in HR,<sup>95</sup> and Apurinic/aprimidinic Endonuclease (APE1) needed for BER.<sup>96, 97</sup> Thus, attaining the required specificity into inhibitors is likely to be very challenging.

### **1.7.3 ERCC1–XPF Heterodimerization Inhibitors**

ERCC1–XPF dimerization through interactions of their HhH2 domains is necessary for the stability of the ERCC1–XPF complex and so is crucial for endonuclease activity. Developing small molecule inhibitors of ERCC1–XPF heterodimerization interface would be expected to potentiate DNA-damaging chemotherapeutics, whose damages are repaired by ERCC1–XPF-dependent pathways in cancer cells. However, blocking the interaction domains of HhH2 in ERCC1–XPF is very challenging and more difficult than the enzyme active site inhibition because of their high binding affinity and the hydrophobic nature of such interactions. The  $K_d$  of ERCC1–XPF binding has been estimated to be 5 nM by a surface plasmon resonance (SPR) assay.<sup>87</sup> Although the development of small molecules to disrupt the ERCC1–XPF heterodimerization interface has been challenging, developing inhibitors of strong protein–protein interactions could be achievable. A study has shown the successful inhibition of p53/MDM2, a strong bound gene complex associated with p53 inactivation, interaction by a small molecule, nutlin. These results suggested that targeting strong protein–protein interactions could be approachable.<sup>98</sup> Moreover, mutagenesis experiments showed that removal of the ERCC1 Phe293 interaction with XPF is enough for preventing the heterodimer formation.<sup>69, 79</sup> Furthermore, with the availability of an X-ray crystal

structure of ERCC1–XPF<sup>99</sup> that clearly depicts the interactions of the HhH2 domains, rational drug design should be possible.

McNeil et al. sought to identify the HhH2 interaction domains of the ERCC1–XPF complex, thus disrupting the heterodimer formation and stability and resulting in enhancing the sensitivity of cancer cells to platinum-based chemotherapeutics. Previously, they identified the ERCC1 Phe293 site on XPF as a potential target.<sup>87</sup> From the current published ERCC1–XPF HhH2 crystal structure (PDB 2A1J),<sup>99</sup> they identified another two important interaction sites on XPF with ERCC1 Cys238 and Ile264 residues (Figure 1.13).<sup>100</sup>

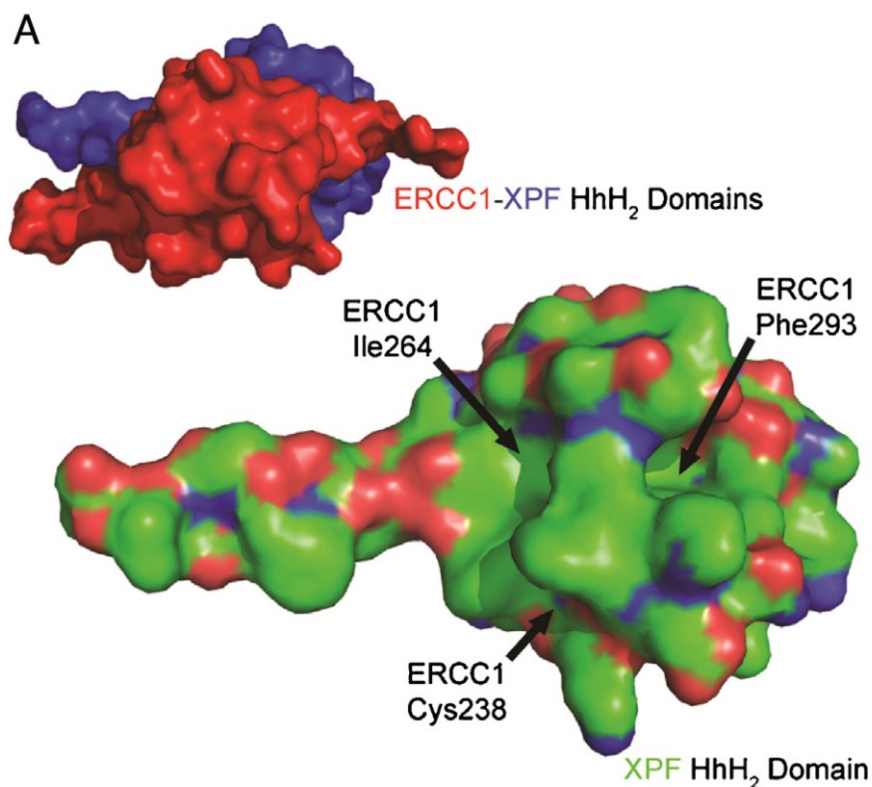


**Figure 1.13.** *In silico* screening for ERCC1–XPF interaction inhibitors. ERCC1–XPF HhH2 heterodimerization complex (PDB Code 2A1J), with ERCC1 on top. Also shown is the heterodimerization surface of XPF (using the Connolly surface), identifying the binding pockets for ERCC1 residues Cys238, Ile264, and Phe293, (copied with permission from McNeil et al.<sup>100</sup>).

They demonstrated the activity of ERCC1–XPF heterodimerization inhibitors by their screening at 100  $\mu\text{M}$  against the  $\Delta\text{XPF}$  protein attached to the SPR surface. Four compounds (Figure 1.14), E-X PPI1 to I4 **10-13**, from the *in silico* screens were shown to be bound specifically to the immobilized  $\Delta\text{XPF}$ , with  $K_d$  values of 17.8, 275, 537, and 200  $\mu\text{M}$  and stoichiometric ratios  $n \sim 1:1$ , 1:2, 1:2, and 1:3 for XPF binding, respectively.

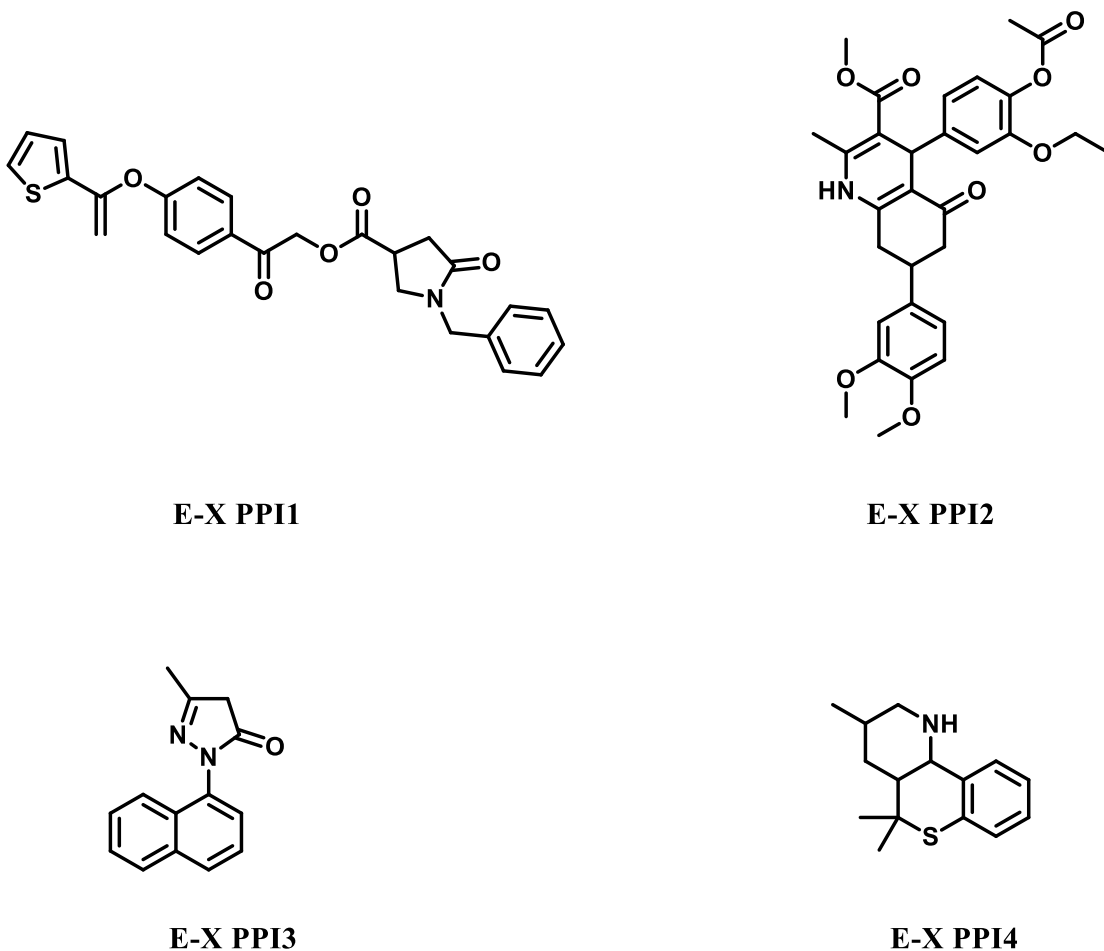


**Figure 1.14.** *In silico* screened products as potential ERCC1–XPF heterodimerization inhibitors.

The assessment of these compounds on their ability to inhibit NER has been performed *in vitro* by using A375 melanoma cells established with a transfection-based assay to evaluate and measure the NER of UV-damaged plasmid DNA. UV was selected

as the lesion agent over cisplatin because all UVC induced damages are substrates for the NER pathway, whereas other repair mechanisms also are involved in the repair of some DNA lesions caused by platinum containing compounds. The results revealed that one of the four interaction disruptor compounds, E-X PPI2, showed a moderate activity in the NER assay with an IC<sub>50</sub> of 20 μM. Therefore, this was the only interaction inhibitor that was investigated further.

The McNeil group further investigated the use of **11** in sensitizing cancer cells *in vitro*. Although an ideal inhibitor should reduce the cisplatin IC<sub>50</sub> by 10-fold, according to their previous observations, when they used siRNA against ERCC1 or XPF for isogenic ERCC1-proficient and -deficient mouse melanoma cells,<sup>101, 102</sup> cisplatin IC<sub>50</sub> was reduced only slightly (1.3-fold) by **11**. They also employed an in-situ proximity ligation assay (PLA) with usage of monoclonal antibodies to ERCC1 and XPF to assess whether E-X PPI2 could influence the heterodimer levels. Signals of PLA (nuclear foci) are generated only when proteins are in close contact. They cultured A2780 human ovarian cancer cells for five days and incubated with 75 μM E-X PPI2. The results showed a significant reduction of 25% in the number of nuclear PLA foci.

To design and develop effective heterodimerization inhibitors, it is necessary to understand the protein–protein interaction site and the manner in which small molecules bind to it. Therefore, Jordheim et al.<sup>103</sup> carried out MD simulations and binding energy analysis via correlating the individual binding energy contributions with the positions of different amino acid residues in the XPF interaction site. Upon mapping XPF sites onto ERCC1, the results showed three interaction sites (Figure 1.15), with only one binding pocket suitable for fitting drug candidates, even after carefully inspecting the

trajectory of the ERCC1–XPF MD simulation. Afterwards, they conducted *in silico* screening using a library databank of compounds to target the Ile264 or Phe293 pockets and pairwise pocket combinations. Next, their ranked compounds were tested for the activity *in vitro*. The ERCC1–XPF endonuclease assay was not used in assessing the interaction inhibitors because once the protein complex

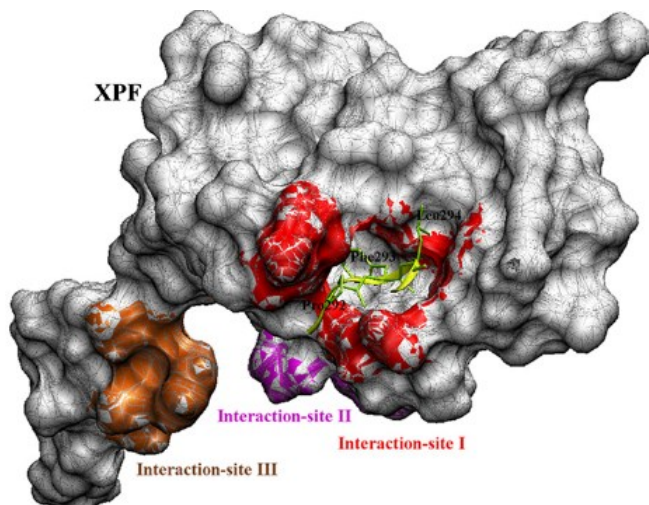


**Figure 1.15.** Binding energy decomposition identified three interaction sites in ERCC1–XPF. The most effective site and the one that was targeted in this study is interaction-site I (red), (copied with permission from Jordheim et al.<sup>103</sup>).

forms, it would be harder to disrupt such an interaction to prevent complex formation than targeting inhibitors to the interaction domains prior to ERCC1–XPF heterodimerization. However, they performed physical binding studies on the XPF target instead using surface plasmon resonance technique.

The Jordheim group<sup>103</sup> also identified potential interaction inhibitors by employing 20 virtual screening simulations of ~3500 distinct structures from the NCI diversity set and Drug-Bank with the use of 20 available NMR snapshots of the protein.<sup>104, 105</sup> The top hits from screening simulations were ranked according to their binding energy values, and the top 73 hits were chosen to be validated further

experimentally after individual docking of all structures to 20 XPF targets. Most of their hits were characteristic, with a side-chain that is embedded within the XPF binding that buries Phe 293, a key residue for ERCC1–XPF interaction. Three hits, **14**, **15**, and **16** were shown to have a lower binding energy, and their binding modes have been studied. The three hits' binding modes indicate that compounds fit well in the XPF-binding pocket, suggesting a high degree of complementarity in shape and feature (Figure 1.16).

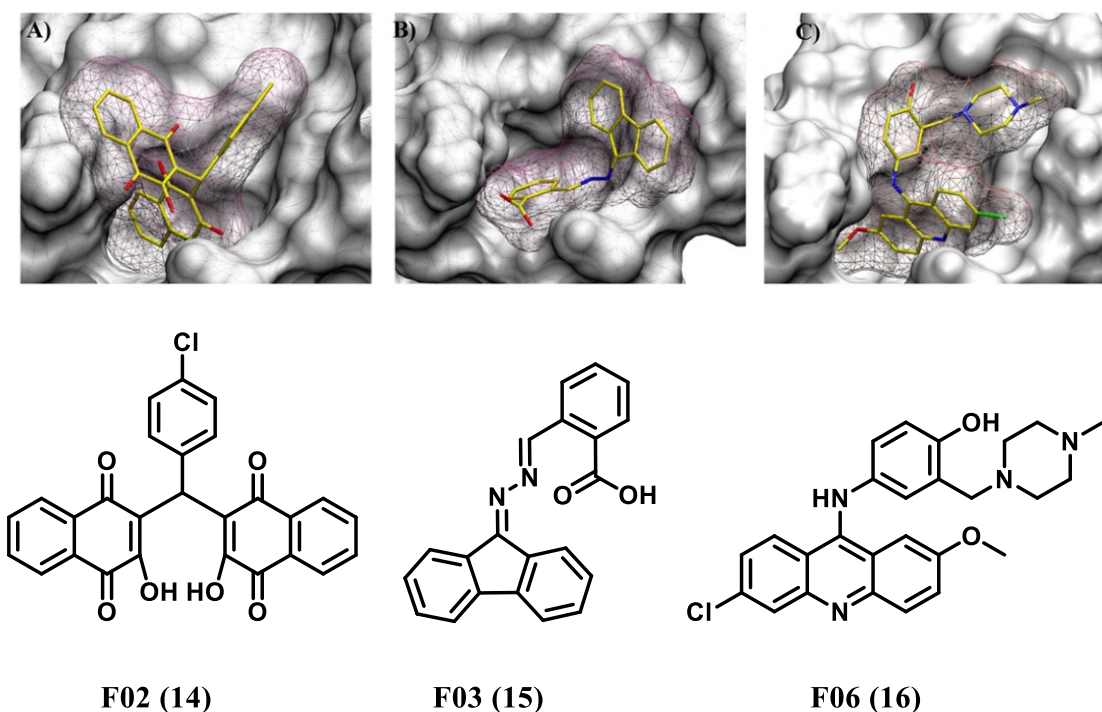


**Figure 1.16.** Binding modes of the three hits, (copied with permission from Jordheim et al.<sup>103</sup>), F02 (A), F03 (B), and F06 (C), and their chemical structures. Atomic colors are as follows: carbon in yellow, nitrogen in blue, oxygen in red, and chlorine in green. Molecular surface grid is shown in pink around the compounds to demonstrate their fitting within the interaction site I of XPF.

In addition, they performed synergy studies with cisplatin and potential inhibitors on HCT116 (colon) and A549 (lung) cells treated with platinum containing derivatives in a conventional MTT assay. Compounds that induced more than 80% decrease in the cell survival (cytotoxicity) at 100  $\mu$ M were selected to conduct this

synergy study. The results show that a synergy was observed between F06 and cisplatin in HCT 116 cells and A549 cells. They also conducted cell survival assays after UVC exposure to measure the NER activity in cells incubated with or without potential inhibitors of the ERCC1–XPF complex. The survival of A549 cells upon exposure to 40 or 80 J/m<sup>2</sup> showed that some compounds moderately sensitize such cells to UVC light, especially **16** (1.8-fold to 80 J/m<sup>2</sup>; *P* = 0.02). To determine and confirm the correct interaction fragments between ERCC1–XPF, Jordheim and co-workers used ΔERCC1–ΔXPF and confirmed the correctness of their XPF<sup>814-905</sup> model by revealing interaction with the ERCC1<sup>220-297</sup> domain (Figure 1.17).

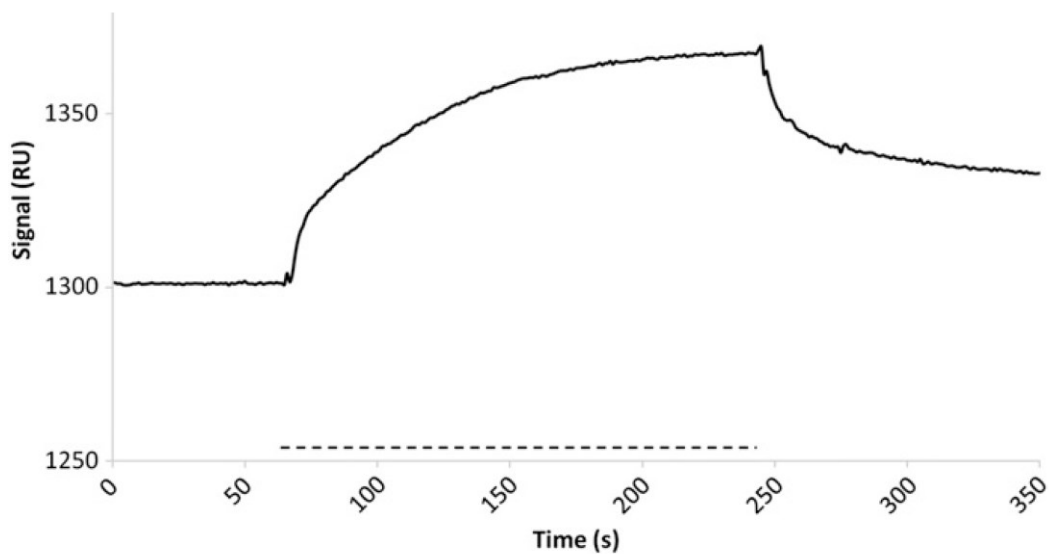


**Figure 1.17.** Sensorgram for interaction between XPF<sup>814-905</sup> and ERCC1<sup>220-297</sup>. ERCC1<sup>220-297</sup> was injected at 10 μM in PBS containing 1 mM dithiothreitol on a chip with immobilized XPF<sup>814-905</sup>. Dotted line indicates time of injection of ERCC1<sup>220-297</sup>, (copied with permission from Jordheim et al.<sup>103</sup>).

Afterwards, they assessed the potential interaction between chosen compounds and XPF<sup>814-905</sup>, and they noticed a significant interaction for **16** by using fluorescence-quenching experiments (Figure 1.18). Different concentrations of **16** were incubated with XPF<sup>814-905</sup>, and a decrease in the intrinsic fluorescence caused by the tyrosine

residue of the protein fragment was observed, as shown by steady-state fluorescence. The dissociation constant ( $K_d$ ) of **16** on XPF<sup>814-905</sup> were found to be  $30 \times 10^{-6}$  M calculated from the Stern-Volmer plot.

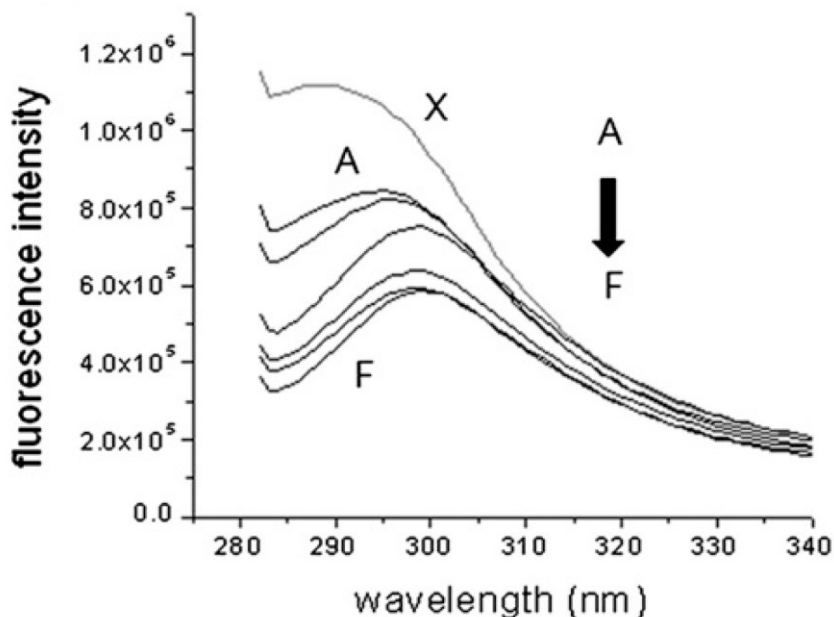


**Figure 1.18.** Fluorescence experiments for the interaction between XPF<sup>814-905</sup> and F06. (A) Emission spectra of XPF<sup>814-905</sup> (2  $\mu$ M) alone (X) and in the presence of different concentrations of F06 (A: 10, B: 15, C: 20, D: 25, E: 27, and F: 30  $\mu$ M). The excitation wavelength was 271 nm, (copied with permission from Jordheim et al.<sup>103</sup>).

They also evaluated the ability of **16**, their best NER inhibitor, to modify the interaction between ERCC1 and XPF in a cellular level. They conducted proximity ligation assays in A549 cells incubated with F06 and/or cisplatin. It was noticed that the mean interactions per cells increased upon cisplatin treatment, detected and determined by dot counts per cell (15.2 versus 35.3). The interaction between ERCC1 and XPF was decreased after adding F06, both in the absence (6.9 dots/cell) and in the presence of cisplatin (15.2 dots/cell), proving that F06 acts as a potent inhibitor of the ERCC1–XPF interaction in a cellular context. This has been confirmed further with an immunoprecipitation assay using cell extracts from A549 cells incubated with various

concentrations of F06 or DMSO as control. By using an anti-ERCC1 antibody as a precipitating agent, they noticed that the quantity of co-immunoprecipitated XPF from these cell extracts was decreased by F06, suggesting that F06 was able to inhibit ERCC1–XPF interactions within an environment of several cellular proteins.

The McNeil and Jordheim groups extensively worked on developing ERCC1–XPF heterodimerization inhibitors, and their preliminary *in vitro* assays confirmed that their reported hits showed promising inhibitory activity for ERCC1–XPF and that it acts synergistically with platinum containing drugs, such as cisplatin. However, the activity of either **11** or **16** (best reported hits for ERCC1–XPF interaction inhibitors) was suboptimal in terms of clinical properties, including potency and safety such as moderate to high micromolar IC<sub>50</sub>, low binding affinity values, and weak to moderate sensitizing agents. Therefore, a derivatization strategy suggested by Jordheim et al.,<sup>103</sup> especially for F06, was adapted to optimize the action of this hit compound. Also, all previous efforts on developing inhibitors for ERCC1–XPF activity were carried out on the truncated version of the heterodimer and not the full-length protein.<sup>88, 90, 101, 103</sup> It is reported that the full length ERCC1–XPF protein was 15-fold more active than the truncated form under standard reaction conditions.<sup>88, 99</sup> Thus, further design and development of potent inhibitors with optimized physio-chemical properties to disrupt the heterodimerization between ERCC1–XPF using the full-length protein was required and, in turn, will be expected to inhibit NER pathway (Figure 1.19) and sensitize cancer cells towards DNA damaging agent.

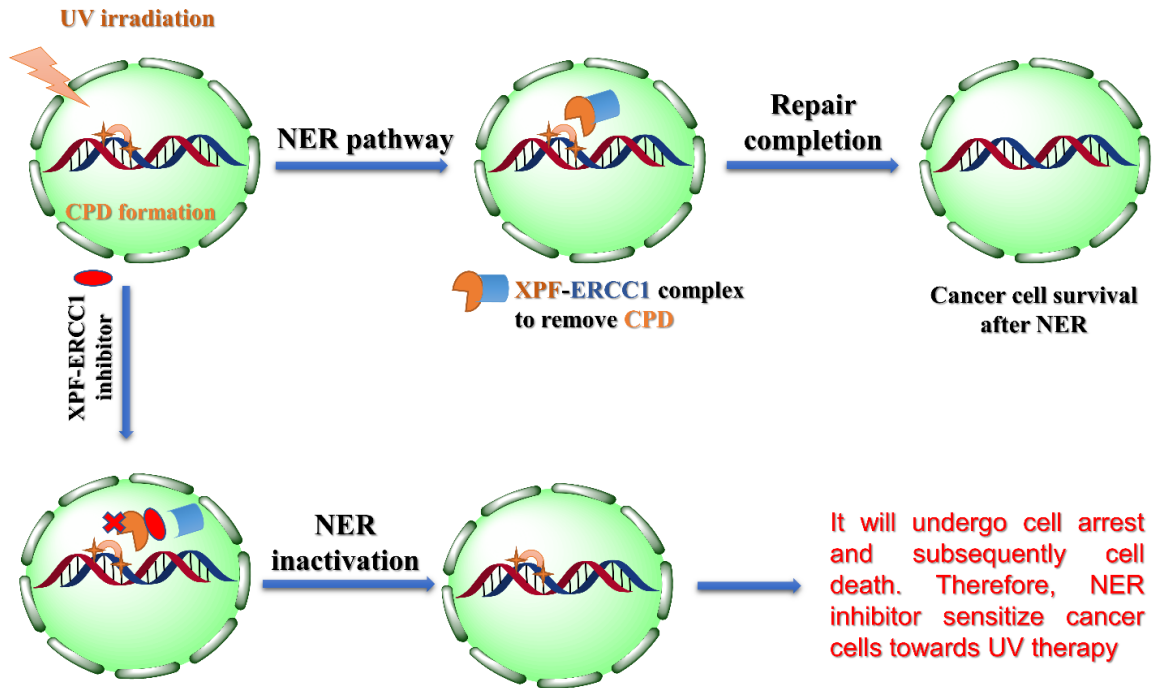


**Figure 1.19.** Potential modality of NER inactivation through ERCC1–XPF heterodimerization inhibition.

## 1.8 Conclusion

Currently, radiotherapy, chemotherapy, surgery, and immunotherapy are the major conventional treatments for cancer. Several chemotherapeutic agents act on damaging the DNA machinery of cancer cells. However, such therapies fail in managing cancer due to the ability of cancer cells to repair the DNA lesions formed by these therapies through several DNA-repair pathways. These repair pathways are responsible for developing the drug resistance and result in drug ineffectiveness. One major DNA repair pathway is NER, which can recognize, verify, and remove several bulky, helix-distorting lesions from the damaged DNA. This repair process requires a cascade of signaling proteins to initiate the cellular repair for the damaged DNA.

ERCC1–XPF protein complex is one of the essential proteins involved in several DNA repair pathways. However, it is very essential for the NER pathway because it

removes the bulky DNA and chemically induced helix-distorting lesions, which are all substrates for the NER mechanism. Therefore, ERCC1–XPF has become an interesting therapeutic target to manipulate the DNA repair pathways, and its inhibition has the potential of potentiating the cytotoxic chemotherapeutic agents and other cross-linking agents against cancer cells.

The activity of ERCC1–XPF heterodimer can be inhibited by developing either nuclease (active site) inhibitors or heterodimerization inhibitors; several promising early hits point to the possibility of developing effective inhibitors of heterodimerization that could sensitize cancer cells to cisplatin or other crosslinking agents. However, the activities of the reported hits to date are suboptimal in terms of clinical properties, including potency and safety, and further optimization is required. In addition, all previous efforts on developing inhibitors for ERCC1–XPF activity were carried out on the truncated version of the heterodimer and not on the full-length protein, which is 15-fold more active than the truncated form under standard reaction conditions. Thus, further design and development of potent inhibitors with optimized physio-chemical properties to disrupt the heterodimerization between ERCC1–XPF using the full-length protein is required. In this thesis, the computer aided drug design (in collaboration with F. Gentile), synthesis, and biological evaluations of improved inhibitors based upon the preliminary results with F06, using full-length protein in a cell-free assay, and various cell-based assays are described.

In Chapter 2, we used the reported F06 (**16**) as a reference hit, which was subjected in docking-based virtual screening. The objectives of *in silico* studies is to 1) identify the potential sites on F06 structure that can be functionalized further with various functional groups to capture more interactions with the XPF residues, and 2)

propose compounds with better binding energy and ligand efficiency values using the XPF interaction domain compared to F06. Afterwards, the synthesis of top computationally ranked F06 derivatives, modified at the external part of piperazine ring (generation A), using a facile, reproducible, and robust method is discussed. The inhibitory activity of the synthesized compounds on ERCC1–XPF by using an *in vitro* ERCC1–XPF endonuclease assay is described. The binding affinity of top ERCC1–XPF inhibitors on the full-length protein is carried out, and their capacity to inhibit the NER pathway and sensitize colorectal cancers cells to cyclophosphamide, cross linking agent, and UV radiation is investigated using various cell-based assays.

Chapter 3 describes the use of multi-step CADD strategy to identify better inhibitors than F06 based on the modification of a different site of F06, methoxy-acridine functional group. The *in silico* screening study identified two compounds that showed improved inhibitory effect on the ERCC1–XPF nuclease activity compared to the parent compound, F06. The synthesis of control compounds and top compounds from the docking-based study is shown through a facile synthetic route. Detailed analysis of the predicted binding mode of the best inhibitor to XPF derived from molecular dynamics simulations is discussed.

Chapter 4 shows an extensive structure activity relationship analysis based on the pharmacophore model that has been studied on the previously identified hit compound, F06. Development of three different series of generations **B**, **C**, and **D** by structure-based design and their synthesis through various modifications on three different sites of F06 are discussed. Screening the inhibition ability of all generation compounds on ERCC–XPF activity is done by using the *in vitro* endonuclease assay.

The screening results revealed that **Gen B9** has a better ERCC1–XPF inhibition with an improved IC<sub>50</sub> compared to F06. The binding affinity of Gen B9 on the full-length protein and the DNA substrate are described. Sensitization of colorectal cancer towards cisplatin, cyclophosphamide, and Mitomycin C is discussed. In addition, heterodimerization disruption by **Gen B9** is confirmed by using the proximity ligation assay.

Chapter 5 provides a general summary of the thesis findings about developing potent inhibitors of ERCC1–XPF and the potential of improving cancer therapy using DNA-repair inhibitors. Also, this chapter addresses the future work needed for our improved inhibitors to ensure the potency, selectivity and safety of the optimized lead compounds through *in vivo* studies.

## 1.9 References

1. Siegel, R. L.; Miller, K. D.; Jemal, A. Cancer statistics, 2020. *CA: A Cancer Journal for Clinicians* **2020**, *70*, 7-30.
2. Holohan, C.; Van Schaeybroeck, S.; Longley, D. B.; Johnston, P. G. Cancer drug resistance: an evolving paradigm. *Nature Reviews Cancer* **2013**, *13*, 714-726.
3. Housman, G.; Byler, S.; Heerboth, S.; Lapinska, K.; Longacre, M.; Snyder, N.; Sarkar, S. Drug resistance in cancer: an overview. *Cancers* **2014**, *6*, 1769-1792.
4. Rueff, J.; Rodrigues, A. S. Cancer drug resistance: A brief overview from a genetic viewpoint. In *Cancer Drug Resistance*, Springer: 2016; pp 1-18.
5. Urruticochea, A.; Alemany, R.; Balart, J.; Villanueva, A.; Viñals, F.; Capella, G. Recent advances in cancer therapy: an overview. *Current Pharmaceutical Design* **2010**, *16*, 3-10.
6. Baskar, R.; Lee, K. A.; Yeo, R.; Yeoh, K.-W. Cancer and radiation therapy: current advances and future directions. *International Journal of Medical Sciences* **2012**, *9*, 193-199.
7. Khalil, D. N.; Smith, E. L.; Brentjens, R. J.; Wolchok, J. D. The future of cancer treatment: immunomodulation, CARs and combination immunotherapy. *Nature Reviews Clinical Oncology* **2016**, *13*, 273-290.
8. Alfarouk, K. O.; Stock, C.-M.; Taylor, S.; Walsh, M.; Muddathir, A. K.; Verduzco, D.; Bashir, A. H. H.; Mohammed, O. Y.; Elhassan, G. O.; Harguindey, S. Resistance to cancer chemotherapy: failure in drug response from ADME to P-gp. *Cancer Cell International* **2015**, *15*, 71-84.
9. Borst, P. Cancer drug pan-resistance: pumps, cancer stem cells, quiescence, epithelial to mesenchymal transition, blocked cell death pathways, persists or what? *Open Biology* **2012**, *2*, 120066-120075.
10. Uramoto, H.; Tanaka, F. Recurrence after surgery in patients with NSCLC. *Translational Lung Cancer Research* **2014**, *3*, 242-249.
11. Castells, M.; Thibault, B.; Delord, J.-P.; Couderc, B. Implication of tumor microenvironment in chemoresistance: tumor-associated stromal cells protect tumor cells from cell death. *International Journal of Molecular Sciences* **2012**, *13*, 9545-9571.
12. O'Connor, D.; Sibson, K.; Caswell, M.; Connor, P.; Cummins, M.; Mitchell, C.; Motwani, J.; Taj, M.; Vora, A.; Wynn, R. Early UK experience in the use of clofarabine in the treatment of relapsed and refractory paediatric acute lymphoblastic leukaemia. *British Journal of Haematology* **2011**, *154*, 482-485.
13. Yazilintas, D.; Özdemir, N.; Hocasade, C.; Demirci, N. S.; Zengin, N. The clinical and pathological features affecting the time of relapse in patients with early stage colorectal cancer. *Journal of Cancer Research and Therapeutics* **2016**, *12*, 1257-1260.

14. De Bont, R.; Van Larebeke, N. Endogenous DNA damage in humans: a review of quantitative data. *Mutagenesis* **2004**, *19*, 169-185.
15. Lindahl, T. Instability and decay of the primary structure of DNA. *Nature* **1993**, *362*, 709-715.
16. Lindahl, T.; Nyberg, B. Rate of depurination of native deoxyribonucleic acid. *Biochemistry* **1972**, *11*, 3610-3618.
17. Sugiyama, H.; Fujiwara, T.; Ura, A.; Tashiro, T.; Yamamoto, K.; Kawanishi, S.; Saito, I. Chemistry of thermal degradation of abasic sites in DNA. Mechanistic investigation on thermal DNA strand cleavage of alkylated DNA. *Chemical Research in Toxicology* **1994**, *7*, 673-683.
18. Yonekura, S.-I.; Nakamura, N.; Yonei, S.; Zhang-Akiyama, Q.-M. Generation, biological consequences and repair mechanisms of cytosine deamination in DNA. *Journal of Radiation Research* **2008**, 0811040073-0811040073.
19. Frederico, L. A.; Kunkel, T. A.; Shaw, B. R. A sensitive genetic assay for the detection of cytosine deamination: determination of rate constants and the activation energy. *Biochemistry* **1990**, *29*, 2532-2537.
20. Krokan, H. E.; Drabløs, F.; Slupphaug, G. Uracil in DNA—occurrence, consequences and repair. *Oncogene* **2002**, *21*, 8935-8948.
21. Kow, Y. W. Repair of deaminated bases in DNA. *Free Radical Biology and Medicine* **2002**, *33*, 886-893.
22. Apel, K.; Hirt, H. Reactive oxygen species: metabolism, oxidative stress, and signal transduction. *Annual Reviews Plant Biology* **2004**, *55*, 373-399.
23. Marnett, L. J. Oxyradicals and DNA damage. *Carcinogenesis* **2000**, *21*, 361-370.
24. Cadet, J.; Berger, M.; Douki, T.; Ravanat, J. L. Oxidative damage to DNA: formation, measurement, and biological significance. In *Reviews of Physiology Biochemistry and Pharmacology* **1997**, *131*, 1-87.
25. Burney, S.; Caulfield, J. L.; Niles, J. C.; Wishnok, J. S.; Tannenbaum, S. R. The chemistry of DNA damage from nitric oxide and peroxynitrite. *Mutation Research/Fundamental and Molecular Mechanisms of Mutagenesis* **1999**, *424*, 37-49.
26. Ravanat, J.-L. Measuring oxidized DNA lesions as biomarkers of oxidative stress: an analytical challenge. *FABAD Journal of Pharmaceutical Sciences* **2005**, *30*, 100-113.
27. Major, G. N.; Collier, J. D. Repair of DNA lesion O 6-methylguanine in hepatocellular carcinogenesis. *Journal of Hepato-Biliary-Pancreatic Surgery* **1998**, *5*, 355-366.
28. Jackson, S. P.; Bartek, J. The DNA-damage response in human biology and disease. *Nature* **2009**, *461*, 1071-1078.
29. Kesari, S.; Advani, S. J.; Lawson, J. D.; Kahle, K. T.; Ng, K.; Carter, B.; Chen, C. C. DNA damage response and repair: insights into strategies for radiation sensitization of gliomas. *Future Oncology* **2011**, *7*, 1335-1346.

30. Vermund, H.; Gollin, F. F. Mechanisms of action of radiotherapy and chemotherapeutic adjuvants: a review. *Cancer* **1968**, 21, 58-76.
31. Zheng, H.-C. The molecular mechanisms of chemoresistance in cancers. *Oncotarget* **2017**, 8, 59950-59964.
32. Berwick, M.; Vineis, P. Markers of DNA repair and susceptibility to cancer in humans: an epidemiologic review. *Journal of the National Cancer Institute* **2000**, 92, 874-897.
33. Longley, D. B.; Johnston, P. G. Molecular mechanisms of drug resistance. *The Journal of Pathology: A Journal of the Pathological Society of Great Britain and Ireland* **2005**, 205, 275-292.
34. Zhou, B.-B. S.; Bartek, J. Targeting the checkpoint kinases: chemosensitization versus chemoprotection. *Nature Reviews Cancer* **2004**, 4, 216-225.
35. Boland, C. R.; Luciani, M. G.; Gasche, C.; Goel, A. Infection, inflammation, and gastrointestinal cancer. *Gut* **2005**, 54, 1321-1331.
36. Peltomäki, P. Deficient DNA mismatch repair: a common etiologic factor for colon cancer. *Human Molecular Genetics* **2001**, 10, 735-740.
37. Larrea, A. A.; Lujan, S. A.; Kunkel, T. A. SnapShot: DNA mismatch repair. *Cell* **2010**, 141, 730-730.
38. Modrich, P. Mechanisms in eukaryotic mismatch repair. *Journal of Biological Chemistry* **2006**, 281, 30305-30309.
39. Fukui, K. DNA mismatch repair in eukaryotes and bacteria. *Journal of Nucleic Acids* **2010**, 260512-260528.
40. Chan, K. K. L.; Zhang, Q.-M.; Dianov, G. L. Base excision repair fidelity in normal and cancer cells. *Mutagenesis* **2006**, 21, 173-178.
41. Sancar, A.; Lindsey-Boltz, L. A.; Ünsal-Kaçmaz, K.; Linn, S. Molecular mechanisms of mammalian DNA repair and the DNA damage checkpoints. *Annual Review of Biochemistry* **2004**, 73, 39-85.
42. van Gent, D. C.; Hoeijmakers, J. H. J.; Kanaar, R. Chromosomal stability and the DNA double-stranded break connection. *Nature Reviews Genetics* **2001**, 2, 196-206.
43. Khanna, K. K.; Jackson, S. P. DNA double-strand breaks: signaling, repair and the cancer connection. *Nature Genetics* **2001**, 27, 247-254.
44. Li, X.; Heyer, W.-D. Homologous recombination in DNA repair and DNA damage tolerance. *Cell Research* **2008**, 18, 99-113.
45. Lieber, M. R. The mechanism of double-strand DNA break repair by the nonhomologous DNA end-joining pathway. *Annual Review of Biochemistry* **2010**, 79, 181-211.
46. Shuck, S. C.; Short, E. A.; Turchi, J. J. Eukaryotic nucleotide excision repair: from understanding mechanisms to influencing biology. *Cell Research* **2008**, 18, 64-72.

47. Costa, R. M. A.; Chiganças, V.; da Silva Galhardo, R.; Carvalho, H.; Menck, C. F. M. The eukaryotic nucleotide excision repair pathway. *Biochimie* **2003**, *85*, 1083-1099.
48. Nospikel, T. Nucleotide excision repair and neurological diseases. *DNA Repair* **2008**, *7*, 1155-1167.
49. Lindahl, T.; Wood, R. D. Quality control by DNA repair. *Science* **1999**, *286*, 1897-1905.
50. Cleaver, J. E.; Lam, E. T.; Revet, I. Disorders of nucleotide excision repair: the genetic and molecular basis of heterogeneity. *Nature Reviews Genetics* **2009**, *10*, 756-768.
51. Vermeulen, W.; De Boer, J.; Citterio, E.; Van Gool, A. J.; Van der Horst, G. T. J.; Jaspers, N. G. J.; De Laat, W. L.; Sijbers, A. M.; Van der Spek, P. J.; Sugawara, K. Mammalian nucleotide excision repair and syndromes. *Biochemical Society Transactions* **1997**, *25*, 309-314.
52. Sugawara, K.; Ng, J. M. Y.; Masutani, C.; Iwai, S.; van der Spek, P. J.; Eker, A. P. M.; Hanaoka, F.; Bootsma, D.; Hoeijmakers, J. H. J. Xeroderma pigmentosum group C protein complex is the initiator of global genome nucleotide excision repair. *Molecular Cell* **1998**, *2*, 223-232.
53. Sugawara, K. XPC: its product and biological roles. In *Molecular Mechanisms of Xeroderma Pigmentosum* **2008**, 637, 47-56.
54. Sugawara, K. Regulation of damage recognition in mammalian global genomic nucleotide excision repair. *Mutation Research/Fundamental and Molecular Mechanisms of Mutagenesis* **2010**, *685*, 29-37.
55. Foustleri, M.; Mullenders, L. H. F. Transcription-coupled nucleotide excision repair in mammalian cells: molecular mechanisms and biological effects. *Cell Research* **2008**, *18*, 73-84.
56. Hanawalt, P. C.; Spivak, G. Transcription-coupled DNA repair: two decades of progress and surprises. *Nature reviews Molecular Cell Biology* **2008**, *9*, 958-970.
57. Schiestl, R. H.; Prakash, S. RAD10, an excision repair gene of *Saccharomyces cerevisiae*, is involved in the RAD1 pathway of mitotic recombination. *Molecular and Cellular Biology* **1990**, *10*, 2485-2491.
58. Ahmad, A.; Robinson, A. R.; Duensing, A.; Van Drunen, E.; Beverloo, H. B.; Weisberg, D. B.; Hastly, P.; Hoeijmakers, J. H. J.; Niedernhofer, L. J. ERCC1-XPF endonuclease facilitates DNA double-strand break repair. *Molecular and Cellular Biology* **2008**, *28*, 5082-5092.
59. Niedernhofer, L. J.; Essers, J.; Weeda, G.; Beverloo, B.; De Wit, J.; Muijtjens, M.; Odijk, H.; Hoeijmakers, J. H. J.; Kanaar, R. The structure-specific endonuclease Ercc1—Xpf is required for targeted gene replacement in embryonic stem cells. *The EMBO Journal* **2001**, *20*, 6540-6549.
60. Al-Minawi, A. Z.; Saleh-Gohari, N.; Helleday, T. The ERCC1/XPF endonuclease is required for efficient single-strand annealing and gene conversion in mammalian cells. *Nucleic Acids Research* **2008**, *36*, 1-9.
61. Wood, R. D. Mammalian nucleotide excision repair proteins and interstrand crosslink repair. *Environmental and Molecular Mutagenesis* **2010**, *51*, 520-526.

62. Deans, A. J.; West, S. C. DNA interstrand crosslink repair and cancer. *Nature Reviews Cancer* **2011**, *11*, 467-480.
63. Kuraoka, I.; Kobertz, W. R.; Ariza, R. R.; Biggerstaff, M.; Essigmann, J. M.; Wood, R. D. Repair of an interstrand DNA cross-link initiated by ERCC1-XPF repair/recombination nuclease. *Journal of Biological Chemistry* **2000**, *275*, 26632-26636.
64. Niedernhofer, L. J.; Odijk, H.; Budzowska, M.; Van Drunen, E.; Maas, A.; Theil, A. F.; De Wit, J.; Jaspers, N. G. J.; Beverloo, H. B.; Hoeijmakers, J. H. J. The structure-specific endonuclease Ercc1-Xpf is required to resolve DNA interstrand cross-link-induced double-strand breaks. *Molecular and Cellular Biology* **2004**, *24*, 5776-5787.
65. Bhagwat, N.; Olsen, A. L.; Wang, A. T.; Hanada, K.; Stuckert, P.; Kanaar, R.; D'Andrea, A.; Niedernhofer, L. J.; McHugh, P. J. XPF-ERCC1 participates in the Fanconi anemia pathway of cross-link repair. *Molecular and Cellular Biology* **2009**, *29*, 6427-6437.
66. Friedberg, E. C.; Walker, G. C.; Siede, W.; Wood, R. D.; Schultz, R. A.; Ellenberger, T. DNA Repair and Mutagenesis. 2nd edn ASM Press. *Washington, DC* **2006**.
67. Hoeijmakers, J. H. J. DNA damage, aging, and cancer. *New England Journal of Medicine* **2009**, *361*, 1475-1485.
68. van Duin, M.; de Wit, J.; Odijk, H.; Westerveld, A.; Yasui, A.; Koken, M.; Hoeijmakers, J.; Bootsma, D. Molecular characterization of the human excision repair gene ERCC-1: cDNA cloning and aminoacid homology with the yeast DNA repair gene RAD10. *Cell* **1986**, *44*, 913-923.
69. Sijbers, A. M.; van der Spek, P. J.; Odijk, H.; van den Berg, J.; van Duin, M.; Westerveld, A.; Jaspers, N. G. J.; Bootsma, D.; Hoeijmakers, J. H. J. Mutational analysis of the human nucleotide excision repair gene ERCC1. *Nucleic Acids Research* **1996**, *24*, 3370-3380.
70. Brookman, K. W.; Lamerdin, J. E.; Thelen, M. P.; Hwang, M.; Reardon, J. T.; Sancar, A.; Zhou, Z.-Q.; Walter, C. A.; Parris, C. N.; Thompson, L. H. ERCC4 (XPF) encodes a human nucleotide excision repair protein with eukaryotic recombination homologs. *Molecular and Cellular Biology* **1996**, *16*, 6553-6562.
71. Niedernhofer, L. J.; Garinis, G. A.; Raams, A.; Lalai, A. S.; Robinson, A. R.; Appeldoorn, E.; Odijk, H.; Oostendorp, R.; Ahmad, A.; Van Leeuwen, W. A new progeroid syndrome reveals that genotoxic stress suppresses the somatotroph axis. *Nature* **2006**, *444*, 1038-1043.
72. Tsodikov, O. V.; Enzlin, J. H.; Schärer, O. D.; Ellenberger, T. Crystal structure and DNA binding functions of ERCC1, a subunit of the DNA structure-specific endonuclease XPF-ERCC1. *Proceedings of the National Academy of Sciences* **2005**, *102*, 11236-11241.
73. Tsodikov, O. V.; Ivanov, D.; Orelli, B.; Staresinic, L.; Shoshani, I.; Oberman, R.; Schärer, O. D.; Wagner, G.; Ellenberger, T. Structural basis for the recruitment of ERCC1-XPF to nucleotide excision repair complexes by XPA. *The EMBO journal* **2007**, *26*, 4768-4776.

74. Tripsianes, K.; Folkers, G.; Eiso, A. B.; Das, D.; Odijk, H.; Jaspers, N. G. J.; Hoeijmakers, J. H. J.; Kaptein, R.; Boelens, R. The structure of the human ERCC1/XPF interaction domains reveals a complementary role for the two proteins in nucleotide excision repair. *Structure* **2005**, *13*, 1849-1858.
75. Choi, Y.-J.; Ryu, K.-S.; Ko, Y.-M.; Chae, Y.-K.; Pelton, J. G.; Wemmer, D. E.; Choi, B.-S. Biophysical characterization of the interaction domains and mapping of the contact residues in the XPF-ERCC1 complex. *Journal of Biological Chemistry* **2005**, *280*, 28644-28652.
76. Gaillard, P.-H. L.; Wood, R. D. Activity of individual ERCC1 and XPF subunits in DNA nucleotide excision repair. *Nucleic Acids Research* **2001**, *29*, 872-879.
77. Sgouros, J.; Gaillard, P.-H. L.; Wood, R. D. A relationship between a DNA-repair/recombination nuclease family and archaeal helicases. *Trends in Biochemical Sciences* **1999**, *24*, 95-97.
78. Nishino, T.; Komori, K.; Tsuchiya, D.; Ishino, Y.; Morikawa, K. Crystal structure and functional implications of *Pyrococcus furiosus* hef helicase domain involved in branched DNA processing. *Structure* **2005**, *13*, 143-153.
79. de Laat, W. L.; Sijbers, A. M.; Odijk, H.; Jaspers, N. G. J.; Hoeijmakers, J. H. J. Mapping of interaction domains between human repair proteins ERCC1 and XPF. *Nucleic Acids Research* **1998**, *26*, 4146-4152.
80. Jaspers, N. G. J.; Raams, A.; Silengo, M. C.; Wijgers, N.; Niedernhofer, L. J.; Robinson, A. R.; Giglia-Mari, G.; Hoogstraten, D.; Kleijer, W. J.; Hoeijmakers, J. H. J. First reported patient with human ERCC1 deficiency has cerebro-oculo-facio-skeletal syndrome with a mild defect in nucleotide excision repair and severe developmental failure. *The American Journal of Human Genetics* **2007**, *80*, 457-466.
81. de Laat, W. L.; Appeldoorn, E.; Jaspers, N. G. J.; Hoeijmakers, J. H. J. DNA structural elements required for ERCC1-XPF endonuclease activity. *Journal of Biological Chemistry* **1998**, *273*, 7835-7842.
82. Jiang, H.; Yang, L.-Y. Cell cycle checkpoint abrogator UCN-01 inhibits DNA repair: association with attenuation of the interaction of XPA and ERCC1 nucleotide excision repair proteins. *Cancer Research* **1999**, *59*, 4529-4534.
83. Barakat, K. H.; Huzil, J. T.; Luchko, T.; Jordheim, L.; Dumontet, C.; Tuszynski, J. Characterization of an inhibitory dynamic pharmacophore for the ERCC1-XPA interaction using a combined molecular dynamics and virtual screening approach. *Journal of Molecular Graphics and Modelling* **2009**, *28*, 113-130.
84. Enzlin, J. H.; Schäfer, O. D. The active site of the DNA repair endonuclease XPF-ERCC1 forms a highly conserved nuclease motif. *The EMBO Journal* **2002**, *21*, 2045-2053.
85. Kelley, L. A.; Sternberg, M. J. E. Protein structure prediction on the Web: a case study using the Phyre server. *Nature Protocols* **2009**, *4*, 363-371.

86. Newman, M.; Murray-Rust, J.; Lally, J.; Rudolf, J.; Fadden, A.; Knowles, P. P.; White, M. F.; McDonald, N. Q. Structure of an XPF endonuclease with and without DNA suggests a model for substrate recognition. *The EMBO Journal* **2005**, *24*, 895-905.
87. McNeil, E. M.; Melton, D. W. DNA repair endonuclease ERCC1–XPF as a novel therapeutic target to overcome chemoresistance in cancer therapy. *Nucleic Acids Research* **2012**, *40*, 9990-10004.
88. McNeil, E. M.; Astell, K. R.; Ritchie, A.-M.; Shave, S.; Houston, D. R.; Bakrania, P.; Jones, H. M.; Khurana, P.; Wallace, C.; Chapman, T.; Wear, M. A.; Walkinshaw, M. D.; Saxty, B.; Melton, D. W. Inhibition of the ERCC1–XPF structure-specific endonuclease to overcome cancer chemoresistance. *DNA Repair* **2015**, *31*, 19-28.
89. Chapman, T. M.; Wallace, C.; Gillen, K. J.; Bakrania, P.; Khurana, P.; Coombs, P. J.; Fox, S.; Bureau, E. A.; Brownlees, J.; Melton, D. W.; Saxty, B. N-Hydroxyimides and hydroxypyrimidinones as inhibitors of the DNA repair complex ERCC1–XPF. *Bioorganic & Medicinal Chemistry Letters* **2015**, *25*, 4104-4108.
90. Chapman, T. M.; Gillen, K. J.; Wallace, C.; Lee, M. T.; Bakrania, P.; Khurana, P.; Coombs, P. J.; Stennett, L.; Fox, S.; Bureau, E. A.; Brownlees, J.; Melton, D. W.; Saxty, B. Catechols and 3-hydroxypyridones as inhibitors of the DNA repair complex ERCC1-XPF. *Bioorganic & Medicinal Chemistry Letters* **2015**, *25*, 4097-4103.
91. Arora, S.; Heyza, J.; Zhang, H.; Kalman-Maltese, V.; Tillison, K.; Floyd, A. M.; Chalfin, E. M.; Bepler, G.; Patrick, S. M. Identification of small molecule inhibitors of ERCC1-XPF that inhibit DNA repair and potentiate cisplatin efficacy in cancer cells. *Oncotarget* **2016**, *7*, 75104-75117.
92. Dorjsuren, D.; Kim, D.; Maloney, D. J.; Wilson Iii, D. M.; Simeonov, A. Complementary non-radioactive assays for investigation of human flap endonuclease 1 activity. *Nucleic Acids Research* **2011**, *39*, e11-e22.
93. Tumey, L. N.; Bom, D.; Huck, B.; Gleason, E.; Wang, J.; Silver, D.; Brunden, K.; Boozer, S.; Rundlett, S.; Sherf, B. The identification and optimization of a N-hydroxy urea series of flap endonuclease 1 inhibitors. *Bioorganic & Medicinal Chemistry Letters* **2005**, *15*, 277-281.
94. Tumey, L. N.; Huck, B.; Gleason, E.; Wang, J.; Silver, D.; Brunden, K.; Boozer, S.; Rundlett, S.; Sherf, B.; Murphy, S. The identification and optimization of 2, 4-diketobutyric acids as flap endonuclease 1 inhibitors. *Bioorganic & Medicinal Chemistry Letters* **2004**, *14*, 4915-4918.
95. Huang, F.; Motlekar, N. A.; Burgwin, C. M.; Napper, A. D.; Diamond, S. L.; Mazin, A. V. Identification of specific inhibitors of human RAD51 recombinase using high-throughput screening. *ACS Chemical Biology* **2011**, *6*, 628-635.
96. Rai, G.; Vyjayanti, V. N.; Dorjsuren, D.; Simeonov, A.; Jadhav, A.; Wilson Iii, D. M.; Maloney, D. J. Synthesis, biological evaluation, and structure–activity relationships of a novel class of apurinic/aprimidinic endonuclease 1 inhibitors. *Journal of Medicinal Chemistry* **2012**, *55*, 3101-3112.

97. Manvilla, B. A.; Wauchope, O.; Seley-Radtke, K. L.; Drohat, A. C. NMR studies reveal an unexpected binding site for a redox inhibitor of AP endonuclease 1. *Biochemistry* **2011**, *50*, 10540-10549.
98. Vassilev, L. T.; Vu, B. T.; Graves, B.; Carvajal, D.; Podlaski, F.; Filipovic, Z.; Kong, N.; Kammlott, U.; Lukacs, C.; Klein, C. In vivo activation of the p53 pathway by small-molecule antagonists of MDM2. *Science* **2004**, *303*, 844-848.
99. Tsodikov, O. V.; Enzlin, J. H.; Schärer, O. D.; Ellenberger, T. Crystal structure and DNA binding functions of ERCC1, a subunit of the DNA structure-specific endonuclease XPF–ERCC1. *Proceedings of the National Academy of Sciences of the United States of America* **2005**, *102*, 11236-11241.
100. McNeil, E. M.; Astell, K. R.; Ritchie, A.-M.; Shave, S.; Houston, D. R.; Bakrania, P.; Jones, H. M.; Khurana, P.; Wallace, C.; Chapman, T. Inhibition of the ERCC1–XPF structure-specific endonuclease to overcome cancer chemoresistance. *DNA Repair* **2015**, *31*, 19-28.
101. Arora, S.; Heyza, J.; Zhang, H.; Kalman-Maltese, V.; Tillison, K.; Floyd, A. M.; Chalfin, E. M.; Bepler, G.; Patrick, S. M. Identification of small molecule inhibitors of ERCC1-XPF that inhibit DNA repair and potentiate cisplatin efficacy in cancer cells. *Oncotarget* **2016**.
102. Song, L.; Ritchie, A. M.; McNeil, E. M.; Li, W.; Melton, D. W. Identification of DNA repair gene *Ercc1* as a novel target in melanoma. *Pigment Cell & Melanoma Research* **2011**, *24*, 966-971.
103. Jordheim, L. P.; Barakat, K. H.; Heinrich-Balard, L.; Matera, E.-L.; Cros-Perrial, E.; Bouledrak, K.; El Sabeh, R.; Perez-Pineiro, R.; Wishart, D. S.; Cohen, R. Small molecule inhibitors of ERCC1-XPF protein-protein interaction synergize alkylating agents in cancer cells. *Molecular Pharmacology* **2013**, *84*, 12-24.
104. Lin, J.-H.; Perryman, A. L.; Schames, J. R.; McCammon, J. A. Computational drug design accommodating receptor flexibility: the relaxed complex scheme. *Journal of the American Chemical Society* **2002**, *124*, 5632-5633.
105. Amaro, R. E.; Baron, R.; McCammon, J. A. An improved relaxed complex scheme for receptor flexibility in computer-aided drug design. *Journal of Computer-Aided Molecular Design* **2008**, *22*, 693-705.

## Chapter 2

# Targeting DNA Repair in Tumor Cells via Inhibition of ERCC1-XPF \*

### 2.1 Introduction

The ERCC1–XPF heterodimer is a critical DNA repair endonuclease. It plays a pivotal role in nucleotide excision repair (NER) of bulky adducts and helix-distorting DNA lesions, such as UV-induced pyrimidine-(6,4)-pyrimidone photoproducts (6-4PPs) and CPDs.<sup>1-4</sup> ERCC1–XPF also is involved in DNA interstrand crosslink (ICL) repair<sup>5</sup> in cells treated with platinum-based and other chemotherapeutic agents, such as cyclophosphamide and mitomycin C (MMC).<sup>6</sup> In a recent study, 72% of colorectal cancer patients showed positive ERCC1 protein expression, which may be a useful biomarker for colorectal cancer patients.<sup>7</sup> There is also evidence that ERCC1–XPF participates in DNA double-strand break (DSB) repair.<sup>8,9</sup> It thus contributes significantly to the response of cancer cells to a range of DNA-damaging chemotherapeutic agents and radiotherapy. In the ERCC1–XPF complex structure, ERCC1 is considered to be catalytically inactive but rather regulates DNA–protein and protein–protein interactions, whereas the endonuclease activity is provided by XPF, which also contains an inactive helicase-like motif that is likely to be involved in protein–protein interactions and DNA binding.<sup>10,11</sup>

\* The contents of this chapter have been copied and/or adapted from the following publication: “Elmenoufy, A. H.; Gentile, F.; Jay, D.; Karimi-Busheri, F.; Yang, X.; Soueidan, O. M.; Weilbeer, C.; Mani, R. S.; Barakat, K. H.; Tuszynski, J. A.; Weinfeld, M.; West, F. G. Targeting DNA Repair in Tumor Cells via Inhibition of ERCC1–XPF. *Journal of Medicinal Chemistry* **2019**, 62, 7684-7696.”

ERCC1–XPF is an attractive target for drug design due to the availability of experimental structures and the presence of multiple sites that can be inhibited with small molecules to stop the activity of the endonuclease. Our collaborator’s earlier drug design studies focused on the XPA–ERCC1 interaction site<sup>12</sup> and the XPF active site,<sup>13</sup> fostering the use of computer-aided drug design to develop DNA repair inhibitors.<sup>14</sup> However, due to the specificity of the ERCC1–XPF interaction and its general involvement in all the ERCC1–XPF mediated repair processes, the dimerization interface is perhaps the most promising domain to target pharmacologically.<sup>4</sup> Dimerization and localization of ERCC1 and XPF is essential for the enzyme’s stability and endonuclease activity.<sup>15</sup> The dimerization of C-terminal regions of ERCC1 and XPF is the key interaction to form a stable heterodimer. C-terminal regions dimerize through the interaction of their double helix–hairpin–helix (HhH2) motifs.<sup>16, 17</sup> It is thought that XPF acts as a scaffold for ERCC1 during protein folding, and ERCC1 may exhibit improper folding *in vitro* in the absence of XPF.<sup>17</sup> It was demonstrated that without dimerization the activity of ERCC1-XPF was abolished because neither protein was stable, and therefore they were degraded rapidly.<sup>18, 19</sup> As a result, development of small molecule inhibitors that can disrupt the HhH2 domain interactions between ERCC1 and XPF would be expected to sensitize cancer cells to chemotherapeutic treatments whose DNA-damaging effects are repaired by ERCC1–XPF-dependent pathways.<sup>4</sup> Moreover, rational drug design methodology can be employed due to the availability of multiple experimental structures of the dimerized HhH2 domains (for example, PDB code 2A1J and 1Z00).<sup>19</sup>

Recently, McNeil et al. employed an *in silico* screening approach targeting three

sites on the XPF HhH2 domain to identify possible inhibitors of dimer formation. They discovered a small molecule able to inhibit the NER activity in melanoma cells and slightly sensitize them to cisplatin treatment. However, the reported  $K_d$  and  $IC_{50}$  values for this compound were in a range (medium to high  $\mu M$ ) which require further optimization.<sup>20</sup> In addition, Chapman et al.<sup>21, 22</sup> and Arora et al.<sup>23</sup> identified and optimized different small molecules targeting the active site on the XPF nuclease domain. These efforts resulted in several endonuclease inhibitors with  $IC_{50}$  in the nanomolar range that were able to diminish NER activity and enhance the cytotoxicity of platinum-based drugs in cancer cells. Although the specificity of these inhibitors to the ERCC1–XPF endonuclease was assessed in some cases, similarities among active sites of various endonucleases could produce off-target interactions from these compounds; the lack of structural insights of the ligand–protein complexes in this case also limits further development of this series. Most recently, Yang et al. proposed the cellular delivery of therapeutic peptides mimicking the ERCC1 HhH2 domain (residues 220–297) as a promising alternative strategy to inhibit NER activity and sensitize cancer cells to DNA-damaging agents.<sup>24</sup>

Development of small molecule inhibitors of the HhH2 domain interaction would be expected to sensitize cells to therapies whose DNA-damaging effects are repaired by ERCC1–XPF-dependent pathways. Jordheim et al., focused on developing small molecule inhibitors of the NER pathway acting through the inhibition of ERCC1–XPF heterodimerization and reported that compound **1** (also called F06, NSC-130813 or NERI02, as depicted in Figure 2.1) interacted with XPF, repressed the interaction between ERCC1 and XPF *in vitro*, and sensitized cancer cells to MMC and cisplatin.<sup>25</sup>

This affirms the hypothesis that targeting this protein–protein interaction can enhance the cytotoxic activity of crosslinking agents, such as cisplatin. The initial hit, **1**, arose from a virtual screening (VS) of a large compound library, and the study also provided a characterization of the XPF binding pocket and the binding mode of the compound to it.<sup>25</sup> Compound **1** was predicted to interfere with the heterodimerization of ERCC1 and XPF, a necessary step to attain DNA repair activity.

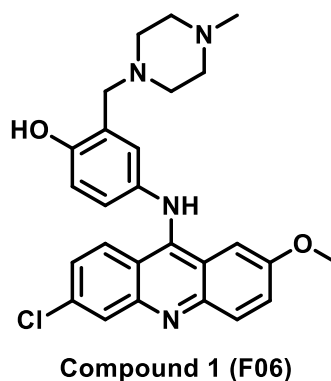


**Figure 2.1.** The structure of the reference hit, compound **1** (F06).

Preliminary *in vitro* assays confirmed that compound **1** shows promising inhibitory activity and acts synergistically with cisplatin. However, the activity of compound **1** is suboptimal in terms of clinical properties, including potency and pharmacokinetic profile, and a derivatization strategy, suggested by Jordheim et al,<sup>25</sup> was adapted to optimize the action of the compound. Also, previous efforts on developing inhibitors for ERCC1–XPF activity were carried out on the truncated version of the heterodimer and not on the full-length protein.<sup>2, 25-27</sup> It is reported that the full length ERCC1–XPF protein was 15-fold more active than the truncated form under standard reaction conditions.<sup>2, 19</sup> To the best of our knowledge, I and my collaborators were the first group to report inhibitors of the activity of the full-length protein. Using

compound **1** as a reference hit, we employed computer-aided drug design techniques, such as electrostatic mapping of the compound **1** binding pocket, molecular docking, pharmacophore modeling, and molecular dynamics (MD)-based rescoring, to rank compound **1** derivatives based on their predicted binding affinities to the XPF domain. The reference compound (compound **1**) and top hits (compounds **2–7**) were synthesized and tested for their ability to inhibit the *in vitro* endonuclease activity of the full length ERCC1–XPF protein, and the most active compound was assessed further as an inhibitor of the repair of UV-induced thymidine dimers in colorectal cancer cells, as well as a sensitizing agent not only to UV radiation but also to cyclophosphamide, which has been used to reduce proliferation of metastatic colorectal cancer significantly.<sup>28</sup>

## 2.2 Results and Discussion

### 2.2.1 Computer-aided Drug Design of Compound **1** Analogues\*

The first step was to investigate the binding mode of the hit compound, **1**, to the pocket on the XPF C-terminus, followed by functionalization and extension of the piperazine ring in compound **1** in order to: 1) provide potential key interactions via hydrogen bond formation or hydrophobic interactions, and 2) optimize the physicochemical properties and binding affinity for better potency of the compound **1** based compounds.

The binding energy for the best docked conformation of **1** to the XPF structures was  $-10.23$  kcal/mol, as calculated by the Autodock scoring function. The compound showed a high shape complementarity with the XPF pocket, which interacts with the F293 residue of ERCC1 in the dimerized complex (Figure 2.2A).

\* The design work was done by AE and FG in collaboration, and FG carried out all the computational work.

Three ligand-receptor hydrogen bonds were observed in the docked pose, namely, with the side chain of E829, the backbone of N834, and the backbone of K860. In addition, the hydrophobic core of **1**, comprised of three aromatic rings, was positioned within a hydrophobic zone constituted by XPF residues Y833, Q838, M856, and H857 (Figure 2.2B). Also, the binding mode of the ligand was in accordance with the spatial distribution of the affinity maps calculated in Molecular Operating Environment 2015 (MOE2015) (Figure 2.2C).

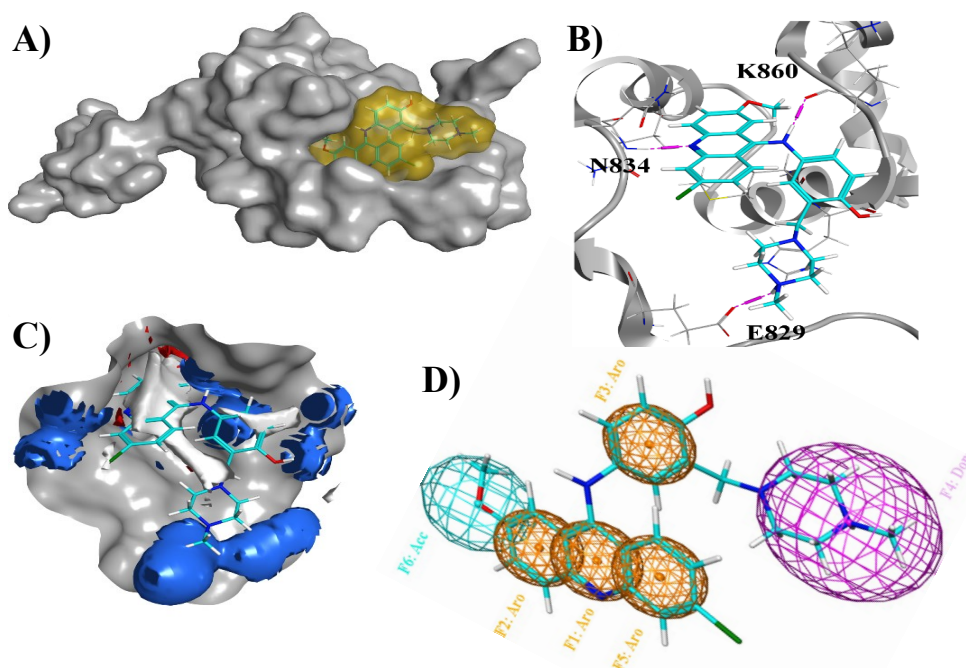


**Figure 2.2.** Visual analysis of **1** docking pose. A) Shape complementarity between the docked pose of **1** and the XPF binding site. The compound was docked to the XPF pocket that wraps around residue F293 of ERCC1 in the dimerization complex. B) Non-bonded interactions. Observed hydrogen bonds are represented in purple. Residues involved in hydrogen bonding or hydrophobic interactions with the ligand are represented explicitly (see text for more details). C) Affinity mapping of the **1** binding site on the XPF HhH2 domain. Blue color indicates zones of interaction where a donor probe atom shows a potential of  $-2$  kcal/mol, therefore, where a ligand donor atom will contribute favourably to the free energy of binding. Red indicates acceptor favorable zones, and white hydrophobic favorable zones. D) Pharmacophore model designed for the lead compound binding to the XPF binding site. Aro features are aromatic, Acc are hydrogen bond acceptors, and Don hydrogen bond donors. Original PDB structure for XPF: 1Z00.

To place the scaffold common to all the analogues within the binding site correctly, a pharmacophore model based on the binding pose of **1** was built using MOE. This model included six features, namely, four aromatic moieties, one hydrogen bond donor, and one hydrogen bond acceptor features (Figure 2.2D) and Table 2.1.

**Table 2.1.** Pharmacophore Features Built from the Docking Pose of **1** to the XPF Site

Feature	Type	Radius (Å)
<b>F1</b>	Aromatic	1.5
<b>F2</b>	Aromatic	1.5
<b>F3</b>	Aromatic	1.5
<b>F4</b>	Donor	3
<b>F5</b>	Aromatic	1.5
<b>F6</b>	Acceptor	2

Upon generation of such features using MOE, we manually adjusted their radii consistently with the spatial distribution of the affinity maps. The total number of molecular structures that were docked was fifty-seven, accounting for all the different states generated during the preparation step. After the docking was performed, just the top scored pose for each analog was retained. The results were ranked according to their Generalized Born Volume Integral/Weighted Surface Area (GBVI/WSA) score, as calculated by MOE. Then, we performed the MD simulations of the complexes and rescored the analogues using the Molecular Mechanics-Generalized Born Surface Area (MM/GBSA) method.

A subset of the top ranked hits was selected for chemical synthesis, as shown in Figure 2.3. According to the *in silico* screening (Table 2.2), seven compounds were

selected to be synthesized among the top hits due to their promising ligand efficiencies and binding energy values in comparison to compound **1**. Derivatization focused primarily on extension of the piperazine ring with different functionalities (i.e., alicyclic (compound **3**), substituted aromatics with electron donating (EDG) or electron withdrawing (EWG) groups (compounds **2**, **5**, **6** and **7**), and an aliphatic chain installed with a basic nitrogen atom (compound **4**)), as shown in Figure 2.3. Compound **8** was synthesized as a control to investigate whether the piperazine ring is crucial for the activity of compounds.

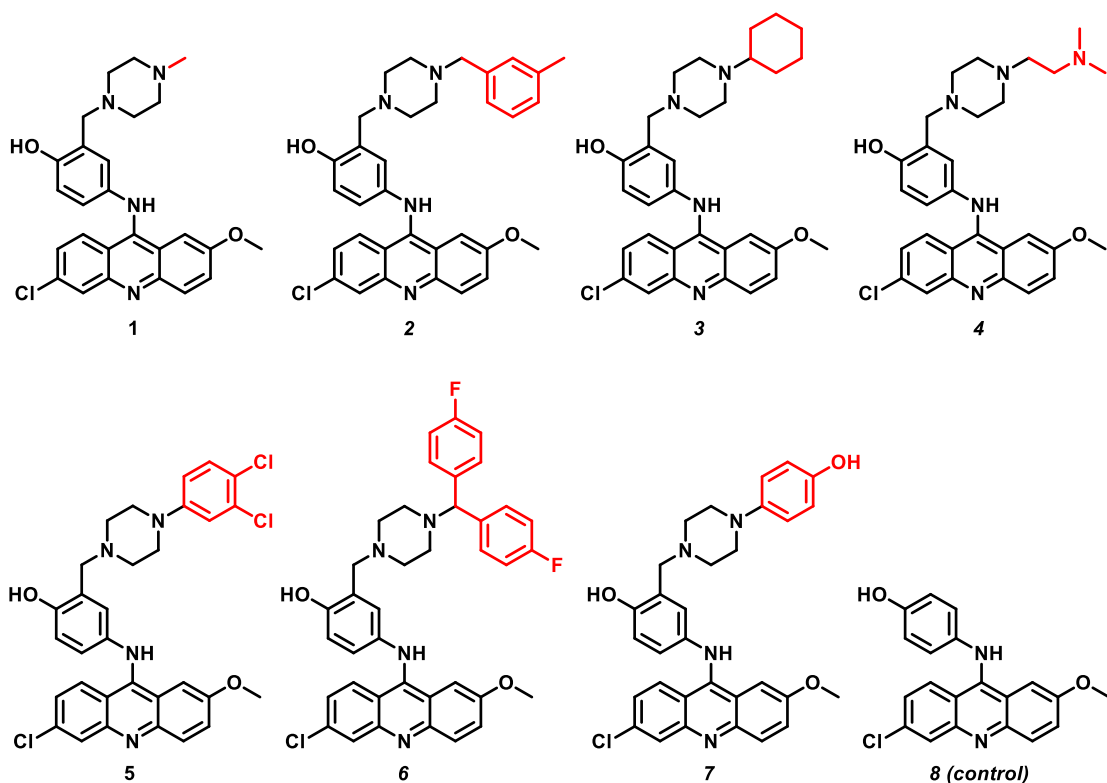


**Figure 2.3.** Compound **1** analogues functionalized with different substituents on the piperazine ring.

The results of the docking-based VS for this subset are reported in Table 2.2. The first two hits (compounds **3** and **4**) were particularly interesting because of their binding

energies in the range of the lead compound, reasonable clogP values, and conserved ligand efficiencies with respect to the hit structure. The decomposition of the binding energies among the residues of the binding pocket revealed a similar pattern of ligand–receptor interactions for the compound **3**, **4** and **1**, although some differences are noticeable for compound **4**.

**Table 2.2.** Computational Results for the Subset of Analogues Chosen for Synthesis

Compound	GBVI/WSA (kcal/mol)	Ligand efficiency ((kcal/mol)/HA) <sup>a</sup>	clogP	MM/GBSA <sup>b</sup> (kcal/mol)
3	-7.06	-0.19	5.80	-21.73
4	-7.52	-0.20	2.61	-13.12
2	-6.83	-0.17	6.24	-11.60
7	-6.93	-0.18	5.50	-11.40
5	-7.57	-0.19	6.98	-9.62
6	-7.13	-0.15	7.63	-9.03
8	-6.44	-0.26	5.50	-4.46
1	-6.70	-0.20	4.10	-17.78

<sup>a</sup>The ligand efficiency was calculated using the GBVI/WSA MOE score divided for the number of heavy atoms (HA) of each molecule. <sup>b</sup>The analogues are ranked based on their MM/GBSA score which includes the entropy contributions. The hit compound **1** is reported as the last entry.

The residues that contribute consistently to the binding of compound **1** analogues were identified as Y833, M856, H857, and V859, where van der Waals interactions dominated the binding. Electrostatic interactions were divided into highly-favorable with acidic residues (D823, E825, E829, E831, D839, E864), and highly-unfavorable with basic residues (K832, K843, K850, R853, H857, H858, K860) due, in part, to the positive protonation state of the piperazine ring of the compounds (Figure 2.4A). Noteworthy, both contributions were generally higher for compound **4**, when compared with compounds **1** and **3**. This may be due to the addition of another positive R-

substituent moiety in compound **4**, different from compounds **1** and **3** where hydrophobic groups were present as R-substituents. A further confirmation of the different nature of the binding was found when analyzing the different contributions of the total binding energy. Indeed, while compounds **1** and **3** showed favorable electrostatic interactions, a highly unfavorable value was observed for compound **4**. An opposite trend was observed for the polar solvation energy, highly favorable for compound **4**, and highly unfavorable for compounds **1** and **3**. Van der Waals and non-polar solvation contributions were similar for all the three compounds (Table 2.3).

**Table 2.3.** Decomposition of Total MM/GBSA Binding Energy in Different Contributions for Compound **1** and the Two Top Analogues

Compound	MM/GBSA (kcal/mol)			
	Van der Waals	Electrostatic	Polar solvation	Non-polar solvation
1	-44.55	-12.69	21.35	-3.41
3	-43.09	-25.99	29.10	-3.47
4	-43.76	63.57	-51.31	-3.12

A detailed analysis of the binding mode of compound **4** is shown in Figure 2.4B. The conserved core structure of the analogue interacted similarly to compound **1** with the residues constituting the binding site, although the backbone of V859 replaces K860 as hydrogen bond partner during the simulation. In addition, a network of water molecules surrounding the binding site and interacting with the exposed substituent at the distal nitrogen of piperazine ring of compound **4** was observed during the 2-ns simulation (Figure 2.4C). These water–ligand interactions may be responsible for the favorable polar solvation contribution to the binding energy of compound **4**. Charge–

charge interactions with the E829 and E831 residues were maintained in terms of average magnitude, when compared with compound **1**. Based on our simulations and because the branch containing the piperazine ring in compound **1** is exposed to the solvent and cannot be accommodated in any additional cleft, we believe that adding a hydrophilic extension such as for compound **4** strongly improves the ligand–solvent interactions and cLogP. Consistent with the importance of limiting the hydrophobicity of the piperazine ring extension, compound **1** analogues carrying aromatic rings in their R-substituents showed reduced calculated binding affinities (Table 2.2). Importantly, electrostatic charge-charge interactions with E829 and E831 residues of XPF were maintained for compound **4**, when compared with compound **1**.

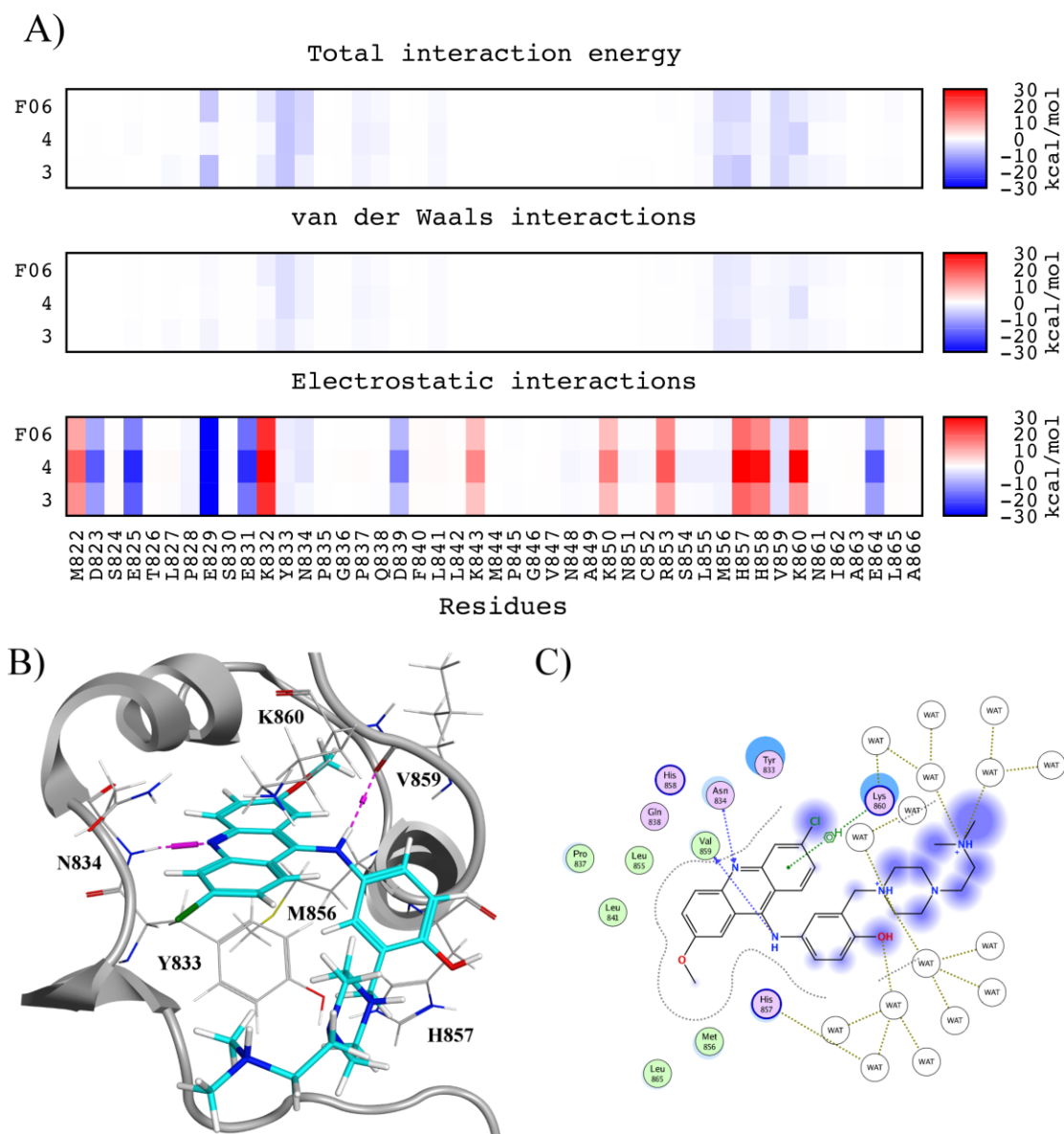
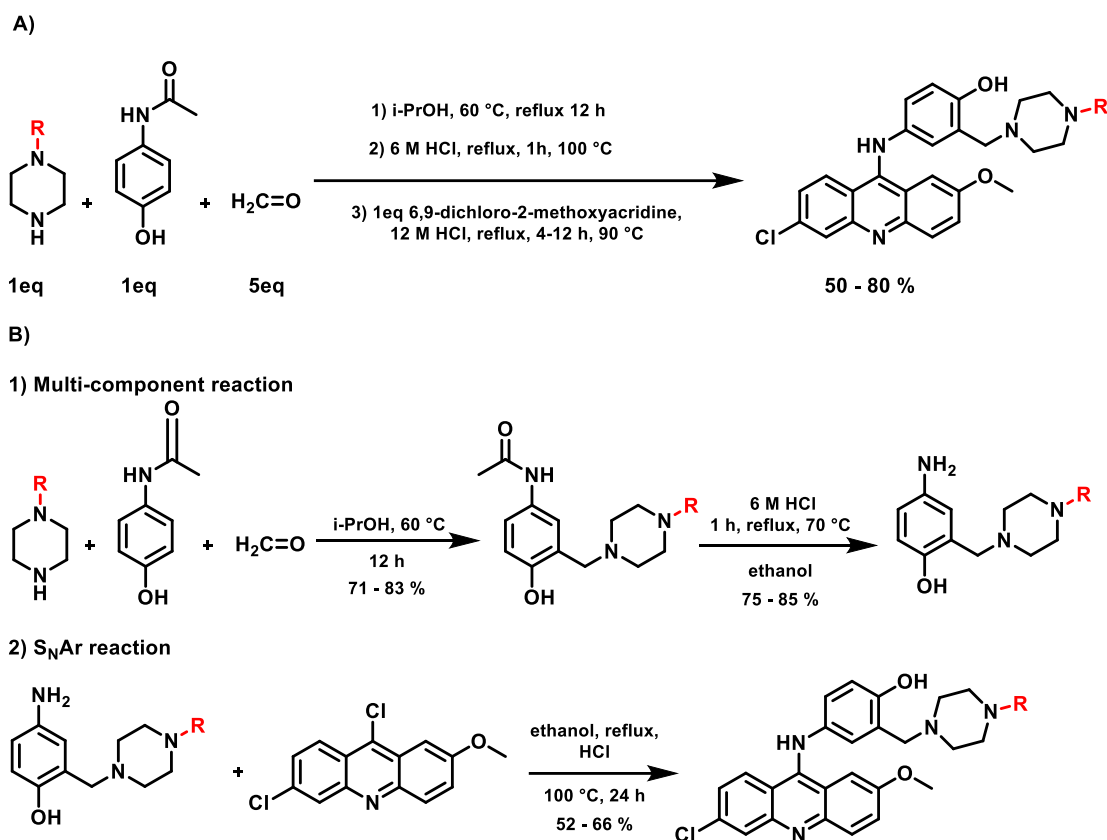


**Figure 2.4.** Analysis of the binding mode of the top hits. A) Per-residue decomposition of ligand–receptor binding energy. Compounds **1\*** and **3** had similar patterns, while compound **4** showed a different pattern of interaction energies. Blue cells indicate favorable interactions, while red cells indicate unfavorable interactions. Refer to the text for more details. B) Lowest potential energy snapshot extracted from the MD simulation of compound **4** bound to XPF. Hydrogen bonds are colored in purple. The highest pocket contributors in terms of total interaction energy are labelled. C) Interaction diagram for compound **4** and surrounding residues and water molecules. The non-bonded interactions established with water molecules was responsible for a highly favorable polar solvation contribution to the binding energy. The diagram refers to the lowest potential energy snapshot extracted from the MD simulation. Original PDB structure for XPF: 1Z00.

\* Compound **1** is represented in Figure 2.4A as **F06**.

## 2.3.2 Synthesis of Compound 1-based Analogues

Synthesis of compounds **1–8** was achieved through a one-pot sequential addition reaction in three steps, as shown in Scheme 2.1.



**Scheme 2.1.** Synthetic route of compounds **1–8** A) One-pot sequential addition reaction. B) Main steps and intermediates included in the one-pot sequential addition reaction.

This Mannich-type reaction of *p*-acetamidophenol with formaldehyde and the appropriate secondary amine in 2-propanol was carried out under reflux for 12 h. The solvent and the excess of unreacted formaldehyde from the resulting mixture were removed under vacuum, and without isolating the compound, the resulting viscous residue was treated with 6 M HCl to deacetylate the acetamido group and furnish the primary amine, as depicted in Scheme 2.1. Afterwards, an equimolar amount of 6,9-

dichloro-2-methoxyacridine was added, affording, after heating, compounds **1–8** in moderate to good yields after isolation. The sequence is general, facile, and reproducible. All synthesized compounds **1–8** were characterized by  $^1\text{H}$  NMR,  $^{13}\text{C}$  NMR, HRMS, IR as depicted in appendix 1, and the purity of the most active compound **4** was determined by HPLC ( $\geq 98\%$  purity), as shown in appendix 2.

### 2.3.3 Inhibition of ERCC1–XPF Endonuclease Activity

Our collaborator, David Jay, used an *in vitro* real-time fluorescence-based assay to assess the inhibitory effect of the synthesized compounds (except compound **2** due to its instability over time caused by low solubility) on ERCC1–XPF endonuclease activity. This assay has been described previously<sup>29</sup> and utilizes a stem–loop substrate (composed of a 10mer-duplex stem and a 20mer-oligodT single-strand loop), labeled on the 5'-terminus with 6-FAM and 3' with the quencher dabcyyl (Q), as shown in Figure 2.5.

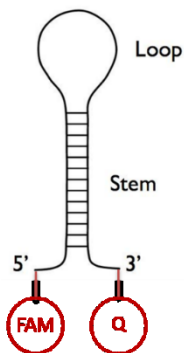


**Figure 2.5.** The structure of DNA stem loop substrate.

Upon ERCC1–XPF cleavage in the 10mer-duplex region, an 8-base 5' FAM-labelled product is released, resulting in an increased fluorescent signal (Figure 2.6A, Control). The other tracings in Figure 2.6A indicate to what extent the different compounds ( $8\ \mu\text{M}$  each) could inhibit scission of the substrate. Nuclease inhibition

results in a decreased slope in the time-dependent increase of the fluorescence signal, with stronger inhibitors leading to a larger decrease in slope (towards the x-axis).

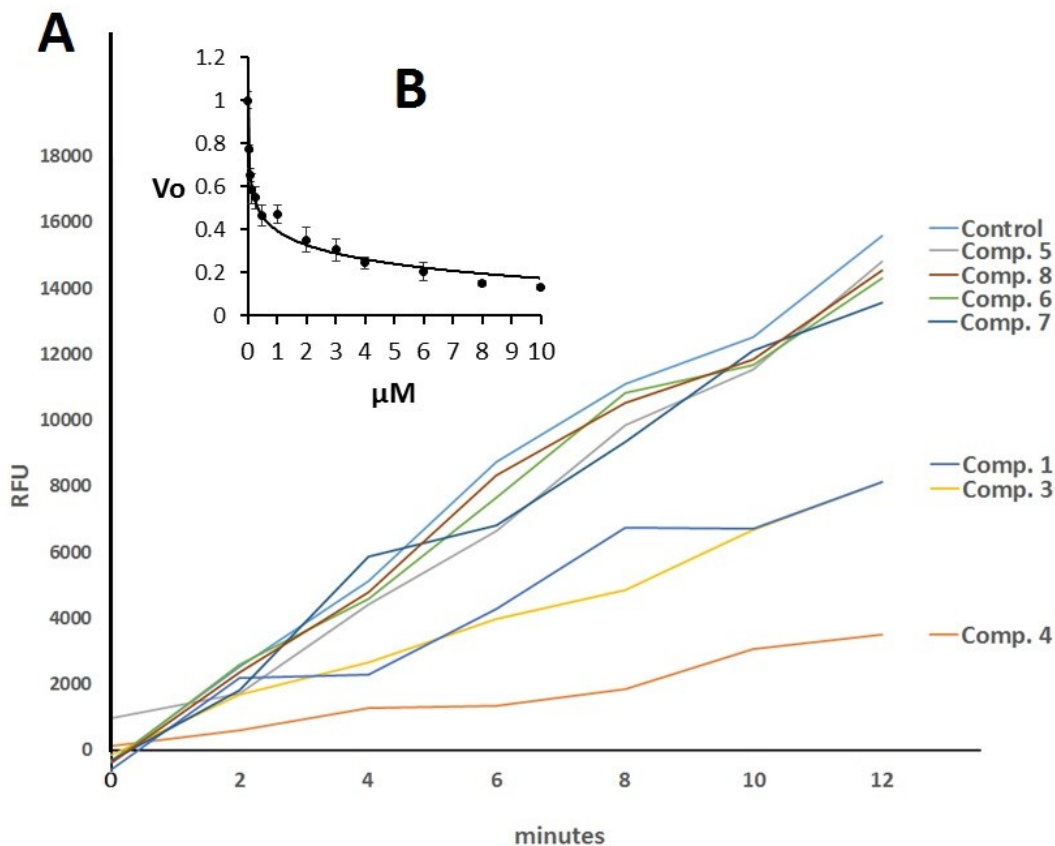


**Figure 2.6.** *In vitro* inhibition of ERCC1-XPF endonuclease activity. A microplate fluorescent assay was used to measure inhibition of ERCC1-XPF endonuclease activity by the different compounds. Incubation of the DNA stem-loop substrate with ERCC1-XPF resulted in the release of a fluorescent 8-base fragment. A) Shows the increase in fluorescence (RFU) with time. A representative tracing of the effect of the different compounds (8  $\mu$ M each) on the incision activity is shown. B) (inset) shows a representative plot of enzyme rate ( $\Delta$ RFU/time) vs compound 4 concentration.

As shown here, three compounds exhibited a marked capacity to inhibit the nuclease activity of ERCC1-XPF, i.e., compounds 1, 3 and 4. For these three compounds, different concentrations of the drugs were plotted against the initial velocity ( $V_o$ , change in relative fluorescence units (RFU)/time) of the enzyme. Figure 2.6B (inset) shows an example of data obtained with compound 4. Half-maximum inhibitory

concentrations ( $IC_{50}$ ) for these compounds were estimated from at least three different experiments for every compound (Table 2.4).

**Table 2.4.** Half-Maximum Inhibitory Concentrations for The Compounds with The Highest Inhibitory Potentials and Their Binding Affinity Values.

Compound	$IC_{50} \pm SD$ ( $\mu M$ ) *	$K_d \pm SD$ (nM)
1	$1.86 \pm 0.25$	$140 \pm 5$
3	$0.38 \pm 0.10$	$145 \pm 5$
4	$0.33 \pm 0.12$	$100 \pm 5$

\*The data was obtained from at least three different experiments of  $V_o$  versus compound concentration.

Since acridine compounds are known to bind nucleic acids via intercalation, the possibility existed that a disruption of the structure of the stem-loop substrate by compound **4** could have been responsible for the inhibition observed in the ERCC1-XPF kinetic assays. To rule out this possibility, the experiment shown in Figure 2.7 was carried out. Pre-incubation of ERCC1-XPF with compound **4** (3  $\mu M$ ) in the reaction medium resulted in a time-dependent loss of enzyme activity. The reactions were started either with addition of the substrate (**T0**) or with substrate that had been pre-incubated in the reaction medium in the presence of compound **4** (3  $\mu M$ ) for 12 min (**T12**). The data indicate that the time-dependent inactivation of ERCC1-XPF by compound **4** was the consequence of the interaction of the drug with the enzyme and was not altered by addition of substrate that had been pre-incubated with the inhibitor. The data in Figure 2.7A were obtained with a concentration of compound **4** approximately 9 times higher than the observed  $IC_{50}$  value of the compound and in the presence of 10% DMSO. When the same test was carried out in the presence of 5% DMSO, a similar time-dependent inhibition was observed, and the substrate exhibited comparable behavior (Figure 2.7B).

(The IC<sub>50</sub> values reported in the present study were obtained by incubating ERCCI–XPF in the presence of the indicated concentrations of the drug for 30 minutes in the reaction medium containing 5% DMSO.)

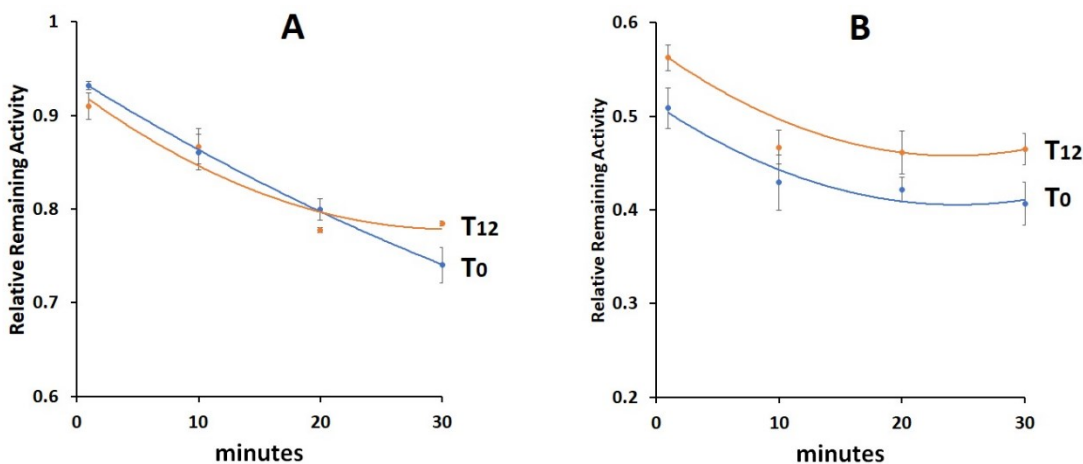


**Figure 2.7.** Time-dependent inactivation of ERCCI–XPF by compound 4. The inactivation experiments were carried out at 25 °C in the reaction medium, indicated in the Section 2.5, which also included 10% or 5% DMSO final concentration (A or B, respectively). The reaction was started (T0) by the addition of ERCCI–XPF (2.5 µg protein/mL), followed by the addition of 3 µM compound 4. 10 µL aliquots from these media (25 ng protein) were withdrawn at the indicated times, and the activity ( $\Delta$ RFU/time) was measured for 6 min by adding 200 nM stem–loop substrate and additional compound 4 diluted in DMSO (10% or 5% DMSO final concentration, A and B, respectively) to render final concentrations of 100 nM stem–loop substrate and 3 µM compound 4 in 10 µL for a final total reaction volume of 20 µL. In T12, the activity was measured by the addition of 200 nM stem–loop substrate that had been pre-incubated with 3 µM compound 4 for 12 min to give the same final concentrations of reagents as indicated for T0.

### 2.3.4 Inhibitor Binding to ERCCI–XPF

Intrinsic fluorescence spectroscopy (of the protein tryptophan residues) was utilized to study the binding affinity of compound 4 (active compound) and compound 5 (inactive compound) to ERCCI–XPF (Figure 2.8). Addition of 2 µM of compound 5 had no significant effect on protein fluorescence, and the observed fluorescence quenching at 330 nm was only  $3 \pm 1\%$ , thus providing no evidence of any interaction (Figure 2.8A). In contrast, addition of compound 4 (2 µM) induced nearly  $23 \pm 2\%$  quenching of protein

fluorescence at 330 nm, clearly indicating interaction of compound 4 with the ERCC1–XPF complex, as depicted in Figure 2.8B.

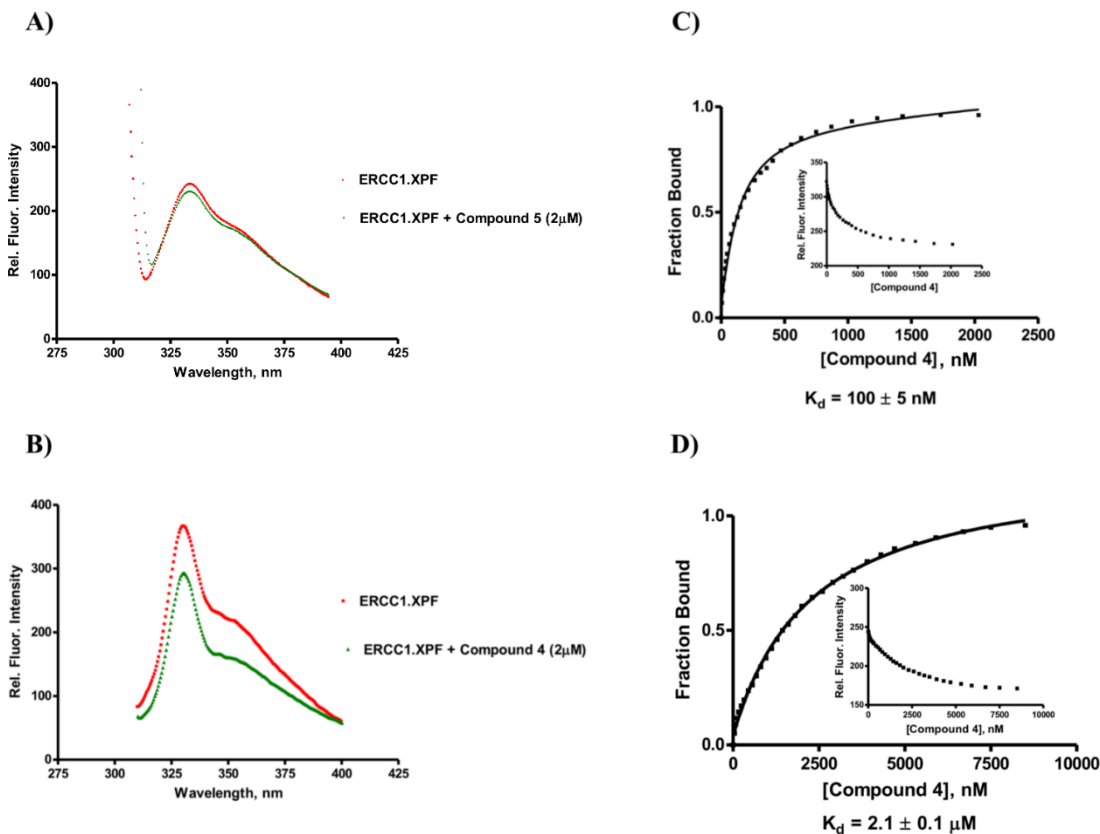


**Figure 2.8.** Determination of the affinity (dissociation constant,  $K_d$ ) between compound 4 and the ERCC1–XPF complex. Quenching of the intrinsic protein fluorescence of the tryptophan residues was used to monitor the interaction between the compounds and the protein. A) Fluorescence of ERCC1–XPF (13 nM and 20 nM) incubated with compound 5 (negative control), and B) compound 4 (active inhibitor), respectively. C) Unimodal binding pattern and the binding affinity of compound 4 with ERCC1–XPF (70 nM). The protein was excited at 295 nm and fluorescence intensity was monitored at 330 nm (see inset). The fraction bound (i.e., relative fluorescence) intensity versus ligand concentration is plotted. D) Binding of Compound 4 to DNA stem–loop substrate of ERCC1–XPF complex. The substrate of ERCC1–XPF was excited at 490 nm, and the fluorescence intensity at 520 nm was monitored as a function of Compound 4 concentration. A unimodal binding pattern was observed and the binding affinity of compound 4 to ERCC1–XPF substrate was  $2.1 \pm 0.1 \mu\text{M}$ .

Binding affinity (in terms of dissociation constant,  $K_d$ ) of compound 4 for ERCC1–XPF complex was determined by following fluorescence quenching (a measure of ligand binding) as a function of ligand concentration. A representative plot of relative fluorescence intensities versus the concentration of compound 4 is shown in Figure 2.8C

(inset). Nonlinear regression analysis (GraphPad Prism Software, San Diego, CA) of the binding data was carried out, as described in an earlier paper by Mani et al.,<sup>30</sup> and revealed a unimodal binding with a  $K_d$  value of  $100 \pm 5$  nM, also shown in Table 2.4. Interestingly, compound **4** has a high binding affinity for ERCC1–XPF that is almost 20-fold greater than its binding affinity to the DNA stem–loop substrate used in the assay, which has a unimodal binding with a  $K_d$  value of  $2.1 \pm 0.1$   $\mu$ M (Figure 2.8D). This disparity in binding affinity strongly suggests that inhibition by **4** results from its interaction with ERCC1–XPF rather than with the DNA substrate.

In an effort to identify a direct interaction between compound **4** and ERCC1–XPF, we decided to utilize microscale thermophoresis (MST). We employed dERCC1 (ERCC1 codons 96–297) and dXPF (XPF codons 667–916) for this analysis because these peptides contain the subunit interaction domains that compound **4** was designed specifically to disrupt. Considering that dERCC1 is produced in low yields in *E. coli* and dXPF, although highly expressed, it is generated mainly as an insoluble fraction in the absence of detergents.<sup>2</sup> A technique that can measure changes in the molecular properties of biomolecules and detect their interactions at low nanomolar concentrations is needed, and MST is such a technique that detects these changes in small amounts of proteins.<sup>31–33</sup> The expectation was that compound **4** would induce a larger change in the thermophoretic properties of the truncated dimer as compared to each of the individual peptides, provided the drug interacted with the enzyme according to the proposed mechanism.

Figure 2.9 shows the thermophoretic property of the fluorescently labeled proteins in the presence or absence of compound **4**. Initiation of the temperature gradient

generated a depletion of the fluorescent signal in the case of dXPF (gray line). In the case of dERCC1, after an initial depletion, the temperature gradient induced a general accumulation of the fluorescent signal (light blue), a behavior that has been observed before for other molecules.<sup>31</sup> The dERCC1–dXPF dimer behaved in an intermediate fashion (dark blue). Addition of compound **4** induced a reproducible minimal change in the dERCC1 (orange) and dXPF (yellow) signals. Importantly, compound **4** changed more dramatically the signal of the dERCC1–dXPF dimer (green vs dark blue), indicating that compound **4** interacts with ERCC1–XPF in the subunit interaction domain and alters the properties of this region.

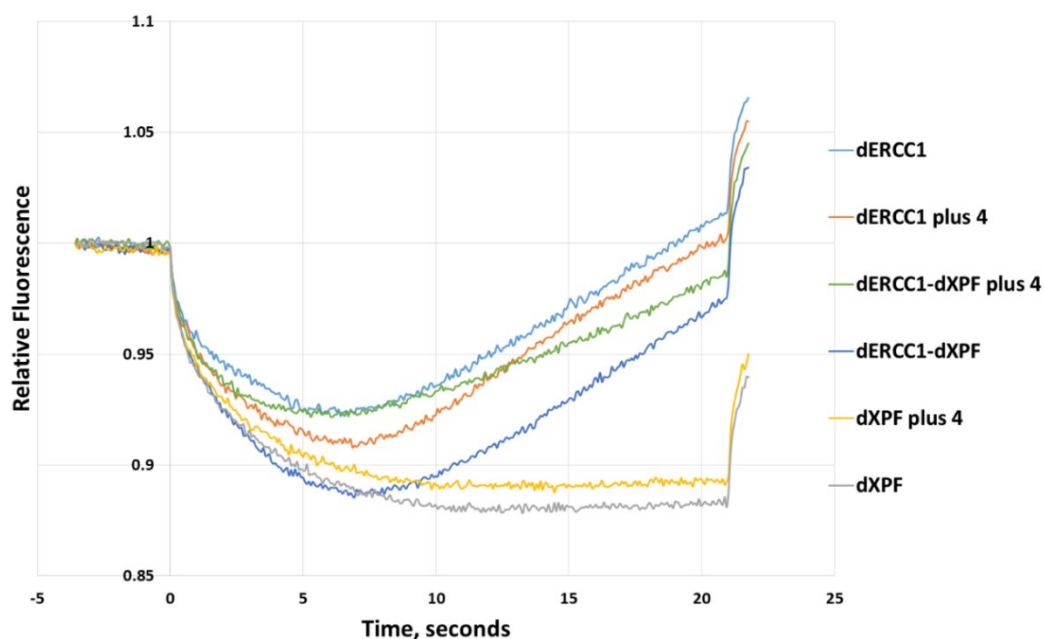


**Figure 2.9.** Microscale thermophoresis measurements. MST was measured in capillaries with a total volume of 10  $\mu$ l. Peptides were incubated with compound **4** or DMSO in MST buffer as indicated in Section 2.5. Relative fluorescence was measured as a function of time (seconds).

### 2.3.5 Inhibition of Cellular Repair of Cyclobutane Pyrimidine Dimers

ERCC1–XPF is required for repair of UV-induced CPDs; these lesions can be formed by exposure of cells in culture to UV irradiation and be detected via an immunofluorescence assay; we irradiated cells with just vehicle (control), either with 2  $\mu\text{M}$  **4**, or with 2  $\mu\text{M}$  **5**. Significant inhibition of NER determined by the removal of UV-induced CPDs compared with control cells over 24 h is depicted in Figure 2.10A. Immunofluorescent detection of CPDs after the exposure of HCT-116 colorectal cells to 8 J/m<sup>2</sup> treated with compound 2  $\mu\text{M}$  **4** showed a significant inhibition of removal of CPDs compared with control cells over 24 h. Based on our results and others,<sup>34</sup> approximately 80% of CPDs are removed over 24 h after UV exposure of HCT-116 cells, but this was reduced to approximately 60% in the presence of compound **4**. On the other hand, compound **5**, which demonstrated very limited inhibition *in vitro*, did not show significant inhibition of cellular removal of CPDs relative to control. Figure 2.10B shows the relative quantification of CPDs after treatment with active (**4**) and inactive (**5**) compounds.

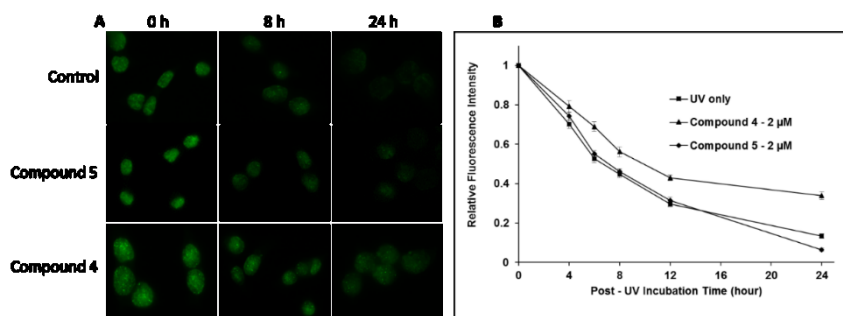


**Figure 2.10.** Inhibition of cellular NER by compound **4**. A) Immunofluorescence images of the UV-based assay for detecting CPDs in HCT-116 cells treated with compounds **4** (2  $\mu\text{M}$ ) and **5** (2  $\mu\text{M}$ ). B) Normalized fluorescence intensity of the treated cells ( $\pm$ S.E.M) based on quantitation of fluorescence from 50 randomly selected cells per treatment. All the values obtained for treatment with compound **4** (2  $\mu\text{M}$ ) from 4–24 h post-irradiation were significantly different ( $p < 0.005$ , Student's t-test) from the values obtained with the control irradiated cells.

### 2.3.6 Increased Sensitization to UV Radiation and Cyclophosphamide

We wanted to look at the ability of **4** to sensitize cytotoxic therapies. However, first we had to identify a concentration of **4** that would not be significantly cytotoxic on its own, so we carried out a clonogenic survival assay and determined that  $\leq 2 \mu\text{M}$  would be acceptable as shown in Figure 2.11. Afterwards, we evaluated the effectiveness of compound **4** (1 and 2  $\mu\text{M}$ ) to sensitize cells to UV irradiation based on clonogenic survival, as shown in Figure 2.12A. In accord with the repair data, 2  $\mu\text{M}$  compound **4** significantly reduced survival of the UV irradiated cells.

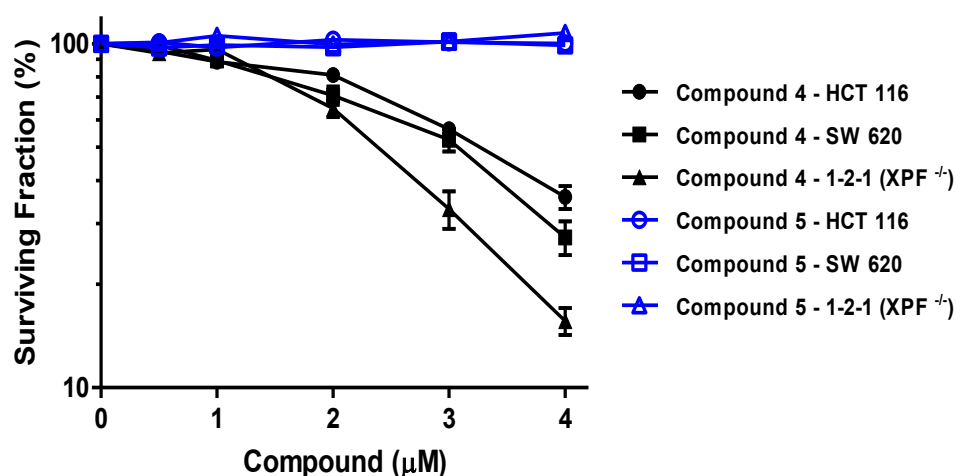


**Figure 2.11.** Survival of HCT-116, SW620, and XPF<sup>-/-</sup> cells treated with increasing doses of compound **4** and compound **5** (negative control) determined by the clonogenic survival assay. The survival curves ( $\pm$ S.E.M) are based on three independent sets of determinations.

We then examined the combined effect of compound **4** (1 and 2  $\mu\text{M}$ ) on cellular survival following exposure to the DNA interstrand crosslinking agent cyclophosphamide using HCT 116 (WT) cells and XPF knockout cell lines. The survival curves shown in Figure 2.12B indicate that, at a concentration of 2  $\mu\text{M}$ , compound **4** significantly sensitized the cells to cyclophosphamide (starting at 50  $\mu\text{M}$ ),

and no colonies were detected on the plates with a cyclophosphamide concentration of 300  $\mu\text{M}$ .

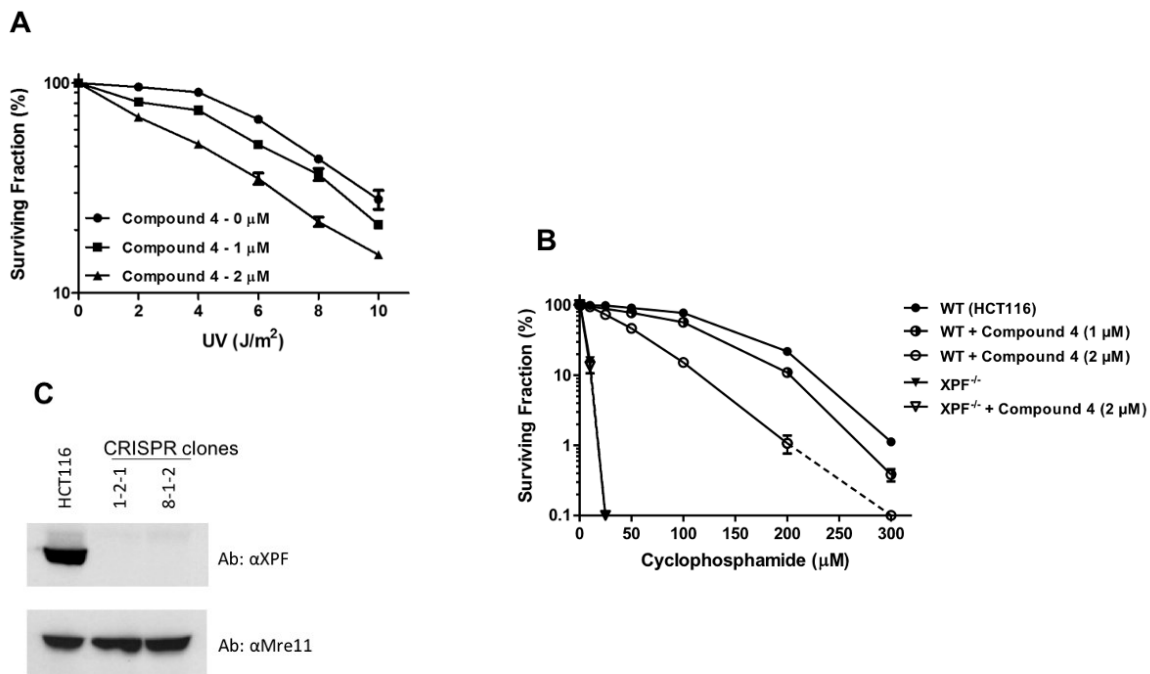


**Figure 2.12.** Sensitization of cells to UV and cyclophosphamide by compound 4. A) Survival of HCT-116 cells exposed to increasing doses of 254 nm UV radiation and treated with 1 and 2  $\mu\text{M}$  compound 4 determined by the clonogenic survival assay. B) Survival of HCT-116 cells exposed to increasing doses of cyclophosphamide and treated with 1 and 2  $\mu\text{M}$  compound 4 determined by the clonogenic survival assay. The dashed line indicates that no colonies were observed after treatment with 300  $\mu\text{M}$  cyclophosphamide + 2  $\mu\text{M}$  compound 4. The survival curves ( $\pm\text{S.E.M}$ ) are based on three independent sets of determinations. All the values obtained with cells treated with 2  $\mu\text{M}$  compound 4 were significantly different ( $p < 0.005$ , Student's t-test) from the values obtained with the control cells not treated with compound 4. C) Human XPF gene knock out confirmation on two positive clone 1-2-1 and 8-1-2 by Western blot analysis using monoclonal antibodies against XPF and Mre11, as control proteins.

### 2.3.7 Pharmacokinetic Properties of Compound 4 and Compound 1

Parental compound 1 and our lead compound 4 was submitted to WuXi AppTec (Shanghai) Co.<sup>44</sup> in China to investigate the ADME profile of the two compounds further and compare their results to determine whether compound 4 is pharmacokinetically more

superior than compound **1**. Compound **4** showed a lower logD (2.86) than **1** (3.86) at pH 7.4 (Table 2.5).

**Table 2.5.** Pharmacokinetic Profile of Compound **4** and Compound **1**

Screening Test	Compound	Results				
LogD at pH 7.4	Compound <b>1</b>	3.86				
	Compound <b>4</b>	2.86				
Metabolic stability in human liver microsomes	Compound <b>1</b>	53.7 (mL/min/kg)				
	Compound <b>4</b>	44.0 (mL/min/kg)				
Metabolic stability in cryopreserved human hepatocytes	Compound <b>1</b>	<17.8 (mL/min/kg)				
	Compound <b>4</b>	48.8 (mL/min/kg)				
Serum protein binding (% bound)	Compound <b>1</b>	99.90				
	Compound <b>4</b>	99.95				
Permeability (Efflux Ratio)	Compound <b>1</b>	11.18				
	Compound <b>4</b>	8.92				
Cytochrome P450 (IC <sub>50</sub> )	Compound <b>1</b>	CYP1A2, 14.1 µM	CYP2C9 21.0 µM	CYP2C19 15.2 µM	CYP2D6 5.20 µM	CYP3A4-M 7.45 µM
	Compound <b>4</b>	CYP1A2, 6.40 µM	CYP2C9 >50 µM	CYP2C19 >50 µM	CYP2D6 16.0 µM	CYP3A4-M 37.1 µM

Metabolism of compound **4**, as measured by exposure to human liver microsome, indicated that it has a metabolism in the midrange, while **1** has a more rapid

metabolism. Both compounds display an efflux ratio of higher than 2 (compound **4** = 8.92 and compound **1** = 11.18). Analysis of five CYP 450 tested enzymes indicates that neither of the compounds has an  $IC_{50}$  lower than 1.00  $\mu$ M, therefore, they are not potent inhibitors of these enzymes. Compound **4**, however, moderately inhibits CYP1A2 with an  $IC_{50}$  of 6.40  $\mu$ M. Compound **1** has the same moderate inhibitory effect on CYP2D6 and CYP3A4-M with an  $IC_{50}$  between 1 and 10  $\mu$ M. Compound **4** acts as a weak inhibitor of CYP2D6 and CYP3A4-M, while compound **1** is a weak inhibitor of three CYP 450 enzymes (CYP1A2, CYP2C9, and CYP2C19) with an  $IC_{50}$  between 10 and 50  $\mu$ M. Both compounds have similar behavior in terms of permeability and binding to serum proteins, as shown in Table 2.5.

To conclude, our comparison of the ADME results between compound **1**, the parental compound, and compound **4** indicated that the latter has more favourable pharmacological properties, particularly a lower logD than **1**, which means that it has a lower lipophilicity, and greater metabolic stability.

## **2.4 Conclusion**

The ERCC1–XPF heterodimer is a structure-specific endonuclease, which is required especially for NER and ICL DNA repair pathways. Although its action is essential to maintain genome integrity and to protect against damage-induced mutations, as part of the NER and ICL machinery it can counteract the effect of DNA damaging therapies, such as platinum-based chemotherapy and radiotherapy. A promising approach to enhance the effect of such therapies is to inhibit the action of DNA repair in cancer cells using small molecules.

In this work, we used a computational drug design workflow to provide a rational design for novel compound **1** analogues, a lead inhibitor targeting the dimerization between XPF and ERCC1, which is required for endonuclease activity. We identified seven compounds for which *in silico* simulations predicted attractive properties, namely, binding affinities and ligand efficiency towards an XPF site on the dimerization interface. The synthesis of the computationally designed compounds was carried out successfully using a simple, robust, and reproducible synthetic strategy. Interestingly, compound **4** has good physicochemical properties, i.e., reasonable logP and ligand efficiency values and small molecular weight, and thus is a potential lead candidate for further optimization. Following structure-activity relationship studies and *in vitro* screening, this approach yielded compounds **3** and **4** as potent inhibitors of ERCC1–XPF activity. An *in vitro* ERCC1–XPF endonuclease assay identified compound **4** as the best ERCC1–XPF inhibitor with an  $IC_{50}$  value of 0.33  $\mu$ M compared to 1.86  $\mu$ M for compound **1**. In addition, the  $K_d$  value for this compound was measured experimentally as 100 nM and interacts with ERCC1–XPF in the subunit interaction domain, altering the related properties of this heterodimerization interface. Compound **4** also showed a significant inhibition of the removal of cyclobutane pyrimidine dimers compared with control cells after exposure of HCT-116 cells to UV radiation and sensitized the cells to UV and cyclophosphamide-induced cytotoxicity, indicating inhibition of NER and ICL repair. Furthermore, compound **4** possesses favourable pharmacokinetic properties, particularly a lower logD than compound **1**, which means that it has a lower lipophilicity and greater metabolic stability. Our computational workflow successfully identified superior compounds from a set of analogues differing by one substituent group.

Additionally, it provided detailed information about the ligand–protein interaction. Compound **4** was our best *in vitro* analogue. Detailed analysis of the MM/GBSA binding energies, together with the visual analysis of the simulation results, suggests a binding mode for compound **4** where the conserved hydrophobic core of the analogue is buried inside the XPF binding site and, different from the other active compounds (**1** and **3**), the positive R-substituent is favorably exposed to the solvent. Although all of the compounds share the acridine moiety, our assay showed that the inhibition activity of compound **4** was the consequence of the interaction of the drug with the enzyme and not the result of binding with DNA. The fact that compounds **4** and **5** (negative control) show drastically different activity despite possessing the same acridine moiety also provides strong evidence that inhibition is not mediated via DNA intercalation. In summary, the use of *in silico* methods to design a superior compound to **1** led to compound **4** that, potentially, can be used in combination with other existing DNA-damaging therapies to amplify their effects by sensitizing cancer cells.

In future work, compound **4** will be the starting point for further optimization towards a drug candidate compound to yield an optimized lead analogue of compound **4**. Since polar side-chain installation at the exterior part of the piperazine position clearly enhances activity, we intend to explore a wider range of polar groups on the remote end of the piperazine. At the same time, we will retain the dimethylaminoethyl group and explore structural changes in parts of the molecule that are intercalated more deeply into the protein binding pocket. Different generations of compound **4** derivatives will be synthesized according to the corresponding *in silico* studies and the current SAR results

in this study for the aim of obtaining a drug like candidate that has superior physicochemical properties to compound 4.

## 2.5 Methods and Experimental Section\*

### 2.5.1 General Experimental Procedures for Preparation of The Top Compound 1 Analogues

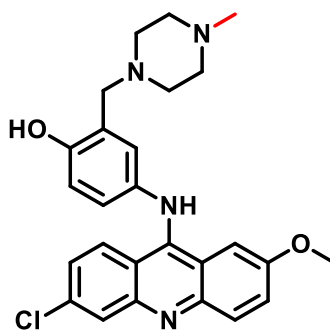
Some reactions were carried out in flame-dried glassware under a positive nitrogen atmosphere, unless otherwise stated. Transfer of anhydrous solvents and reagents was accomplished with oven-dried syringes or cannulae. Chemicals were purchased from Sigma Aldrich Inc. and were used without further purification. Thin layer chromatography was performed on glass plates pre-coated with 0.25 mm silica gel. Flash chromatography columns were packed with 230–400 mesh silica gel. Proton nuclear magnetic resonance spectra ( $^1\text{H}$  NMR) were recorded at 500 MHz, and coupling constants (J) are reported in hertz (Hz). Standard notation was used to describe the multiplicity of signals observed in  $^1\text{H}$  NMR spectra: broad (br), multiplet (m), singlet (s), doublet (d), triplet (t), etc. Carbon nuclear magnetic resonance spectra ( $^{13}\text{C}$  NMR) were recorded at 125 MHz and are reported (ppm) relative to the center line of the triplet from chloroform-d (77.0 ppm) or the center line of the septet from methanol-d<sub>4</sub> (49.0 ppm). Infrared (IR) spectra were measured with a FT-IR 3000 spectrophotometer. Mass spectra were determined on a high-resolution electrospray positive ion mode spectrometer.

\* I was responsible for the synthesis and design of all compounds. F.G. designed the computational studies of the compounds. D.J. expressed and purified ERCC1–XPF, employed the *in vitro* ERCC–XPF1 assay, and conducted microscale thermophoresis measurements. F.K.B and Y.X. carried out cell culture, UV dimer repair assay, and clonogenic survival assay. R.M. conducted the binding affinity studies of the compounds.

The high-performance liquid chromatography (HPLC) analyses were performed using an Agilent 1100 LC/MSD instrument. Elution was done with a gradient of 10–95% solvent B in solvent A (solvent A was 0.1% TFA in water, and solvent B was 0.1% acetic acid in MeCN) through an Agilent column eclipse XDB- C18 (4.6 × 250 mm, 5 μm) column at 1.0 mL/min. The area % purity was measured at 210 and 254 nm. The purity of the most active compound **4** was assessed by HPLC (98%).

## 2.5.2 Synthesis and Characterization of Inhibitors (1-8)

### 4-((6-Chloro-2-methoxyacridin-9-yl)amino)-2-((4-methylpiperazin-1-yl)methyl)phenol (**1**)

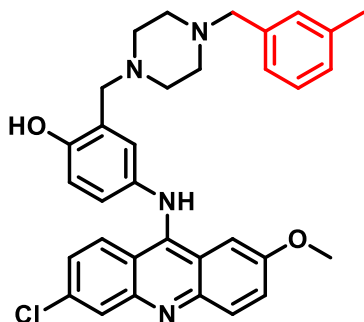


**1**

Synthesis of compound **1** was achieved through a one-pot sequential addition reaction in three steps. A mixture of *N*-methyl piperazine (0.12 mL, 1.0 mmol), *p*-acetamidophenol (0.15 g, 1.0 mmol) and 37% formaldehyde (0.10 mL, 5.0 mmol) in isopropyl alcohol (2 mL) was taken in a 10 mL single neck round bottom flask. Then, the reaction mixture was stirred and heated under reflux at 65 °C for 6 h. Upon completion of the reaction (monitored by TLC with 15% MeOH/DCM eluent system), the solvent was removed on a rotatory evaporator. Next, the residue was dissolved in 3

mL ethanol and 3 drops of 12 M HCl were added. Subsequently, the reaction mixture was heated at 90 °C under reflux for 90 min. Afterwards, 6,9-dichloro-methoxyacridine (0.28 g, 1.0 mmol) was added to the mixture and further stirred at 90 °C under reflux, and the course of reaction followed by TLC until little or no starting material was detected (around 12 h). On cooling to room temperature, the reaction mixture was diluted with cold water and neutralized to pH of 8–9 with 28% v/v ammonia solution. The alkaline solution was extracted with dichloromethane. The organic layer was washed with brine, concentrated in vacuum, and purified by column chromatography (gradient elution with 5% to 10% MeOH:DCM system) to afford compound **1** as an orange reddish semisolid (0.08 g) in 78% yield;  $R_f$  0.50 (2:8, MeOH:DCM); IR (cast film)  $\nu_{\max}$  = 3272, 2923, 1629, 1254, 1231, 1032, 926, 816, 815, 775  $\text{cm}^{-1}$ ;  $^1\text{H}$  NMR (500 MHz,  $\text{CDCl}_3$ )  $\delta$  7.99 (s, 1H), 7.91 (d,  $J$  = 8.7 Hz, 1H), 7.80 (d,  $J$  = 9.2 Hz, 1H), 7.29 (dd,  $J$  = 9.4, 2.6 Hz, 1H), 7.11 (d,  $J$  = 10.7 Hz, 1H), 7.03 (s, 1H), 6.77 – 6.70 (m, 2H), 6.49 (d,  $J$  = 2.5 Hz, 1H), 3.63 (s, 3H), 3.53 (s, 2H), 2.75 – 2.32 (m, 8H), 2.27 (s, 3H), OH and NH protons were not observed;  $^{13}\text{C}$  NMR (125 MHz,  $\text{CDCl}_3$ )  $\delta$  155.9, 153.2, 147.8, 143.9, 137.0, 135.0, 125.0, 124.9, 122.0, 121.8, 120.0, 119.9, 119.7, 117.6, 116.8, 116.5, 116.1, 115.9, 100.3, 61.1, 55.2, 54.8 (2C), 52.4 (2C), 45.8; HRMS (ESI) calcd for  $\text{C}_{26}\text{H}_{28}\text{ClN}_4\text{O}_2$   $[\text{M} + \text{H}]^+$  463.1895; found 463.1890.

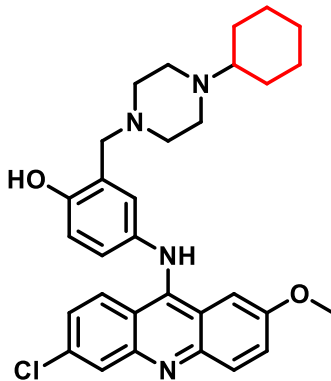
**4-((6-Chloro-2-methoxyacridin-9-yl)amino)-2-((4-(3-methylbenzyl)piperazin-1-yl)methyl)phenol (2)**



**2**

The previous method was employed to synthesize compound **2** with the following stoichiometric amounts: 1-(3-methylbenzyl)piperazine (0.19 g, 1.0 mmol) and 6,9-dichloroacridine (0.28 g, 1.0 mmol) to afford it as an orange reddish semisolid (0.14 g) in 73% yield;  $R_f$  0.44 (1:9, MeOH:DCM); IR (cast film)  $\nu_{\max}$  = 3258, 2921, 1629, 1560, 1493, 1253, 1133, 1007, 927, 826, 775  $\text{cm}^{-1}$ ;  $^1\text{H}$  NMR (500 MHz,  $\text{CDCl}_3$ )  $\delta$  8.05 (s, 1H), 7.95 (d,  $J$  = 9.2 Hz, 1H), 7.83 (d,  $J$  = 9.2 Hz, 1H), 7.32 (d,  $J$  = 7.6 Hz, 1H), 7.21 (t,  $J$  = 7.5 Hz, 1H), 7.17 – 7.06 (m, 5H), 6.87 (d,  $J$  = 7.1 Hz, 1H), 6.77 (d,  $J$  = 8.6 Hz, 1H), 6.62 (d,  $J$  = 1.9 Hz, 1H), 3.70 (s, 3H), 3.59 (s, 2H), 3.49 (s, 2H), 2.79 – 2.40 (m, 8H), 2.35 (s, 3H). OH and NH protons were not observed;  $^{13}\text{C}$  NMR (125 MHz,  $\text{CDCl}_3$ )  $\delta$  156.1, 153.9, 150.4, 146.8, 144.5, 137.9, 137.6, 136.3, 135.5, 129.9, 128.2, 127.9, 126.2, 125.4, 125.0, 122.1, 121.8, 120.6, 120.3, 119.2, 116.9, 116.5, 116.1, 115.9, 100.4, 62.8, 61.2, 55.4, 52.8 (2C), 52.5 (2C), 21.4; HRMS (ESI) calcd for  $\text{C}_{33}\text{H}_{34}\text{ClN}_4\text{O}_2$   $[\text{M} + \text{H}]^+$  553.2357; found 553.2365.

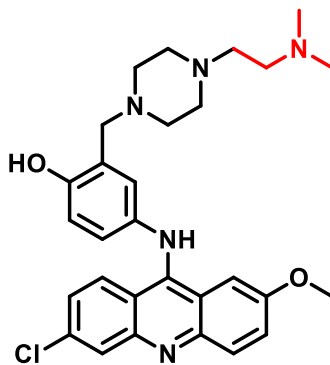
**4-((6-Chloro-2-methoxyacridin-9-yl)amino)-2-((4-cyclohexylpiperazin-1-yl)methyl)phenol (3)**



**3**

The previous method was employed to synthesize compound **3** with the following stoichiometric amounts: 1-cyclohexyl piperazine (0.17 g, 1.0 mmol) and 6,9-dichloroacridine (0.28 g, 1.0 mmol) to afford it as an orange reddish semisolid (0.13 g) in 81% yield;  $R_f$  0.52 (0.5:9.5, MeOH: EtOAc); IR (cast film)  $\nu_{\max}$  = 3313, 2918, 1736, 1560, 1468, 1255, 1235, 1181, 1032, 929, 829, 722  $\text{cm}^{-1}$ ;  $^1\text{H}$  NMR (500 MHz,  $\text{CDCl}_3$ )  $\delta$  8.03 (d,  $J$  = 1.4 Hz, 1H), 7.92 (d,  $J$  = 9.6 Hz, 1H), 7.80 (d,  $J$  = 9.5 Hz, 1H), 7.28 (d,  $J$  = 5.7 Hz, 1H), 7.11 (d,  $J$  = 9.1 Hz, 2H), 6.91 (d,  $J$  = 9.3 Hz, 1H), 6.77 (d,  $J$  = 8.5 Hz, 1H), 6.69 (s, 1H), 3.71 (s, 3H), 3.60 (s, 2H), 2.73 – 2.22 (m, 8H), 1.83 (m, 4H), 1.63 (d,  $J$  = 12.8 Hz, 1H), 1.26 – 1.18 (m, 6H). OH and NH protons were not observed;  $^{13}\text{C}$  NMR (125 MHz,  $\text{CDCl}_3$ )  $\delta$  156.1, 153.8, 146.9, 144.5, 136.3, 135.5, 125.4 – 116.8 (10 C), 101.3, 100.4, 98.8, 63.4, 61.3, 52.9 (2 C), 48.7 (2 C), 29.7, 28.9 (2 C), 26.2, 25.8 (2 C); HRMS (ESI) calcd for  $\text{C}_{31}\text{H}_{35}\text{ClN}_4\text{O}_2$   $[\text{M} + \text{H}]^+$  531.2521; found 531.2527.

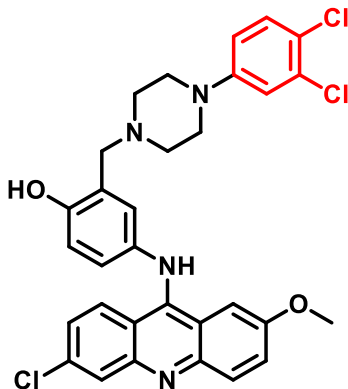
**4-((6-Chloro-2-methoxyacridin-9-yl)amino)-2-((4-(2-(dimethylamino)ethyl) piperazin-1-yl) methyl) phenol (4)**



4

The previous method was employed to synthesize compound **4** with the following stoichiometric amounts: 1-[2-(dimethylamino)ethyl] piperazine (0.16 g, 1.0 mmol) and 6,9-dichloroacridine (0.28 g, 1.0 mmol) to afford it as an orange reddish semisolid (0.13 g) in 80 % yield;  $R_f$  0.40 (1.3: 8.5: 0.2, MeOH: DCM: Et<sub>3</sub>N); IR (cast film)  $\nu_{\max}$  = 3361, 2918, 1736, 1562, 1467, 1295, 1255, 1143, 1032, 945, 828, 763, 722  $\text{cm}^{-1}$ ; <sup>1</sup>H NMR (500 MHz, CDCl<sub>3</sub>)  $\delta$  8.10 (s, 1H), 8.00 (s, 1H), 7.89 (d,  $J$  = 9.1 Hz, 1H), 7.40 (d,  $J$  = 9.8 Hz, 1H), 7.24 (d,  $J$  = 8.0 Hz, 1H), 7.09 (s, 1H), 6.85 (dd,  $J$  = 8.6, 2.7 Hz, 1H), 6.78 (d,  $J$  = 8.6 Hz, 1H), 6.56 (d,  $J$  = 2.3 Hz, 1H), 3.74 (s, 3H), 3.59 (s, 2H), 2.70 – 2.40 (m, 12H), 2.27 (s, 6H). OH and NH protons were not observed; <sup>13</sup>C NMR (125 MHz, CDCl<sub>3</sub>)  $\delta$  156.2, 153.6, 147.5, 144.0, 136.6, 135.2, 125.3, 125.1, 124.8, 122.0, 120.3, 120.2, 120.0, 119.8, 119.6, 117.5, 116.9, 116.3, 100.2, 61.2, 56.7, 56.7, 55.3, 53.3 (2C), 52.4 (2C), 45.8 (2C); HRMS (ESI) calcd for C<sub>29</sub>H<sub>35</sub>ClN<sub>5</sub>O<sub>2</sub> [M + H]<sup>+</sup> 520.2474; found 520.2473.

**4-((6-Chloro-2-methoxyacridin-9-yl)amino)-2-((4-(3,4-dichlorophenyl)piperazin-1-yl)methyl)phenol (5)**

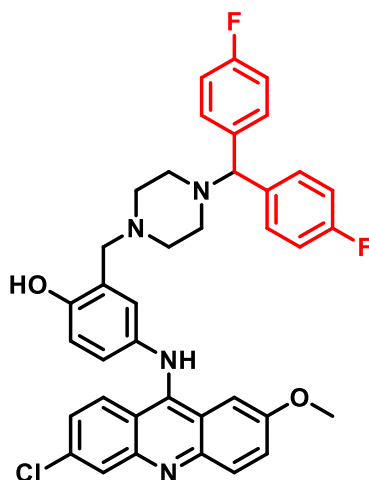


5

The previous method was employed to synthesize compound **5** with the following stoichiometric amounts: 1-(3,4-dichlorophenyl) piperazine (0.23 g, 1.0 mmol), *p*-acetamidophenol (0.15 g, 1.0 mmol), 37% formaldehyde (0.10 mL, 5 mmol) and 6,9-dichloroacridine (0.28 g, 1.0 mmol) to afford it as an orange reddish semisolid (0.16 g) in 71% yield;  $R_f$  0.56 (0.5:9.5, MeOH:DCM); IR (cast film)  $\nu_{\max}$  = 3271, 2918, 1736, 1563, 1227, 1180, 1080, 1031, 803, 721  $\text{cm}^{-1}$ ;  $^1\text{H}$  NMR (500 MHz,  $\text{CDCl}_3$ )  $\delta$  8.09 (s, 1H), 8.00 (s, 1H), 7.88 (d,  $J$  = 9.2 Hz, 1H), 7.40 (d,  $J$  = 9.3 Hz, 1H), 7.28 (d,  $J$  = 8.7 Hz, 1H), 7.24 (d,  $J$  = 9.0 Hz, 1H), 7.09 (s, 1H), 6.95 (d,  $J$  = 2.8 Hz, 1H), 6.87 (dd,  $J$  = 8.6, 2.7 Hz, 1H), 6.80 (d,  $J$  = 8.6 Hz, 1H), 6.73 (dd,  $J$  = 8.9, 2.8 Hz, 1H), 6.54 (d,  $J$  = 2.6 Hz, 1H), 3.74 (s, 3H), 3.63 (s, 2H), 3.27 – 3.15 (m, 4H), 2.72 – 2.62 (m, 4H), OH and NH protons were not observed;  $^{13}\text{C}$  NMR (125 MHz,  $\text{CDCl}_3$ )  $\delta$  156.3, 153.1, 150.2, 147.9, 143.3, 137.0, 135.0, 132.9, 130.5, 125.2, 124.7, 122.9, 121.6, 121.4, 120.2, 120.0, 119.7, 117.9, 117.6, 117.0, 116.7, 116.2, 115.6, 115.5, 100.0, 61.2, 55.4 (2C),

52.2 (2C), 48.7; HRMS (ESI) calcd for C<sub>31</sub>H<sub>28</sub>Cl<sub>3</sub>N<sub>4</sub>O<sub>2</sub> [M + H]<sup>+</sup> 593.1272; found 593.1272.

**2-((4-(Bis(4-fluorophenyl)methyl)piperazin-1-yl)methyl)-4-((6-chloro-2-methoxyacridin-9-yl)amino)phenol (6)**

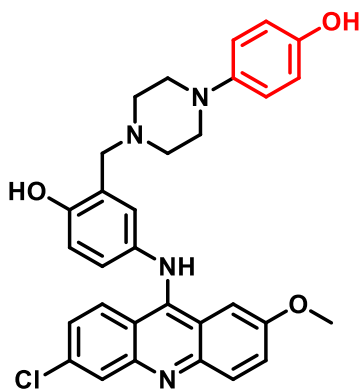


6

The previous method was employed to synthesize compound **6** with the following stoichiometric amounts: 1-bis (4-fluorophenyl)methylpiperazine (0.29 g, 1.0 mmol), *p*-acetamidophenol (0.15 g, 1.0 mmol), 37% formaldehyde (0.10 mL, 5 mmol) and 6,9-dichloroacridine (0.28 g, 1.0 mmol) to afford it as an orange reddish semisolid (0.19 g) in 65% yield; *R<sub>f</sub>* 0.56 (0.5:9.5, MeOH:DCM); IR (cast film)  $\nu_{\text{max}} = 3275, 2919, 1737, 1566, 1255, 1217, 1181, 1032, 828, 722 \text{ cm}^{-1}$ ; <sup>1</sup>H NMR (500 MHz, CDCl<sub>3</sub>)  $\delta$  8.07 (s, 1H), 7.98 (d, *J* = 9.0 Hz, 1H), 7.84 (d, *J* = 9.2 Hz, 1H), 7.34 (m, 6H), 7.18 (d, *J* = 8.0 Hz, 1H), 7.06 (d, *J* = 1.8 Hz, 1H), 6.97 (m, 5H), 6.83 (dd, *J* = 8.5, 2.6 Hz, 1H), 6.75 (d, *J* = 8.6 Hz, 1H), 6.53 (d, *J* = 2.2 Hz, 1H), 4.23 (s, 1H), 3.69 (s, 3H), 3.57 (s, 2H), 2.74 – 2.21 (m, 8H); <sup>13</sup>C NMR (125 MHz, CDCl<sub>3</sub>)  $\delta$  161.9 (2C), 156.2, 153.5, 150.3, 147.7,

143.7, 137.8 (2C), 136.7, 135.0, 129.2 (4C), 125.2, 124.8, 121.9, 121.7, 120.2, 119.9, 119.7, 117.6, 116.8, 116.5, 116.1, 115.5 (4C), 100.0, 74.3, 61.1, 55.3, 52.6 (2C), 51.5 (2C); HRMS (ESI) calcd for C<sub>38</sub>H<sub>34</sub>ClF<sub>2</sub>N<sub>4</sub>O<sub>2</sub> [M + H]<sup>+</sup> 651.2333; found 651.2328.

**4-((6-Chloro-2-methoxyacridin-9-yl)amino)-2-((4-(4-hydroxyphenyl)piperazin-1-yl)methyl)phenol (7)**

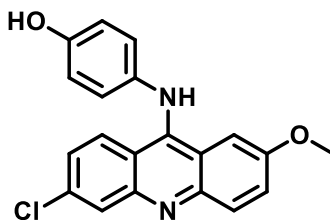


7

The previous method was employed to synthesize compound 7 with the following stoichiometric amounts: 1-(4-hydroxyphenyl)piperazine (0.30 g, 1.0 mmol), *p*-acetamidophenol (0.15 g, 1.0 mmol), 37% formaldehyde (0.10 mL, 5 mmol) and 6,9-dichloroacridine (0.28 g, 1.0 mmol) to afford it as an orange reddish semisolid (0.17 g) in 59% yield; *R<sub>f</sub>* 0.58 (1.5:8.5, MeOH:DCM); IR (cast film)  $\nu_{\max}$  = 3334, 2918, 1737, 1564, 1468, 1235, 1181, 1031, 930, 830, 722 cm<sup>-1</sup>; <sup>1</sup>H NMR (500 MHz, CD<sub>3</sub>OD)  $\delta$  8.07 (d, *J* = 9.3 Hz, 1H), 7.87 (d, *J* = 1.8 Hz, 1H), 7.82 (d, *J* = 9.3 Hz, 1H), 7.51–7.46 (m, 1H), 7.41 (d, *J* = 2.5 Hz, 1H), 7.29–7.24 (m, 1H), 7.04 (dd, *J* = 8.7, 2.4 Hz, 1H), 6.93–6.89 (m, 1H), 6.88–6.81 (m, 3H), 6.70 (dd, *J* = 8.9, 2.3 Hz, 2H), 3.72 (s, 3H), 3.61 (s, 2H), 3.11–2.99 (m, 4H), 2.82–2.67 (m, 4H), OH and NH protons were not

observed;  $^{13}\text{C}$  NMR (125 MHz,  $\text{CDCl}_3$ )  $\delta$  156.3, 153.5, 152.1, 150.2, 150.1, 145.3, 145.2, 144.0, 125.3, 124.7, 122.5, 121.9, 121.5, 120.4, 120.0, 118.8 (2C), 118 (2C), 118.4, 118.1, 117.0, 116.5, 116.1, 115.9, 61.3, 55.4, 52.7 (2C), 50.7 (2C); HRMS (ESI) calcd for  $\text{C}_{31}\text{H}_{30}\text{ClN}_4\text{O}_3$   $[\text{M} + \text{H}]^+$  541.2001; found 541.2010.

#### 4-((6-Chloro-2-methoxyacridin-9-yl)amino)phenol (**8**)



**8**

Synthesis of compound **8** was carried out according to the reported procedures<sup>21</sup> with minor modifications. The synthesis was performed by mixing 4-aminophenol (0.11 g, 1.0 mmol) and 6,9-dichloroacridine (0.28 g, 1.0 mmol) in a 10 mL single neck round bottom flask and stirred at 90 °C under reflux. The course of the reaction was followed by TLC until little or no starting material was detected (around 12 h). On cooling to room temperature, the reaction mixture was diluted with cold water and neutralized to pH of 8–9 with 28% v/v ammonia solution. The alkaline solution was extracted with dichloromethane. The organic layer was washed with brine, concentrated in vacuum, and purified by column chromatography (gradient elution with 1% to 5% MeOH:DCM system) to afford it as an orange reddish semisolid in 73% yield;  $R_f$  0.47 (1.5:8.5, MeOH:DCM); IR (cast film)  $\nu_{\text{max}}$  = 3325, 2918, 1737, 1562, 1468, 1236, 1180, 1103, 1050, 722  $\text{cm}^{-1}$ ;  $^1\text{H}$  NMR (500 MHz,  $\text{CD}_3\text{OD}$ )  $\delta$  8.12 (d,  $J$  = 9.4 Hz, 1H), 7.84 – 7.83

(m, 1H), 7.78 (d,  $J = 9.3$  Hz, 1H), 7.61 (dd,  $J = 9.3, 2.6$  Hz, 1H), 7.48 (d,  $J = 1.5$  Hz, 1H), 7.35 (dd,  $J = 9.4, 2.1$  Hz, 1H), 7.27 – 7.22 (m, 2H), 6.95 – 6.91 (m, 2H), 3.88 (s, 1H), 3.69 (s, 3H). OH proton was not observed;  $^{13}\text{C}$  NMR (125 MHz,  $\text{CD}_3\text{OD}$ )  $\delta$  158.9, 157.7, 141.7, 137.9, 133.2, 129.8, 128.4, 127.8 (2C), 126.6, 125.7, 122.2, 120.1, 119.3, 117.8 (2C), 116.1, 113.3, 104.5, 56.1.; HRMS (ESI) calcd for  $\text{C}_{20}\text{H}_{16}\text{ClN}_2\text{O}_2$   $[\text{M} + \text{H}]^+$  351.0908; found 351.0896.

### 2.5.3 Molecular Docking of Compound 1

The first step of our VS study was to investigate the binding mode of the lead compound **1**<sup>25</sup> to the pocket on the XPF C-terminus. We used twenty XPF structures as single targets for a relaxed complex scheme (RCS) docking protocol in order to account for protein flexibility accurately.<sup>35,36</sup> These structures were extracted from the Protein Data Bank (PDB)<sup>37</sup> entry 1Z00,<sup>17</sup> reporting the NMR ensemble of the dimerization complex between the ERCC1 and XPF HhH2 domains. The XPF structures were optimized with a minimization process. The binding site of each target was defined as the geometric center of the residues Y833, N834, P837, Q838, M856, K860, N861, and I862 on the XPF HhH2 domain, as reported in our previous study,<sup>25</sup> where the residues are numbered according to the 1Z00 PDB file. Molecular docking simulations were performed using the Lamarckian Genetic Algorithm (LGA)<sup>38</sup> and the built-in scoring function<sup>39</sup> of Autodock4.<sup>40</sup>

### 2.5.4 Characterization of The Binding Pocket and Pharmacophore Modeling

To characterize the binding site and the binding mode of compound **1**, electrostatic

maps were generated in the MOE2015 software package,<sup>41</sup> based on the docked pose of compound **1**, using  $-2$  kcal/mol for the potential iso-surfaces of hydrophobic, acceptor, and donor probe atoms, and the Poisson–Boltzmann equation to compute the potentials. The maps were built within  $4.5$  Å of the ligand pose obtained from docking. Using the information from the docking and electrostatic mapping, a pharmacophore model for compound **1** was built with the MOE Pharmacophore Query Editor and the EHT scheme.<sup>42</sup>

### **2.5.5 Docking-based Virtual Screening of Compound 1 Analogues**

Fifty-seven analogues of compound **1** structure were designed by replacement of the piperazine N-methyl group with other moieties expected to capture additional binding interactions of the piperazine ring. The structures were prepared using Schrödinger LigPrep<sup>43</sup> to account for multiple tautomers, protonation states, and low-energy ring conformations, using the same approach as for compound **1**. The molecular docking simulations were performed with MOE Dock. Only the XPF structure from the best compound **1** complex was used as a target for the VS study. Different conformations of the analogues were obtained using Conformation Import. The previously built pharmacophore model was used for the placement step, in which 30 poses are returned according to the London dG scoring method.<sup>44</sup> To account for the local arrangement of the pocket residues upon ligand binding, the Induced Fit method was selected for the refinement step, where the side chains of the binding pocket were left to move freely. At the end, one pose scored with the Generalized Born Volume Integral/Weighted Surface Area (GBVI/WSA) function was returned.<sup>44</sup> Water/octanol partition coefficients (logP) of the molecules were calculated in MOE using the SlogP function,<sup>45</sup>

which takes into account the given protonation state of the molecule under examination. Ligand efficiencies were calculated as the ratio between the computed binding energies and the number of heavy atoms of each analog.

### **2.5.6 Molecular Dynamics Simulations and MM/GBSA Rescoring of the Analogues**

To calculate an average binding energy for the hits, we performed 2 ns of MD simulations for the top ranked compound-XPF complexes. Free energy calculations were performed over the trajectories with the MM/GBSA method using the MMPBSA.py script.<sup>46</sup> The calculations were performed on snapshots extracted every 10 ps from the MD trajectories, and per-residue decompositions of the binding energies also were performed for the residues within 10 Å of any analog atom at the beginning of the simulations. We also calculated the entropic contribution of ligand binding using the normal mode analysis (NMA) method.<sup>47</sup> The final binding energies used to rank the compounds were calculated combining the MM/GBSA and entropy contributions.

### **2.5.7 ERCC1–XPF Protein Preparation**

David Jay used human ERCC1–XPF wild-type protein that was obtained as previously described.<sup>29</sup> Basically, the recombinant protein was expressed from a bi-cistronic plasmid (kindly provided by Dr. Richard Wood, University of Texas MD Anderson Cancer Center, Smithville, TX) in the *E. coli* BL21 (DE3) strain. Since both XPF and ERCC1 contained a polyhistidine (His-6) tag, the proteins extracted from *E. coli* were incubated with a ProBond Nickel-Chelating Resin (Thermo Fisher Scientific). Protein eluted from the Ni affinity column subsequently was loaded into a Hi-trap heparin

column (GE Healthcare). Fractions recovered from the heparin column that contained ERCC1-XPF were dialyzed, concentrated, and stored at -80 °C in 10 mM HEPES pH 7.4, 2.5 mM  $\beta$ -mercaptoethanol, 0.01% CHAPS, 0.25 mM EDTA, 50% glycerol, and 25 mM NaCl.

### **2.5.8 Microplate Fluorescence Incision Assay**

David Jay followed a previously described protocol.<sup>2,29</sup> Briefly, reactions were carried out in a 384-well black, flat-bottomed microtiter plates (OptiPlate – 384 F, Perkin Elmer) in a total volume of 20  $\mu$ l containing the indicated concentrations of inhibitor compounds, 100 nM stem-loop substrate [6-FAM-5'-CAGCGCTCGG(20T)CCGAGCGCTG-3'-dabcyl], 25 ng ERCC1-XPF, 50 mM Tris-Cl pH 8, 20 mM NaCl, 0.5 mM DDT, and 0.75 mM MnCl<sub>2</sub> at 25 °C. Fluorescent readings were obtained using a FLUOstar Optima fluorimeter (BMG Labtech) with Optima software at an excitation of and emission wavelengths of 485 and 520 nm, respectively, for 12 min.

### **2.5.9 Steady-state Fluorescence Assay**

Steady-state fluorescence spectra were measured at room temperature on a Perkin-Elmer LS-55 spectrofluorometer (Freemont, CA) with 5 nm spectral resolution for excitation and emission using 30–80 nM solution of purified recombinant ERCC1–XPF protein complex. Protein fluorescence was excited at 295 nm, and fluorescence emission spectra were recorded in the 300–400 nm range: changes in fluorescence intensity were monitored at the emission maximum (330 nm). In studying the effects of inhibitors on protein fluorescence intensities, additions to protein samples were made from inhibitors stock solutions, keeping the protein dilution below 3%.

### **2.5.10 Expression and Purification of Recombinant Truncated Forms of ERCC1 and XPF**

Synthetic DNA sequences encoding for human ERCC1 codons 96–297 (dERCC1) and XPF codons 667–916 (dXPF) inserted into separate pET-28a expression plasmids were used to transform BL21(DE3) cells and express the corresponding recombinant proteins.<sup>2</sup> Since the truncated form of the proteins both contained N-terminal polyhistidine-tags (His-tags), they were purified utilizing a nickel-chelating resin (ThermoFisher Scientific) under conditions similar to the ones described.<sup>2</sup> Both truncated peptides were solubilized finally to final concentrations for the experiments of 40 nM dXPF and 20 nM dERCC1 in a buffer (MST buffer) containing 20 mM HEPES pH 7.4, 50 mM NaCl, 1 mM DTT, 2 mM MgCl<sub>2</sub>, 5% glycerol, and 0.01% CHAPS.

### **2.5.11 Microscale Thermophoresis (MST) Measurements**

We tried to remove the His-tag from one of the truncated peptides (preferentially dERCC1 because of its low yield) to carry out MST equilibrium experiments. However, the peptides proved to be resistant to thrombin treatment, so we decided to follow a different qualitative approach. Both, dXPF and dERCC1 were labelled with 20 nM and 10 nM RED-tris-NTA (NanoTemper Technologies), respectively, following the manufacturer instructions. Individual peptides (20 nM final concentration) or equimolar amounts of dERCC1 and dXPF (20 nM final concentration of the dimer) were incubated in MST buffer in the presence of compound **4** (10 µM) or DMSO. After 20 minutes of incubation time at room temperature, 10 µl of the samples were placed in standard capillaries (NanoTemper Technologies), and the emitted red fluorescence (670 nm) was

measured in a Monolith NT.115 instrument (NanoTemper Technologies) with a High MST-Power, 70% Excitation Power, and a Nano-RED Excitation type. Pretest and binding check experiments did not show any change in fluorescence of the RED-tris-NTA dye induced by compound **4**. In addition, the peak shape did not indicate any adsorption of the components of the solution to the surface of the capillaries.

### **2.5.12 Cell Culture**

The human colorectal cancer HCT-116 cell line was obtained from the American Type Culture Collection (ATCC). The cell population was expanded immediately after arrival, aliquoted, and stored frozen in liquid nitrogen. Freshly thawed cells were used for each experiment. The cells were cultured in a 1:1 DMEM/F12 media supplemented with 10% FBS, 50 units/mL penicillin, 50 µg/mL streptomycin, mM l-glutamine, 0.1 mM nonessential amino acids, and 1 mM sodium pyruvate, and maintained under 5% CO<sub>2</sub> in a humidifier incubator at 37 °C. All the supplies for cell culture were obtained from Gibco/BRL.

### **2.5.13 Cellular Repair of Cyclobutane Pyrimidine Dimers**

We followed the protocol of Mirzayans et al. with minor modifications.<sup>34</sup> Approximately  $1 \times 10^5$  HCT-116 cells were seeded on each coverslip and allowed to attach overnight. Then, the medium was removed, and the cells were treated for 1 h with the desired compound. The medium was removed, and the cells were exposed to 8 J/m<sup>2</sup> UV-C radiation (G15T8 254 nm lamp, Ushio America Inc, Cypress, CA), followed by adding fresh medium containing the compound. The plates were incubated at 37 °C for different periods of time up to 24 h and fixed in a 50:50 methanol/1X phosphate-buffered saline (PBS) solution, followed by replacing the methanol/PBS

solution with 100% methanol and incubation in  $-20\text{ }^{\circ}\text{C}$ . After 20 min, the methanol was removed, and the cells were treated with PBS for 5 min at room temperature. After fixing, the cells were permeabilized in 0.5% Triton/PBS and washed with PBS, denatured in 2 N HCl, and neutralized by twice washing with 0.1 M borate buffer pH 8.5. Cells on cover slips were washed once with PBS followed by blocking with 5% non-fat dry milk/PBS for 30 min. Mouse anti-thymine dimer monoclonal antibody (Cat. No. MC-062, Kamiya Biomedical Company, Seattle, WA) was applied to the cover slips for 1 h in the dark and at room temperature. Cells were then washed with PBS containing 0.1% Tween-20 and incubated with rabbit anti-mouse IgG-Alexafluor antibody (Invitrogen, Carlsbad, CA) followed by two washes with PBS/(0.1%)Tween-20. Cells on coverslips were then washed with PBS, rinsed with water, and mounted on slides using DAPI glycerol mounting solution. Slides were kept at  $4\text{ }^{\circ}\text{C}$  before fluorescent microscopic evaluation and measurement of fluorescence intensity with MetaXpress Version: 6.2.1.704 software (Molecular Devices, Sunnyvale, California).

#### **2.5.14 Clonogenic Survival Assay**

UV treatment: HCT-116 cells (100–800 cells depending on the UV dose) were plated in triplicate in 60-mm petri dishes. The cells were incubated overnight at  $37\text{ }^{\circ}\text{C}$  in a humidified atmosphere containing 5%  $\text{CO}_2$  to allow for cell attachment. Then, the medium was removed, and the cells were treated with 1 or 2  $\mu\text{M}$  compound **4** for 1 h. The medium was removed again, and the cells were exposed to increasing doses (0–10  $\text{J}/\text{m}^2$ ) of UV-C radiation and then incubated for a further 10 days in the presence of inhibitor at  $37\text{ }^{\circ}\text{C}$  in a 5%  $\text{CO}_2$  atmosphere to allow for colony formation. After this period, the plates were stained with crystal violet and colonies were counted using a

Colcount instrument (Oxford Optronix, Abingdon UK). Finally, plating efficiency and surviving fraction were calculated.

Cyclophosphamide treatment: A similar protocol was followed as described for the UV treatment, except that cells were treated with 1 or 2  $\mu\text{M}$  compound **4** for 4 h, followed by addition of increasing doses of cyclophosphamide (0–300  $\mu\text{M}$ ). After 24 h, the medium was replaced with fresh medium containing compound **4** alone. The plates were incubated for another 8 days at 37 °C in a 5% CO<sub>2</sub> atmosphere for colony formation. After this period the plates were stained with crystal violet, colonies were counted, and plating efficiency and surviving fraction were calculated.

#### **2.5.14 PK Assessment of Compound 4 and Compound 1**

Standard protocols were used for assessing the absorption, distribution, metabolism, and excretion (ADME) profile of our lead compound **4** and compound **1** (reference hit). Screening were performed at WuXi AppTec (Shanghai) Co<sup>48</sup> to conduct the following assays according to the standard protocols: distribution coefficient (Log D at pH 7.4), aqueous solubility (Kinetic), metabolic stability in human liver microsomes and cryopreserved human hepatocytes, bidirectional permeability in Caco-2 cells, serum protein binding, and cytochromes P450 (CYPs) inhibition (CYP1A2, CYP2C9, CYP2C19, CYP2D6, CYP3A4-M).

## 2.10 References

1. Sijbers, A. M.; de Laat, W. L.; Ariza, R. R.; Biggerstaff, M.; Wei, Y.-F.; Moggs, J. G.; Carter, K. C.; Shell, B. K.; Evans, E.; de Jong, M. C. Xeroderma pigmentosum group F caused by a defect in a structure-specific DNA repair endonuclease. *Cell* **1996**, *86*, 811-822.
2. McNeil, E. M.; Astell, K. R.; Ritchie, A.-M.; Shave, S.; Houston, D. R.; Bakrania, P.; Jones, H. M.; Khurana, P.; Wallace, C.; Chapman, T.; Wear, M. A.; Walkinshaw, M. D.; Saxty, B.; Melton, D. W. Inhibition of the ERCC1–XPF structure-specific endonuclease to overcome cancer chemoresistance. *DNA Repair* **2015**, *31*, 19-28.
3. Friedberg, E. C.; Walker, G. C.; Siede, W.; Wood, R. D.; Schultz, R. A.; Ellenberger, T. DNA Repair and Mutagenesis. 2nd edn ASM.; Press. *Washington, DC* **2006**.
4. McNeil, E. M.; Melton, D. W. DNA repair endonuclease ERCC1–XPF as a novel therapeutic target to overcome chemoresistance in cancer therapy. *Nucleic Acids Research* **2012**, *40*, 9990-10004.
5. Douwel, D. K.; Hoogenboom, W. S.; Boonen, R. A. C. M.; Knipscheer, P. Recruitment and positioning determine the specific role of the XPF-ERCC1 endonuclease in interstrand crosslink repair. *The EMBO Journal* **2017**, *36*, 2034-2046.
6. Yagi, T.; Katsuya, A.; Koyano, A.; Takebe, H. Sensitivity of group F xeroderma pigmentosum cells to UV and mitomycin C relative to levels of XPF and ERCC1 overexpression. *Mutagenesis* **1998**, *13*, 595-599.
7. Gajjar, K. K.; Yadav, D. K.; Kobawala, T. P.; Trivedi, T. I.; Vora, H. H.; Ghosh, N. R. ERCC1 expression in patients with colorectal cancer: a pilot study. *Journal of Cancer Metastasis and Treatment* **2016**, *2*, 471-476.
8. McHugh, P. J.; Spanswick, V. J.; Hartley, J. A. Repair of DNA interstrand crosslinks: molecular mechanisms and clinical relevance. *The Lancet Oncology* **2001**, *2*, 483-490.
9. Ahmad, A.; Robinson, A. R.; Duensing, A.; van Drunen, E.; Beverloo, H. B.; Weisberg, D. B.; Hasty, P.; Hoeijmakers, J. H. J.; Niedernhofer, L. J. ERCC1-XPF endonuclease facilitates DNA double-strand break repair. *Molecular and Cellular Biology* **2008**, *28*, 5082-5092.
10. De Laat, W. L.; Appeldoorn, E.; Jaspers, N. G. J.; Hoeijmakers, J. H. J. DNA structural elements required for ERCC1-XPF endonuclease activity. *Journal of Biological Chemistry* **1998**, *273*, 7835-7842.
11. Gaillard, P.-H. L.; Wood, R. D. Activity of individual ERCC1 and XPF subunits in DNA nucleotide excision repair. *Nucleic Acids Research* **2001**, *29*, 872-879.

12. Gentile, F.; Tuszynski, J. A.; Barakat, K. H. New design of nucleotide excision repair (NER) inhibitors for combination cancer therapy. *Journal of Molecular Graphics and Modelling* **2016**, *65*, 71-82.
13. Gentile, F.; Barakat, K. H.; Tuszynski, J. A. Computational Characterization of Small Molecules Binding to the Human XPF Active Site and Virtual Screening to Identify Potential New DNA Repair Inhibitors Targeting the ERCC1-XPF Endonuclease. *International Journal of Molecular Sciences* **2018**, *19*, 1328–1341 .
14. Gentile, F.; A Tuszynski, J.; H Barakat, K. Modelling DNA repair pathways: recent advances and future directions. *Current Pharmaceutical Design* **2016**, *22*, 3527-3546.
15. Ahmad, A.; Enzlin, J. H.; Bhagwat, N. R.; Wijgers, N.; Raams, A.; Appeldoorn, E.; Theil, A. F.; Hoeijmakers, J. H. J.; Vermeulen, W.; Jaspers, N. G. J. Mislocalization of XPF-ERCC1 nuclease contributes to reduced DNA repair in XP-F patients. *PLoS Genetics* **2010**, *6*, e1000871-e1000882.
16. De Laat, W. L.; Sijbers, A. M.; Odijk, H.; Jaspers, N. G. J.; Hoeijmakers, J. H. J. Mapping of interaction domains between human repair proteins ERCC1 and XPF. *Nucleic Acids Research* **1998**, *26*, 4146-4152.
17. Tripsianes, K.; Folkers, G.; Eiso, A. B.; Das, D.; Odijk, H.; Jaspers, N. G. J.; Hoeijmakers, J. H. J.; Kaptein, R.; Boelens, R. The structure of the human ERCC1/XPF interaction domains reveals a complementary role for the two proteins in nucleotide excision repair. *Structure* **2005**, *13*, 1849-1858.
18. Choi, Y.-J.; Ryu, K.-S.; Ko, Y.-M.; Chae, Y.-K.; Pelton, J. G.; Wemmer, D. E.; Choi, B.-S. Biophysical characterization of the interaction domains and mapping of the contact residues in the XPF-ERCC1 complex. *Journal of Biological Chemistry* **2005**, *280*, 28644-28652.
19. Tsodikov, O. V.; Enzlin, J. H.; Schärer, O. D.; Ellenberger, T. Crystal structure and DNA binding functions of ERCC1, a subunit of the DNA structure-specific endonuclease XPF–ERCC1. *Proceedings of the National Academy of Sciences of the United States of America* **2005**, *102*, 11236-11241.
20. McNeil, E. M.; Astell, K. R.; Ritchie, A.-M.; Shave, S.; Houston, D. R.; Bakrania, P.; Jones, H. M.; Khurana, P.; Wallace, C.; Chapman, T. Inhibition of the ERCC1–XPF structure-specific endonuclease to overcome cancer chemoresistance. *DNA Repair* **2015**, *31*, 19-28.
21. Chapman, T. M.; Gillen, K. J.; Wallace, C.; Lee, M. T.; Bakrania, P.; Khurana, P.; Coombs, P. J.; Stennett, L.; Fox, S.; Bureau, E. A. Catechols and 3-hydroxypyridones as inhibitors of the

- DNA repair complex ERCC1-XPF. *Bioorganic & Medicinal Chemistry Letters* **2015**, *25*, 4097-4103.
22. Chapman, T. M.; Wallace, C.; Gillen, K. J.; Bakrania, P.; Khurana, P.; Coombs, P. J.; Fox, S.; Bureau, E. A.; Brownlees, J.; Melton, D. W. N-Hydroxyimides and hydroxypyrimidinones as inhibitors of the DNA repair complex ERCC1–XPF. *Bioorganic & Medicinal Chemistry Letters* **2015**, *25*, 4104-4108.
23. Arora, S.; Heyza, J.; Zhang, H.; Kalman-Maltese, V.; Tillison, K.; Floyd, A. M.; Chalfin, E. M.; Bepler, G.; Patrick, S. M. Identification of small molecule inhibitors of ERCC1-XPF that inhibit DNA repair and potentiate cisplatin efficacy in cancer cells. *Oncotarget* **2016**, *7*, 75104-75117.
24. Yang, L.; Ritchie, A.-M.; Melton, D. W. Disruption of DNA repair in cancer cells by ubiquitination of a destabilising dimerization domain of nucleotide excision repair protein ERCC1. *Oncotarget* **2017**, *8*, 55246-55264.
25. Jordheim, L. P.; Barakat, K. H.; Heinrich-Balard, L.; Matera, E.-L.; Cros-Perrial, E.; Bouledrak, K.; El Sabeh, R.; Perez-Pineiro, R.; Wishart, D. S.; Cohen, R. Small molecule inhibitors of ERCC1-XPF protein-protein interaction synergize alkylating agents in cancer cells. *Molecular Pharmacology* **2013**, *84*, 12-24.
26. Chapman, T. M.; Gillen, K. J.; Wallace, C.; Lee, M. T.; Bakrania, P.; Khurana, P.; Coombs, P. J.; Stennett, L.; Fox, S.; Bureau, E. A.; Brownlees, J.; Melton, D. W.; Saxty, B. Catechols and 3-hydroxypyridones as inhibitors of the DNA repair complex ERCC1-XPF. *Bioorganic & Medicinal Chemistry Letters* **2015**, *25*, 4097-4103.
27. Arora, S.; Heyza, J.; Zhang, H.; Kalman-Maltese, V.; Tillison, K.; Floyd, A. M.; Chalfin, E. M.; Bepler, G.; Patrick, S. M. Identification of small molecule inhibitors of ERCC1-XPF that inhibit DNA repair and potentiate cisplatin efficacy in cancer cells. *Oncotarget* **2016**, *7*, 75104–75117
28. Scurr, M.; Pembroke, T.; Bloom, A.; Roberts, D.; Thomson, A.; Smart, K.; Bridgeman, H.; Adams, R.; Brewster, A.; Jones, R.; Gwynne, S.; Blount, D.; Harrop, R.; Hills, R.; Gallimore, A.; Godkin, A. Low-Dose Cyclophosphamide Induces Antitumor T-Cell Responses, which Associate with Survival in Metastatic Colorectal Cancer. *Clinical Cancer Research : an Official Journal of the American Association for Cancer Research* **2017**, *23*, 6771-6780.
29. Bowles, M.; Lally, J.; Fadden, A. J.; Mouilleron, S.; Hammonds, T.; McDonald, N. Q. Fluorescence-based incision assay for human XPF–ERCC1 activity identifies important elements of DNA junction recognition. *Nucleic Acids Research* **2012**, *40*, e101-e101.

30. Mani, R. S.; Karimi-Busheri, F.; Fanta, M.; Caldecott, K. W.; Cass, C. E.; Weinfeld, M. Biophysical characterization of human XRCC1 and its binding to damaged and undamaged DNA. *Biochemistry* **2004**, *43*, 16505-16514.
31. Jerabek-Willemsen, M.; Wienken, C. J.; Braun, D.; Baaske, P.; Duhr, S. Molecular interaction studies using microscale thermophoresis. *Assay and Drug Development Technologies* **2011**, *9*, 342-353.
32. Wienken, C. J.; Baaske, P.; Rothbauer, U.; Braun, D.; Duhr, S. Protein-binding assays in biological liquids using microscale thermophoresis. *Nature communications* **2010**, *1*, 100-107.
33. Zillner, K.; Jerabek-Willemsen, M.; Duhr, S.; Braun, D.; Längst, G.; Baaske, P. Microscale thermophoresis as a sensitive method to quantify protein: nucleic acid interactions in solution. In *Functional Genomics*, Springer: 2012; pp 241-252.
34. Mirzayans, R.; Pollock, S.; Scott, A.; Gao, C. Q.; Murray, D. Metabolic labeling of human cells with tritiated nucleosides results in activation of the ATM-dependent p53 signaling pathway and acceleration of DNA repair. *Oncogene* **2003**, *22*, 5562-5571.
35. Philippopoulos, M.; Lim, C. Exploring the dynamic information content of a protein NMR structure: Comparison of a molecular dynamics simulation with the NMR and X-ray structures of Escherichia coli ribonuclease HI. *Proteins: Structure, Function, and Bioinformatics* **1999**, *36*, 87-110.
36. Ishima, R.; Torchia, D. A. Protein dynamics from NMR. *Nature Structural & Molecular Biology* **2000**, *7*, 740-743.
37. Berman, H. M.; Westbrook, J.; Feng, Z.; Gilliland, G.; Bhat, T. N.; Weissig, H.; Shindyalov, I. N.; Bourne, P. E. The Protein Data Bank. *Nucleic Acids Research* **2000**, *28*, 235-242.
38. Morris, G. M.; Goodsell, D. S.; Halliday, R. S.; Huey, R.; Hart, W. E.; Belew, R. K.; Olson, A. J. Automated docking using a Lamarckian genetic algorithm and an empirical binding free energy function. *Journal of Computational Chemistry* **1998**, *19*, 1639-1662.
39. Huey, R.; Morris, G. M.; Olson, A. J.; Goodsell, D. S. A semiempirical free energy force field with charge-based desolvation. *Journal of Computational Chemistry* **2007**, *28*, 1145-1152.
40. Morris, G. M.; Huey, R.; Lindstrom, W.; Sanner, M. F.; Belew, R. K.; Goodsell, D. S.; Olson, A. J. AutoDock4 and AutoDockTools4: Automated docking with selective receptor flexibility. *Journal of Computational Chemistry* **2009**, *30*, 2785-2791.
41. Chemical Computing Group, I. *Molecular Operating Environment (MOE)*, 2013.08; **2017**.
42. Lin, A. Overview of Pharmacophore Applications in MOE. In **2004**.

43. Schrödinger. LigPrep. In **2013**.
44. Labute, P. The generalized Born/volume integral implicit solvent model: estimation of the free energy of hydration using London dispersion instead of atomic surface area. *Journal of Computational Chemistry* **2008**, 29, 1693-1698.
45. Wildman, S. A.; Crippen, G. M. Prediction of physicochemical parameters by atomic contributions. *Journal of Chemical Information and Computer Sciences* **1999**, 39, 868-873.
46. Miller Iii, B. R.; McGee Jr, T. D.; Swails, J. M.; Homeyer, N.; Gohlke, H.; Roitberg, A. E. MMPBSA. py: an efficient program for end-state free energy calculations. *Journal of Chemical Theory and Computation* **2012**, 8, 3314-3321.
47. Kassem, S.; Ahmed, M.; El-Sheikh, S.; Barakat, K. H. Entropy in bimolecular simulations: A comprehensive review of atomic fluctuations-based methods. *Journal of Molecular Graphics and Modelling* **2015**, 62, 105-117.
48. WuXi AppTech Inc., <https://www.wuxiapptec.com>

## Chapter 3

# Computer-Aided Drug Design of The Second- Generation ERCC1–XPF Inhibitors\*

### 3.1 Introduction

Genomic instability is associated with the aging process<sup>1</sup> and an enabling characteristic to acquire the hallmarks of cancer.<sup>2</sup> Therefore, it is not surprising that cells require a well-functioning DNA repair apparatus to be protected from endogenous and exogenous damaging agents and to preserve their healthy status. Likewise, defective DNA repair pathways are associated with rare genetic diseases, such as xeroderma pigmentosum, Cockayne's syndrome, and trichothiodystrophy, whose affected individuals show a propensity for cancer, neurological deficiencies, and physical abnormalities.<sup>3, 4</sup> Although DNA repair is essential to maintain genomic stability, these pathways can interfere with cancer therapies and repair the damage inflicted on tumor cells, allowing cancer to progress. Combination cancer therapy is a relatively new strategy in which a DNA-damaging agent (e.g., cisplatin) and a DNA repair inhibitor are administered jointly to the patient in order to potentiate the effect of the former.<sup>5</sup>

The therapeutic potential of DNA repair inhibitors was demonstrated recently by the successful development of inhibitors for poly(ADP-ribose) polymerase

\* The contents of this chapter have been copied and/or adapted from the following publication: Gentile, F.<sup>a</sup>; Elmenoufy, A. H.<sup>a</sup>; Ciniero, G.; Jay, D.; Karimi-Busheri, F.; Barakat, K. H.; Weinfeld, M.; West, F. G.; Tuszynski, J. A. Computer-aided drug design of small molecule inhibitors of the ERCC1-XPF protein–protein interaction. *Chemical Biology & Drug Design* **2020**, *95*, 460-471.

<sup>a</sup>Authors equally contributed to this work.

(PARP) enzymes with several molecules that either entered clinical trials or are FDA-approved.<sup>6</sup> Despite the increasing interest in DNA repair proteins as potential drug targets, there are very few known inhibitors besides the aforementioned PARP inhibitors. In particular, there are a number of other, complementary DNA repair mechanisms that could be exploited for anti-cancer therapy.<sup>7</sup>

The heterodimeric protein ERCC1–XPF, made up of the DNA excision repair protein ERCC1 and the DNA repair endonuclease XPF, is a 5′-3′ structure-specific endonuclease, which cleaves double-strand/single-strand DNA junctions.<sup>8</sup> The catalytic activity of ERCC1–XPF is essential for the nucleotide excision repair (NER) pathway in order to repair helix-distorting damage, such as UV-induced cyclobutane pyrimidine dimers, and it also is involved in the repair of double-strand breaks (DSBs) and inter-strand crosslinks (ICLs)<sup>9</sup> (Figure 3.1).

NER and ICL repair are the main mechanisms responsible for removing damage induced by platinum-based and other crosslinking chemotherapy and modulation or downregulation of ERCC1, XPF, and interacting partners. Inhibiting this process sensitizes cancer cells to chemotherapy,<sup>8, 11, 12</sup> hence, ERCC1–XPF is an attractive target for developing DNA repair inhibitors.<sup>8</sup> Due to its central role in mediating therapeutic damage inflicted as part of cancer treatment, ERCC1–XPF has been the subject of a number of studies aimed at developing inhibitors of the endonuclease activity.<sup>13</sup> A first line of research was devoted to the discovery of inhibitors of the NER-specific interaction between the DNA repair protein complementing XP-A cells (XPA) and ERCC1.<sup>13, 14</sup> ERCC1–XPF is recruited to the

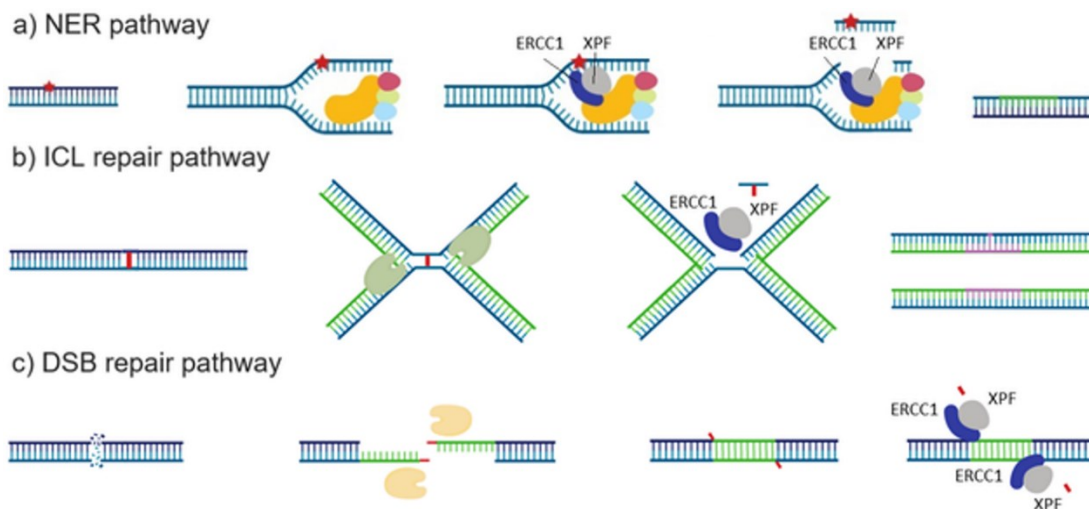


**Figure 3.1.** Involvement of ERCC1–XPF complex in three major DNA repair pathways: a) in NER, adduct-caused distortions of the double helix are detected and the double stranded filament opened and stabilized by the repair machinery; then, ERCC1–XPF and XPG endonucleases are recruited at 5' and 3', respectively, for the cleavage and removal of the single-strand lesion. Next, the free 3'-OH terminal is used as a primer for the synthesis of the missing fragment. b) ICLs seriously hinder the replication machinery, eventually leading to formation of double-strand breaks. ERCC1–XPF is involved in the incision either side of an ICL from one strand allowing the passage of polymerases and the filling of the gaps. c) In DSB repair pathway the damaged DNA can be fixed either by homologous recombination or microhomology-mediated end joining. Independently of the repair mechanism, ERCC1–XPF is needed to remove 3' single strand flaps formed by non-homologous fragments at the edges of the former break to allow ligases to seal gaps and restore the integrity of the double helix, (copied with permission from Gentile et al.<sup>10</sup>).

damaged zone through this interaction in NER, and some XPA–ERCC1 inhibitors showed promising pre-clinical potential to enhance the effect of cisplatin on tumors, although this approach would be effective on NER only without affecting other ERCC1–XPF-mediated pathways not involving XPA.<sup>14</sup> The catalytic site of the endonuclease has been explored as a target for inhibition as well. The site is on the XPF nuclease domain and contains a series of charged residues and metal ions, which make it an attractive target for binding by small molecules. Recently, several inhibitors were discovered, some of which have been shown to enhance chemotherapy in cell and xenograft tumor models.<sup>11, 15-18</sup> However, the similarity between catalytic sites of several human divalent cation-based DNA-cleaving enzymes constitutes an obstacle to designing XPF-specific inhibitors, and an X-ray structure of the human XPF nuclease

domain has not been solved yet.<sup>8</sup> Lastly, the ERCC1–XPF protein–protein interaction represents another interesting target for pharmacological inhibition since dimerization is required to generate a functional endonuclease. Despite the high-affinity, hydrophobic-driven interaction between the two HhH2 domains of ERCC1 and XPF, the interaction is specific to the endonuclease, and the deletion of a single residue (F293) at the ERCC1 side is enough to abrogate dimerization and nuclease activity. These characteristics make the ERCC1–XPF dimerization interface a promising, yet challenging, drug target for DNA repair inhibition.<sup>8</sup>

Jordheim et al. previously reported **1** (Figure 3.2), the first ERCC1–XPF dimerization inhibitor. **1** is a small molecule, which binds at the XPF pocket interacting with ERCC1's F293, disrupts the protein–protein interaction, selectively blocks ERCC1–XPF-mediated DNA repair, and sensitizes cancer cell lines to UV and DNA-damaging drugs, such as cisplatin and mitomycin C.<sup>19</sup>

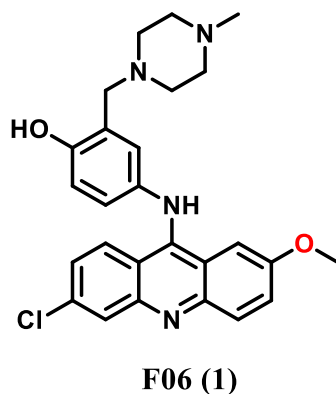


**Figure 3.2.** Chemical structure of **1**, ERCC1-XPF heterodimerization inhibitor.

Chapter 2 describes a successful way to combine a computer-aided drug design (CADD) with a structure-activity relationship approach to extend the piperazine ring of **1** with different substituents in order to improve the biological activities of this class of

compounds. In this way, my collaborator, Francesco Gentile (F.G.) and I assessed **1** as a suitable scaffold for developing a DNA repair inhibitor drug candidate.<sup>20</sup> Building on our previous results, F.G. report a new CADD strategy for further improvement of **1**, which uses molecular dynamics (MD) to characterize in detail the structural changes introduced by **1** binding to XPF compared to XPF free form and ERCC1–XPF heterodimer. During the simulation, F.G. also evaluated the hydrogen bond network of **1** with XPF in order to drive the design of **1** analogues with enhanced protein interactions. In particular, **B9** showed improved inhibition of the ERCC1–XPF incision activity *in vitro*. In contrast to the work was described in Chapter 2 where we modified a solvent-exposed group of **1**,<sup>20</sup> here, we focused on a different modification, such as truncation of the lateral branch of **1** and substitution of the methoxy group substituted by hydrogen bond acceptor groups to improve buried ligand–receptor interactions. Through our CADD-driven medicinal chemistry strategy, I obtained analogues showing 3-fold increased potencies *in vitro*. Our results confirm **1** as a suitable scaffold for designing DNA repair drugs and suggest a rational approach to improving its target affinity.

## **3.2 Results and Discussion**

### **3.2.1 Molecular Dynamics Simulations**

The MD simulation of the unbound form of XPF revealed a dramatic change from the initial structure extracted from the complex with ERCC1, with an  $\sim 8$  Å of difference in RMSD (shown in red in Figure 3.3A) with the ERCC1-bound form (shown in

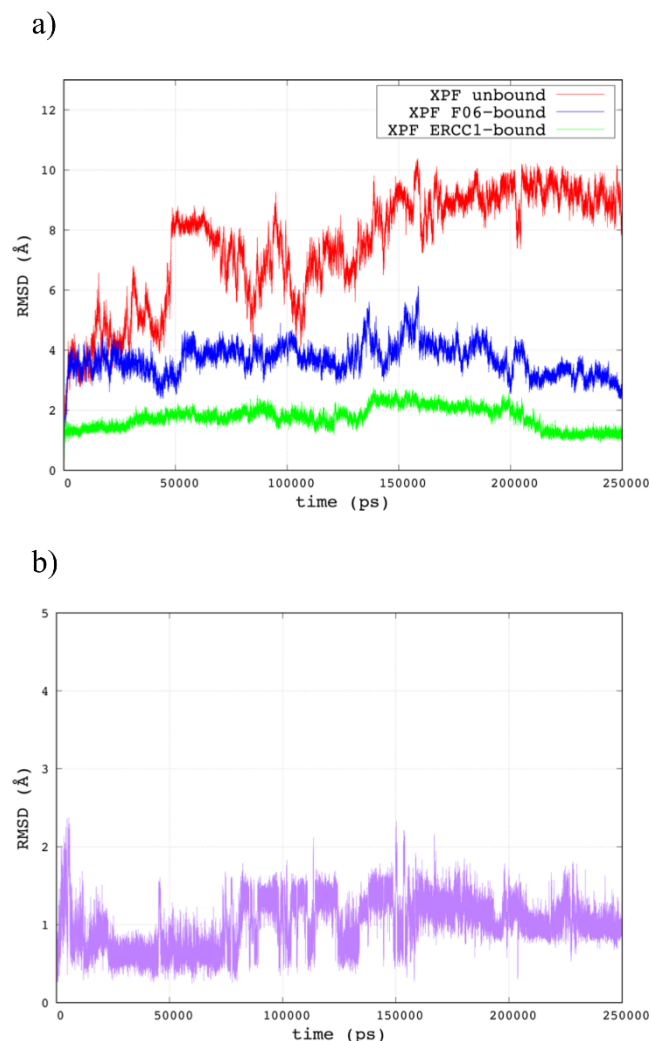


**Figure 3.3.** RMSDs analysis of F06 and ERCC1. a) RMSDs of backbone atoms of unbound (red), F06 (1)-bound (blue) and ERCC1-bound XPF (green) from MD simulations. The initial structure was the same in all three cases, i.e., the XPF conformation bound to ERCC1. The systems reached a plateau after  $\sim 150$  ns of simulation in explicit solvent. Binding of F06, despite the reduced size of the ligand compared to the ERCC1 HhH2 domain, partially restored the RMSD trend to the ERCC1-bound form, indicating a stabilizing effect upon binding to the F293-interacting pocket of XPF, and confirming F06 (1) as a dimerization inhibitor able to replace ERCC1 as a binding partner. b) RMSD of F06 (1) heavy atoms. The ligand maintained a stable pose within the binding pocket of XPF, with an average displacement of  $\sim 1$  Å from the starting structure.

green in Figure 3.3A). Remarkably, despite the small size of F06 (1) compared to the ERCC1 HhH2 domain, the binding of the ligand to the XPF cavity (hosting ERCC1's F293 in the heterodimer) led to a stable XPF conformation, which diverged from the ERCC1-bound equilibrated structure by only  $\sim 2$  Å in terms of RMSD (shown in blue in Figure 3.3A). MD results suggest that the binding of 1 to the F293 hotspot-interacting

pocket on XPF<sup>8, 21-23</sup> can substitute for ERCC1 as a binding partner of XPF and induce an XPF conformation similar to the ERCC1-bound one. The RMSD of the heavy atoms of F06 during the production MD simulation fluctuated around an average value of 1 Å from the starting conformation, indicating a stable pose of the ligand within the binding site of XPF (Figure 3.3B).

To assess further the structural differences between the three XPF models, we extracted and superposed the lowest potential energy structures of XPF from the MD trajectories. The ERCC1-bound (shown in green in Figure 3.4A) and F06-bound (shown in blue in Figure 3.4A) form showed a similar tertiary structure, suggesting again that **1** may mimic the natural ERCC1 partner and, subsequently, cause a similar conformation of XPF to be maintained. As anticipated by the reduced size of **1**, the F06 (**1**)–XPF complex was less stable compared to ERCC1–XPF, with higher fluctuations of the XPF backbone, as visible from the RMSF trends for the last 100 ns of MD simulation (Figure 3.5). The unbound XPF (shown in red in Figure 3.4A) showed a less ordered conformation compared to the other two structures. The main structural change observable in the unbound form was the disruption of the H1 alpha helix (residue 834-845) and the loss of the HhH2 typical domain structure (Figure 3.4B), as revealed also by the DSSP analysis carried on the last 100 ns of MD simulation (Figure 3.4C). Importantly, H1 is part of the F06 binding site. Overall, the ERCC1-bound and the F06-bound structures showed more globular shapes compared to the unbound form, with less exposure of the hydrophobic regions devoted to interact with ERCC1, in agreement with previous experimental observations.<sup>8, 23</sup>

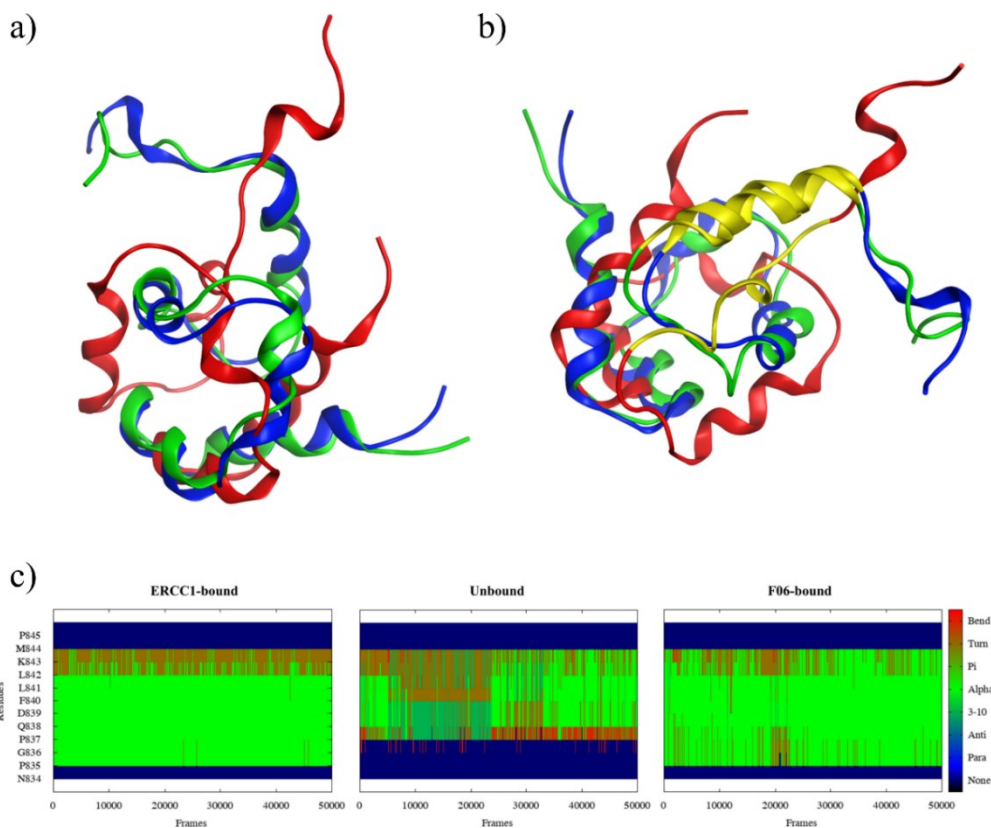


**Figure 3.4.** Structural differences between bound and unbound forms of XPF. a) ERCC1-bound (green) and F06 (1)-bound (blue) displayed a similar tertiary structure of the domain, with a well-formed HhH2 domain, despite the difference in size and interaction interface between ERCC1 and F06 (1). The unbound form (red) lost the HhH2 structure and adopted a less globular conformation. b) Residues constituting H1 showed an alpha helical structure for the two bound forms, while a more disordered structure was observed in the unbound form. H1 is part of the binding site of F06 (1). c) DSSP analysis of H1 residues in the last 50000 frames (100 ns) of the MD simulations, confirming the presence of alpha helical conformations for the XPF bound forms and less organized conformations for the unbound form.

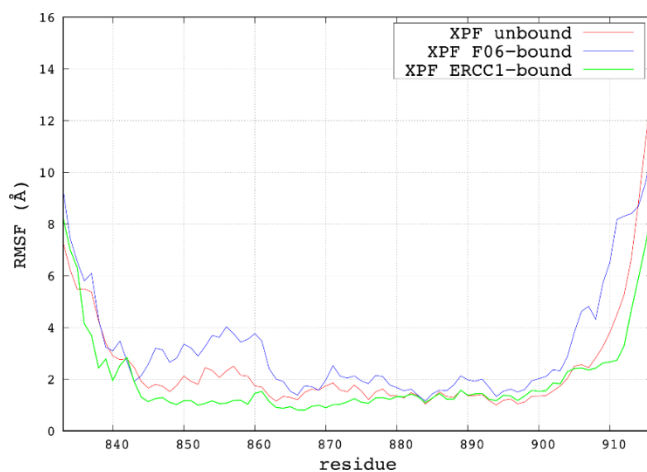


**Figure 3.5.** RMSF for the XPF backbone atoms calculated for the last 100 ns of MD simulation for the unbound (red), F06-bound (blue) and ERCC1-bound (green) XPF structure. Over the equilibrated parts of the trajectories the F06-bound model was the highest-fluctuating one.

### 3.2.2 Interactions of F06 with The XPF Binding Site

In Chapter 2, we synthesized and tested F06 (1) analogues where a hydrophobic, solvent-exposed moiety was modified. In this chapter, we focused on polar groups of F06 (1). We carried out hydrogen bond analysis of the last 100 ns of the XPF–F06 (1) trajectory in order to assess polar interactions of the ligand with the receptor and the solvent (Table 3.1).

**Table 3.1.** Main Ligand–Receptor and Ligand–Solvent Hydrogen Bonds Detected for the XPF–F06 Complex During the Last 100 ns of MD Simulation<sup>a</sup>

Donor	Acceptor	Ratio <sup>b</sup>	Average distance (Å)	Average angle (°)
F06@N2	E831	0.37	2.88	160.24
F06@N3	V859	0.15	2.98	159.68
F06@N3	M856	0.11	3.19	142.63
F06@N2	S830	0.08	2.98	140.18
F06@O1	Solvent <sup>c</sup>	0.92	2.78	160.81
F06@N3	Solvent <sup>c</sup>	0.75	3.02	160.20
F06@N2	Solvent <sup>c</sup>	0.68	2.95	155.90
N834	F06@N4	0.09	3.10	155.05
Solvent <sup>d</sup>	F06@N4	0.96	3.02	154.51
Solvent <sup>d</sup>	F06@N1	0.82	2.94	160.17
Solvent <sup>d</sup>	F06@CL1	0.49	3.28	138.81
Solvent <sup>d</sup>	F06@O1	0.41	3.07	148.57
Solvent <sup>d</sup>	F06@N3	0.13	3.24	145.08

<sup>a</sup> Only the bonds present in at least 5% of the trajectory are reported. Names of F06 polar atoms follow the scheme of Figure 3.3.2.1. <sup>b</sup>Ratio = (frames where the interaction was present)/(total number of frames). <sup>c</sup>Water, Na<sup>+</sup> and Cl<sup>-</sup>. <sup>d</sup>Water.

The charge-assisted hydrogen bond between the N2-H atoms of F06 (Figure 3.6) and the negatively charged side chain of E831 of XPF was the most prevalent

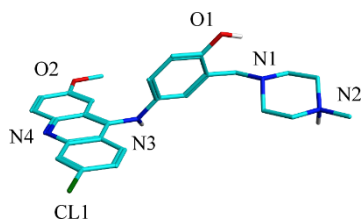


**Figure 3.6.** Protonated 3D structure of F06 (**1**). Polar atoms are labelled with their names.

interaction, present in 37% of the last 100 ns of the MD trajectory. N3 of F06 (**1**) also established hydrogen bond interactions with the backbone atoms of V859 and M856 over 26% of the equilibrated trajectory. In our simulation, N4 was the main hydrogen bond acceptor atom of F06, establishing a hydrogen bond with N834 of XPF for 9% of the 100 ns (Table 3.1). These three interactions also showed good hydrogen bond geometries in terms of distances (2.88–3.10 Å) and angles ( $\sim 160^\circ$ ), which are consistent with our previous observations.<sup>20</sup> The other polar moieties of F06 (**1**) were involved in hydrogen bonds with solvent molecules during the simulation, rather than specific interactions with XPF (Table 3.1). Interestingly, O2 of F06 (**1**) was the only polar atom not involved in any hydrogen bond with XPF, despite its buried position and both acceptor and donor-favourable interaction spots present around it (Figure 3.7).

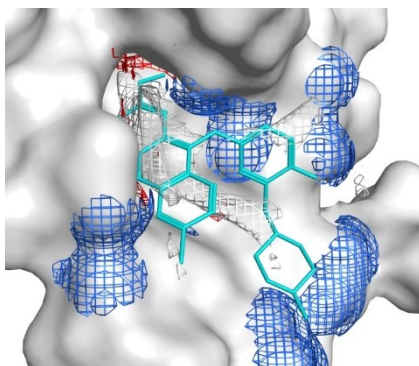


**Figure 3.7.** Poisson–Boltzmann electrostatic feature maps of the F06 binding site on XPF. Blue, red and white color indicate zones where donor, acceptor and hydrophobic probe atoms show a potential of  $-2$  kcal/mol, respectively.

### 3.2.3 Virtual Screening of F06 (1) Analogues

F.G and I generated a virtual library of analogues by modifying two groups of F06 (1) (Figure 3.2), namely 1) the methoxy group of F06 (Gen B), as we expected modifications of this moiety to generate an additional favourable hydrogen bond and 2) the lateral branch of the acridine scaffold of F06 to reduce the solvent-exposed portion of the compound (Gen A). We also included the piperazine ring extension of compound 4, the most active F06 (1) analogue identified in the previous medicinal chemistry campaign.

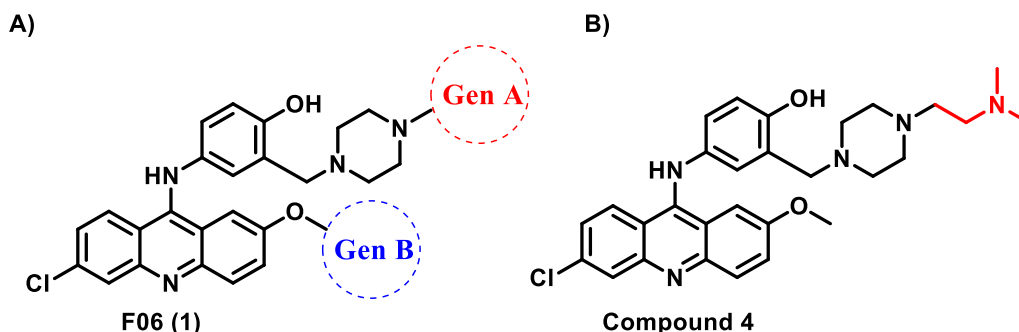


**Figure 3.8.** F06 (1) analogues. A) modification sites of F06 (1) explored using a CADD strategy. The choice of sites was driven by the analysis of the binding mode of the original compound F06 (1). B) structure of compound 4, best ERCC1–XPF inhibitor among Gen A compounds.

The resulting library includes 5650 structures. Because different features were introduced in the analogues, we defined an essential pharmacophore model, based on the conserved acridine core, with three aromatic features accounting for the aromatic rings anchoring the compounds to the hydrophobic floor of the binding site (Figure 3.9), and we used it for pharmacophore-assisted docking in MOE, followed by MD-MM/GBSA-based rescoring. Among the top ranked virtual hits, we selected five compounds for synthesis, based on visual inspection of the predicted binding modes, MM/GBSA score, and synthetic chemistry feasibility.

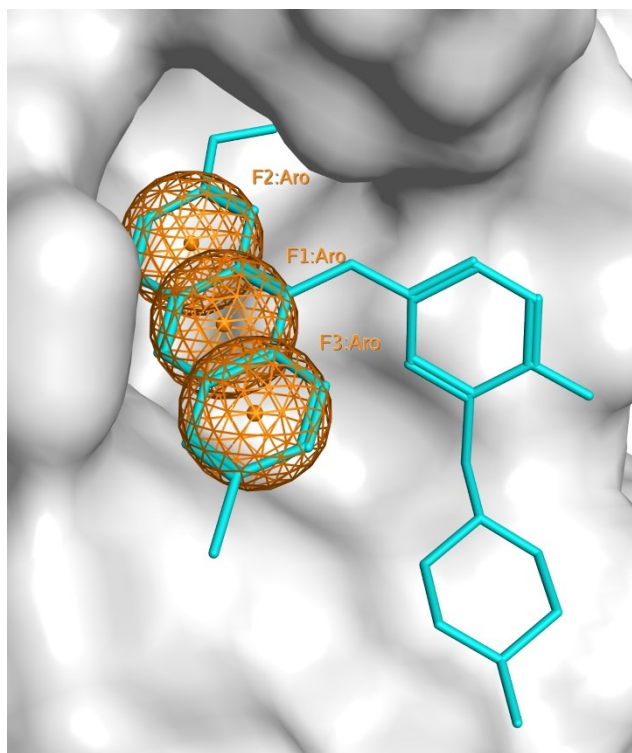


**Figure 3.9.** Pharmacophore model of the scaffold common to all the compounds, including three aromatic features, each one centered at one of the acridine rings.

### 3.2.4 Chemistry

In Chapter 1, we reported the first generation (**Gen A**) of F06 (**1**) analogues based on the modification of the piperazine ring with solvent-exposed moieties, according to our reported computational studies.<sup>20</sup> In this chapter, we focused on further modifying different sites of F06 (**1**), according to our suggested pharmacophore model, and extensively investigating their structure activity relationship.

For the second generation series (**Gen B**) including controls, **B2**, **B3** (lacks the aminophenol linked with piperazine), and **B4** which lacks acridine (Figure 3.10), we modified the acridine-methoxy group of **F06** with polar hydrogen bond donor groups, such as OH (**B2**) or its functionalization such as esterification (**B6**) or alkylation (**B7** and **8**) to gain more insight into the role of this group on the activity of ERCC1–XPF.

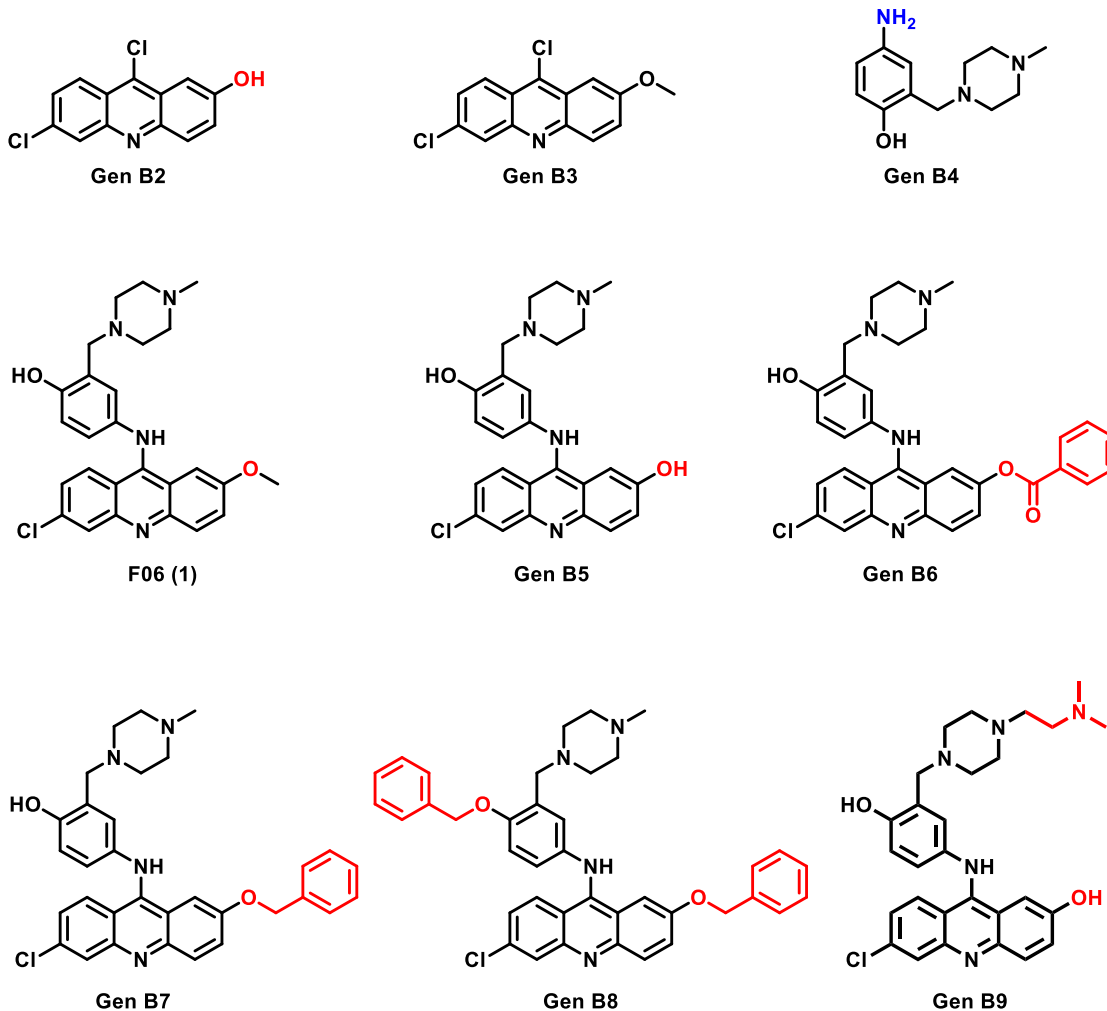
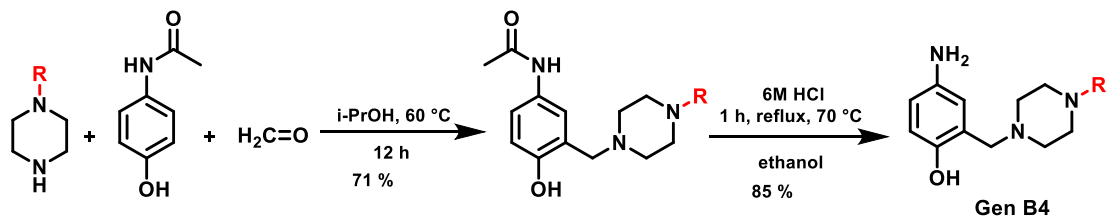


**Figure 3.10.** Structures of **Gen B** compounds including controls.

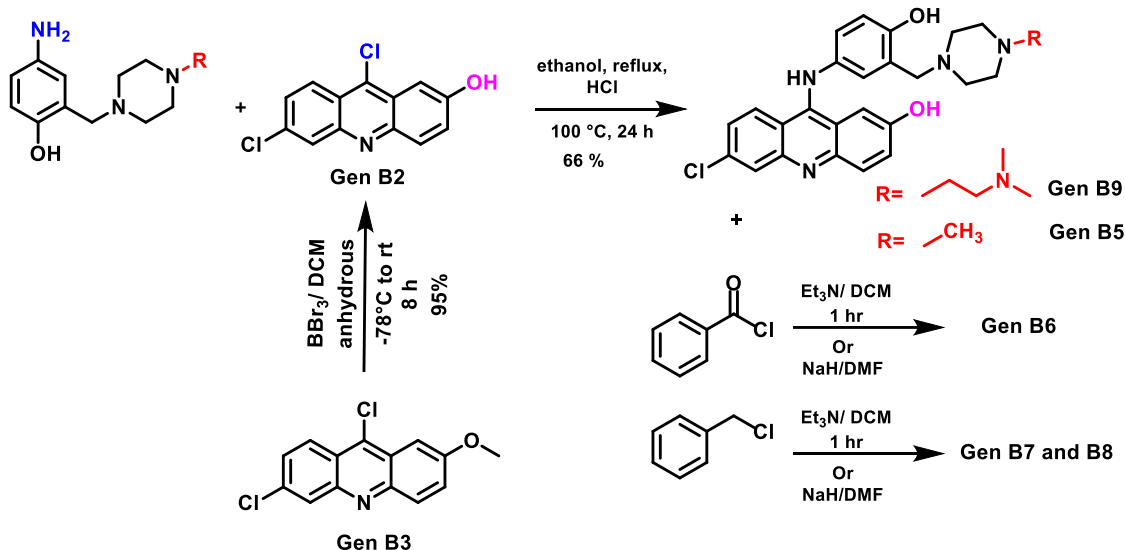
The general synthesis of the **Gen B** compounds was achieved through a nucleophilic substitution reaction of **B5** and acyl chloride or benzyl chloride derivatives to afford compounds **B6**, **B7** and **B8**, respectively, as depicted in Scheme 3.1. The synthesis of **Gen B2** was achieved through dealkylation of **Gen B3** (2-methoxy-6,9-dichloroacridine) using  $\text{BBr}_3$  in dichloromethane under nitrogen for 8 h at room temperature. The synthesis of **F06 (1)**, **B5**, and **B9** was performed according to our

reported procedure<sup>20</sup> with minor modifications, which was through a one-pot three sequential addition reaction protocol. The first step was the Mannich-like reaction

1) Multi-component reaction



2)  $\text{S}_{\text{N}}\text{Ar}$  reaction



Scheme 3.1. General synthetic route of Gen B compounds.

of *p*-acetamidophenol with formaldehyde, followed by reaction with the appropriate secondary amine in 2-propanol carried out under reflux for 12 h. The solvent and excess unreacted formaldehyde from the resulting mixture were removed under vacuum, and, without isolating the compound, the resulting viscous residue was treated with 6 M HCl to deacetylate the acetamido group to furnish the primary amine. Afterwards, an equimolar amount of 2-methoxy 6,9 chloroacridine or 2-hydroxy 6,9 chloroacridine was added, affording, after heating, compounds F06 (**1**) and **B5**, respectively, in moderate to good yields after isolation. The synthesis is general, facile, and reproducible. Binding

energies and other computationally derived values for F06 and the series of analogues are reported in Table 3.2.

**Table 3.2.** Computational Results for the Series of F06 Analogues Selected for Chemical Synthesis<sup>a</sup>

Compound	GBVI/WSA <sup>b</sup> (kcal/mol)	Ligand efficiency <sup>c</sup> (kcal/mol/ha)	MM/GBSA (kcal/mol)	LogP
<b>F06</b>	-6.70	-0.20	-17.78	4.10
<b>B6</b>	-8.56	-0.21	-14.19	5.31
<b>B9</b>	-7.00	-0.19	-12.44	2.31
<b>B7</b>	-5.17	-0.13	-8.15	5.93
<b>B2</b>	-5.21	-0.31	-7.11	4.40
<b>B5</b>	-5.90	-0.18	-3.79	3.79

<sup>a</sup>The list is in ascending order based on MM/GBSA scores. <sup>b</sup>From MOE Dock. <sup>c</sup>Docking binding energy/heavy atoms (ha).

### 3.2.5 Inhibitory Effect of Gen B Compounds on ERCC1–XPF Activity

Two compounds, **B5** and **B9**, exhibited a marked capacity to inhibit the nuclease activity of ERCC1–XPF compared to **F06** (Figure 3.11). The inhibitory activity of **B5** is superior to that of **F06**, which is probably attributable to the hydrogen bond donor phenolic group installed in replacement of the acridine-methoxy group of **F06**. This suggestion is also consistent with **B2** (methoxy acridine) and **B3** (hydroxy acridine), although they are not as active as **B5** or **B9**. Removal of the piperazine substituted aminophenol as in **B2** or acridine as in **B4** resulted in complete loss of inhibition. To measure the half-maximum inhibitory concentrations (IC<sub>50</sub>) for the best inhibitor **B9** on the full-length protein, different concentrations of the drug were plotted against the initial velocity (V<sub>o</sub>, change in relative fluorescence units (RFU)/time) of the enzyme (Figure. 3.11B). The IC<sub>50</sub> of **B9** was estimated as 0.49 ± 0.04 μM, which was

approximately four times more efficient than **F06**, which has an estimated  $IC_{50}$  of  $1.86 \pm 0.25 \mu\text{M}$ .<sup>20</sup> Although compound **4** has superior inhibitory activity on ERCC1–XPF relative to **B9** (Figure 3.12), the improved inhibitory activity of **B9** suggests the replacement of the acridine-methoxy group with a hydrogen bond donor group together with the conservation or extension of the piperazine ring enhances the activity of this generation of compounds in comparison of F06 (**1**).

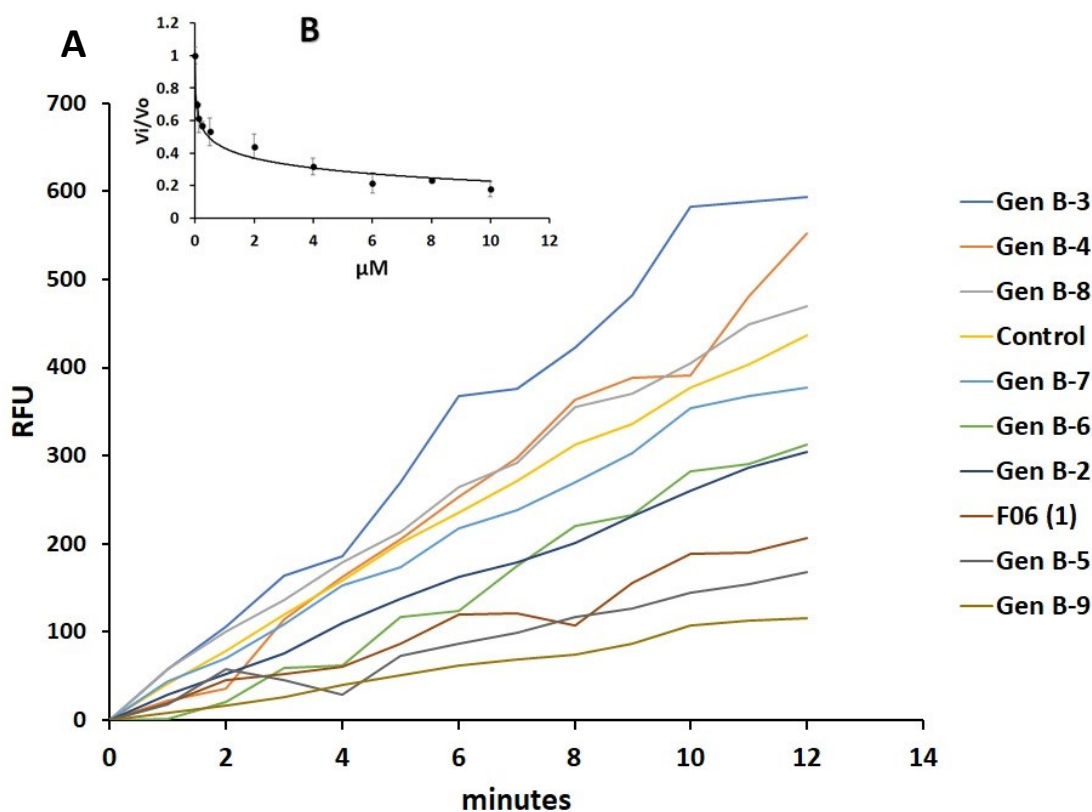


**Figure 3.11.** *In vitro* inhibition of ERCC1–XPF endonuclease activity. A microplate fluorescent assay was used to measure inhibition of ERCC1–XPF endonuclease activity by the different compounds. Incubation of the DNA stem–loop substrate with ERCC1–XPF resulted in the release of a fluorescent 8-base fragment accompanied by an increase in fluorescence (RFU) with time. A) A representative tracing of the effect of the different compounds (10  $\mu\text{M}$  each) on the incision activity is shown. B) Plot of enzyme rate ( $\Delta\text{RFU}/\text{time}$ ) vs **B9** concentration.

### 3.2.6 Predicted Binding Mode of B9 to XPF

Since **B9** was the most active analogue of the series, we carried out a detailed analysis of its predicted binding pose, based on the 2 ns-long MD simulation and MM-GBSA calculations, and compared it with the analysis for F06. The lowest potential energy conformation of the XPF-**B9** complex extracted from the 2ns MD simulation (Figure 3.12A) showed a hydrophobic stacking of the acridine moiety of **B9** between

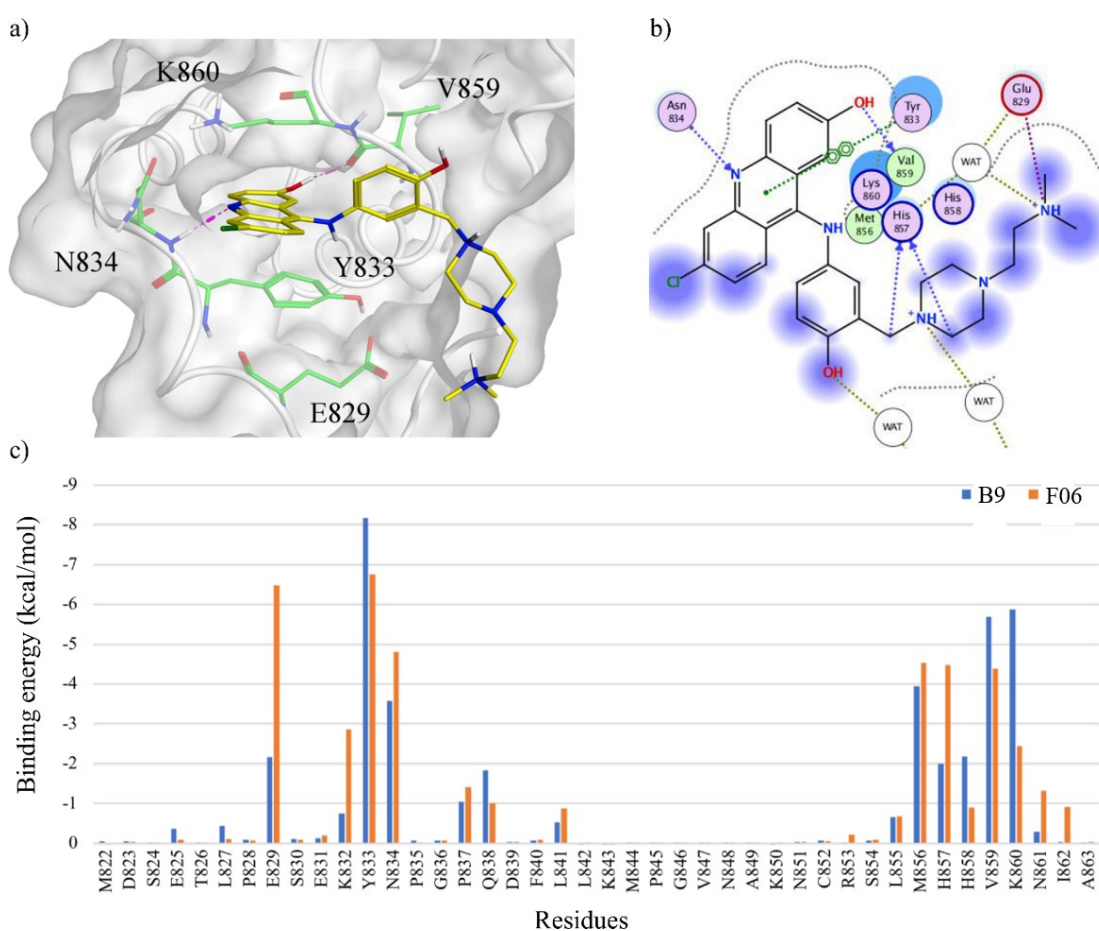


**Figure 3.12.** Detailed analysis of the predicted binding mode of **B9** to XPF derived from the 2 ns-long MD simulation. a) lowest potential energy XPF (white), **B9** (yellow) conformation extracted from the simulation. The acridine moiety was stacked between the side chains of Y833 and K860. Hydrogen bonds between **B9** and N834 and V859 were observed. b) Ligand interaction diagram of the lowest potential energy conformation; the lateral branch of **B9** containing the piperazine ring extension was solvent-exposed (blue clouds) thanks to its polar and charged groups that favourably interacted with the surrounding water molecules. c) Per-residue decomposition of the total MM/GBSA binding energy of **B9** (blue) and F06 (orange).

the side chains of Y833 and K860 of F06 (Figure 3.12A and B), resulting in more favourable contributions to the overall binding affinity by these residues compared to XPF–F06 (Figure 3.12C). N834 was involved in a hydrogen bond with **B9**, similarly to F06 (**1**) (Figure 3.12A and B). Interestingly, the hydroxyl group substituting the methoxy in **B9** was involved in a new hydrogen bond established with the side chain of V859, which was not observed for F06 or our previous compound **4**.<sup>20</sup> Consistent with our previous observations, the acridine moiety was buried stably inside the XPF pocket, while the piperazine ring extension derived from compound **4** resulted in enhanced interactions with the solvent and E829 (Figure 3.12B), although the latter was less strong than the one observed for F06 (Figure 3.12C).

### 3.3 Conclusion

Interest is growing in the role of the ERCC1–XPF endonuclease as a drug target in cancer treatment due to its critical role in repairing DNA damage inflicted by platinum-based and cross-linking chemotherapy. Abnormal regulation of levels of XPF, ERCC1, or related proteins has been linked with modulation of the response to DNA-damaging treatments, either showing resistance in the case of over-regulation or sensitization in the case of down-regulation. Thus, ERCC1–XPF inhibition is a viable strategy to circumvent DNA damage-related drug resistance and improve the outcome of cancer therapy.

In this work we focused on the disruption of the ERCC1–XPF protein–protein interaction with small molecules, as heterodimerization of ERCC1 and XPF is required to constitute a functional complex,<sup>8</sup> by developing ERCC1–XPF dimerization inhibitors

using a multi-step CADD strategy. Two compounds, **B5** and **B9**, have been identified by the *in vitro* endonuclease assay with improved inhibition of the ERCC1–XPF incision activity compared to the parent compound F06 (**1**). Compound **B1**, a truncated version of **B9** and **B5**, also may be a promising starting structure for further modifications due to the observation of inhibitory activity, despite the replacement of the bulky lateral branch with a chlorine.

To conclude, the workflow we introduced here provides a blueprint for future modification of other sites of F06 (**1**) in order to advance towards a preclinical drug candidate for DNA repair inhibition. Likewise, the set of analogues described in this study, especially **B5**, and **B9**, and their structure-activity relationships, provide important information for the lead optimization process of F06 (**1**).

## **3.4 Methods and Experimental Section\***

### **3.4.1 Molecular Dynamics of XPF HhH2 Domain Alone, F06-bound and ERCC1-bound**

We computationally predicted F06 binding to a pocket of the human XPF double helix–hairpin–helix (HhH2) domain, replacing the side chain of F293 from ERCC1 in the dimer.<sup>19</sup> Using classical MD simulations, we compared the unbound, F06-bound and ERCC1-bound form of the HhH2 domain of XPF (residues 822–905). For the F06-XPF complex, we used the structure previously obtained from docking simulations.<sup>20</sup>

\* I was responsible for the synthesis and design of all compounds. F.G. carried out the computational studies on the ERCC1-XPF heterodimer and the virtual screening of compounds. D.J. expressed and purified ERCC1–XPF, employed the *in vitro* ERCC–XPF1 assay.

The unbound and ERCC1-bound forms were extracted from the NMR ensemble of ERCC1–XPF dimerized HhH2 domains (PDB 1Z00),<sup>23</sup> where the bound ERCC1 structure was excluded and included in the simulation, respectively.

The protonation states of the systems were assigned using the H++ server by setting pH = 7, a salinity of 0.15 M, a dielectric constant of 10 for the solute, and a solvent dielectric constant of 80 as input parameters.<sup>24</sup> In AmberTools14 tleap,<sup>25</sup> we assigned Amber ff14SB force field parameters to the proteins<sup>26</sup> and the 12-6-4 parameters for mono- and divalent ions in TIP3P water to the ions, as previously recommended.<sup>27, 28</sup> We assigned the parameters of the Generalized Amber Force Field (GAFF)<sup>29</sup> and AM1-BCC charges<sup>30</sup> to F06 using Antechamber.<sup>29</sup> The three systems were solvated with octahedral boxes of TIP3P explicit water molecules<sup>31</sup> with 15 Å of buffer. The required numbers of Na<sup>+</sup> and Cl<sup>-</sup> ions were added to neutralize the overall charge and establish a 0.15 M physiological ionic concentration. We then ran MD simulations of the systems using pmemd.cuda<sup>32</sup> with the following procedure: relaxation of ions and water molecules through 1000 steps of steepest descent and 1000 steps of conjugate gradient minimization, keeping protein and ligand atoms harmonically restrained with a force constant of 500 kcal/mol/Å<sup>2</sup>; 2000 steps of steepest descent, followed by 3000 conjugate gradient steps without any restraint; gradual heating from 0 to 300 K over 100 ps using the Langevin thermostat, keeping the backbone and ligand heavy atoms harmonically restrained (2 kcal/mol/Å<sup>2</sup>), and using a time step of 0.5 fs and NVT conditions; gradual release of the restraints in four NPT phases of 50 ps where the force constant was reduced by 0.5 kcal/mol/Å<sup>2</sup> at each phase

with a time step of 2 fs and 250 ns of NPT production simulation with a time step of 2 fs. The cut-off for long-range interactions was set to 9 Å.

After the simulations, we calculated the mass-weighted root-mean square deviation (RMSD) of protein backbone and ligand heavy atoms using cpptraj from AmberTools. We also evaluated the root-mean square fluctuation (RMSF) of the XPF residues over the equilibrated portions of the three MD trajectories. We also carried out a secondary structure analysis over the MD trajectories using the dictionary of protein secondary structure (DSSP) method from cpptraj.<sup>33</sup>

### **3.4.2 Analysis of The Binding Mode of F06**

In order to investigate the dynamics of the F06–XPF interactions, we carried out the analysis of hydrogen bonds occurring between F06 and the receptor and F06 and solvent, respectively, during the equilibrated part of the MD trajectory using cpptraj. We defined as hydrogen bonds non-bonded interactions occurring between donor-hydrogen and acceptor atoms that deviated no more than 60° from linearity and with a maximum distance of 3.5 Å between the two heavy atoms involved in the interaction.

Using the MOE (Molecular Operating Environment) Pharmacophore Query Editor and the EHT scheme, we generated a set of essential pharmacophore features of F06, based on the docking pose.<sup>34</sup> Electrostatic maps of the binding site were generated as reported previously.<sup>20</sup>

### **3.4.3 Computer-aided Design of F06 Analogues**

We used the binding pose of F06 previously obtained as a starting point for our computer-aided generation of analogues. We created an extensive, non-redundant

collection of multi-conformational fragments by merging the MOE Linker library,<sup>35</sup> the ChEMBL fragment database,<sup>35</sup> the Cambridge Structure Linker database,<sup>36</sup> and a collection of fragments derived from the ZINC15 3D database.<sup>37</sup> This last library was generated using the MOE 2015 SD Pipelining Command tools to obtain different protonation states and tautomers, remove non-lead-like, reactive, and large-ring structures, and generate molecular fragments. Up to five conformations for each ZINC15-derived fragment were obtained using Conformation Import and imposing a strain limit of 4 kcal/mol. We then used the entire collection of fragments for MOE2015 Scaffold Replacement<sup>35</sup> of F06 substructures. We also used the MOE MedChem transformation tool (175 modification rules)<sup>35</sup> on the same F06 groups, with six iterations and a protein–ligand clash energy limit of 0.5 kcal/mol/ligand atom. For both Scaffold Replacement and MedChem transformations, we ran minimization of the resulting poses with protein side chains free to move and generalized Born Volume Integral/Weighted Surface Area (GBVI/WSA) function for scoring.<sup>38</sup>

### **3.4.4 Structure-based Virtual Screening**

We adopted the same structure-based virtual screening (VS) strategy used before for F06 analogues because of its proven ability to identify highly active compounds.<sup>20</sup> Molecular docking simulations were run with MOE Dock.<sup>35</sup> The pharmacophore model was used for the placement step, in which 30 high-scoring poses were returned, based on the London dG scores.<sup>38</sup> Poses were minimized together with the side chains of the binding site (Induced Fit), and one pose was returned as the top-scored by the GBVI/WSA scoring function. We calculated log P values of the molecules from the

SlogP function in MO<sup>39</sup> as well as docking ligand efficiencies (final score/number of ligand heavy atoms).

We ran MD simulations of the top 200 analogue-XPF complexes resulting from docking. The systems were prepared in the same way as the F06–XPF system, and simulation setups were the same, except for the length of the production simulations (2 ns). For MD snapshots extracted every 10 ps from the production simulations, we calculated the enthalpic portion of the binding energy using the Molecular Mechanics/Generalized Born Surface Area (MM/GBSA) method<sup>40</sup> implemented in the MMPBSA.py script.<sup>41</sup> In MM/GBSA, the free energy change due to ligand binding is calculated as:

$$\Delta G_{\text{bind,solv}} = \Delta G_{\text{MM,vac}} + \Delta G_{\text{solv,complex}} - \Delta G_{\text{solv,ligand}} - \Delta G_{\text{solv,protein}} - T\Delta S \quad \text{Eq. 1}$$

where  $\Delta G_{\text{MM,vac}}$  includes averaged non-bonded molecular mechanics terms (electrostatic and van der Waals) occurring between protein and ligand. Solvation terms are modeled as:

$$\Delta G_{\text{solv}} = \Delta G_{\text{solv,polar}} + \Delta G_{\text{solv,npolar}} \quad \text{Eq. 2}$$

where the polar contribution of the solvent is calculated by the Generalized Born equation.<sup>42</sup> Here, we used the GB<sup>OCB</sup>II model and the modified radii from Onufriev et al.,<sup>40</sup> and an ionic concentration of 0.15 M. The hydrophobic contribution to the solvation free energy is calculated as:

$$\Delta G_{\text{solv,npolar}} = \gamma \cdot \text{SASA} \quad \text{Eq. 3}$$

with  $\gamma$  (surface tension) as 0.005 kcal/mol/Å<sup>2</sup>, and the solvent-accessible surface area (SASA) is calculated using the linear combinations of pairwise overlaps (LCPO) model method.<sup>43</sup> Averaged values were estimated for the ligand–receptor (LR) complex,

receptor (R), and ligand (L) alone, and final values were calculated as a difference between these three values (LR-R-L).

The entropy,  $S$ , is represented in the free energy by the  $T\Delta S$  term. It was calculated for each trajectory using the Amber normal mode analysis (NMA) method for the LR, R, and L systems and then calculating the difference between the three systems.<sup>44</sup> Pairwise decomposition of binding energies also was carried out for the top compounds and the binding pocket residues.

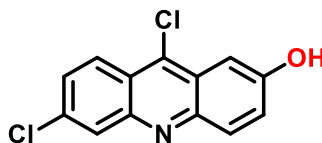
### 3.4.5 Preparation of F06-based Analogues (Gen B Compounds)

#### 3.4.5.1 4-((6-Chloro-2-methoxyacridin-9-yl)amino)-2-((4-methylpiperazin-1-yl)methyl)phenol (F06(1))

The hit compound **F06 (1)** has been synthesized according to our previously reported procedures.<sup>20</sup>

#### 3.4.5.2 Synthesis of Gen B Compounds

##### 3.4.5.2.1 6,9-dichloroacridin-2-ol (B2)



**Gen B2**

Synthesis of **B2** was achieved by the reported procedures<sup>45</sup> but with minor modifications: a mixture of the commercially available 6,9-dichloro-methoxyacridine, **B3**, (0.28 g, 1.0 mmol) and  $\text{BBr}_3$  in DCM solvent (2.87 mL, 2.87 mmol) was taken in a

10 mL single neck round bottom flask under nitrogen conditions. Then, the reaction mixture was stirred at  $-78\text{ }^{\circ}\text{C}$  for 20 min and heated to room temperature overnight. Upon completion of the reaction (monitored by TLC with 20% MeOH/DCM eluent system), the reaction was quenched by adding a saturated solution of  $\text{NaHCO}_3$  to yield a yellowish solid. Next, the solid residue was filtered and washed with  $\text{H}_2\text{O}$  and a saturated solution of  $\text{NaHCO}_3$  three times, followed by drying overnight under high vacuum to yield a pure yellowish solid (**B2**), as reported.

#### 3.4.5.2.2 4-amino-2-((4-methylpiperazin-1-yl)methyl)phenol (**B4**)

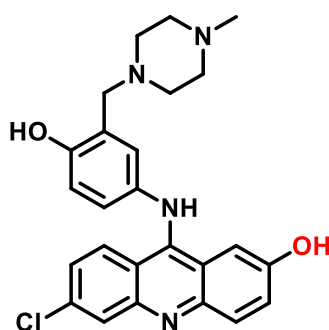


**Gen B4**

**B4** was synthesized according to the reported procedures<sup>46</sup> with minor changes: A mixture of *N*-methyl piperazine (0.12 mL, 1.0 mmol), *p*-acetaminophen (0.15 g, 1.0 mmol), and 37% formaldehyde (0.10 mL, 5 mmol) in isopropyl alcohol (2 ml) was taken in a 10 mL single neck round bottom flask. Then, the reaction mixture was stirred and heated under reflux at  $65\text{ }^{\circ}\text{C}$  for 6 h. Upon completion of the reaction (monitored by TLC with 15% MeOH/DCM eluent system), the solvent was removed on a rotatory evaporator. Next, the residue was dissolved in 3 mL ethanol, and 3 drops of 12 M HCl were added. Subsequently, the reaction mixture was heated at  $110\text{ }^{\circ}\text{C}$  under reflux for 90 min to yield an orange reddish solution. Afterwards, the reaction was left to cool down to room temperature, the reaction mixture was diluted with cold water, and

neutralized to pH of 8–9 with 28% v/v ammonia solution. The alkaline solution was extracted with dichloromethane. The organic layer was washed with brine, concentrated in vacuum, and purified by column chromatography (gradient elution with 5% to 10% MeOH:DCM system) to afford **B4** as a brownish oil, which is the same as reported before.

#### 3.4.5.2.3 6-chloro-9-((4-hydroxy-3-((4-methylpiperazin-1-yl)methyl)phenyl)amino)acridin-2-ol (**B5**)

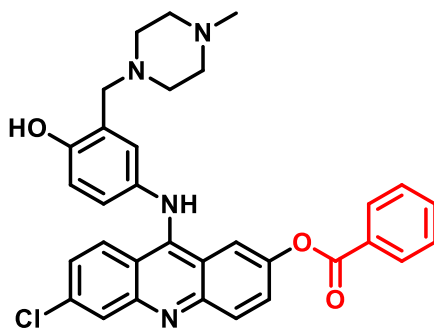


Gen B5

The previous method of **F06** synthesis was employed to synthesize **B5** with the following stoichiometric amounts: *N*-methyl piperazine (0.12 mL, 1.0 mmol), *p*-acetaminophenol (0.15 g, 1.0 mmol), 37% formaldehyde (0.10 mL, 5 mmol), and 6,9-dichloro-hydroxyacridine **B2** (0.26 g, 1.0 mmol) to afford it as an orange reddish semisolid (0.25 g) in 56% yield;  $R_f$  0.40 (1:9, MeOH:DCM); IR (cast film)  $\nu_{\max}$  = 3266, 2923, 1628, 1572, 1496, 1250, 1138, 1002, 929, 826, 778  $\text{cm}^{-1}$ ;  $^1\text{H}$  NMR (500 MHz,  $\text{CD}_3\text{OD}$ )  $\delta$  8.02 (d,  $J$  = 9.3 Hz, 1H), 7.88 (d,  $J$  = 2.1 Hz, 1H), 7.83 (d,  $J$  = 9.3 Hz, 1H), 7.36 (d,  $J$  = 9.3 Hz, 1H), 7.24 (d,  $J$  = 2.6 Hz, 1H), 7.18 (dd,  $J$  = 9.3, 2.1 Hz, 1H), 6.84 (dd,  $J$  = 8.6, 1.8 Hz, 1H), 6.71 (d,  $J$  = 8.6 Hz, 1H), 6.64 (d,  $J$  = 2.6 Hz, 1H), 3.54 (s, 2H), 2.88 – 2.29 (m, 8H), 2.27 (s, 3H). OH and NH protons were not observed;  $^{13}\text{C}$

NMR (126 MHz, CD<sub>3</sub>OD)  $\delta$  155.0, 153.9, 148.2, 147.2, 146.1, 138.7, 136.4, 129.7, 127.2, 126.3, 124.9, 123.8, 122.1, 121.4, 121.3, 118.2, 117.3, 105.9, 60.4, 55.8 (2C), 53.0 (2C), 49.0, 45.8; HRMS (ESI) calcd for C<sub>25</sub>H<sub>26</sub>ClN<sub>4</sub>O<sub>2</sub> [M + H]<sup>+</sup> 449.1739; found 449.1739.

#### 3.4.5.2.4 6-chloro-9-((4-hydroxy-3-((4-methylpiperazin-1-yl)methyl)phenyl)amino)acridin-2-yl benzoate (B6)

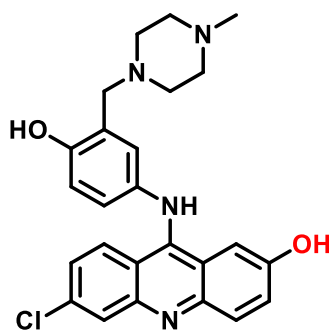


Gen B6

The synthesis of **B6** was achieved by mixing **B5** (0.05 g, 0.1 mmol) with benzoyl chloride (0.01 mL, 0.1 mmol) in 3 mL of anhydrous solvent mixture DCM/Et<sub>3</sub>N (20:1) and stirred for 1 h at room temperature. Afterwards, the reaction mixture was diluted with water, and the organic layer was extracted with DCM. The organic layer was washed with brine, concentrated in vacuum, and purified by column chromatography (gradient elution with 2% to 15% MeOH:DCM system) to afford it as an orange reddish semisolid (0.04 g) in 74% yield;  $R_f$  0.45 (1:9, MeOH:DCM); IR (cast film)  $\nu_{\max}$  = 3268, 2926, 1692, 1628, 1582, 1490, 1238, 1135, 1002, 923, 828, 772 cm<sup>-1</sup>; <sup>1</sup>H NMR (500 MHz, CD<sub>3</sub>OD)  $\delta$  8.09 – 8.05 (m, 2H), 7.88 (d,  $J$  = 9.2 Hz, 1H), 7.73 – 7.62 (m, 4H), 7.54 – 7.47 (m, 3H), 7.04 (dd,  $J$  = 9.2, 2.1 Hz, 1H), 6.83 (dd,  $J$  = 8.5, 2.6 Hz, 1H), 6.73 (d,  $J$  = 8.5 Hz, 1H), 6.70 (d,  $J$  = 2.6 Hz, 1H), 3.55 (s, 2H), 2.70 – 2.29 (m, 8H), 2.26 (s,

3H). OH and NH protons were not observed;  $^{13}\text{C}$  NMR (126 MHz,  $\text{CD}_3\text{OD}$ )  $\delta$  166.5, 155.1, 151.2, 147.4, 146.9, 145.5, 139.5, 138.1, 135.1, 131.0 (2C), 130.4, 129.9 (2C), 128.3, 128.1, 126.2, 124.1, 124.0, 123.4, 123.2, 122.8, 118.7, 118.0, 117.7, 116.9, 60.3, 55.5 (2C), 52.8 (2C), 45.6; HRMS (ESI) calcd for  $\text{C}_{32}\text{H}_{30}\text{ClN}_4\text{O}_3$   $[\text{M} + \text{H}]^+$  553.2001; found 553.1995.

#### 3.4.5.2.5 4-((2-(benzyloxy)-6-chloroacridin-9-yl)amino)-2-((4-methylpiperazin-1-yl) methyl)phenol (B7)

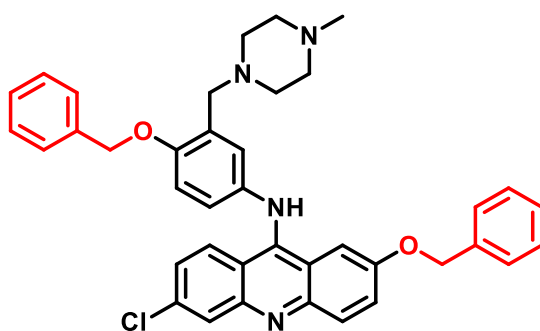


Gen B7

The synthesis of **B7** was achieved as follows: NaH (60% dispersion in mineral oil 0.15 g, 0.4 mmol) in DMF (2 mL) was added dropwise to a stirred solution of **Gen B5** (0.08 g, 0.2 mmol) in DMF (2 mL) and stirred for 10 min prior to the addition of benzyl bromide (0.05 mL, 0.4 mmol). After 1.5 h stirring, the reaction mixture was concentrated under vacuum, and the residue was diluted with DCM prior to washing with saturated solution of  $\text{NH}_4\text{Cl}$ . The organic layer was extracted with DCM, washed with brine, concentrated in vacuum, and purified by column chromatography (gradient elution with 3% to 10% MeOH:DCM system) to afford it as a light orange reddish semisolid (0.03 g) in 30% yield;  $R_f$  0.40 (1:9, MeOH:DCM); IR (cast film)  $\nu_{\text{max}} = 3268$ ,

2926, 1692, 1628, 1582, 1490, 1238, 1135, 1002, 923, 828, 772  $\text{cm}^{-1}$ ;  $^1\text{H}$  NMR (500 MHz,  $\text{CD}_3\text{OD}$ )  $\delta$  8.10 (d,  $J = 9.3$  Hz, 1H), 7.88 (d,  $J = 2.1$  Hz, 1H), 7.83 (d,  $J = 9.3$  Hz, 1H), 7.45 (dd,  $J = 9.4, 2.7$  Hz, 1H), 7.39 – 7.29 (m, 6H), 7.24 (dd,  $J = 9.3, 2.1$  Hz, 1H), 6.89 (dd,  $J = 8.5, 2.7$  Hz, 1H), 6.80 – 6.75 (m, 2H), 4.84 (s, 2H), 3.59 (s, 2H), 2.73 – 2.28 (m, 8H), 2.24 (s, 3H). OH and NH protons were not observed;  $^{13}\text{C}$  NMR (126 MHz,  $\text{CD}_3\text{OD}$ )  $\delta$  165.2, 155.8, 154.6, 149.1, 140.7, 138.5, 137.9, 137.0, 129.5 (2C), 129.1, 128.7 (2C), 127.2, 126.7, 125.9, 125.0, 124.0, 123.3, 122.8, 119.5, 117.93, 117.4, 104.6, 103.8, 71.2, 60.5, 55.7 (2C), 53.0 (2C), 45.7; HRMS (ESI) calcd for  $\text{C}_{32}\text{H}_{32}\text{ClN}_4\text{O}_2$   $[\text{M} + \text{H}]^+$  539.2208; found 539.2216.

#### 3.4.5.2.6 2-(benzyloxy)-N-(4-(benzyloxy)-3-((4-methylpiperazin-1-yl)methyl)phenyl)-6-chloroacridin-9-amine (B8)

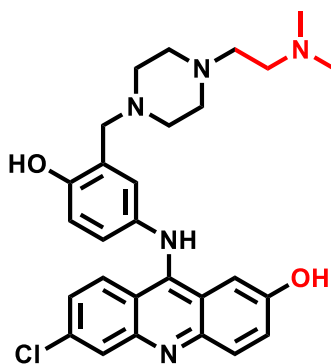


Gen B8

The synthesis of **Gen B8** followed the synthesis of **B7** with minor changes as follows: NaH (60% dispersion in mineral oil 0.15 g, 0.4 mmol) in DMF (2 mL) was added dropwise to a stirred solution of **B5** (0.08 g, 0.2 mmol) in DMF (2 mL), and the reaction was further stirred for 10 min prior to the addition of benzyl bromide (0.05 mL, 0.4 mmol). After 2.5 h stirring, the reaction mixture was concentrated under vacuum, and the residue was diluted with DCM prior to washing with a saturated solution of  $\text{NH}_4\text{Cl}$ .

The organic layer was extracted with DCM, washed with brine, concentrated in vacuum, and purified by column chromatography (gradient elution with 3% to 10% MeOH:DCM system) to afford it as a light orange reddish semisolid (0.04 g) in 40% yield;  $R_f$  0.50 (1:9, MeOH:DCM); IR (cast film)  $\nu_{\max}$  = 3159, 2906, 1687, 1623, 1577, 1480, 1222, 1125, 1001, 922, 825, 769  $\text{cm}^{-1}$ ;  $^1\text{H}$  NMR (500 MHz,  $\text{CD}_3\text{OD}$ )  $\delta$  8.09 (d,  $J$  = 9.2 Hz, 1H), 7.96 – 7.82 (m, 2H), 7.47 – 7.40 (m, 3H), 7.37 – 7.21 (m, 10H), 7.04 (d,  $J$  = 8.7 Hz, 1H), 6.97 (dd,  $J$  = 8.7, 2.8 Hz, 1H), 6.86 (d,  $J$  = 2.8 Hz, 1H), 5.08 (s, 2H), 4.83 (s, 2H), 3.48 (s, 2H), 2.48 – 2.19 (m, 8H), 2.16 (s, 3H). OH and NH protons were not observed;  $^{13}\text{C}$  NMR (126 MHz,  $\text{CD}_3\text{OD}$ )  $\delta$  171.9, 156.0, 154.2, 138.8, 137.9, 136.7, 129.5, 129.5, 129.0 (2C), 128.9 (2C), 128.7 (4C), 128.5 (4C), 128.2, 127.3, 126.6, 125.9, 125.6, 123.6, 121.2, 120.3, 118.6, 114.7, 100.2, 71.7, 70.7, 56.7, 55.6 (2C), 53.4 (2C), 45.8; HRMS (ESI) calcd for  $\text{C}_{39}\text{H}_{38}\text{ClN}_4\text{O}_2$   $[\text{M} + \text{H}]^+$  629.2678; found 629.2687.

#### 3.4.5.2.7 6-chloro-9-((3-((4-(2-(dimethylamino)ethyl)piperazin-1-yl)methyl)-4-hydroxyphenyl)amino)acridin-2-yl) (B9)



Gen B9

Synthesis of **B9** was performed according to our previous method for compound 4 synthesis with minor modifications.<sup>20</sup> The reaction was carried out in a one pot sequential addition in three steps. A mixture of 1-[2-(dimethylamino)ethyl] piperazine

(0.16 g, 1.0 mmol), *p*-acetaminophenol (0.15 g, 1.0 mmol) and 37% formaldehyde (0.10 mL, 5 mmol) in isopropyl alcohol (2 mL) was taken in a 10 mL single neck round bottom flask. Then, the reaction mixture was stirred and heated under reflux at 65 °C for 6 h. Upon completion of the reaction (monitored by TLC with 15% MeOH/DCM eluent system), the solvent was removed on a rotatory evaporator. Next, the residue was dissolved in 3 mL ethanol and 3 drops of 12 M HCl were added. Subsequently, the reaction mixture was heated at 90 °C under reflux for 90 min. Afterwards, 6,9-dichloro-hydroxyacridine **B2** (0.26 g, 1.0 mmol) was added to the mixture and stirred further at 90 °C under reflux, and the course of reaction followed by TLC until little or no starting material was detected (around 12 h). On cooling to room temperature, the reaction mixture was diluted with cold water and neutralized to pH of 8–9 with 28% v/v ammonia solution. The alkaline solution was extracted with dichloromethane. The organic layer was washed with brine, concentrated in vacuum, and purified by column chromatography (gradient elution with 5% to 10% MeOH:DCM system) to afford **B9** as an orange reddish semisolid (0.35 g) in 70 % yield;  $R_f$  0.48 (2:8, MeOH:DCM); IR (cast film)  $\nu_{\max}$  = 3030, 2946, 2876, 2820, 1621, 1494, 1254, 1150, 1008, 932, 816, 736  $\text{cm}^{-1}$ ;  $^1\text{H}$  NMR (500 MHz,  $\text{CD}_3\text{OD}$ )  $\delta$  7.97 – 7.90 (m, 1H), 7.85 – 7.77 (m, 2H), 7.34 (dd,  $J$  = 9.3, 1.5 Hz, 1H), 7.12 – 7.06 (m, 1H), 6.81 – 6.75 (m, 1H), 6.71 – 6.64 (m, 1H), 6.63 – 6.42 (m, 2H), 3.47 (s, 2H), 2.60 – 2.31 (m, 12H), 2.24 (s, 6H). OH and NH protons were not observed;  $^{13}\text{C}$  NMR (125 MHz,  $\text{CD}_3\text{OD}$ )  $\delta$  155.3, 153.9, 148.1, 146.9, 146.1, 138.6, 136.2, 129.7, 127.2, 126.5, 126.4, 124.8, 123.7, 121.9, 121.3, 121.2, 118.3, 118.1, 117.3, 60.5, 57.0, 56.5, 54.3 (2C), 53.1 (2C), 45.7 (2C); HRMS (ESI) calcd for  $\text{C}_{28}\text{H}_{33}\text{ClN}_5\text{O}_2$   $[\text{M} + \text{H}]^+$  506.2317; found 506.2307.

### **3.4.6 ERCC1–XPF Protein Preparation**

David Jay conducted this experiment using human ERCC1–XPF wild-type protein was obtained as described in section 2.5.7 in chapter 2.<sup>20, 47</sup>

### **3.4.7 Microplate Fluorescence Incision Assay**

ERCC1–XPF incision was measured in a microplate incision assay by David Jay, as described in section 2.5.8 in chapter 2.<sup>20, 47</sup>

### 3.5 References

1. López-Otín, C.; Blasco, M. A.; Partridge, L.; Serrano, M.; Kroemer, G. The hallmarks of aging. *Cell* **2013**, *153*, 1194-1217.
2. Hanahan, D.; Weinberg, R. A. Hallmarks of cancer: the next generation. *Cell* **2011**, *144*, 646-674.
3. Bukowska, B.; Karwowski, B. T. Actual state of knowledge in the field of diseases related with defective nucleotide excision repair. *Life Sciences* **2018**, *195*, 6-18.
4. Cleaver, J. E.; Lam, E. T.; Revet, I. Disorders of nucleotide excision repair: the genetic and molecular basis of heterogeneity. *Nature Reviews Genetics* **2009**, *10*, 756-768.
5. Helleday, T.; Petermann, E.; Lundin, C.; Hodgson, B.; Sharma, R. A. DNA repair pathways as targets for cancer therapy. *Nature Reviews Cancer* **2008**, *8*, 193-204.
6. Ohmoto, A.; Yachida, S. Current status of poly (ADP-ribose) polymerase inhibitors and future directions. *OncoTargets and Therapy* **2017**, *10*, 5195-5208.
7. Brown, J. S.; O'Carrigan, B.; Jackson, S. P.; Yap, T. A. Targeting DNA repair in cancer: beyond PARP inhibitors. *Cancer Discovery* **2017**, *7*, 20-37.
8. McNeil, E. M.; Melton, D. W. DNA repair endonuclease ERCC1–XPF as a novel therapeutic target to overcome chemoresistance in cancer therapy. *Nucleic Acids Research* **2012**, *40*, 9990-10004.
9. Faridounnia, M.; Folkers, G. E.; Boelens, R. Function and interactions of ERCC1-XPF in DNA damage response. *Molecules* **2018**, *23*, 3205-323.
10. Gentile, F.; Elmenoufy, A. H.; Ciniero, G.; Jay, D.; Karimi-Busheri, F.; Barakat, K. H.; Weinfeld, M.; West, F. G.; Tuszynski, J. A. Computer-aided drug design of small molecule inhibitors of the ERCC1-XPF protein–protein interaction. *Chemical Biology & Drug Design* **2020**, *95*, 460-471.
11. Arora, S.; Heyza, J.; Zhang, H.; Kalman-Maltese, V.; Tillison, K.; Floyd, A. M.; Chalfin, E. M.; Bepler, G.; Patrick, S. M. Identification of small molecule inhibitors of ERCC1-XPF that inhibit DNA repair and potentiate cisplatin efficacy in cancer cells. *Oncotarget* **2016**, *7*, 75104-75117.
12. Mendoza, J.; Martínez, J.; Hernández, C.; Pérez-Montiel, D.; Castro, C.; Fabián-Morales, E.; Santibáñez, M.; González-Barrios, R.; Díaz-Chávez, J.; Andonegui, M. A. Association between ERCC1 and XPA expression and polymorphisms and the response to cisplatin in testicular germ cell tumours. *British Journal of Cancer* **2013**, *109*, 68-75.
13. Gentile, F.; Tuszynski, J. A.; Barakat, K. H. New design of nucleotide excision repair (NER) inhibitors for combination cancer therapy. *Journal of Molecular Graphics and Modelling* **2016**, *65*, 71-82.

14. Barakat, K. H.; Jordheim, L. P.; Perez-Pineiro, R.; Wishart, D.; Dumontet, C.; Tuszynski, J. A. Virtual screening and biological evaluation of inhibitors targeting the XPA-ERCC1 interaction. *PloS One* **2012**, *7*.
15. Chapman, T. M.; Wallace, C.; Gillen, K. J.; Bakrania, P.; Khurana, P.; Coombs, P. J.; Fox, S.; Bureau, E. A.; Brownlees, J.; Melton, D. W. N-Hydroxyimides and hydroxypyrimidinones as inhibitors of the DNA repair complex ERCC1–XPF. *Bioorganic & Medicinal Chemistry Letters* **2015**, *25*, 4104-4108.
16. Chapman, T. M.; Gillen, K. J.; Wallace, C.; Lee, M. T.; Bakrania, P.; Khurana, P.; Coombs, P. J.; Stennett, L.; Fox, S.; Bureau, E. A. Catechols and 3-hydroxypyridones as inhibitors of the DNA repair complex ERCC1-XPF. *Bioorganic & Medicinal Chemistry Letters* **2015**, *25*, 4097-4103.
17. McNeil, E. M.; Astell, K. R.; Ritchie, A.-M.; Shave, S.; Houston, D. R.; Bakrania, P.; Jones, H. M.; Khurana, P.; Wallace, C.; Chapman, T. Inhibition of the ERCC1–XPF structure-specific endonuclease to overcome cancer chemoresistance. *DNA Repair* **2015**, *31*, 19-28.
18. Gentile, F.; Barakat, K. H.; Tuszynski, J. A. Computational characterization of small molecules binding to the human XPF active site and virtual screening to identify potential new DNA repair inhibitors targeting the ERCC1-XPF endonuclease. *International Journal of Molecular Sciences* **2018**, *19*, 1328-1341.
19. Jordheim, L. P.; Barakat, K. H.; Heinrich-Balard, L.; Matera, E.-L.; Cros-Perrial, E.; Bouledrak, K.; El Sabeh, R.; Perez-Pineiro, R.; Wishart, D. S.; Cohen, R. Small molecule inhibitors of ERCC1-XPF protein-protein interaction synergize alkylating agents in cancer cells. *Molecular Pharmacology* **2013**, *84*, 12-24.
20. Elmenoufy, A. H.; Gentile, F.; Jay, D.; Karimi-Busheri, F.; Yang, X.; Soueidan, O. M.; Weilbeer, C.; Mani, R. S.; Barakat, K. H.; Tuszynski, J. A.; Weinfeld, M.; West, F. G. Targeting DNA Repair in Tumor Cells via Inhibition of ERCC1–XPF. *Journal of Medicinal Chemistry* **2019**, *62*, 7684-7696.
21. de Laat, W. L.; Sijbers, A. M.; Odijk, H.; Jaspers, N. G. J.; Hoeijmakers, J. H. J. Mapping of interaction domains between human repair proteins ERCC1 and XPF. *Nucleic Acids Research* **1998**, *26*, 4146-4152.
22. Sijbers, A. M.; van der Spek, P. J.; Odijk, H.; van den Berg, J.; van Duin, M.; Westerveld, A.; Jaspers, N. G. J.; Bootsma, D.; Hoeijmakers, J. H. J. Mutational analysis of the human nucleotide excision repair gene ERCC1. *Nucleic Acids Research* **1996**, *24*, 3370-3380.
23. Tripsianes, K.; Folkers, G.; Eiso, A. B.; Das, D.; Odijk, H.; Jaspers, N. G. J.; Hoeijmakers, J. H. J.; Kaptein, R.; Boelens, R. The structure of the human ERCC1/XPF interaction domains reveals a complementary role for the two proteins in nucleotide excision repair. *Structure* **2005**, *13*, 1849-1858.

24. Anandakrishnan, R.; Aguilar, B.; Onufriev, A. V. H++ 3.0: automating p K prediction and the preparation of biomolecular structures for atomistic molecular modeling and simulations. *Nucleic Acids Research* **2012**, *40*, W537-W541.
25. Case, D. A.; Babin, V.; Berryman, J.; Betz, R. M.; Cai, Q.; Cerutti, D. S.; Cheatham Iii, T. E.; Darden, T. A.; Duke, R. E.; Gohlke, H. AMBER 14, 2014. *University of California, San Francisco* **2014**.
26. Maier, J. A.; Martinez, C.; Kasavajhala, K.; Wickstrom, L.; Hauser, K. E.; Simmerling, C. ff14SB: improving the accuracy of protein side chain and backbone parameters from ff99SB. *Journal of Chemical Theory and Computation* **2015**, *11*, 3696-3713.
27. Li, P.; Roberts, B. P.; Chakravorty, D. K.; Merz Jr, K. M. Rational design of particle mesh Ewald compatible Lennard-Jones parameters for 2 metal cations in explicit solvent. *Journal of Chemical Theory and Computation* **2013**, *9*, 2733-2748.
28. Li, P.; Song, L. F.; Merz Jr, K. M. Systematic parameterization of monovalent ions employing the nonbonded model. *Journal of Chemical Theory and Computation* **2015**, *11*, 1645-1657.
29. Wang, J.; Wolf, R. M.; Caldwell, J. W.; Kollman, P. A.; Case, D. A. Development and testing of a general amber force field. *Journal of Computational Chemistry* **2004**, *25*, 1157-1174.
30. Jakalian, A.; Jack, D. B.; Bayly, C. I. Fast, efficient generation of high-quality atomic charges. AM1-BCC model: II. Parameterization and validation. *Journal of Computational Chemistry* **2002**, *23*, 1623-1641.
31. Jorgensen, W. L.; Chandrasekhar, J.; Madura, J. D.; Impey, R. W.; Klein, M. L. Comparison of simple potential functions for simulating liquid water. *The Journal of Chemical Physics* **1983**, *79*, 926-935.
32. Salomon-Ferrer, R.; Götz, A. W.; Poole, D.; Le Grand, S.; Walker, R. C. Routine microsecond molecular dynamics simulations with AMBER on GPUs. 2. Explicit solvent particle mesh Ewald. *Journal of Chemical Theory and Computation* **2013**, *9*, 3878-3888.
33. Kabsch, W.; Sander, C. Dictionary of protein secondary structure: pattern recognition of hydrogen-bonded and geometrical features. *Biopolymers: Original Research on Biomolecules* **1983**, *22*, 2577-2637.
34. Lin, A. Overview of Pharmacophore Applications in MOE. In **2004**.
35. Inc., C. C. G. Molecular Operating Environment (MOE). *Chemical Computing Group Inc., Canada website: <http://www.chemcomp.com>* **2015**.
36. Groom, C. R.; Bruno, I. J.; Lightfoot, M. P.; Ward, S. C. The Cambridge structural database. *Acta Crystallographica Section B: Structural Science, Crystal Engineering and Materials* **2016**, *72*, 171-179.
37. Sterling, T.; Irwin, J. J. ZINC 15–ligand discovery for everyone. *Journal of Chemical Information and Modeling* **2015**, *55*, 2324-2337.

38. Labute, P. The generalized Born/volume integral implicit solvent model: estimation of the free energy of hydration using London dispersion instead of atomic surface area. *Journal of Computational Chemistry* **2008**, *29*, 1693-1698.
39. Wildman, S. A.; Crippen, G. M. Prediction of physicochemical parameters by atomic contributions. *Journal of Chemical Information and Computer Sciences* **1999**, *39*, 868-873.
40. Onufriev, A.; Bashford, D.; Case, D. A. Exploring protein native states and large-scale conformational changes with a modified generalized born model. *Proteins: Structure, Function, and Bioinformatics* **2004**, *55*, 383-394.
41. Miller III, B. R.; McGee Jr, T. D.; Swails, J. M.; Homeyer, N.; Gohlke, H.; Roitberg, A. E. MMPBSA.py: an efficient program for end-state free energy calculations. *Journal of Chemical Theory and Computation* **2012**, *8*, 3314-3321.
42. Genheden, S.; Ryde, U. The MM/PBSA and MM/GBSA methods to estimate ligand-binding affinities. *Expert Opinion on Drug Discovery* **2015**, *10*, 449-461.
43. Weiser, J.; Shenkin, P. S.; Still, W. C. Approximate atomic surfaces from linear combinations of pairwise overlaps (LCPO). *Journal of Computational Chemistry* **1999**, *20*, 217-230.
44. Kassem, S.; Ahmed, M.; El-Sheikh, S.; Barakat, K. H. Entropy in bimolecular simulations: A comprehensive review of atomic fluctuations-based methods. *Journal of Molecular Graphics and Modelling* **2015**, *62*, 105-117.
45. Carlson, W. W.; Cretcher, L. H. The Hydroxyethyl Analog of Quinacrine. *Journal of the American Chemical Society* **1948**, *70*, 597-599.
46. Sriram, D.; Devakaram, R. V.; Dinakaran, M.; Yogeewari, P. Aromatic amino analogues of artemisinin: synthesis and in vivo antimalarial activity. *Medicinal Chemistry Research* **2010**, *19*, 524-532.
47. Bowles, M.; Lally, J.; Fadden, A. J.; Mouilleron, S.; Hammonds, T.; McDonald, N. Q. Fluorescence-based incision assay for human XPF-ERCC1 activity identifies important elements of DNA junction recognition. *Nucleic Acids Research* **2012**, *40*, e101-e101.

## **Chapter 4**

### **Design, Synthesis and *In vitro* Cell-free/Cell-based**

### **Biological Evaluations of Novel ERCC1–XPF**

### **Inhibitors Targeting DNA Repair Pathway**

#### **4.1 Introduction**

The ERCC1–XPF heterodimer is a highly conserved structure-specific endonuclease that plays a central function in various DNA repair pathways, including interstrand crosslink (ICL) repair, double-strand break (DSB) repair, and nucleotide excision repair.<sup>1-3</sup> As such, it has a pivotal role in the response of various cancers to a wide array of DNA-damaging chemotherapeutics, such as platinum-containing compounds, cyclophosphamide, and mitomycin C (MMC).<sup>4, 5</sup> The enzyme also has the important role of removing bulky adducts and helix-distorting DNA lesions, such as UV-induced pyrimidine-(6,4)-pyrimidone photoproducts (6-4PPs) and cyclobutane pyrimidine dimers, CPDs.<sup>6</sup> A recent study revealed that 72% of patients with colorectal cancer exhibited high expression levels of ERCC1 protein,<sup>7</sup> raising the potential importance of developing inhibitors of ERCC1–XPF that could increase the sensitivity of cancer cells towards conventional cancer therapeutics, which would impact the survival rate of cancer patients in the clinic positively. Thanks to the availability of molecular structures of ERCC1–XPF and the multiple sites that could be targeted by small molecules to inhibit the endonuclease activity,<sup>8</sup> the enzyme complex has become an attractive target for drug design studies.

In the ERCC1–XPF heterodimer, the ERCC1 is catalytically inactive but regulates DNA–protein and protein–protein interactions, whereas XPF possesses the endonuclease active site as well as an inactive helicase-like motif and is involved in additional protein–protein interactions and DNA binding.<sup>9</sup> However, enzymatic activity requires the dimerization of the two proteins because neither protein alone is stable, and both are degraded rapidly.<sup>8,10,11</sup> Dimerization between ERCC1 and XPF is mediated by the interaction of their double helix–hairpin–helix (HhH2) motifs in their C-terminal domains. As a result, small molecule inhibitors that can disrupt the interaction domains linking XPF and ERCC1 would be expected to sensitize cancer cells to conventional DNA crosslinking chemotherapeutic treatments and radiotherapy.

The availability of several experimental structures of the dimerized HhH2 domains (for example, PDB code 2A1J and 1Z00) allows rational drug design studies to be employed to develop small molecules that disrupt the heterodimerization interface. Our initial drug design studies, which focused on the XPA active site<sup>12</sup> and the XPA–ERCC1 interaction site,<sup>13</sup> validated the use of computer-aided drug design approaches to develop and optimize DNA repair inhibitors;<sup>14</sup> however, due to the contribution of ERCC1–XPF interaction in many DNA repair pathways, targeting the dimerization interface is regarded as more promising.<sup>9</sup>

Several studies have been carried out recently to develop ERCC1–XPF inhibitors. Yang et al.<sup>15</sup> proposed a cellular delivery approach of therapeutic peptides that mimic the ERCC1 HhH2 domain (residues 220–297) as a potential alternative strategy to inhibit the NER pathway and potentiate DNA-damaging agents to cancer cells. However, the translation of this modality into the clinic is challenging in terms of

the cost and applicability. Arora et al.<sup>16</sup> and Chapman et al.<sup>17, 18</sup> have identified and optimized various small molecules targeting the XPF endonuclease active site. Their results revealed that some of the endonuclease inhibitors, with IC<sub>50</sub> in the nanomolar range, were capable of diminishing NER activity and enhancing the cytotoxicity of platinum-containing drugs in cancer cells. However, specific inhibition of the XPF endonuclease through metal ion chelation with inhibitors is challenging due to the similarities among various endonuclease active sites that could lead to off-target interactions from these inhibitors; thus, the development of this series will be limited due to the lack of structural insights of the compound–protein complexes.<sup>9</sup> McNeil et al. conducted an *in silico* screening approach that targeted only three different sites on the XPF HhH2 domain with the aim of identifying potential inhibitors that could stably bind to it and hinder the interaction between ERCC1 and XPF domains but also disrupt the XPF endonuclease domain.<sup>19</sup> They demonstrated that one of their compounds that had the ability of binding to the XPF domain *in vitro* also was able to inhibit the NER pathway in melanoma cells and sensitize them to cisplatin. However, the reported *K<sub>d</sub>* and IC<sub>50</sub> values for this compound, in the medium to high micromolar range, were suboptimal. Jordheim et al.<sup>20</sup> developed small molecule ERCC1–XPF inhibitors acting through the XPF interaction domain, which led to heterodimerization disruption *in vitro*. They also reported that **1** (also called NSC-130813 or NERI02) sensitized cancer cells to cisplatin and MMC. This affirmed that enhancing the cytotoxicity of cross-linking agents, such as cisplatin, could be achieved via targeting ERCC1–XPF protein–protein interaction. However, the clinical properties of **1** were suboptimal in terms of toxicity

and potency, and a derivatization strategy, suggested by Jordheim et al.,<sup>20</sup> was required to optimize the compound.

Most of the previous efforts to develop ERCC1–XPF inhibitors were tested using a truncated form of the heterodimer and not the full-length protein.<sup>17-19, 21</sup> It has been shown that the truncated form of ERCC1–XPF is ~15-fold less active than the full length ERCC1–XPF protein under standard reaction conditions.<sup>9, 10</sup> Using **1** as a reference hit, we employed computer-aided drug design techniques, such as electrostatic mapping of the compound **1** binding pocket, pharmacophore modeling, molecular docking, and molecular dynamics (MD)- based rescoring, to rank compound **1** analogues based on their predicted binding affinities to the XPF domain.<sup>22</sup>

Interestingly, one of the derivatives that has good physiochemical properties showed significant inhibition of the removal of CPDs in UV-irradiated cells and increased capacity to sensitize colorectal cancer cells to UV radiation and cyclophosphamide relative to the initial hit.<sup>22</sup> More recently, our group has conducted a study that followed a multi-step computational approach to investigate one of the potential sites of compound **1** and propose potential candidates to be synthesized and tested *in vitro*.<sup>23</sup> The results of the previous study in Chapter 3 yielded one compound that showed an improved IC<sub>50</sub> value of 0.49 μM for the inhibition of ERCC1–XPF endonuclease activity compared to the IC<sub>50</sub> value of 1.86 μM for **1**. Having a potential lead compound and a solid computational approach, previously mentioned in Chapter 3, stimulated us to develop DNA repair inhibitors further. Therefore, in this study, we have conducted an extensive structure activity relationship analysis through synthesis

of different series of compounds based on modification of specific sites of **1** in comparison with **B9**.

All the compounds were synthesized and tested for their capability to inhibit the endonuclease activity of the full-length ERCC1–XPF *in vitro*. The top active compound was assessed further for its inhibition of repair of UV-induced thymidine dimers in human colorectal cancer cells as well as a sensitizing agent to UV irradiation and cyclophosphamide. Cyclophosphamide is being examined now as a part of chemotherapeutic combination for colorectal cancer.<sup>24,25</sup>

## 4.2 Results and Discussion

### 4.2.1 Chemistry

In Chapter 2, we synthesized the first generation (**Gen A**) of F06 (**1**) analogues based on the modification of the piperazine ring with solvent-exposed moieties, according to our reported computational studies.<sup>22</sup> In this chapter, we focused on further modifying two different sites of F06 (**1**), according to our suggested pharmacophore model, and extensively investigating their structure activity relationship (Figure 4.1).

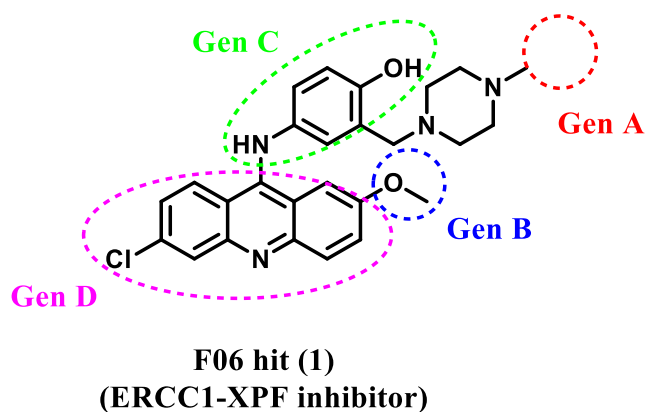


**Figure 4.1.** Structure of F06 (**1**) hit and the potential modification sites for hit to lead optimization.

For the third generation (**Gen C**), compounds were modified with different substituted anilines that are considered to be medicinally favorable, such as heterocyclic, gem dimethyl, aliphatic, and hydrophobic groups (Figure 4.2). Also, this series lacks the piperazine moiety to contrast their activity on ERCC1–XPF as compared to the second-generation analogues, which retain the piperazine group. General synthesis of **Gen C** compounds was carried out through nucleophilic aromatic substitution of **B2** and different substituted aniline derivatives, as seen in Scheme 4.1.

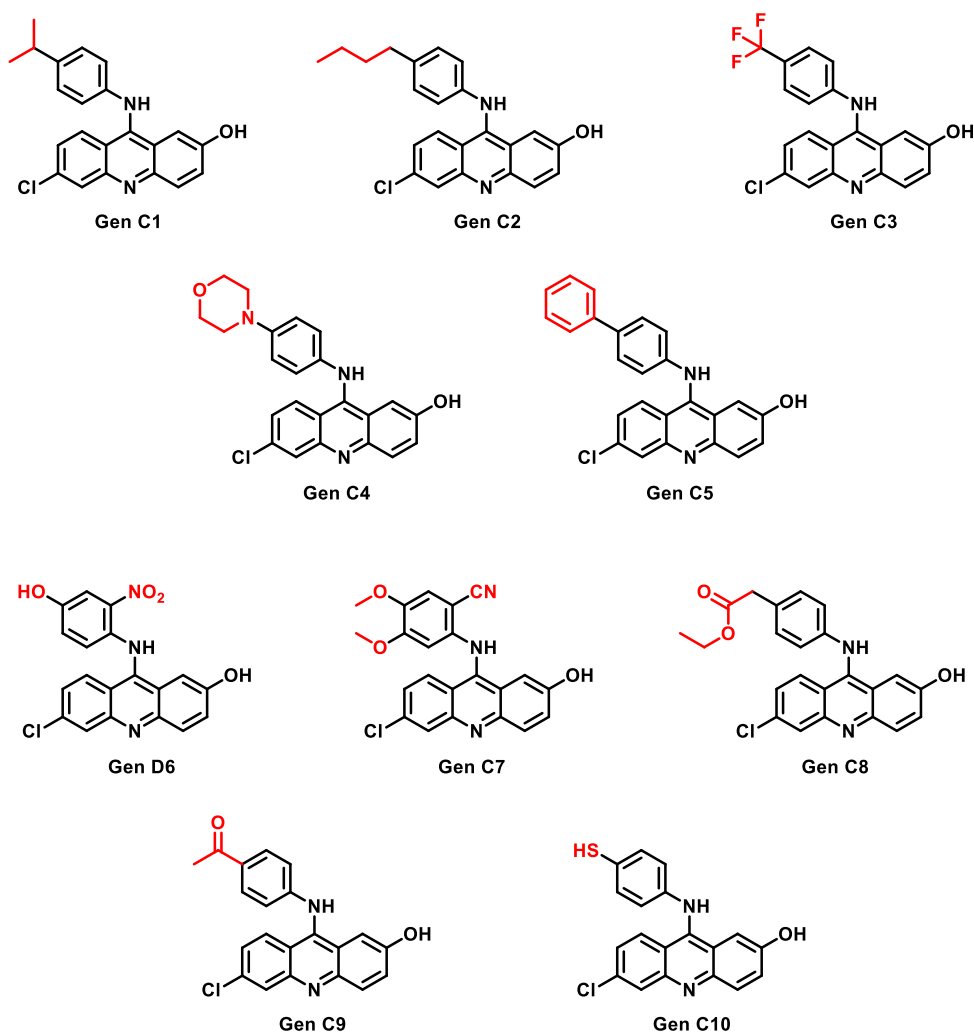
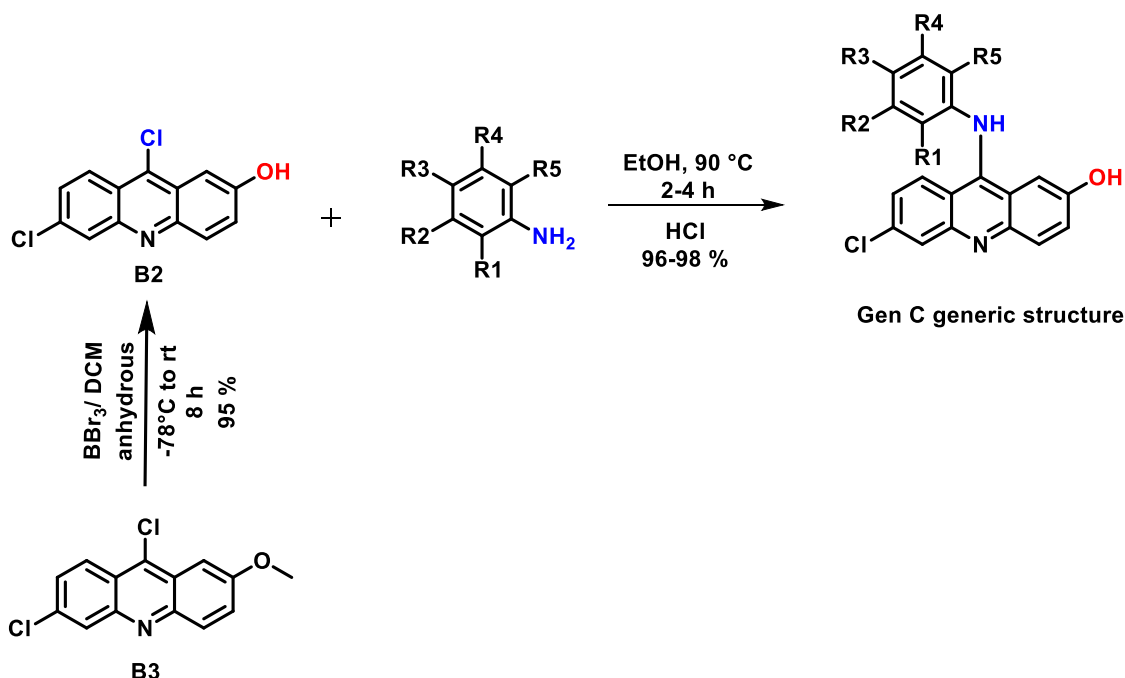


**Figure 4.2.** Chemical structures of **Gen C** analogues.



**Scheme 4.1.** General synthetic route for **Gen C** compounds.

Regarding **Gen D** compounds (Figure 4.3), their design was based on the modification of the acridine moiety, such as installing quinoline and phenyl groups to investigate the role of these functionalities on the activity of ERCC1–XPF compared to the hit compound. **D2** and **D3** were used as controls. **D2** was synthesized via nucleophilic aromatic substitution of **D1** (4-chloro-7-methoxyquinoline) and 4-aminophenol. **D1** and **D3** and were purchased from Sigma Aldrich Inc. in high purity. **D4** and **D5** and were synthesized with the same experimental procedure of **B9**, except for the last S<sub>N</sub>Ar step that occurred between the top aniline intermediate of **B9** and **D1** or **D1** in TFA solvent to yield **D4** and **D5**, respectively.

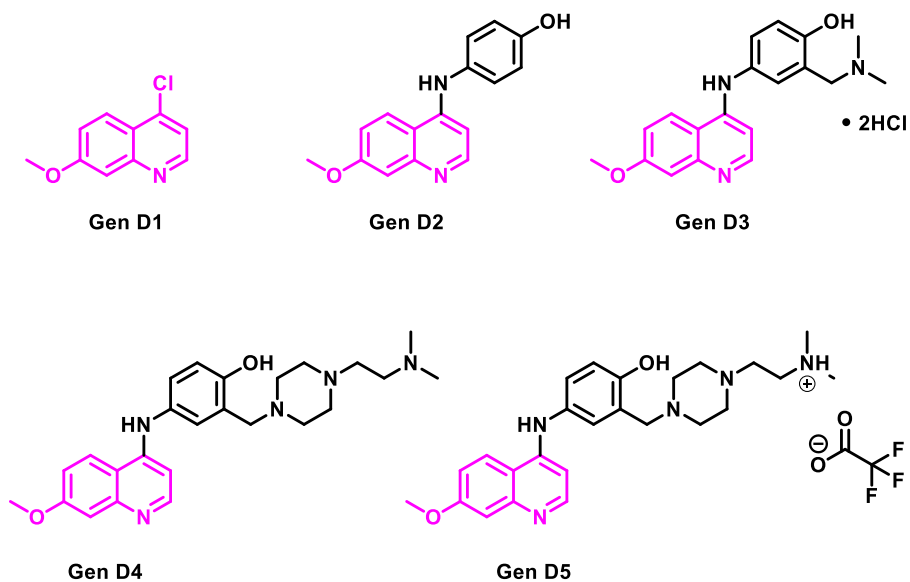


**Figure 4.3.** Chemical structures of **Gen D** analogues.

## 4.2.2 Inhibition of ERCC1–XPF Endonuclease Activity

We previously<sup>22</sup> used an *in vitro* assay based on real-time fluorescence to evaluate the inhibitory effect of the synthesized derivatives on ERCC1–XPF endonuclease activity. This assay has been described in Chapter 2 and utilizes a stem–loop substrate (composed of a 10mer-duplex stem and a 20mer-oligo-dT single-strand loop), labeled on the 3'-terminus with the quencher dabcy1 and the 5'-terminus with 6-FAM.<sup>26</sup> Upon cleavage of the 10mer-duplex region by ERCC1–XPF, a product consisting of an 8-base 5'-labeled FAM fragment is released, which leads to an increase in the fluorescent signal.

### 4.2.2.1 Inhibitory Effect of Gen C Compounds on ERCC1–XPF Activity

The purpose for designing **Gen C** compounds was to study the aniline structure activity relationship without the piperazine moiety in order to simplify the structures but to retain the acridine with the phenolic group and compare their activity with the hit **F06 (1)** and

the best inhibitor from the B series of compounds, **B9**. Different aniline substituents were selected for their known favourable medicinal features.<sup>27</sup>

Unfortunately, the inhibitory effect of **Gen C** compounds on ERCC1–XPF activity decreased relative to either **B9** (structure is shown in Chapter 3, Figure 3.10) or **F06 (1)**, as depicted in Figure 4.4. However, **C7** showed modest inhibition of the endonuclease activity. These results support the idea that the presence of the piperazine ring is critical for maintaining inhibitory activity, regardless of the substitution on the aminophenol ring.

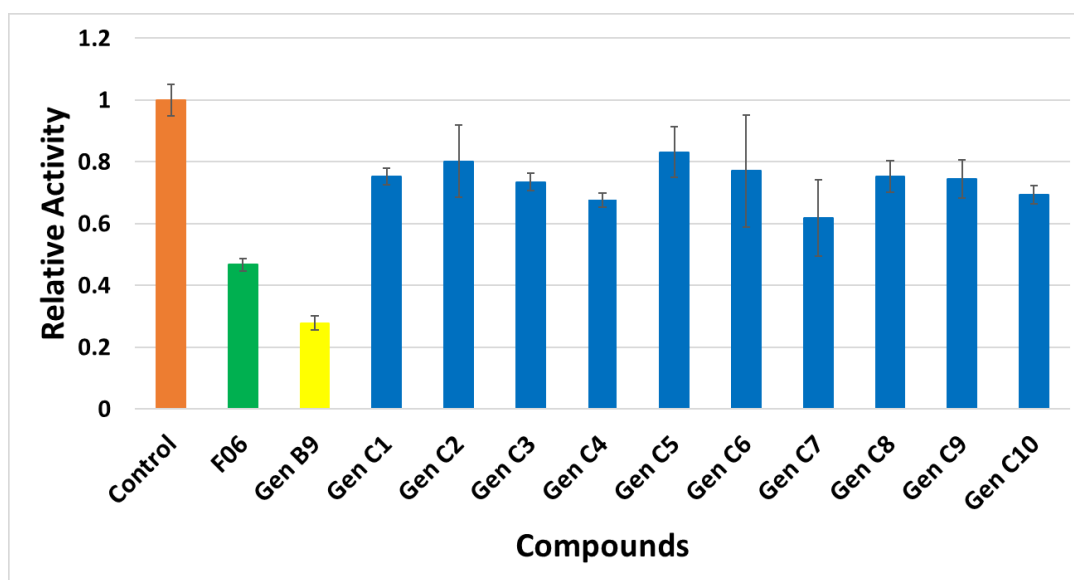


**Figure 4.4.** *In vitro* inhibition of ERCC1–XPF endonuclease activity by **Gen C** compounds (10  $\mu$ M each).

#### 4.2.2.2 Inhibitory Effect of Gen D Compounds on ERCC1-XPF Activity

Our previous computational studies of **F06 (1)** indicated that the planar aromatic rings of the acridine moiety buried in the XPF binding pocket engaged in  $\pi$ – $\pi$  interactions and contributed to the binding energy and ligand efficiency of **F06 (1)**.<sup>22, 23</sup> However,

this has not been investigated experimentally to determine whether reduced aromaticity would impact the inhibition of ERCC1–XPF. Therefore, we chose to replace the acridine moiety with a quinolone ring, which is a smaller unit that provides compounds much less likely to intercalate into the DNA substrate. As can be seen in Figure 4.5, **D1**, **D2**, and **D5** (the salt form of **D4** for enhanced solubility) failed to inhibit ERCC1–XPF.

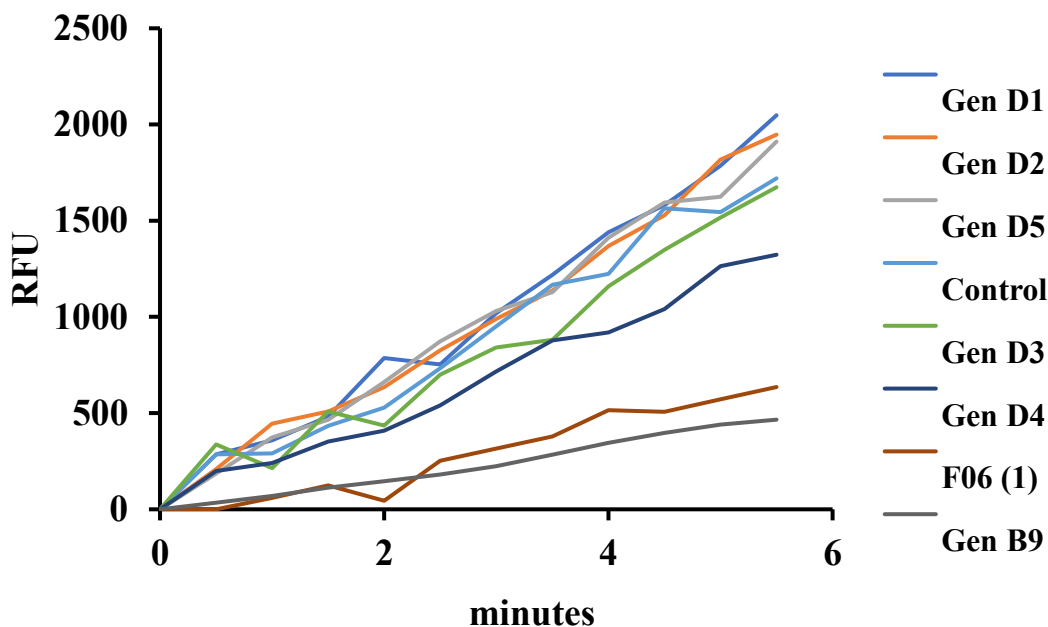


**Figure 4.5.** *In vitro* inhibition of ERCC1–XPF endonuclease activity by **Gen D** compounds (10  $\mu$ M each). The increase of fluorescence signal as a function of time.

Although **D3** and **D4** displayed modest inhibitory activity, it was less than **1** and **B9**, indicating the importance of retaining an extended aromatic feature as in acridine to maintain high inhibition. Interestingly, **D4** bears the same dimethylaminoethyl substituent on the piperazine ring as in **B9**, supporting its role in inhibiting ERCC1–XPF. Since **B9** displayed the most effective inhibition *in vitro* it was subjected to further analysis.

### 4.2.3 Gen B9 Binding to ERCC1–XPF

Intrinsic fluorescence spectroscopy (of the protein tryptophan residues) was utilized, as previously described,<sup>22</sup> to study the binding affinity of **B9** (active compound) and **B7** (inactive compound) (structure shown in Chapter 3, Figure 3.10) to ERCC1–XPF. Addition of 4  $\mu\text{M}$  **B7** had no significant effect on protein fluorescence (Figure 4.6A),

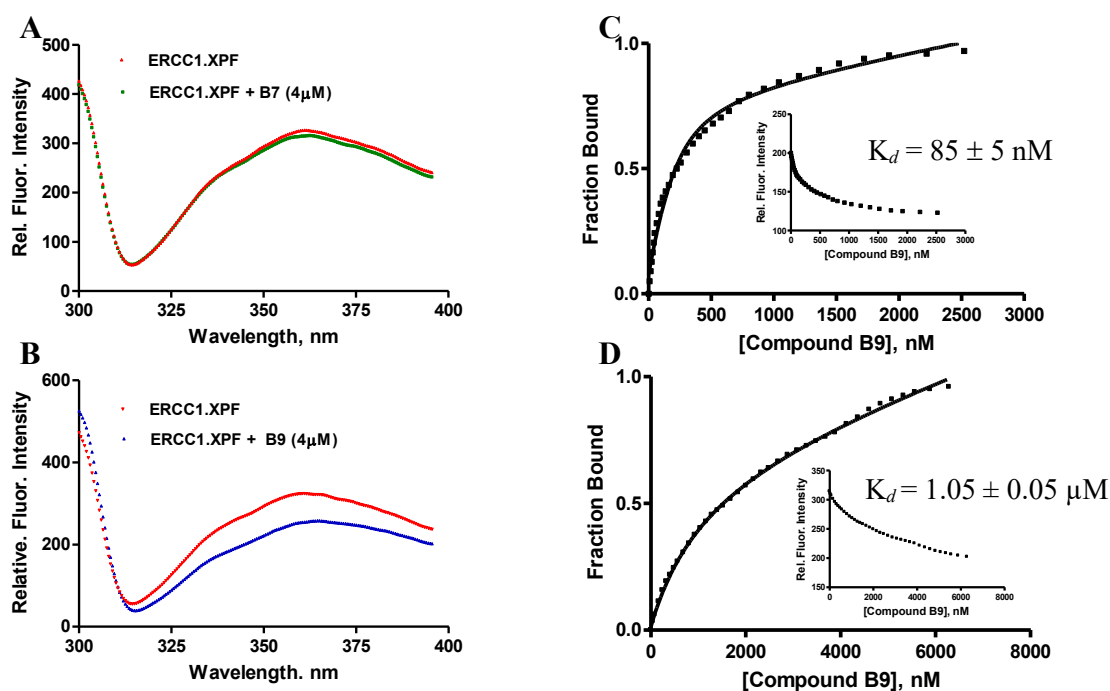


**Figure 4.6.** Determination of the affinity ( $K_d$ ) between ERCC1–XPF complex and **B9** (active inhibitor) and **B7** (negative control). Quenching of the intrinsic protein fluorescence of the tryptophan residues was used to monitor the interaction between the compounds and the protein. Fluorescence of ERCC1–XPF (50 nM) incubated with (A) **B7** (negative control) and (B) **B9** (active inhibitor). (C) Unimodal binding pattern and the binding affinity of **B9** with ERCC1–XPF (85 nM). The protein was excited at 295 nm, and the fluorescence intensity was monitored at 345 nm (see inset). The fraction bound (i.e., relative fluorescence intensity) versus ligand concentration is plotted. (D) Unimodal binding of **B9** to DNA substrate of the ERCC1–XPF protein. The stem–loop substrate (lacking the quenching group) of the ERCC1–XPF complex (100 nM) was excited at 490 nm and the intensity of fluorescence signal at 520 nm was monitored as a function of **B9** concentration. The binding affinity of **B9** to ERCC1–XPF substrate was  $1.05 \pm 0.05 \mu\text{M}$ , as shown in Table 4.1.

and the observed fluorescence quenching at 330 nm was less than 2%, thus providing no evidence of any interaction. In contrast, addition of **B9** (4  $\mu\text{M}$ ) induced nearly 25%  $\pm$  3% quenching of protein fluorescence at 330 nm, clearly indicating interaction of **B9** with the ERCC1–XPF complex, as depicted in Figure 4.6B. The binding affinity (in terms of dissociation constant,  $K_d$ ) of **B9** for ERCC1–XPF complex was determined by following fluorescence quenching (a measure of ligand binding) as a function of ligand concentration. A representative plot of relative fluorescence intensity versus the concentration of **B9** is shown in Figure 4.6C (inset). Nonlinear regression analysis (GraphPad Prism Software, San Diego, CA) of the binding data was carried out, as described in our earlier paper,<sup>28</sup> and revealed a unimodal binding with a  $K_d$  value of 85  $\pm$  5 nM (Table 4.1).

**Table 4.1.** The Half-maximum Inhibitory Concentrations ( $\text{IC}_{50}$ ) and Binding Constants Values of Inhibitors<sup>a</sup>.

Compound	$K_d$ protein (nM)	$K_d$ DNA (nM)	$\text{IC}_{50}$ ( $\mu\text{M}$ )
<b>F06 (1)</b>	140 $\pm$ 5	N.D.*	1.86 $\pm$ 0.25
<b>Gen B7</b>	N.D.	200 $\pm$ 10	N.D.
<b>Gen B9</b>	85 $\pm$ 5	1050 $\pm$ 50	0.49 $\pm$ 0.04

<sup>a</sup>The  $\text{IC}_{50}$  data was obtained from at least three different experiments of  $V_o$  versus compound concentration. \* Not determined.

All the **B** compounds, except **B4** (structure is shown in Chapter 3, Figure 3.10), share an acridine moiety that is known to bind nucleic acids as intercalators. To determine if the binding to the DNA substrate plays a major role in the inhibitory

activity of **B9**, we compared the interaction of **B9** and **B7** with the stem-loop substrate (lacking the dabcy1 quencher) by following the change in fluorescence with increasing concentration of inhibitor. We observed that **B9** has a binding affinity for the DNA stem-loop ( $K_d = 1.05 \pm 0.05 \mu\text{M}$ , Figure 4.6D) that is almost 12-fold lower than for ERCC1-XPF. This disparity in binding affinity values strongly suggests that inhibition by **B9** results from its interaction with ERCC1-XPF rather than with the DNA substrate. Regarding **B7** binding to the DNA stem-loop but is not an effective substrate, it showed a unimodal binding with a  $K_d$  value of  $200 \pm 10 \text{ nM}$  (Figure 4.7).

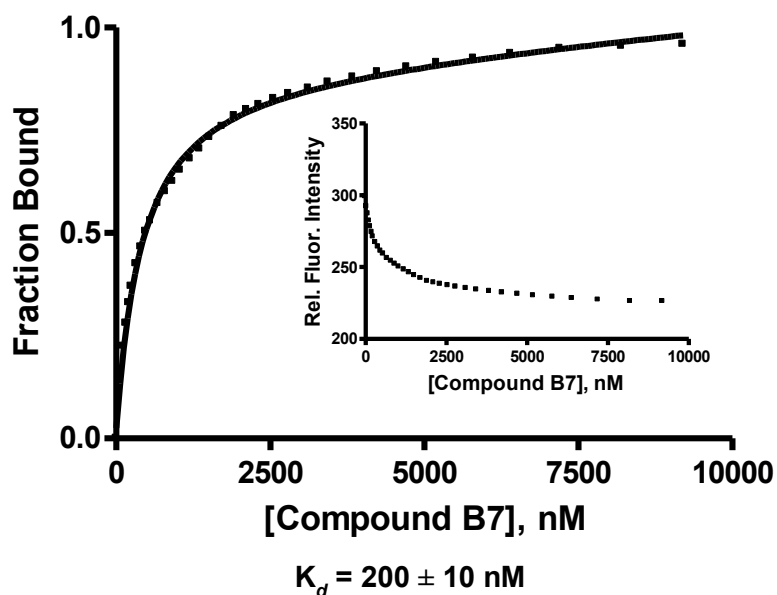


**Figure 4.7.** The binding affinity measurement of **B7** on the stem-loop DNA substrate.

This means that **B7** (negative control) binds more tightly to the DNA than **B9** but is not an inhibitor of ERCC1-XPF, although they share the same acridine moiety. This provides further support that inhibition is not a result of the compounds binding to DNA. In addition, as shown in Chapter 2 using microscale thermophoresis, another

compound with a similar structure to **B9** interacted with ERCC1–XPF in the subunit interaction domain.<sup>22</sup> This provides additional evidence that **B9** inhibition of ERCC1–XPF endonuclease activity is mediated by disruption of heterodimerization between ERCC1 and XPF.

#### 4.2.4 Inhibition of DNA Repair by B9

To test for inhibition of nucleotide excision repair, we monitored the cellular removal of UVC-induced cyclobutane pyrimidine dimers (CPDs) in HCT 116 cells over a 24 hour period using an immunochemical assay. The results (Fig. 4.8) show that **B9** significantly inhibited the removal of CPDs compared with control cells or cells treated with **B7**. Twenty-four hours after irradiation, the residual percentage of CPDs in the cells treated with **B7** was 35% compared to 16% in the untreated cells.

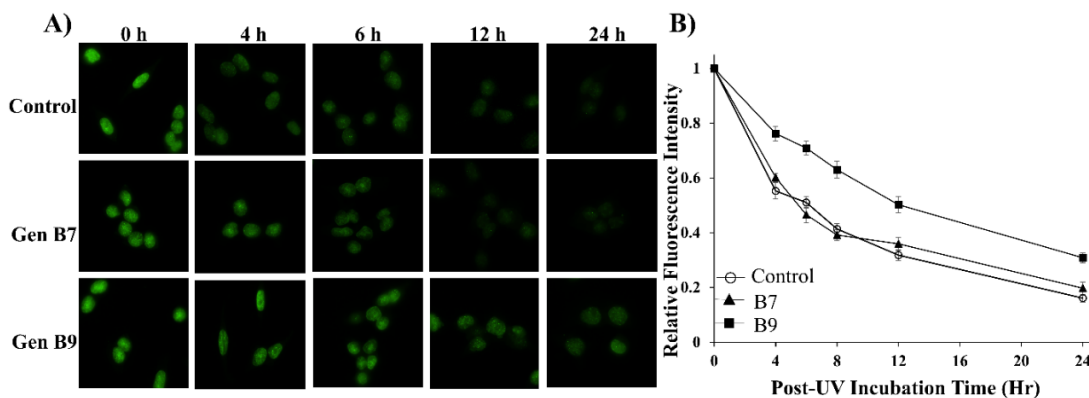


**Figure 4.8.** Inhibition of cellular NER by compound **B9**. (A) Immunofluorescence images of the UV-based assay for detecting CPDs in HCT-116 colorectal cancer cells treated with compounds **B9** (at 2  $\mu$ M) and compared it to negative control **B7** and the control. (B) Normalized fluorescence intensity of the treated cells ( $\pm$ SEM) based on quantitation of fluorescence from 100 randomly selected cells per treatment. Treated cells with active inhibitor **B9** were significantly different from the non-inhibitory negative control **B7** from 4 to 24 h post-irradiation ( $p < 0.005$ , Student's *t* test).

#### 4.2.5 Cytotoxicity Profile of Inhibitors

Crystal violet viability assays were carried out to assess the cellular toxicity of these compounds to HCT 116 cells and to choose relatively non-cytotoxic concentrations to be utilized further in sensitizing cells to UV radiation or cyclophosphamide. As can be seen in Figure 4.9, **B7** as a negative control is the least cytotoxic compound to HCT 116 cells. The cytotoxicity of the hit **F06 (1)** to the cells is more than **B9**, especially at concentrations  $\geq 5 \mu\text{M}$ . In the case of **F06 (1)**, about 35% of the cells survived after three days exposure of **F06 (1)** to a dose of  $5 \mu\text{M}$ , whereas approximately 95% of the HCT116 cells survived exposure to **B9** at the same dose. As a result, we selected  $2 \mu\text{M}$  as a maximum low-cytotoxic concentration for **F06 (1)**, while  $4 \mu\text{M}$  of **Gen B9** and **Gen B7** was chosen as a maximum concentration to be used in the following assay.

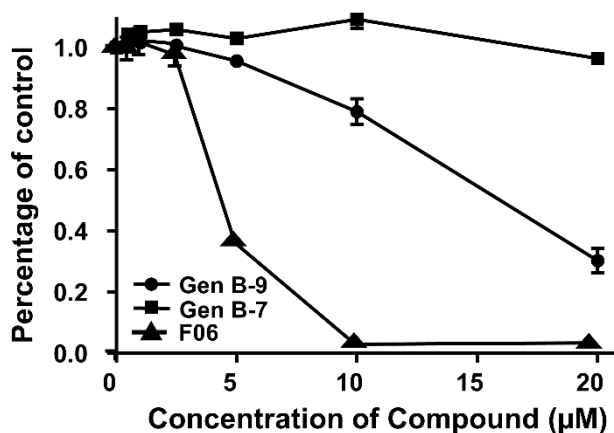


**Figure 4.9.** Crystal violet-based viability assay to assess the cytotoxicity profile of **B9** (active inhibitor), **B7** (negative control), and **F06 (1)** (hit).

#### 4.2.6 Increased Sensitization to UV Radiation and Cyclophosphamide

The effectiveness of **B9** to sensitize HCT 116 cells to UV radiation and cyclophosphamide was evaluated. As depicted in Fig. 4.10A, neither 2 nor 4  $\mu\text{M}$  **B7** (negative control) had a significant sensitisation effect on HCT 116 cells to UV radiation, which is consistent with the failure of **B7** to inhibit ERCC1–XPF endonuclease. In contrast, 2  $\mu\text{M}$  **F06 (1)** displayed a modest sensitization capacity with increasing dose (Figure 4.10B), while 2 and 4  $\mu\text{M}$  **B9** significantly reduced the survival of cells irradiated with UV (Figure 4.10C). We then measured the effect of **B9** on the survival of cells exposed to the DNA interstrand cross-linking agent cyclophosphamide. The survival curves shown in Figure 10D, indicate that **B9**, at a concentration of 2  $\mu\text{M}$ , significantly sensitized the HCT 116 cells to cyclophosphamide (starting at 50  $\mu\text{M}$ ), whereas there was no significant sensitization effect with **B7** (at a higher dose of 4  $\mu\text{M}$ ), which is in accordance with the UV survival data.

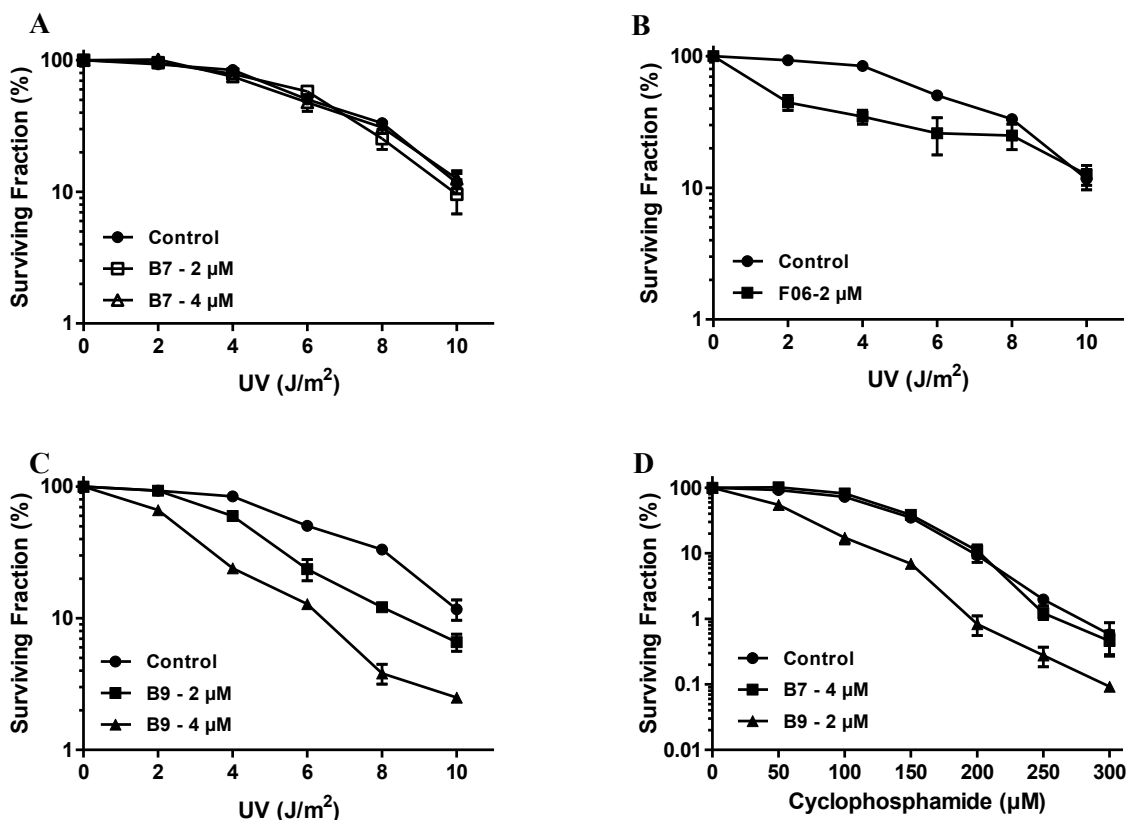


**Figure 4.10.** Sensitization of HCT 116 cells to UV and cyclophosphamide. A) Cellular survival upon exposure to increasing doses of 254 nm UV radiation and treated with 2 and 4 µM **B7**, B) 2 µM **F06 (1)**, and C) 2 and 4 µM **B9** determined by the clonogenic survival assay. D) HCT 116 cell survival following exposure to increasing doses of cyclophosphamide and treated with 4 and 2 µM of **B7** and **B9**, respectively, determined by the clonogenic survival assay. The cell survival curves ( $\pm$ SEM) are based on three independent sets of experiments. All the values related to cells treated with 2 µM **B9** were significantly different ( $p < 0.005$ , Student's test) from the values obtained with the control cells not treated with **B9**.

#### 4.2.7 Pharmacokinetic Properties (PK) of **B9** and **F06 (1)**

The results obtained from PK properties were compared to the parental compound **F06 (1)**<sup>22</sup> to determine if compound **B9** is pharmacokinetically superior to compound **F06 (1)**. **B9** showed a lower log D (2.01) than **F06 (1)** (3.86) at pH 7.4. Metabolism of **B9**, as measured by exposure to human liver microsomes, indicated that it has a moderate metabolism, while compound **F06 (1)** has a more rapid metabolism and high clearance

from the liver. Both compounds display an efflux ratio greater than 2 (**B9** = >43.39 and **F06 (1)** = 11.18).

#### **4.2.8 Cell Death by a Combination of Compound 4 (Gen A) or B9 with Chemotherapeutic Agents**

As can be seen clearly in Figure 4.11A, cisplatin alone induced A549 cell death with a rate of 50% or less at different concentrations. However, **B9** caused more than 80% of cell death when it was used in a combination with cisplatin. Also, the same effect was observed for **B9** when it is incubated with Mitomycin C (MMC) relative to the MMC alone. In HCT 116 cells (Figure 4.11B), using cisplatin alone at 50  $\mu$ M caused about 40% cell death only, while incubating **B9** with cisplatin at the same concentration induced more than 80% of HCT 116 cell death. On the other hand, a combination of **A4** and cisplatin or MMC did not cause a significant cell death relative to either cisplatin or MMC alone treated cells.

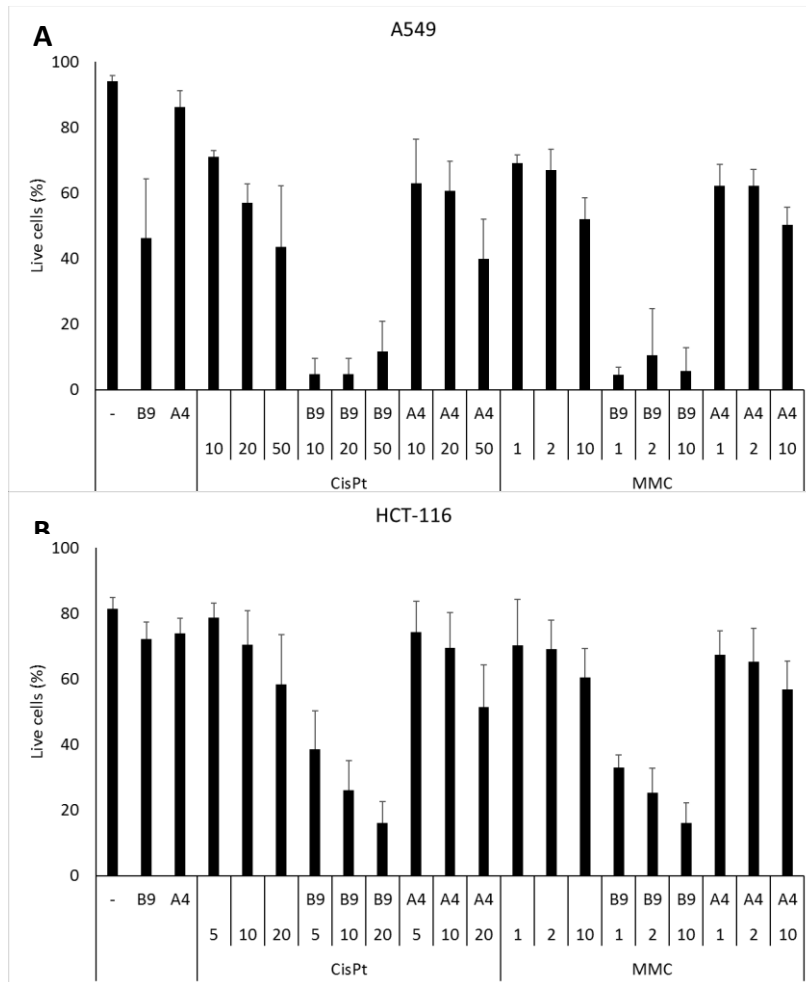


**Figure 4.11.** Survival of A549 (A) and HCT-116 (B) cells after exposure to alkylating agents and NER inhibitors alone or in combination. Cisplatin and MMC were used at indicated concentrations, an **B9** and **A4** at 1  $\mu$ M. Graphs show mean values of three independent experiments performed in duplicate, and error bars are standard deviations.

#### 4.2.9 Heterodimerization Inhibition of ERCC1–XPF by A4 and B9

To confirm the inhibition of ERCC1–XPF interaction in a cellular context, our collaborators, Dr. L P. Jordheim and G. Ciniero, performed a proximity ligation assay (Figure 4.12) in A549 cells incubated with **B9** or **A4** and/or cisplatin. As expected, cisplatin increased the mean interactions per cells. The addition of either **B9** or **A4** decreased the interaction between ERCC1 and XPF in the presence of cisplatin, showing that **B9** is a potent inhibitor of the ERCC1–XPF interaction in whole cells.

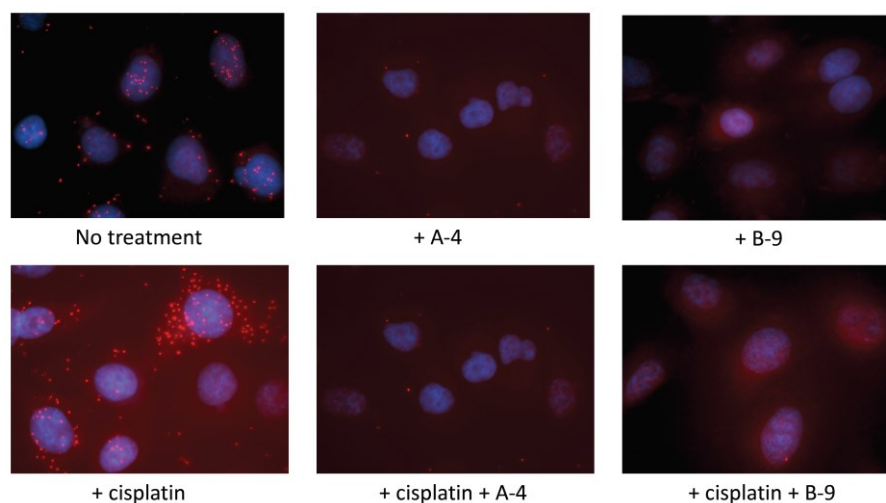


**Figure 4.12.** Interaction between endogenous ERCC1 and XPF revealed by a proximity ligation assay (red dots) in A549 cells incubated alone (NT) or in the presence of **A4** or **B9** (2  $\mu$ M) or cisplatin (20  $\mu$ M) for 24 h.

### 4.3 Conclusion

The ERCC1–XPF complex is a 5′–3′ structure-specific endonuclease that has a central role in different DNA repair pathways, especially NER and ICL. It is required to protect the integrity of the genome as well as to prevent damage-induced mutations by different insults; however, it hampers the efficacy of genotoxic cancer therapeutics, such as radiotherapy or chemotherapy based on platinum containing compounds. Therefore, inhibiting the mechanism of DNA repair in cancer cells by small molecules is a promising approach to potentiate the effect of such therapies.

In Chapter 3, we employed a computational drug design workflow to design novel compounds based on the hit **F06 (1)** rationally, resulting in a pharmacophore model that suggested further optimization to modulate the chemical space of different sites on **F06 (1)**. Herein, we further explored different modifications on the suggested sites on **F06 (1)**, which yielded three different series of compounds, and dissected their

structure activity relationships with regard to their ability to inhibit the ERCC1–XPF heterodimer and sensitize colorectal cancer cells to either UV radiation or cyclophosphamide.

All the designed compounds were synthesized via robust, facile, and reproducible methods. The inhibitory effects of all compounds on the full-length ERCC1–XPF protein activity were assessed *in vitro*. The results in Chapter 3 revealed that the *in vitro* ERCC1–XPF endonuclease assay identified **B9** as a potent inhibitor of the ERCC1–XPF nuclease activity with an  $IC_{50}$  value of  $0.49 \pm 0.04 \mu\text{M}$  compared to  $1.86 \pm 0.25 \mu\text{M}$  for **F06 (1)**. This result suggests that incorporating the piperazine ring with a polar side-chain on the exterior face of the piperazine and a large hydrophobic moiety (acridine) is important for optimized activity, which is in accord with the results of the effect of **Gen C** and **D** on the protein complex. However, installing a hydrogen bond donor group on the acridine, as in **B9**, increased the inhibitory effect by almost two-fold compared to having a hydrogen bond acceptor, such as the methoxy group in **F06 (1)**. The docking studies indicated that this resulted in additional hydrogen bond interaction with the side chain of the buried V859 residue the XPF binding pocket. The binding constant for **B9** was measured experimentally as 85 nM, which has a higher affinity for ERCC1–XPF relative to **F06 (1)** with a  $K_d$  value of 140 nM. The fact that **Gen B7** (negative control) and **B9** show disparity in their activity and binding profiles on ERCC1–XPF, despite having the same acridine moiety, also provides strong evidence that the protein complex inhibition is not mediated through DNA intercalation. **B9** elicited inhibition of CPDs removal upon UV irradiation and sensitized the HCT 116 cells to cyclophosphamide- and UV-induced cytotoxicity, indicating inhibition of

ICL and NER. Furthermore, comparison of the partial pharmacokinetics screening results of **B9** and **F06 (1)** indicates that our lead second generation compound, **B9**, has more favorable qualities than the **F06 (1)**, by showing a moderate clearance from the liver, a better permeability, and a lower log D, which means that it has a lower lipophilicity and greater metabolic stability. In addition, **B9** showed a significant synergistic effect when used with cisplatin, which caused an 80% cell death relative to the effect of cisplatin alone. Furthermore, the **B9** inhibitory activity is attributed to the heterodimerization disruption of ERCC1–XPF on a cellular level.

Having shown that hydrogen bond donor group installation on the acridine moiety clearly enhances the activity, we intend to explore a wider range of polar hydrogen bond donor groups to be installed on the hydrophobic acridine structure and contrast their ERCC1–XPF inhibitory activity with our best lead compound, **B9**. In summary, the analysis of the conducted comprehensive SAR studies identified **B9**, which can be combined with other existing DNA-damaging therapies to synergize their effects by sensitizing cancer cells.

## **4.4 Methods and Experimental Section\***

### **4.4.1 Synthesis of C and D Compounds**

Reactions were conducted in flame-dried glassware. Transfer of anhydrous reagents and solvents was done with cannula or oven-dried syringes. Chemicals were purchased from Sigma Aldrich Inc. and were used without further purification.

\* I was responsible for the synthesis and design of all compounds. F.G. carried out the computational studies of the compounds. D.J. expressed and purified ERCC1–XPF, employed the *in vitro* ERCC–XPF1 assay. F.K.B and Y.X. carried out cell culture, UV dimer repair assay, and clonogenic survival assay. R.M. conducted the binding affinity studies of the compounds. G.C conducted the synergy experiment and PLA assay.

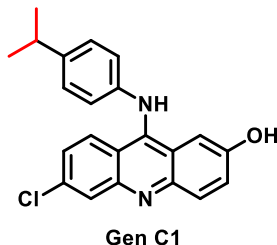
Thin layer chromatography (TLC) was performed on glass plates pre-coated with 0.25 mm silica gel. Flash chromatography columns were packed with 230-400 mesh silica gel. Proton nuclear magnetic resonance spectra ( $^1\text{H}$  NMR) were recorded at 500 MHz, and coupling constants (J) are reported in hertz (Hz). Standard notation was used to describe the multiplicity of signals observed in  $^1\text{H}$  NMR spectra: broad (br), multiplet (m), singlet (s), doublet (d), triplet (t), etc. Carbon nuclear magnetic resonance spectra ( $^{13}\text{C}$  NMR) were recorded at 125 MHz and are reported (ppm) relative to the center line of the triplet from chloroform-d (77.0 ppm) or the center line of the septet from methanol-d<sub>4</sub> (49.0 ppm). Infrared (IR) spectra were measured with a FT-IR 3000 spectrophotometer. Mass spectra were determined on a high-resolution electrospray positive ion mode spectrometer.

**4-((6-Chloro-2-methoxyacridin-9-yl)amino)-2-((4-methylpiperazin-1-yl)methyl)phenol (F06(1))**

The hit compound **F06 (1)** has been synthesized according to our previously reported procedures.<sup>22</sup>

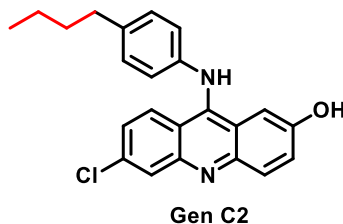
#### 4.4.1.1 Synthesis of Gen C Compounds

##### 6-chloro-9-((4-isopropylphenyl)amino)acridin-2-ol (C1)



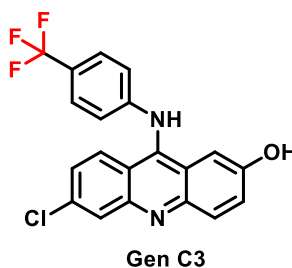
Synthesis of **C1** was performed by mixing 6,9-dichloro-hydroxyacridine **B2** (0.26 g, 1.0 mmol) and 4-isopropylaniline (0.14 g, 1.0 mmol) in 8 mL ethanol (95%), and 5 drops of 12 M HCl were added. Subsequently, the reaction mixture was heated at 90 °C under reflux for 12 h. Then, a reddish orange solid was formed after the reaction completion, which was monitored by TLC (0.5:9.5, MeOH:DCM). On cooling to room temperature, the solid precipitate was filtered, washed with cold ethanol 2–3 times, and dried overnight under high vacuum to afford **D1** as an orange reddish semisolid (0.24 g) in 67% yield;  $R_f$  0.40 (0.5:9.5, MeOH:DCM); mp 222–224 °C; IR (cast film)  $\nu_{\max}$  = 3100, 3032, 2960, 2925, 1628, 1582, 1512, 1266, 1162, 1086, 936, 829, 765  $\text{cm}^{-1}$ ;  $^1\text{H}$  NMR (500 MHz,  $\text{CD}_3\text{OD}$ )  $\delta$  8.03 (d,  $J$  = 9.4 Hz, 1H), 7.87 (d,  $J$  = 2.1 Hz, 1H), 7.83 (d,  $J$  = 9.2 Hz, 1H), 7.62 (dd,  $J$  = 9.2, 2.5 Hz, 1H), 7.50 (d,  $J$  = 2.5 Hz, 1H), 7.42 – 7.36 (m, 2H), 7.34 – 7.26 (m, 3H), 3.00 (hept,  $J$  = 6.9 Hz, 1H), 1.30 (d,  $J$  = 6.9 Hz, 6H). OH and NH protons were not observed;  $^{13}\text{C}$  NMR (125 MHz,  $\text{CD}_3\text{OD}$ )  $\delta$  156.21, 155.17, 150.24, 141.85, 141.34, 139.66, 136.50, 129.61, 129.23, 128.64 (2C), 125.58, 125.42 (2C), 121.95, 119.08, 117.47, 113.24, 107.60, 35.10, 24.32 (2C); HRMS (ESI) calcd for  $\text{C}_{22}\text{H}_{20}\text{ClN}_2\text{O}$   $[\text{M} + \text{H}]^+$  363.1259; found 363.1254. The purity of **C1** was 99.5 %, was determined by HPLC.

**6-chloro-9-((4-isopropylphenyl)amino)acridin-2-ol (C2)**



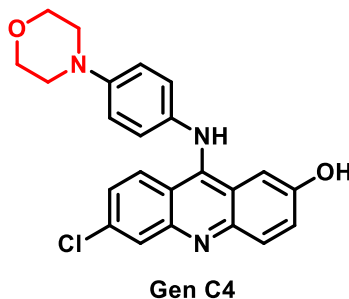
The previous method was employed to synthesize **C2** with the following stoichiometric amounts: 6,9-dichloro-hydroxyacridine **B2** (0.26 g, 1.0 mmol) and 4-butylaniline (0.15 g, 1.0 mmol) to afford **C2** as an orange reddish solid (0.27 g) in 72% yield;  $R_f$  0.50 (0.5:9.5, MeOH:DCM); mp 233–237 °C; IR (cast film)  $\nu_{\max}$  = 3084, 2954, 2928, 1628, 1581, 1510, 1266, 1162, 1085, 936, 832, 765  $\text{cm}^{-1}$ ;  $^1\text{H}$  NMR (700 MHz, DMSO- $d_6$ )  $\delta$  10.42 (s, 1H), 8.17 – 8.12 (m, 2H), 8.04 (d,  $J$  = 9.2 Hz, 1H), 7.69 (dd,  $J$  = 9.2, 2.5 Hz, 1H), 7.47 (d,  $J$  = 2.5 Hz, 1H), 7.40 (dd,  $J$  = 9.4, 2.1 Hz, 1H), 7.32 – 7.25 (m, 4H), 2.64 (t,  $J$  = 7.7 Hz, 2H), 1.63 – 1.56 (m, 2H), 1.33 (h,  $J$  = 7.4 Hz, 2H), 0.91 (t,  $J$  = 7.4 Hz, 3H). OH proton was not observed;  $^{13}\text{C}$  NMR (176 MHz, DMSO- $d_6$ )  $\delta$  154.1, 152.8, 141.3, 139.4, 138.6, 138.4, 134.8, 129.5 (2C), 128.2, 127.6, 123.9 (2C), 123.84, 120.91, 117.8, 115.9, 111.9, 106.7, 34.3, 32.9, 21.6, 13.7; HRMS (ESI) calcd for  $\text{C}_{23}\text{H}_{22}\text{ClN}_2\text{O}$   $[\text{M} + \text{H}]^+$  377.1415; found 377.1414. The purity of **D2** was 99.3%, was determined by HPLC.

### 6-chloro-9-((4-(trifluoromethyl)phenyl)amino)acridin-2-ol (C3)



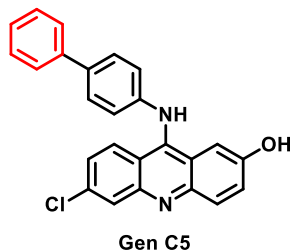
The previous method was employed to synthesize **C3** with the following stoichiometric amounts: 6,9-dichloro-hydroxyacridine **B2** (0.26 g, 1.0 mmol) and 4-(trifluoromethyl)aniline (0.16 g, 1.0 mmol) to afford **C3** as an orange reddish solid (0.29 g) in 74% yield;  $R_f$  0.45 (0.5:9.5, MeOH:DCM); mp 272–274 °C; IR (cast film)  $\nu_{\max}$  = 3086, 2926, 1629, 1583, 1518, 1434, 1325, 1267, 1165, 1119, 1068, 936, 837, 764  $\text{cm}^{-1}$ ;  $^1\text{H}$  NMR (700 MHz, DMSO- $d_6$ )  $\delta$  10.61 (s, 1H), 8.31 (d,  $J$  = 9.3 Hz, 1H), 8.27 (d,  $J$  = 2.1 Hz, 1H), 8.17 (d,  $J$  = 9.2 Hz, 1H), 7.73 (dd,  $J$  = 9.0, 2.8 Hz, 3H), 7.55 (dd,  $J$  = 9.3, 2.2 Hz, 1H), 7.42 (d,  $J$  = 8.2 Hz, 2H), 7.39 (d,  $J$  = 2.6 Hz, 1H). OH proton was not observed;  $^{13}\text{C}$  NMR (176 MHz, DMSO- $d_6$ )  $\delta$  154.8, 151.3, 145.7, 139.4, 138.7, 135.5, 129.2, 127.5, 126.6, 126.6 (q,  $J_{\text{C-F}}$  = 3.7 Hz), 126.6, 126.5, 125.2, 125.0, 123.5, 121.6, 118.5, 118.2, 114.7, 106.0; HRMS (ESI) calcd for  $\text{C}_{20}\text{H}_{13}\text{ClF}_3\text{N}_2\text{O}$   $[\text{M} + \text{H}]^+$  389.0663; found 389.0659. The purity of **C3** was 99.2 %, was determined by HPLC.

**6-chloro-9-((4-morpholinophenyl)amino)acridin-2-ol (C4)**



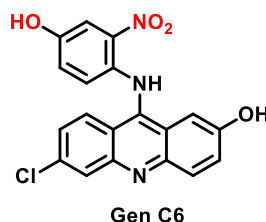
The previous method was employed to synthesize **C4** with the following stoichiometric amounts: 6,9-dichloro-hydroxyacridine **B2** (0.26 g, 1.0 mmol) and 4-morpholinoaniline (0.18 g, 1.0 mmol) to afford **C4** as a reddish brown solid (0.33 g) in 81% yield;  $R_f$  0.40 (0.5:9.5, MeOH:DCM); mp 281–285 °C; IR (cast film)  $\nu_{\max}$  = 3360, 3075, 2955, 1627, 1583, 1512, 1450, 1375, 1229, 1119, 1086, 935, 815, 762  $\text{cm}^{-1}$ ;  $^1\text{H}$  NMR (500 MHz,  $\text{CD}_3\text{OD}$ )  $\delta$  8.05 (d,  $J$  = 9.4 Hz, 1H), 7.83 (d,  $J$  = 2.1 Hz, 1H), 7.78 (d,  $J$  = 9.2 Hz, 1H), 7.59 (dd,  $J$  = 9.2, 2.5 Hz, 1H), 7.50 (d,  $J$  = 2.5 Hz, 1H), 7.34 – 7.22 (m, 3H), 7.11 – 7.05 (m, 2H), 3.88 – 3.82 (m, 4H), 3.27 – 3.20 (m, 4H). OH and NH protons were not observed;  $^{13}\text{C}$  NMR (126 MHz,  $\text{CD}_3\text{OD}$ )  $\delta$  155.9, 155.1, 152.4, 141.6, 141.3, 136.3, 133.0, 129.2, 128.6, 126.6 (2C), 125.3, 121.8, 118.9, 117.4 (2C), 117.0, 112.8, 107.70, 67.8 (2C), 50.9 (2C); HRMS (ESI) calcd for  $\text{C}_{23}\text{H}_{21}\text{ClN}_3\text{O}_2$   $[\text{M} + \text{H}]^+$  406.1317; found 406.1244. The purity of **C4** was 94.2 %, was determined by HPLC.

### 9-([1,1'-biphenyl]-4-ylamino)-6-chloroacridin-2-ol (**C5**)



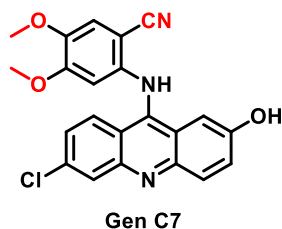
The previous method was employed to synthesize **C5** with the following stoichiometric amounts— 6,9-dichloro-hydroxyacridine **B2** (0.26 g, 1.0 mmol) and 4-aminobiphenyl (0.17 g, 1.0 mmol) to afford **C5** as a reddish orange solid (0.33 g) in 84% yield;  $R_f$  0.60 (0.5:9.5, MeOH:DCM); mp 269–272 °C; IR (cast film)  $\nu_{\max}$  = 3396, 3214, 2923, 1627, 1581, 1510, 1437, 1403, 1253, 1161, 1086, 1008, 936, 866, 763  $\text{cm}^{-1}$ ;  $^1\text{H}$  NMR (700 MHz, DMSO- $d_6$ )  $\delta$  10.48 (s, 1H), 8.26 (d,  $J$  = 9.4 Hz, 1H), 8.16 (d,  $J$  = 2.1 Hz, 1H), 8.07 (d,  $J$  = 9.2 Hz, 1H), 7.82 – 7.78 (m, 2H), 7.77 – 7.73 (m, 2H), 7.71 (dd,  $J$  = 9.2, 2.5 Hz, 1H), 7.55 (d,  $J$  = 2.5 Hz, 1H), 7.52 – 7.47 (m, 3H), 7.44 – 7.36 (m, 3H). OH proton was not observed;  $^{13}\text{C}$  NMR (176 MHz, DMSO- $d_6$ )  $\delta$  154.3, 152.8, 140.5, 139.5, 138.9, 138.7, 137.8, 135.2, 129.0 (2C), 128.5, 127.6 (2C), 127.6, 127.6, 126.4 (2C), 124.3 (2C), 123.6, 121.2, 118.1, 116.6, 112.8, 106.5; HRMS (ESI) calcd for  $\text{C}_{25}\text{H}_{18}\text{ClN}_2\text{O}$   $[\text{M} + \text{H}]^+$  397.1102; found 397.1089. The purity of **C5** was 99.2 %, determined by HPLC.

### 6-chloro-9-((4-hydroxy-2-nitrophenyl)amino)acridin-2-ol (C6)



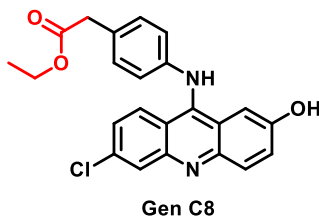
The previous method was employed to synthesize **C6** with the following stoichiometric amounts: 6,9-dichloro-hydroxyacridine **B2** (0.26 g, 1.0 mmol) and 4-amino-3-nitrophenol (0.16 g, 1.0 mmol) to afford **C6** as an orange reddish solid (0.26 g) in 68% yield;  $R_f$  0.40 (0.5:9.5, MeOH:DCM); mp 276–280 °C; IR (cast film)  $\nu_{\max}$  = 3107, 2956, 1628, 1584, 1532, 1443, 1345, 1242, 1164, 1086, 936, 814, 763  $\text{cm}^{-1}$ ;  $^1\text{H}$  NMR (500 MHz,  $\text{CD}_3\text{OD}$ )  $\delta$  8.08 (d,  $J$  = 9.4 Hz, 1H), 7.91 (d,  $J$  = 2.0 Hz, 1H), 7.85 (d,  $J$  = 9.2 Hz, 1H), 7.64 (dd,  $J$  = 9.2, 2.6 Hz, 2H), 7.43 (dd,  $J$  = 9.4, 2.2 Hz, 1H), 7.38 – 7.30 (m, 2H), 7.19 (dd,  $J$  = 8.7, 2.9 Hz, 1H). OH and NH protons were not observed;  $^{13}\text{C}$  NMR (126 MHz,  $\text{CD}_3\text{OD}$ )  $\delta$  159.4, 156.5, 145.9, 142.0, 141.1, 136.6, 130.2, 129.9, 127.7, 126.4, 123.3, 122.8, 122.2, 119.9, 119.3, 117.2, 113.3, 109.0, 106.9; HRMS (ESI) calcd for  $\text{C}_{19}\text{H}_{11}\text{ClN}_3\text{O}_4$   $[\text{M} - \text{H}]^-$  380.0444; found 380.0434. The purity of **C6** was 93.4 %, determined by HPLC.

**2-((6-chloro-2-hydroxyacridin-9-yl)amino)-4,5-dimethoxybenzotrile (C7)**



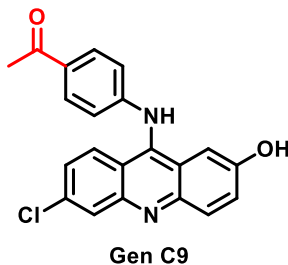
The previous method was employed to synthesize **C7** with the following stoichiometric amounts: 6,9-dichloro-hydroxyacridine **B2** (0.26 g, 1.0 mmol) and 2-amino-4,5-dimethoxybenzotrile (0.18 g, 1.0 mmol) to afford **C7** as an orange yellowish solid (0.33 g) in 82% yield;  $R_f$  0.45 (0.5:9.5, MeOH:DCM); mp 285–288 °C; IR (cast film)  $\nu_{\max}$  = 3541, 3131, 2851, 2777, 2225, 1626, 1584, 1555, 1467, 1355, 1269, 1165, 1083, 937, 857, 769  $\text{cm}^{-1}$ ;  $^1\text{H}$  NMR (500 MHz,  $\text{CD}_3\text{OD}$ )  $\delta$  8.11 (d,  $J$  = 9.4 Hz, 1H), 7.95 (d,  $J$  = 2.0 Hz, 1H), 7.89 (d,  $J$  = 9.2 Hz, 1H), 7.66 (dd,  $J$  = 9.2, 2.5 Hz, 1H), 7.47 (dd,  $J$  = 9.4, 2.1 Hz, 1H), 7.34 (d,  $J$  = 2.5 Hz, 2H), 7.25 (s, 1H), 3.93 (s, 3H), 3.90 (s, 3H). OH and NH protons were not observed;  $^{13}\text{C}$  NMR (126 MHz,  $\text{CD}_3\text{OD}$ )  $\delta$  156.6, 156.1, 155.0, 150.4, 142.1, 140.9, 139.3, 136.8, 130.2, 127.6, 126.6, 122.2, 119.3, 117.58, 117.36, 115.7, 113.8, 110.9, 106.8, 101.2, 57.1, 57.0; HRMS (ESI) calcd for  $\text{C}_{22}\text{H}_{15}\text{ClN}_3\text{O}_3$  [ $\text{M} - \text{H}$ ] $^-$  404.0807; found 404.0801. The purity of **C7** was 96.8%, determined by HPLC.

### Ethyl 2-(4-((6-chloro-2-hydroxyacridin-9-yl)amino)phenyl)acetate (**C8**)



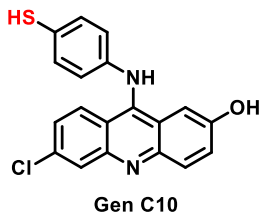
The previous method was employed to synthesize **C8** with the following stoichiometric amounts: 6,9-dichloro-hydroxyacridine **B2** (0.26 g, 1.0 mmol) and 4-aminophenylacetic acid (0.15 g, 1.0 mmol) to afford **C8** as a reddish orange solid (0.27 g) in 67% yield;  $R_f$  0.65 (0.5:9.5, MeOH:DCM); mp 274–277 °C; IR (cast film)  $\nu_{\max}$  = 3361, 3186, 2906, 1724, 1628, 1583, 1509, 1466, 1343, 1226, 1184, 1087, 1029, 936, 860, 760  $\text{cm}^{-1}$ ;  $^1\text{H}$  NMR (700 MHz,  $\text{DMSO-}d_6$ )  $\delta$  10.46 (s, 1H), 8.16 (dd,  $J$  = 5.8, 3.5 Hz, 2H), 8.06 (d,  $J$  = 9.2 Hz, 1H), 7.70 (dd,  $J$  = 9.2, 2.5 Hz, 1H), 7.50 (d,  $J$  = 2.5 Hz, 1H), 7.42 (dd,  $J$  = 9.4, 2.1 Hz, 1H), 7.38 – 7.35 (m, 2H), 7.33 – 7.27 (m, 2H), 4.10 (q,  $J$  = 7.1 Hz, 2H), 3.74 (s, 2H), 1.20 (t,  $J$  = 7.1 Hz, 3H). OH proton was not observed;  $^{13}\text{C}$  NMR (176 MHz,  $\text{DMSO-}d_6$ )  $\delta$  170.9, 154.2, 152.7, 139.7, 139.4, 138.6, 134.9, 132.9, 130.7 (2C), 128.4, 127.6 (2C), 124.0, 123.5, 121.0, 117.9, 116.3, 112.3, 106.58, 60.98, 40.0, 14.0; HRMS (ESI) calcd for  $\text{C}_{23}\text{H}_{18}\text{ClN}_2\text{O}_3$   $[\text{M} - \text{H}]^-$  405.1011; found 405.1009.

### 1-(4-((6-chloro-2-hydroxyacridin-9-yl)amino)phenyl)ethan-1-one (C9)



The previous method was employed to synthesize **C9** with the following stoichiometric amounts: 6,9-dichloro-hydroxyacridine **B2** (0.26 g, 1.0 mmol) and 4-aminoacetophenone (0.15 g, 1.0 mmol) to afford **C9** as a reddish orange solid (0.29 g) in 82% yield;  $R_f$  0.65 (0.5:9.5, MeOH:DCM); mp 295–296 °C; IR (cast film)  $\nu_{\max}$  = 3322, 3214, 2908, 1684, 1629, 1582, 1509, 1473, 1406, 1265, 1089, 1029, 937, 859, 761  $\text{cm}^{-1}$ ;  $^1\text{H}$  NMR (700 MHz, DMSO- $d_6$ )  $\delta$  10.60 (s, 1H), 8.30 – 8.24 (m, 2H), 8.16 (d,  $J$  = 9.2 Hz, 1H), 8.01 – 7.95 (m, 2H), 7.74 (dd,  $J$  = 9.2, 2.5 Hz, 1H), 7.57 (dd,  $J$  = 9.4, 2.1 Hz, 1H), 7.43 (d,  $J$  = 2.5 Hz, 1H), 7.36 – 7.31 (m, 2H), 2.57 (s, 3H). OH proton was not observed;  $^{13}\text{C}$  NMR (176 MHz, DMSO- $d_6$ )  $\delta$  196.5, 154.8, 151.1, 146.4, 139.6, 138.7, 136.1, 132.9, 129.9 (2C), 129.2, 127.5 (2C), 125.2, 122.0, 120.9, 118.7, 118.3, 114.8, 106.0, 26.5; HRMS (ESI) calcd for  $\text{C}_{21}\text{H}_{14}\text{ClN}_2\text{O}_2$   $[\text{M} - \text{H}]^-$  361.0749; found 361.0747. The purity of **C9** was 99.4%, determined by HPLC.

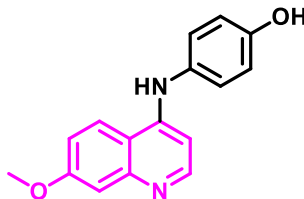
**6-chloro-9-((4-mercaptophenyl)amino)acridin-2-ol (C10)**



The previous method was employed to synthesize **C10** with the following stoichiometric amounts: 6,9-dichloro-hydroxyacridine **B2** (0.26 g, 1.0 mmol) and 4-aminothiophenol (0.13 g, 1.0 mmol) to afford **C10** as an orange brownish solid (0.26 g) in 75% yield;  $R_f$  0.55 (0.5:9.5, MeOH:DCM); mp 223–226 °C; IR (cast film)  $\nu_{\max}$  = 3309, 3131, 2851, 2777, 2225, 1622, 1581, 1461, 1395, 1262, 1165, 1081, 936, 857, 765  $\text{cm}^{-1}$ ;  $^1\text{H}$  NMR (500 MHz,  $\text{CD}_3\text{OD}$ )  $\delta$  8.21 (dd,  $J$  = 8.4, 1.3 Hz, 1H), 8.09 – 7.99 (m, 1H), 7.85 – 7.72 (m, 1H), 7.65 – 7.51 (m, 2H), 7.46 – 7.35 (m, 4H), 7.35 – 7.25 (m, 2H), 7.23 – 7.08 (m, 2H);  $^{13}\text{C}$  NMR (126 MHz,  $\text{CD}_3\text{OD}$ )  $\delta$  178.9, 154.1, 142.6, 140.4, 136.5, 131.2, 129.8, 129.2, 128.3, 126.0, 123.1, 122.6, 121.8, 119.8, 119.2, 118.9, 117.3, 117.3, 109.2; HRMS (ESI) calcd for  $\text{C}_{19}\text{H}_{14}\text{ClN}_2\text{OS}$   $[\text{M} + \text{H}]^+$  353.0510; found 353.0505.

#### 4.4.1.2 Synthesis of Gen D Compounds

##### 4-((7-methoxyquinolin-4-yl)amino)phenol (**D2**)



Gen **D2**

Synthesis of **D2** was carried out by the same protocol used for **C1** with minor modification. The synthesis was performed by mixing 4-hydroxyaniline (0.11 g, 1.0 mmol) and the commercially available 4-chloro-7-methoxyquinoline, **D1**, (0.19 g, 1.0 mmol) in 11 mL ethanol (95%), and 5 drops of 12 M HCl were added. Subsequently, the reaction mixture was heated at 90 °C under reflux for 12 h. Then, a yellowish solid was formed after the reaction completion, which was monitored by TLC (0.5:9.5, MeOH:DCM). On cooling to room temperature, the solid precipitate was filtered, washed with cold ethanol 2–3 times, and dried overnight under high vacuum to afford **D2** as a yellowish solid (0.16 g) in 62% yield;  $R_f$  0.55 (0.5:9.5, MeOH:DCM); mp 270–272 °C; IR (cast film)  $\nu_{\max}$  = 3153, 3095, 3020, 2967, 2913, 2827, 2355, 2206, 1623, 1571, 1513, 1265, 1240, 1171, 1020, 831, 771, 698  $\text{cm}^{-1}$ ;  $^1\text{H}$  NMR (500 MHz,  $\text{CD}_3\text{OD}$ )  $\delta$  8.40 (d,  $J$  = 9.4 Hz, 1H), 8.19 (d,  $J$  = 7.1 Hz, 1H), 7.35 (dd,  $J$  = 9.4, 2.5 Hz, 1H), 7.26 – 7.20 (m, 3H), 6.96 – 6.91 (m, 2H), 6.62 (d,  $J$  = 7.1 Hz, 1H), 4.01 (s, 3H). OH and NH protons were not observed;  $^{13}\text{C}$  NMR (125 MHz,  $\text{CD}_3\text{OD}$ )  $\delta$  165.5, 158.7, 157.6, 142.5, 142.1, 129.6, 128.4 (2C), 125.7, 119.8, 117.6 (2C), 112.6, 100.6, 100.30, 56.72; HRMS (ESI) calcd for  $\text{C}_{16}\text{H}_{15}\text{N}_2\text{O}_2$   $[\text{M} + \text{H}]^+$  267.1128; found 267.1126.



#### 4.4.2 ERCC1–XPF Protein Preparation

Human ERCC1–XPF wildtype protein was prepared as previously described by David Jay.<sup>22, 26</sup> Briefly, the expression of recombinant protein was performed using a bicistronic plasmid (kindly provided by Dr. Richard Wood, University of Texas, MD Anderson Cancer Center, Smithville, TX) in the *E. coli* BL21(DE3) strain. The proteins extracted from *E. coli* were incubated with a ProBond NickelChelating Resin (Thermo Fisher Scientific) to purify ERCC1 and XPF containing a polyhistidine (His-6) tag. Afterwards, protein eluted from the Ni affinity column was loaded onto a Hi-trap heparin column (GE Healthcare). Fractions recovered from the heparin column that contained ERCC1–XPF were dialyzed, concentrated, and stored at –80 °C in 10 mM HEPES, pH 7.4, 2.5 mM β-mercaptoethanol, 0.01% CHAPS, 0.25 mM EDTA, 50% glycerol, and 25 mM NaCl.

#### 4.4.3 *In vitro* ERCC1-XPF Endonuclease Assay

A previous described protocol was followed to conduct the fluorescence-based DNA incision assay by David Jay.<sup>22,31</sup> Basically, reactions were performed in 384-well black, flat-bottomed microtiter plates (OptiPlate –384 F, PerkinElmer) in a total volume of 20 μL containing 100 nM DNA stem–loop substrate [6-FAM-5'-CAGCGCTCGG(20T)CCGAGCGCTG-3'-dabcyl], the indicated concentrations of incubated inhibitors, 25 ng of ERCC1–XPF, 50 mM Tris-Cl, pH 8, 20 mM NaCl, 0.5 mM DDT, and 0.75 mM MnCl<sub>2</sub> at 25 °C. A FLUOstar Optima fluorimeter (BMG Labtech) with Optima software was used to monitor the enzyme activity at excitation and emission wavelengths of 485 and 520 nm, respectively. The fluorescent signal was followed during the times indicated in the Section 4.2.

#### **4.4.4 Steady-State Fluorescence Assays**

Fluorescence spectra were measured by Rajam Mani, as previously described,<sup>22</sup> on a PerkinElmer LS-55 spectrofluorometer (Freemont, CA) with 5 nm spectral resolution for excitation and emission using a 30–80 nM solution of purified recombinant ERCC1–XPF protein complex at room temperature. Excitation of protein fluorescence was at 295 nm, and the fluorescence emission spectra were obtained in the 300–400 nm range; the change in the intensity of the fluorescence signal was monitored at the emission maximum of 330 nm. To study effect of the inhibitors on the intensities of the protein fluorescence, inhibitor stock solutions were added to protein samples to keep the protein dilution below 3%. For DNA binding, the substrate was excited at 490 nm, and the fluorescent intensity was monitored at 520 nm.

#### **4.4.5 Cell Culture**

The human colorectal cancer HCT-116 cell line was obtained from the American Type Culture Collection (ATCC). Cells were expanded in a 1:1 DMEM/F12 medium supplemented with 10% FBS, 50 units/mL penicillin, 50 µg/mL streptomycin, 2.5 mM L-glutamine, 0.1 mM non-essential amino acids, and 1 mM sodium pyruvate, and maintained under 5% CO<sub>2</sub> in a humidifier incubator at 37 °C. All the products were obtained from Gibco/BRL.

#### **4.4.6 Cellular Repair of Cyclobutane Pyrimidine Dimers**

Repair or the inhibition of the repair of cyclobutane pyrimidine dimers (CPD) was detected following a protocol that has been described previously, carried out by Xiaoyang Yang.<sup>22, 32</sup> Briefly, approximately  $1 \times 10^5$  HCT-116 cells were seeded on each

coverslip and allowed to attach overnight, followed by treatment with the inhibitors for 1 h. Then, the cells were exposed to 8 J/m<sup>2</sup> UV-C radiation, followed by addition of fresh medium containing the compounds. The plates were incubated at 37 °C for different periods of time up to 24 h and hand fixed in 50:50 methanol/1 × phosphate-buffered saline (PBS) solution, followed by replacement of the methanol/PBS solution with 100% methanol and incubation at −20 °C. After 20 min, the methanol was removed and the cells were fixed and then permeabilized in 0.5% Triton/PBS, washed, denatured in 2 N HCl, and neutralized by twice washing with 0.1 M borate buffer, pH 8.5. Next, the Cells were blocked with 5% non-fat dry milk/PBS for 30 min and then treated with mouse anti-thymine dimer monoclonal antibody (cat. no. MC-062, Kamiya Biomedical Company, Seattle, WA) for 1 h in the dark and at room temperature. Then, the cells were washed with PBS containing 0.1% Tween-20 and incubated with rabbit anti-mouse IgG–Alexafluor antibody (Invitrogen, Carlsbad, CA), followed by two washes with PBS/ (0.1%) Tween-20. Cells on coverslips were mounted on slides using DAPI glycerol mounting solution. The slides were kept at 4 °C before fluorescent microscopic evaluation and measurement of fluorescence intensity with MetaXpress, version 6.2.1.704, software (Molecular Devices, Sunnyvale, California).

#### **4.4.7 Rapid Cell Viability Assay**

The crystal violet assay was used to determine the cell viability of HCT 116 cells following exposure to the inhibitors according to a published procedure, conducted by Xiaoyang Yang.<sup>33</sup> Briefly, 3 x 10<sup>3</sup> cells were seeded in each well of a 96-well plate. After 18–24 h, the medium was removed and replaced with 100 µL medium supplemented with appropriate drug concentrations of the inhibitory compounds. After

72 h, the medium was removed, 50  $\mu\text{L}$  of 0.5% crystal violet staining solution was added to each well, and the dishes were held at room temperature for 20 min. Then, the wells were washed four times with water and allowed to air-dry before adding 200  $\mu\text{L}$  of methanol and incubating for 20 min. The absorbance at 570 nm was obtained using a microplate reader, and the corrected absorbance (after subtracting the average  $\text{OD}_{570}$  of the wells without cells) was plotted against the inhibitor concentration.

#### **4.4.8 Clonogenic Survival Assay Following UV Treatment**

Similar to what was described previously<sup>22</sup> and depending on the UV dose, 100 to 800 HCT-116 cells were plated in triplicate in 60mm Petri dishes and incubated overnight at 37 °C in a 5%  $\text{CO}_2$  atmosphere to allow the cells to attach. Then, the medium was removed, and the cells were treated with 2 or 4  $\mu\text{M}$  **Gen B9** or **Gen B7**, or 2  $\mu\text{M}$  **F06 (1)** for 4 h. After this period, the medium was removed, and the cells were exposed to increasing doses of UV-C radiation (0–10  $\text{J}/\text{m}^2$ ) and incubated for a further 8 days in the presence of inhibitors at 37 °C in a 5%  $\text{CO}_2$  atmosphere to allow for colony formation. After this period, the plates were stained with crystal violet and the colonies were counted using a Colcount instrument (Oxford Optronix, Abingdon UK). Finally, the plating efficiency and surviving fraction were calculated.

#### **4.4.9 Combination Effect of B9 and Cisplatin and MMC**

A similar protocol was followed as described for the UV treatment, except that cells were treated with 2  $\mu\text{M}$  compounds **B9** and 4  $\mu\text{M}$  **B7** (as negative control) for 4 h, followed by addition of increasing doses of cyclophosphamide (0–300  $\mu\text{M}$ ). After 24 h, the medium was replaced with fresh medium containing compounds **B9** and **B7**

alone. The plates were incubated at 37 °C in a 5% CO<sub>2</sub> atmosphere for colony formation. After 8 days, the plates were stained with crystal violet, the colonies were counted, and the plating efficiency and surviving fraction were determined.

#### **4.4.10 Partial Pharmacokinetic Profile of Compounds Gen B9 and F06 (1)**

**B9** was screened by WuXi AppTec (Shanghai) Co in China for the following assays according to the standard protocols:<sup>34</sup> distribution coefficient (log D at pH 7.4), metabolic stability in human liver microsomes, and bidirectional permeability in Caco-2 cells.

#### **4.4.11 Partial Pharmacokinetic Profile of Compounds B9 and F06 (1)**

The cells (50,000 per well) were seeded in complete media in 24-well plates and left overnight to adhere before the compounds (cisplatin, mitomycin C, A4, B9) were added at indicated concentrations. After 48 h, the cells were washed with PBS and stained with AnnexinV-Fluos Staining kit (Roche) as indicated by the manufacturer. The cells were analyzed by FACS (Fortessa, BD Biosciences), and the percentage of alive cells (AnnexinV negative and propidium iodide negative) was used to measure the activity of drugs and combinations.

#### **4.4.12 Proximity Ligation Assay**

A549 cells were incubated in the absence or presence of **A4** or **B9** (2 µM) and cisplatin (20 µM) for 24 h and, subsequently, treated for Duolink assay (Olink Bioscience, Uppsala, Sweden), with the use of ERCC1 antibody (FL-297, 1 mg; Santa Cruz Biotechnology, Santa Cruz, CA) and XPF antibody (LS-C33719, 1/1000; LifeSpan BioSciences, Seattle, WA). Dots corresponding to protein–protein interaction were

counted using the Blobfinder software (The Center for Image Analysis, Uppsala University, Uppsala, Sweden) in at least 150 cells from at least five microscopic fields, and the results are mean values from two independent experiments.

## 4.5 References

1. Manandhar, M.; Boulware, K. S.; Wood, R. D. The ERCC1 and ERCC4 (XPF) genes and gene products. *Gene* **2015**, 569, 153-161.
2. Staresinic, L.; Fagbemi, A. F.; Enzlin, J. H.; Gourdin, A. M.; Wijgers, N.; Dunand-Sauthier, I.; Giglia-Mari, G.; Clarkson, S. G.; Vermeulen, W.; Schärer, O. D. Coordination of dual incision and repair synthesis in human nucleotide excision repair. *The EMBO Journal* **2009**, 28, 1111-1120.
3. Ahmad, A.; Robinson, A. R.; Duensing, A.; van Drunen, E.; Beverloo, H. B.; Weisberg, D. B.; Hastly, P.; Hoeijmakers, J. H. J.; Niedernhofer, L. J. ERCC1-XPF endonuclease facilitates DNA double-strand break repair. *Molecular and Cellular Biology* **2008**, 28, 5082-5092.
4. McHugh, P. J.; Spanswick, V. J.; Hartley, J. A. Repair of DNA interstrand crosslinks: molecular mechanisms and clinical relevance. *The Lancet Oncology* **2001**, 2, 483-490.
5. Yagi, T.; Katsuya, A.; Koyano, A.; Takebe, H. Sensitivity of group F xeroderma pigmentosum cells to UV and mitomycin C relative to levels of XPF and ERCC1 overexpression. *Mutagenesis* **1998**, 13, 595-599.
6. Sijbers, A. M.; de Laat, W. L.; Ariza, R. R.; Biggerstaff, M.; Wei, Y.-F.; Moggs, J. G.; Carter, K. C.; Shell, B. K.; Evans, E.; de Jong, M. C. Xeroderma pigmentosum group F caused by a defect in a structure-specific DNA repair endonuclease. *Cell* **1996**, 86, 811-822.
7. Gajjar, K. K.; Yadav, D. K.; Kobawala, T. P.; Trivedi, T. I.; Vora, H. H.; Ghosh, N. R. ERCC1 expression in patients with colorectal cancer: a pilot study. *Journal of Cancer Metastasis and Treatment* **2016**, 12, 471-476.
8. Tripsianes, K.; Folkers, G.; Eiso, A. B.; Das, D.; Odijk, H.; Jaspers, N. G. J.; Hoeijmakers, J. H. J.; Kaptein, R.; Boelens, R. The structure of the human ERCC1/XPF interaction domains reveals a complementary role for the two proteins in nucleotide excision repair. *Structure* **2005**, 13, 1849-1858.
9. McNeil, E. M.; Melton, D. W. DNA repair endonuclease ERCC1-XPF as a novel therapeutic target to overcome chemoresistance in cancer therapy. *Nucleic Acids Research* **2012**, 40, 9990-10004.
10. Tsodikov, O. V.; Enzlin, J. H.; Schärer, O. D.; Ellenberger, T. Crystal structure and DNA binding functions of ERCC1, a subunit of the DNA structure-specific endonuclease XPF-ERCC1. *Proceedings of the National Academy of Sciences* **2005**, 102, 11236-11241.
11. Choi, Y.-J.; Ryu, K.-S.; Ko, Y.-M.; Chae, Y.-K.; Pelton, J. G.; Wemmer, D. E.; Choi, B.-S. Biophysical characterization of the interaction domains and mapping of the contact residues in the XPF-ERCC1 complex. *Journal of Biological Chemistry* **2005**, 280, 28644-28652.
12. Gentile, F.; Barakat, K. H.; Tuszynski, J. A. Computational Characterization of Small Molecules Binding to the Human XPF Active Site and Virtual Screening to Identify Potential New DNA

- Repair Inhibitors Targeting the ERCC1-XPF Endonuclease. *International Journal of Molecular Sciences* **2018**, *19*, 1328-1340.
13. Gentile, F.; Tuszynski, J. A.; Barakat, K. H. New design of nucleotide excision repair (NER) inhibitors for combination cancer therapy. *Journal of Molecular Graphics and Modelling* **2016**, *65*, 71-82.
  14. Gentile, F.; A Tuszynski, J.; H Barakat, K. Modelling DNA repair pathways: recent advances and future directions. *Current Pharmaceutical Design* **2016**, *22*, 3527-3546.
  15. Yang, L.; Ritchie, A.-M.; Melton, D. W. Disruption of DNA repair in cancer cells by ubiquitination of a destabilising dimerization domain of nucleotide excision repair protein ERCC1. *Oncotarget* **2017**, *8*, 55246-55264.
  16. Arora, S.; Heyza, J.; Zhang, H.; Kalman-Maltese, V.; Tillison, K.; Floyd, A. M.; Chalfin, E. M.; Bepler, G.; Patrick, S. M. Identification of small molecule inhibitors of ERCC1-XPF that inhibit DNA repair and potentiate cisplatin efficacy in cancer cells. *Oncotarget* **2016**, *7*, 75104-75117.
  17. Chapman, T. M.; Wallace, C.; Gillen, K. J.; Bakrania, P.; Khurana, P.; Coombs, P. J.; Fox, S.; Bureau, E. A.; Brownlees, J.; Melton, D. W. N-Hydroxyimides and hydroxypyrimidinones as inhibitors of the DNA repair complex ERCC1-XPF. *Bioorganic & Medicinal Chemistry Letters* **2015**, *25*, 4104-4108.
  18. Chapman, T. M.; Gillen, K. J.; Wallace, C.; Lee, M. T.; Bakrania, P.; Khurana, P.; Coombs, P. J.; Stennett, L.; Fox, S.; Bureau, E. A. Catechols and 3-hydroxypyridones as inhibitors of the DNA repair complex ERCC1-XPF. *Bioorganic & Medicinal Chemistry Letters* **2015**, *25*, 4097-4103.
  19. McNeil, E. M.; Astell, K. R.; Ritchie, A.-M.; Shave, S.; Houston, D. R.; Bakrania, P.; Jones, H. M.; Khurana, P.; Wallace, C.; Chapman, T.; Wear, M. A.; Walkinshaw, M. D.; Saxty, B.; Melton, D. W. Inhibition of the ERCC1-XPF structure-specific endonuclease to overcome cancer chemoresistance. *DNA Repair* **2015**, *31*, 19-28.
  20. Jordheim, L. P.; Barakat, K. H.; Heinrich-Balard, L.; Matera, E.-L.; Cros-Perrial, E.; Bouledrak, K.; El Sabeh, R.; Perez-Pineiro, R.; Wishart, D. S.; Cohen, R. Small molecule inhibitors of ERCC1-XPF protein-protein interaction synergize alkylating agents in cancer cells. *Molecular Pharmacology* **2013**, *84*, 12-24.
  21. Arora, S.; Heyza, J.; Zhang, H.; Kalman-Maltese, V.; Tillison, K.; Floyd, A. M.; Chalfin, E. M.; Bepler, G.; Patrick, S. M. Identification of small molecule inhibitors of ERCC1-XPF that inhibit DNA repair and potentiate cisplatin efficacy in cancer cells. *Oncotarget* **2016**, *46*, 75104-75117.
  22. Elmenoufy, A. H.; Gentile, F.; Jay, D.; Karimi-Busheri, F.; Yang, X.; Soueidan, O. M.; Weilbeer, C.; Mani, R. S.; Barakat, K. H.; Tuszynski, J. A.; Weinfeld, M.; West, F. G. Targeting DNA Repair in Tumor Cells via Inhibition of ERCC1-XPF. *Journal of Medicinal Chemistry* **2019**, *62*, 7684-7696.

23. Gentile, F.; Elmenoufy, A. H.; Ciniero, G.; Jay, D.; Karimi-Busheri, F.; Barakat, K. H.; Weinfeld, M.; West, F. G.; Tuszynski, J. A. Computer-Aided Drug Design of Small Molecule Inhibitors of the ERCC1-XPF Protein-Protein Interaction. *Chemical Biology & Drug Design* **2020**, 00, 1-12.
24. Kelley, R. K.; Hwang, J.; Magbanua, M. J. M.; Watt, L.; Beumer, J. H.; Christner, S. M.; Baruchel, S.; Wu, B.; Fong, L.; Yeh, B. M.; Moore, A. P.; Ko, A. H.; Korn, W. M.; Rajpal, S.; Park, J. W.; Tempero, M. A.; Venook, A. P.; Bergsland, E. K. A phase 1 trial of imatinib, bevacizumab, and metronomic cyclophosphamide in advanced colorectal cancer. *British Journal of Cancer* **2013**, 109, 1725-1734.
25. Cremolini, C.; Marmorino, F.; Bergamo, F.; Aprile, G.; Salvatore, L.; Masi, G.; Dell'Aquila, E.; Antoniotti, C.; Murgioni, S.; Allegrini, G. Phase II randomised study of maintenance treatment with bevacizumab or bevacizumab plus metronomic chemotherapy after first-line induction with FOLFOXIRI plus Bevacizumab for metastatic colorectal cancer patients: the MOMA trial. *European Journal of Cancer* **2019**, 109, 175-182.
26. Bowles, M.; Lally, J.; Fadden, A. J.; Mouilleron, S.; Hammonds, T.; McDonald, N. Q. Fluorescence-based incision assay for human XPF-ERCC1 activity identifies important elements of DNA junction recognition. *Nucleic Acids Research* **2012**, 40, 101-112.
27. Kourounakis, A. P.; Xanthopoulos, D.; Tzara, A. Morpholine as a privileged structure: A review on the medicinal chemistry and pharmacological activity of morpholine containing bioactive molecules. *Medicinal Research Reviews* **2019**, 1-44.
28. Mani, R. S.; Karimi-Busheri, F.; Fanta, M.; Caldecott, K. W.; Cass, C. E.; Weinfeld, M. Biophysical characterization of human XRCC1 and its binding to damaged and undamaged DNA. *Biochemistry* **2004**, 43, 16505-16514.
29. Carlson, W. W.; Cretcher, L. H. The Hydroxyethyl Analog of Quinacrine. *Journal of the American Chemical Society* **1948**, 70, 597-599.
30. Sriram, D.; Devakaram, R. V.; Dinakaran, M.; Yogeewari, P. Aromatic amino analogues of artemisinin: synthesis and *in-vivo* antimalarial activity. *Medicinal Chemistry Research* **2010**, 19, 524-532.
31. McNeil, E. M.; Astell, K. R.; Ritchie, A.-M.; Shave, S.; Houston, D. R.; Bakrania, P.; Jones, H. M.; Khurana, P.; Wallace, C.; Chapman, T. Inhibition of the ERCC1-XPF structure-specific endonuclease to overcome cancer chemoresistance. *DNA Repair* **2015**, 31, 19-28.
32. Mirzayans, R.; Pollock, S.; Scott, A.; Gao, C. Q.; Murray, D. Metabolic labeling of human cells with tritiated nucleosides results in activation of the ATM-dependent p53 signaling pathway and acceleration of DNA repair. *Oncogene* **2003**, 22, 5562-5571.
33. Feoktistova, M.; Geserick, P.; Leverkus, M. Crystal violet assay for determining viability of cultured cells. *Cold Spring Harbor Protocols* **2016**, 4, pdb-prot087379.
34. WuXi AppTech Inc., <https://www.wuxiapptec.com>

# Chapter 5

## General Conclusions and Future Directions

### 5.1 General Conclusions

As outlined in the thesis, major conventional cancer therapies, such as radiotherapy and chemotherapy, face major issues due to the problem of resistance caused by the capacity of cancer cells to repair the DNA damage produced by such therapies. This is one of the leading causes for relapses and cancer related deaths. A significant portion of these therapeutics work by causing DNA damage to cancer cells; however, the damage also takes place from endogenous events in origin, such as spontaneous hydrolysis, oxidation by reactive oxygen species (ROS) or reactive nitrogen species, and alkylation to external factors, such as IR and chemotherapeutics. Although normal cells are able to repair such lesions to their DNA by initiating the corresponding repair pathways, cancerous cells have a similar capacity to recognize, verify, and repair these DNA damages effectively, a phenomenon that results in treatment resistance to several cancer therapeutics. Several repair pathways can be initiated by cells to repair different types of damages caused by different DNA damaging agents, such as 1) mismatch repair (MMR), which correct the mis-incorporated nucleobases, 2) base excision repair (BER), which remove and repair bases with lesions that are caused by oxidation, alkylation, ring saturation or ionizing radiation, 3) double-strand break repair, which includes both homologous recombination (HR) and non-homologous end joining (NHEJ), and 4) nucleotide excision repair (NER).

In this thesis work, we focused on inhibiting NER through targeting an essential DNA-repair heterodimer, ERCC1–XPF, because it is a highly versatile repair pathway that can recognize, verify, and remove several bulky, helix-distorting lesions from the damaged DNA. One of the crucial substrates in NER pathway is cisplatin-DNA products, which cause intra-strand crosslinks, and cyclobutane pyrimidine dimers (CPD) and pyrimidine dimers, such as 6–4 photoproducts, which are photo adducts produced by the UV component of sunlight.

ERCC1–XPF heterodimer plays a central role in nucleotide excision repair (NER) of bulky adducts and helix-distorting DNA lesions, such as UV-induced pyrimidine-(6,4)-pyrimidone photoproducts (6-4PPs) and CPDs. ERCC1–XPF also is involved in a different repair pathway, DNA inter-strand crosslink (ICL) repair in cells treated with platinum containing compounds and other chemotherapeutic agents, such as cyclophosphamide and mitomycin C (MMC). Therefore, it contributes significantly to the response of cancer cells to a wide array of DNA-damaging chemotherapeutic agents and radiotherapy.

The heterodimerization interface is probably the most promising domain to be targeted pharmacologically, as previously reported. Furthermore, dimerization and localization of ERCC1 and XPF fragments is crucial for the enzyme's stability and endonuclease activity. To form a stable heterodimer, the C-terminal regions of ERCC1 and XPF (HhH2 domains) should be dimerized. It was illustrated that without the dimerization being formed, the activity of ERCC1–XPF was abolished due to losing the stability of the protein; therefore, they were rapidly degraded.

As a result, developing of ERCC1–XPF heterodimerization inhibitors would be expected to potentiate chemotherapeutic treatments whose DNA-damaging effects are repaired by ERCC1–XPF-dependent pathways to cancer cells. Moreover, computer aided drug design methods can be employed due to the availability of several experimental structures of the dimerized HhH2 domains (for example, PDB code 2A1J and 1Z00). In this thesis work, we report the design and development of potent inhibitors with optimized physio-chemical properties to disrupt the interaction domain between ERCC1–XPF using the full-length protein and their ability to sensitize cancer cells towards contemporary cancer therapies, such as chemotherapy or radiotherapy.

In Chapter 2 of this thesis, we used the reported ERCC1–XPF inhibitor hit, compound **1** (F06), to optimize and develop more potent inhibitors with enhanced physicochemical properties. My collaborator, Francesco Gentile, employed a computational drug design workflow to provide a rational model for novel compound **1** analogues with the aim of finding a lead inhibitor targeting the dimerization between XPF and ERCC1, and thus inhibiting the endonuclease activity. Seven compounds were identified by a virtual screening study on the XPF interaction domain. Additionally, *in silico* simulations predicted attractive properties, such as binding affinities and ligand efficiency towards an XPF site on the interaction interface. The synthesis of selected computationally designed compounds was carried out successfully using a simple, robust, and reproducible synthetic approach. Interestingly, compound **4** showed reasonable cLog P, ligand efficiency values and small molecular weight; therefore, it was considered to be a potential lead candidate for further optimization. Following structure-activity relationship studies in this generation and *in vitro* screening, the

results yielded compounds **3** and **4** as potent inhibitors of ERCC1–XPF activity. An *in vitro* ERCC1–XPF endonuclease assay identified compound **4** as the best ERCC1–XPF inhibitor with an  $IC_{50}$  value of 0.33  $\mu$ M compared to 1.86  $\mu$ M for **1**. In addition, the binding affinity value for this compound was measured experimentally as 100 nM. It interacts with ERCC1–XPF in the subunit interaction domain and altered the related properties of this heterodimerization interface. The lead compound **4** also showed not only a significant inhibition of NER pathway by inhibiting the removal of cyclobutane pyrimidine dimers compared with control cells after exposure of HCT-116 cells to UV radiation but also sensitized the cells to UV and cyclophosphamide-induced cytotoxicity. In addition, compound **4** possessed a favorable pharmacokinetic profile, particularly a lower log D than the hit compound **1**, which indicated that it has a lower lipophilicity and greater metabolic stability. Our computational design workflow successfully identified superior compounds from a set of analogues differing by one substituent group, and it is providing detailed information about the ligand–protein interaction. Compound **4** was our best *in vitro* analogue. Detailed analysis of the MM/GBSA binding energies, together with the visual analysis of the simulation results, suggested a binding mode for compound **4** where the conserved hydrophobic core of the analogue is buried inside the XPF binding site and, differently to the other active compounds (**1** and **3**), the positively charged R-substituent is exposed favorably to the solvent that was engaged in the formation of solvent ( $H_2O$ ) interaction in the binding pocket. Although all of the compounds share the acridine moiety, our assay showed that the inhibition activity of the best **1** analogue, compound **4**, was the consequence of the interaction of the drug with the enzyme instead of the binding with DNA. The fact that

compounds **4** and **5** (negative control) show drastically different activity despite possessing the same acridine moiety also provides strong evidence that inhibition is not mediated via DNA intercalation.

In Chapter 3, we focused on using a multi-step CADD strategy to identify better inhibitors than **1** by considering the substitution of a methoxy-acridine group by different polar moieties. These *in silico* screened inhibitors are expected also to disrupt the ERCC1–XPF heterodimerization interface, as this interaction between ERCC1 and XPF is required to constitute a functional stable complex. The virtual screening identified two compounds, which were subjected to the cell-free assay and showed improved inhibition of the ERCC1-XPF incision activity compared to the parent compound **1**.

In Chapter 4, the workflow we introduced provided a blueprint for further modification of other sites of **1** in order to advance towards a preclinical drug candidate for DNA repair inhibition. We further explored two different sites modifications (acridine hydrophobic and aniline moieties) on **1**, according to the pharmacophore model, which yielded two series of compounds (**C** and **D**), and dissected their structure activity relationships with regard to their ability to inhibit the ERCC1–XPF heterodimer and sensitize colorectal cancer cells to either UV radiation or other clinical chemotherapeutic agents, such as cyclophosphamide, cisplatin, and MMC. All the designed compounds were synthesized via a robust, facile, and reproducible strategy. The inhibitory effects of all compounds on the full-length ERCC1–XPF protein activity were assessed *in vitro*. The results of the *in vitro* ERCC1–XPF endonuclease assay identified **B9** as a potent inhibitor of the ERCC1–XPF nuclease activity with an  $IC_{50}$

value of  $0.49 \pm 0.04 \mu\text{M}$  compared to  $1.86 \pm 0.25 \mu\text{M}$  for **1**. This result suggested that incorporating the piperazine ring with a polar side-chain on the exterior face of the piperazine and a large hydrophobic moiety (acridine) is essential for optimized activity, which is in accord with the results of the effect of **C** and **D** compounds on the protein complex. However, installing a hydrogen bond donor group on the acridine, as in **Gen B9**, increased the inhibitory effect by almost two-fold compared to having a hydrogen bond acceptor, such as the methoxy group in **1**. The docking studies indicated that this resulted in additional hydrogen bond interaction with the side chain of the buried V859 residue in the XPF binding pocket. The binding constant for **B9** was measured experimentally as 85 nM, which has a higher affinity for ERCC1–XPF relative to **1** with a  $K_d$  value of 140 nM. The fact that **B7** (negative control) and **B9** show disparity in their activity and binding profiles on ERCC1–XPF, despite having the same acridine moiety, also provides strong evidence that the protein complex inhibition is not mediated through DNA intercalation. **B9** elicited inhibition of CPDs removal upon UV irradiation and sensitized the HCT 116 cells to cyclophosphamide- and UV- induced cytotoxicity, indicating inhibition of ICL and NER pathways. Furthermore, comparison of the partial pharmacokinetics screening results of **B9** and **F06** indicates that our lead second generation compound **B9** has more favorable properties than the **1**, particularly by showing a moderate clearance from the liver, a better permeability, and a lower log D, which means that it has a lower lipophilicity and greater metabolic stability. In addition, **B9** also showed a significant synergistic effect when used with cisplatin, causing 80% cell death relative to the effect of cisplatin alone. Furthermore, the **B9** inhibitory activity is attributed to the heterodimerization disruption of ERCC1–XPF on a cellular level. In

summary, the analysis of the conducted comprehensive SAR studies identified **B9**, which can be combined with other existing DNA-damaging therapies to synergize their effects by sensitizing cancer cells.

## 5.2 Future Directions

Future work is needed to explore a wider range of polar hydrogen bond donor groups to be installed on the hydrophobic acridine structure (Figure 5.1) since hydrogen bond donor group installation on the acridine moiety clearly enhances the activity and to contrast their ERCC1–XPF inhibitory activity with our best lead compound **B9**. Furthermore, exchange the toxophore, phenolic group on the acridine moiety, with other polar hydrogen bond groups such as NH<sub>2</sub> or SH might reduce the toxicity of these compounds *in vivo* by avoid formation the quinone like structures. In addition, structural modifications on the *N, N* dimethyl ethyl group installed at the distal nitrogen atom of the piperazine ring is important. This could be attained by installing different linkers or by changing the heteroatom and its substituents (Figure 5.1). By doing these modifications, we will get a better understanding and deep insight of which part of this group is crucial for the activity and the potential of optimizing our lead compounds to have enhanced activity and better ADME profile.

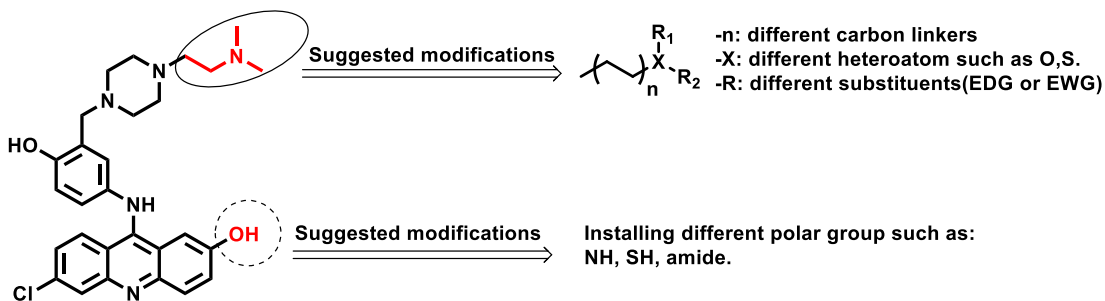


Figure 5.1. Structural modifications on **B9** or **A4** for lead optimization.

A recent study has indicated that using DNA-damaging drugs along with P53 reactivators has a significant synergistic effect on ovarian cancer.<sup>1</sup> Thus, the studying of the *in vitro* synergy effects of the lead compounds with regard to ERCC1–XPF inhibition in the presence and absence of P53 mutants and their activators is ongoing with our collaborators, Gloria Ciniero and co-workers at Lyon University, France. The aim of this joint work is to assess the synergistic ability of compound **4** and **B9** to potentiate conventional chemotherapies towards different cell lines with P53 positive or negative mutants.

In addition, finding an active targeting modality to selectively target compound **4** and **B9** to the cancer cells is required urgently. The importance of this approach is to reduce the off-target toxicity of inhibitors, thus reducing a wide array of adverse effects associated with such off-targeting. To address this issue, we plan to implement a nanoparticle-based drug delivery approach. Our collaborator, Dr. Afsaneh Lavasanifar at the Faculty of Pharmacy, University of Alberta, has developed polymeric micelle nanoparticles grafted with an active targeting peptide GE11 to target the epidermal growth factor receptor (EGFR) on HCT 116, colorectal cancer cells.<sup>2</sup> These nanoparticles will be employed as nanocarriers for selective delivery of compound **4** and **B9** to colorectal cancer cells *in vitro* and *in vivo* using the modified nanocarrier previously reported by Igor and co-workers.<sup>2</sup> Currently, the *in vitro* cellular uptake and release studies of the nanoparticles encapsulated with compound **4** are ongoing.

Future work is still needed to validate the *in vitro* results of the active inhibitors by performing *in vivo* studies using nude mice with +/+ or -/- ERCC1–XPF xenografts. Assessing the *in vivo* safety and toxicity of the lead compounds is required, and

monitoring the tumor growth after administration of inhibitors, along with conventional chemotherapeutics is needed. Our collaborator, Dr. Jirik, at the University of Calgary, has developed different mice models to be subjected to the previous-mentioned assays. These *in vivo* studies will soon be started after a successful nano-formulation with the active inhibitors.

## 5.3 References

1. Fransson, Å.; Glaessgen, D.; Alfredsson, J.; Wiman, K. G.; Bajalica-Lagercrantz, S.; Mohell, N. Strong synergy with APR-246 and DNA-damaging drugs in primary cancer cells from patients with TP53 mutant High-Grade Serous ovarian cancer. *Journal of Ovarian Research* **2016**, *9*, 27-37.
2. Paiva, I.; Mattingly, S.; Wuest, M.; Leier, S.; Vakili, M. R.; Weinfeld, M.; Lavasanifar, A.; Wuest, F. Synthesis and analysis of <sup>64</sup>Cu-labeled GE11-modified polymeric micellar nanoparticles for EGFR-targeted molecular imaging in a colorectal cancer model. *Molecular Pharmaceutics* **2020**, Just Accepted.

# Compiled References

## Chapter 1

1. Siegel, R. L.; Miller, K. D.; Jemal, A. Cancer statistics, 2020. *CA: A Cancer Journal for Clinicians* **2020**, *70*, 7-30.
2. Holohan, C.; Van Schaeybroeck, S.; Longley, D. B.; Johnston, P. G. Cancer drug resistance: an evolving paradigm. *Nature Reviews Cancer* **2013**, *13*, 714-726.
3. Housman, G.; Byler, S.; Heerboth, S.; Lapinska, K.; Longacre, M.; Snyder, N.; Sarkar, S. Drug resistance in cancer: an overview. *Cancers* **2014**, *6*, 1769-1792.
4. Rueff, J.; Rodrigues, A. S. Cancer drug resistance: A brief overview from a genetic viewpoint. In *Cancer Drug Resistance*, Springer: 2016; pp 1-18.
5. Urruticochea, A.; Alemany, R.; Balart, J.; Villanueva, A.; Viñals, F.; Capella, G. Recent advances in cancer therapy: an overview. *Current Pharmaceutical Design* **2010**, *16*, 3-10.
6. Baskar, R.; Lee, K. A.; Yeo, R.; Yeoh, K.-W. Cancer and radiation therapy: current advances and future directions. *International Journal of Medical Sciences* **2012**, *9*, 193-199.
7. Khalil, D. N.; Smith, E. L.; Brentjens, R. J.; Wolchok, J. D. The future of cancer treatment: immunomodulation, CARs and combination immunotherapy. *Nature Reviews Clinical Oncology* **2016**, *13*, 273-290.
8. Alfarouk, K. O.; Stock, C.-M.; Taylor, S.; Walsh, M.; Muddathir, A. K.; Verduzco, D.; Bashir, A. H. H.; Mohammed, O. Y.; Elhassan, G. O.; Harguindey, S. Resistance to cancer chemotherapy: failure in drug response from ADME to P-gp. *Cancer Cell International* **2015**, *15*, 71-84.
9. Borst, P. Cancer drug pan-resistance: pumps, cancer stem cells, quiescence, epithelial to mesenchymal transition, blocked cell death pathways, persists or what? *Open Biology* **2012**, *2*, 120066-120075.
10. Uramoto, H.; Tanaka, F. Recurrence after surgery in patients with NSCLC. *Translational Lung Cancer Research* **2014**, *3*, 242-249.
11. Castells, M.; Thibault, B.; Delord, J.-P.; Couderc, B. Implication of tumor microenvironment in chemoresistance: tumor-associated stromal cells protect tumor cells from cell death. *International Journal of Molecular Sciences* **2012**, *13*, 9545-9571.
12. O'Connor, D.; Sibson, K.; Caswell, M.; Connor, P.; Cummins, M.; Mitchell, C.; Motwani, J.; Taj, M.; Vora, A.; Wynn, R. Early UK experience in the use of clofarabine in the treatment of relapsed and refractory paediatric acute lymphoblastic leukaemia. *British Journal of Haematology* **2011**, *154*, 482-485.

13. Yazilitas, D.; Özdemir, N.; Hocasade, C.; Demirci, N. S.; Zengin, N. The clinical and pathological features affecting the time of relapse in patients with early stage colorectal cancer. *Journal of Cancer Research and Therapeutics* **2016**, *12*, 1257-1260.
14. De Bont, R.; Van Larebeke, N. Endogenous DNA damage in humans: a review of quantitative data. *Mutagenesis* **2004**, *19*, 169-185.
15. Lindahl, T. Instability and decay of the primary structure of DNA. *Nature* **1993**, *362*, 709-715.
16. Lindahl, T.; Nyberg, B. Rate of depurination of native deoxyribonucleic acid. *Biochemistry* **1972**, *11*, 3610-3618.
17. Sugiyama, H.; Fujiwara, T.; Ura, A.; Tashiro, T.; Yamamoto, K.; Kawanishi, S.; Saito, I. Chemistry of thermal degradation of abasic sites in DNA. Mechanistic investigation on thermal DNA strand cleavage of alkylated DNA. *Chemical Research in Toxicology* **1994**, *7*, 673-683.
18. Yonekura, S.-I.; Nakamura, N.; Yonei, S.; Zhang-Akiyama, Q.-M. Generation, biological consequences and repair mechanisms of cytosine deamination in DNA. *Journal of Radiation Research* **2008**, 0811040073-0811040073.
19. Frederico, L. A.; Kunkel, T. A.; Shaw, B. R. A sensitive genetic assay for the detection of cytosine deamination: determination of rate constants and the activation energy. *Biochemistry* **1990**, *29*, 2532-2537.
20. Krokan, H. E.; Drabløs, F.; Slupphaug, G. Uracil in DNA—occurrence, consequences and repair. *Oncogene* **2002**, *21*, 8935-8948.
21. Kow, Y. W. Repair of deaminated bases in DNA. *Free Radical Biology and Medicine* **2002**, *33*, 886-893.
22. Apel, K.; Hirt, H. Reactive oxygen species: metabolism, oxidative stress, and signal transduction. *Annual Reviews Plant Biology* **2004**, *55*, 373-399.
23. Marnett, L. J. Oxyradicals and DNA damage. *Carcinogenesis* **2000**, *21*, 361-370.
24. Cadet, J.; Berger, M.; Douki, T.; Ravanat, J. L. Oxidative damage to DNA: formation, measurement, and biological significance. In *Reviews of Physiology Biochemistry and Pharmacology* **1997**, *131*, 1-87.
25. Burney, S.; Caulfield, J. L.; Niles, J. C.; Wishnok, J. S.; Tannenbaum, S. R. The chemistry of DNA damage from nitric oxide and peroxynitrite. *Mutation Research/Fundamental and Molecular Mechanisms of Mutagenesis* **1999**, *424*, 37-49.
26. Ravanat, J.-L. Measuring oxidized DNA lesions as biomarkers of oxidative stress: an analytical challenge. *FABAD Journal of Pharmaceutical Sciences* **2005**, *30*, 100-113.
27. Major, G. N.; Collier, J. D. Repair of DNA lesion O 6-methylguanine in hepatocellular carcinogenesis. *Journal of Hepato-Biliary-Pancreatic Surgery* **1998**, *5*, 355-366.
28. Jackson, S. P.; Bartek, J. The DNA-damage response in human biology and disease. *Nature* **2009**, *461*, 1071-1078.

29. Kesari, S.; Advani, S. J.; Lawson, J. D.; Kahle, K. T.; Ng, K.; Carter, B.; Chen, C. C. DNA damage response and repair: insights into strategies for radiation sensitization of gliomas. *Future Oncology* **2011**, *7*, 1335-1346.
30. Vermund, H.; Gollin, F. F. Mechanisms of action of radiotherapy and chemotherapeutic adjuvants: a review. *Cancer* **1968**, *21*, 58-76.
31. Zheng, H.-C. The molecular mechanisms of chemoresistance in cancers. *Oncotarget* **2017**, *8*, 59950-59964.
32. Berwick, M.; Vineis, P. Markers of DNA repair and susceptibility to cancer in humans: an epidemiologic review. *Journal of the National Cancer Institute* **2000**, *92*, 874-897.
33. Longley, D. B.; Johnston, P. G. Molecular mechanisms of drug resistance. *The Journal of Pathology: A Journal of the Pathological Society of Great Britain and Ireland* **2005**, *205*, 275-292.
34. Zhou, B.-B. S.; Bartek, J. Targeting the checkpoint kinases: chemosensitization versus chemoprotection. *Nature Reviews Cancer* **2004**, *4*, 216-225.
35. Boland, C. R.; Luciani, M. G.; Gasche, C.; Goel, A. Infection, inflammation, and gastrointestinal cancer. *Gut* **2005**, *54*, 1321-1331.
36. Peltomäki, P. Deficient DNA mismatch repair: a common etiologic factor for colon cancer. *Human Molecular Genetics* **2001**, *10*, 735-740.
37. Larrea, A. A.; Lujan, S. A.; Kunkel, T. A. SnapShot: DNA mismatch repair. *Cell* **2010**, *141*, 730-730.
38. Modrich, P. Mechanisms in eukaryotic mismatch repair. *Journal of Biological Chemistry* **2006**, *281*, 30305-30309.
39. Fukui, K. DNA mismatch repair in eukaryotes and bacteria. *Journal of Nucleic Acids* **2010**, 260512-260528.
40. Chan, K. K. L.; Zhang, Q.-M.; Dianov, G. L. Base excision repair fidelity in normal and cancer cells. *Mutagenesis* **2006**, *21*, 173-178.
41. Sancar, A.; Lindsey-Boltz, L. A.; Ünsal-Kaçmaz, K.; Linn, S. Molecular mechanisms of mammalian DNA repair and the DNA damage checkpoints. *Annual Review of Biochemistry* **2004**, *73*, 39-85.
42. van Gent, D. C.; Hoeijmakers, J. H. J.; Kanaar, R. Chromosomal stability and the DNA double-stranded break connection. *Nature Reviews Genetics* **2001**, *2*, 196-206.
43. Khanna, K. K.; Jackson, S. P. DNA double-strand breaks: signaling, repair and the cancer connection. *Nature Genetics* **2001**, *27*, 247-254.
44. Li, X.; Heyer, W.-D. Homologous recombination in DNA repair and DNA damage tolerance. *Cell Research* **2008**, *18*, 99-113.
45. Lieber, M. R. The mechanism of double-strand DNA break repair by the nonhomologous DNA end-joining pathway. *Annual Review of Biochemistry* **2010**, *79*, 181-211.

46. Shuck, S. C.; Short, E. A.; Turchi, J. J. Eukaryotic nucleotide excision repair: from understanding mechanisms to influencing biology. *Cell Research* **2008**, *18*, 64-72.
47. Costa, R. M. A.; Chiganças, V.; da Silva Galhardo, R.; Carvalho, H.; Menck, C. F. M. The eukaryotic nucleotide excision repair pathway. *Biochimie* **2003**, *85*, 1083-1099.
48. Nospikel, T. Nucleotide excision repair and neurological diseases. *DNA Repair* **2008**, *7*, 1155-1167.
49. Lindahl, T.; Wood, R. D. Quality control by DNA repair. *Science* **1999**, *286*, 1897-1905.
50. Cleaver, J. E.; Lam, E. T.; Revet, I. Disorders of nucleotide excision repair: the genetic and molecular basis of heterogeneity. *Nature Reviews Genetics* **2009**, *10*, 756-768.
51. Vermeulen, W.; De Boer, J.; Citterio, E.; Van Gool, A. J.; Van der Horst, G. T. J.; Jaspers, N. G. J.; De Laat, W. L.; Sijbers, A. M.; Van der Spek, P. J.; Sugawara, K. Mammalian nucleotide excision repair and syndromes. *Biochemical Society Transactions* **1997**, *25*, 309-314.
52. Sugawara, K.; Ng, J. M. Y.; Masutani, C.; Iwai, S.; van der Spek, P. J.; Eker, A. P. M.; Hanaoka, F.; Bootsma, D.; Hoeijmakers, J. H. J. Xeroderma pigmentosum group C protein complex is the initiator of global genome nucleotide excision repair. *Molecular Cell* **1998**, *2*, 223-232.
53. Sugawara, K. XPC: its product and biological roles. In *Molecular Mechanisms of Xeroderma Pigmentosum* **2008**, *637*, 47-56.
54. Sugawara, K. Regulation of damage recognition in mammalian global genomic nucleotide excision repair. *Mutation Research/Fundamental and Molecular Mechanisms of Mutagenesis* **2010**, *685*, 29-37.
55. Foustari, M.; Mullenders, L. H. F. Transcription-coupled nucleotide excision repair in mammalian cells: molecular mechanisms and biological effects. *Cell Research* **2008**, *18*, 73-84.
56. Hanawalt, P. C.; Spivak, G. Transcription-coupled DNA repair: two decades of progress and surprises. *Nature reviews Molecular Cell Biology* **2008**, *9*, 958-970.
57. Schiestl, R. H.; Prakash, S. RAD10, an excision repair gene of *Saccharomyces cerevisiae*, is involved in the RAD1 pathway of mitotic recombination. *Molecular and Cellular Biology* **1990**, *10*, 2485-2491.
58. Ahmad, A.; Robinson, A. R.; Duensing, A.; Van Drunen, E.; Beverloo, H. B.; Weisberg, D. B.; Hastly, P.; Hoeijmakers, J. H. J.; Niedernhofer, L. J. ERCC1-XPF endonuclease facilitates DNA double-strand break repair. *Molecular and Cellular Biology* **2008**, *28*, 5082-5092.
59. Niedernhofer, L. J.; Essers, J.; Weeda, G.; Beverloo, B.; De Wit, J.; Muijtjens, M.; Odijk, H.; Hoeijmakers, J. H. J.; Kanaar, R. The structure-specific endonuclease Ercc1—Xpf is required for targeted gene replacement in embryonic stem cells. *The EMBO Journal* **2001**, *20*, 6540-6549.
60. Al-Minawi, A. Z.; Saleh-Gohari, N.; Helleday, T. The ERCC1/XPF endonuclease is required for efficient single-strand annealing and gene conversion in mammalian cells. *Nucleic Acids Research* **2008**, *36*, 1-9.

61. Wood, R. D. Mammalian nucleotide excision repair proteins and interstrand crosslink repair. *Environmental and Molecular Mutagenesis* **2010**, 51, 520-526.
62. Deans, A. J.; West, S. C. DNA interstrand crosslink repair and cancer. *Nature Reviews Cancer* **2011**, 11, 467-480.
63. Kuraoka, I.; Kobertz, W. R.; Ariza, R. R.; Biggerstaff, M.; Essigmann, J. M.; Wood, R. D. Repair of an interstrand DNA cross-link initiated by ERCC1-XPF repair/recombination nuclease. *Journal of Biological Chemistry* **2000**, 275, 26632-26636.
64. Niedernhofer, L. J.; Odijk, H.; Budzowska, M.; Van Drunen, E.; Maas, A.; Theil, A. F.; De Wit, J.; Jaspers, N. G. J.; Beverloo, H. B.; Hoeijmakers, J. H. J. The structure-specific endonuclease Ercc1-Xpf is required to resolve DNA interstrand cross-link-induced double-strand breaks. *Molecular and Cellular Biology* **2004**, 24, 5776-5787.
65. Bhagwat, N.; Olsen, A. L.; Wang, A. T.; Hanada, K.; Stuckert, P.; Kanaar, R.; D'Andrea, A.; Niedernhofer, L. J.; McHugh, P. J. XPF-ERCC1 participates in the Fanconi anemia pathway of cross-link repair. *Molecular and Cellular Biology* **2009**, 29, 6427-6437.
66. Friedberg, E. C.; Walker, G. C.; Siede, W.; Wood, R. D.; Schultz, R. A.; Ellenberger, T. DNA Repair and Mutagenesis. 2nd edn ASM Press. *Washington, DC* **2006**.
67. Hoeijmakers, J. H. J. DNA damage, aging, and cancer. *New England Journal of Medicine* **2009**, 361, 1475-1485.
68. van Duin, M.; de Wit, J.; Odijk, H.; Westerveld, A.; Yasui, A.; Koken, M.; Hoeijmakers, J.; Bootsma, D. Molecular characterization of the human excision repair gene ERCC-1: cDNA cloning and aminoacid homology with the yeast DNA repair gene RAD10. *Cell* **1986**, 44, 913-923.
69. Sijbers, A. M.; van der Spek, P. J.; Odijk, H.; van den Berg, J.; van Duin, M.; Westerveld, A.; Jaspers, N. G. J.; Bootsma, D.; Hoeijmakers, J. H. J. Mutational analysis of the human nucleotide excision repair gene ERCC1. *Nucleic Acids Research* **1996**, 24, 3370-3380.
70. Brookman, K. W.; Lamerdin, J. E.; Thelen, M. P.; Hwang, M.; Reardon, J. T.; Sancar, A.; Zhou, Z.-Q.; Walter, C. A.; Parris, C. N.; Thompson, L. H. ERCC4 (XPF) encodes a human nucleotide excision repair protein with eukaryotic recombination homologs. *Molecular and Cellular Biology* **1996**, 16, 6553-6562.
71. Niedernhofer, L. J.; Garinis, G. A.; Raams, A.; Lalai, A. S.; Robinson, A. R.; Appeldoorn, E.; Odijk, H.; Oostendorp, R.; Ahmad, A.; Van Leeuwen, W. A new progeroid syndrome reveals that genotoxic stress suppresses the somatotroph axis. *Nature* **2006**, 444, 1038-1043.
72. Tsodikov, O. V.; Enzlin, J. H.; Schärer, O. D.; Ellenberger, T. Crystal structure and DNA binding functions of ERCC1, a subunit of the DNA structure-specific endonuclease XPF-ERCC1. *Proceedings of the National Academy of Sciences* **2005**, 102, 11236-11241.

73. Tsodikov, O. V.; Ivanov, D.; Orelli, B.; Staresincic, L.; Shoshani, I.; Oberman, R.; Schärer, O. D.; Wagner, G.; Ellenberger, T. Structural basis for the recruitment of ERCC1-XPF to nucleotide excision repair complexes by XPA. *The EMBO journal* **2007**, *26*, 4768-4776.
74. Tripsianes, K.; Folkers, G.; Eiso, A. B.; Das, D.; Odijk, H.; Jaspers, N. G. J.; Hoeijmakers, J. H. J.; Kaptein, R.; Boelens, R. The structure of the human ERCC1/XPF interaction domains reveals a complementary role for the two proteins in nucleotide excision repair. *Structure* **2005**, *13*, 1849-1858.
75. Choi, Y.-J.; Ryu, K.-S.; Ko, Y.-M.; Chae, Y.-K.; Pelton, J. G.; Wemmer, D. E.; Choi, B.-S. Biophysical characterization of the interaction domains and mapping of the contact residues in the XPF-ERCC1 complex. *Journal of Biological Chemistry* **2005**, *280*, 28644-28652.
76. Gaillard, P.-H. L.; Wood, R. D. Activity of individual ERCC1 and XPF subunits in DNA nucleotide excision repair. *Nucleic Acids Research* **2001**, *29*, 872-879.
77. Sgouros, J.; Gaillard, P.-H. L.; Wood, R. D. A relationship between a DNA-repair/recombination nuclease family and archaeal helicases. *Trends in Biochemical Sciences* **1999**, *24*, 95-97.
78. Nishino, T.; Komori, K.; Tsuchiya, D.; Ishino, Y.; Morikawa, K. Crystal structure and functional implications of *Pyrococcus furiosus* hef helicase domain involved in branched DNA processing. *Structure* **2005**, *13*, 143-153.
79. de Laat, W. L.; Sijbers, A. M.; Odijk, H.; Jaspers, N. G. J.; Hoeijmakers, J. H. J. Mapping of interaction domains between human repair proteins ERCC1 and XPF. *Nucleic Acids Research* **1998**, *26*, 4146-4152.
80. Jaspers, N. G. J.; Raams, A.; Silengo, M. C.; Wijgers, N.; Niedernhofer, L. J.; Robinson, A. R.; Giglia-Mari, G.; Hoogstraten, D.; Kleijer, W. J.; Hoeijmakers, J. H. J. First reported patient with human ERCC1 deficiency has cerebro-oculo-facio-skeletal syndrome with a mild defect in nucleotide excision repair and severe developmental failure. *The American Journal of Human Genetics* **2007**, *80*, 457-466.
81. de Laat, W. L.; Appeldoorn, E.; Jaspers, N. G. J.; Hoeijmakers, J. H. J. DNA structural elements required for ERCC1-XPF endonuclease activity. *Journal of Biological Chemistry* **1998**, *273*, 7835-7842.
82. Jiang, H.; Yang, L.-Y. Cell cycle checkpoint abrogator UCN-01 inhibits DNA repair: association with attenuation of the interaction of XPA and ERCC1 nucleotide excision repair proteins. *Cancer Research* **1999**, *59*, 4529-4534.
83. Barakat, K. H.; Huzil, J. T.; Luchko, T.; Jordheim, L.; Dumontet, C.; Tuszynski, J. Characterization of an inhibitory dynamic pharmacophore for the ERCC1-XPA interaction using a combined molecular dynamics and virtual screening approach. *Journal of Molecular Graphics and Modelling* **2009**, *28*, 113-130.

84. Enzlin, J. H.; Schärer, O. D. The active site of the DNA repair endonuclease XPF–ERCC1 forms a highly conserved nuclease motif. *The EMBO Journal* **2002**, *21*, 2045-2053.
85. Kelley, L. A.; Sternberg, M. J. E. Protein structure prediction on the Web: a case study using the Phyre server. *Nature Protocols* **2009**, *4*, 363-371.
86. Newman, M.; Murray-Rust, J.; Lally, J.; Rudolf, J.; Fadden, A.; Knowles, P. P.; White, M. F.; McDonald, N. Q. Structure of an XPF endonuclease with and without DNA suggests a model for substrate recognition. *The EMBO Journal* **2005**, *24*, 895-905.
87. McNeil, E. M.; Melton, D. W. DNA repair endonuclease ERCC1–XPF as a novel therapeutic target to overcome chemoresistance in cancer therapy. *Nucleic Acids Research* **2012**, *40*, 9990-10004.
88. McNeil, E. M.; Astell, K. R.; Ritchie, A.-M.; Shave, S.; Houston, D. R.; Bakrania, P.; Jones, H. M.; Khurana, P.; Wallace, C.; Chapman, T.; Wear, M. A.; Walkinshaw, M. D.; Saxty, B.; Melton, D. W. Inhibition of the ERCC1–XPF structure-specific endonuclease to overcome cancer chemoresistance. *DNA Repair* **2015**, *31*, 19-28.
89. Chapman, T. M.; Wallace, C.; Gillen, K. J.; Bakrania, P.; Khurana, P.; Coombs, P. J.; Fox, S.; Bureau, E. A.; Brownlees, J.; Melton, D. W.; Saxty, B. N-Hydroxyimides and hydroxypyrimidinones as inhibitors of the DNA repair complex ERCC1–XPF. *Bioorganic & Medicinal Chemistry Letters* **2015**, *25*, 4104-4108.
90. Chapman, T. M.; Gillen, K. J.; Wallace, C.; Lee, M. T.; Bakrania, P.; Khurana, P.; Coombs, P. J.; Stennett, L.; Fox, S.; Bureau, E. A.; Brownlees, J.; Melton, D. W.; Saxty, B. Catechols and 3-hydroxypyridones as inhibitors of the DNA repair complex ERCC1-XPF. *Bioorganic & Medicinal Chemistry Letters* **2015**, *25*, 4097-4103.
91. Arora, S.; Heyza, J.; Zhang, H.; Kalman-Maltese, V.; Tillison, K.; Floyd, A. M.; Chalfin, E. M.; Bepler, G.; Patrick, S. M. Identification of small molecule inhibitors of ERCC1-XPF that inhibit DNA repair and potentiate cisplatin efficacy in cancer cells. *Oncotarget* **2016**, *7*, 75104-75117.
92. Dorjsuren, D.; Kim, D.; Maloney, D. J.; Wilson Iii, D. M.; Simeonov, A. Complementary non-radioactive assays for investigation of human flap endonuclease 1 activity. *Nucleic Acids Research* **2011**, *39*, e11-e22.
93. Tumey, L. N.; Bom, D.; Huck, B.; Gleason, E.; Wang, J.; Silver, D.; Brunden, K.; Boozer, S.; Rundlett, S.; Sherf, B. The identification and optimization of a N-hydroxy urea series of flap endonuclease 1 inhibitors. *Bioorganic & Medicinal Chemistry Letters* **2005**, *15*, 277-281.
94. Tumey, L. N.; Huck, B.; Gleason, E.; Wang, J.; Silver, D.; Brunden, K.; Boozer, S.; Rundlett, S.; Sherf, B.; Murphy, S. The identification and optimization of 2, 4-diketobutyric acids as flap endonuclease 1 inhibitors. *Bioorganic & Medicinal Chemistry Letters* **2004**, *14*, 4915-4918.
95. Huang, F.; Motlekar, N. A.; Burgwin, C. M.; Napper, A. D.; Diamond, S. L.; Mazin, A. V. Identification of specific inhibitors of human RAD51 recombinase using high-throughput screening. *ACS Chemical Biology* **2011**, *6*, 628-635.

96. Rai, G.; Vyjayanti, V. N.; Dorjsuren, D.; Simeonov, A.; Jadhav, A.; Wilson Iii, D. M.; Maloney, D. J. Synthesis, biological evaluation, and structure–activity relationships of a novel class of apurinic/aprimidinic endonuclease 1 inhibitors. *Journal of Medicinal Chemistry* **2012**, *55*, 3101-3112.
97. Manvilla, B. A.; Wauchope, O.; Seley-Radtke, K. L.; Drohat, A. C. NMR studies reveal an unexpected binding site for a redox inhibitor of AP endonuclease 1. *Biochemistry* **2011**, *50*, 10540-10549.
98. Vassilev, L. T.; Vu, B. T.; Graves, B.; Carvajal, D.; Podlaski, F.; Filipovic, Z.; Kong, N.; Kammlott, U.; Lukacs, C.; Klein, C. In vivo activation of the p53 pathway by small-molecule antagonists of MDM2. *Science* **2004**, *303*, 844-848.
99. Tsodikov, O. V.; Enzlin, J. H.; Schärer, O. D.; Ellenberger, T. Crystal structure and DNA binding functions of ERCC1, a subunit of the DNA structure-specific endonuclease XPF–ERCC1. *Proceedings of the National Academy of Sciences of the United States of America* **2005**, *102*, 11236-11241.
100. McNeil, E. M.; Astell, K. R.; Ritchie, A.-M.; Shave, S.; Houston, D. R.; Bakrania, P.; Jones, H. M.; Khurana, P.; Wallace, C.; Chapman, T. Inhibition of the ERCC1–XPF structure-specific endonuclease to overcome cancer chemoresistance. *DNA Repair* **2015**, *31*, 19-28.
101. Arora, S.; Heyza, J.; Zhang, H.; Kalman-Maltese, V.; Tillison, K.; Floyd, A. M.; Chalfin, E. M.; Bepler, G.; Patrick, S. M. Identification of small molecule inhibitors of ERCC1-XPF that inhibit DNA repair and potentiate cisplatin efficacy in cancer cells. *Oncotarget* **2016**.
102. Song, L.; Ritchie, A. M.; McNeil, E. M.; Li, W.; Melton, D. W. Identification of DNA repair gene Ercc1 as a novel target in melanoma. *Pigment Cell & Melanoma Research* **2011**, *24*, 966-971.
103. Jordheim, L. P.; Barakat, K. H.; Heinrich-Balard, L.; Matera, E.-L.; Cros-Perrial, E.; Bouledrak, K.; El Sabeh, R.; Perez-Pineiro, R.; Wishart, D. S.; Cohen, R. Small molecule inhibitors of ERCC1-XPF protein-protein interaction synergize alkylating agents in cancer cells. *Molecular Pharmacology* **2013**, *84*, 12-24.
104. Lin, J.-H.; Perryman, A. L.; Schames, J. R.; McCammon, J. A. Computational drug design accommodating receptor flexibility: the relaxed complex scheme. *Journal of the American Chemical Society* **2002**, *124*, 5632-5633.
105. Amaro, R. E.; Baron, R.; McCammon, J. A. An improved relaxed complex scheme for receptor flexibility in computer-aided drug design. *Journal of Computer-Aided Molecular Design* **2008**, *22*, 693-705.

## Chapter 2

1. Sijbers, A. M.; de Laat, W. L.; Ariza, R. R.; Biggerstaff, M.; Wei, Y.-F.; Moggs, J. G.; Carter, K. C.; Shell, B. K.; Evans, E.; de Jong, M. C. Xeroderma pigmentosum group F caused by a defect in a structure-specific DNA repair endonuclease. *Cell* **1996**, 86, 811-822.
2. McNeil, E. M.; Astell, K. R.; Ritchie, A.-M.; Shave, S.; Houston, D. R.; Bakrania, P.; Jones, H. M.; Khurana, P.; Wallace, C.; Chapman, T.; Wear, M. A.; Walkinshaw, M. D.; Saxty, B.; Melton, D. W. Inhibition of the ERCC1–XPF structure-specific endonuclease to overcome cancer chemoresistance. *DNA Repair* **2015**, 31, 19-28.
3. Friedberg, E. C.; Walker, G. C.; Siede, W.; Wood, R. D.; Schultz, R. A.; Ellenberger, T. DNA Repair and Mutagenesis. 2nd edn ASM.; Press. *Washington, DC* **2006**.
4. McNeil, E. M.; Melton, D. W. DNA repair endonuclease ERCC1–XPF as a novel therapeutic target to overcome chemoresistance in cancer therapy. *Nucleic Acids Research* **2012**, 40, 9990-10004.
5. Douwel, D. K.; Hoogenboom, W. S.; Boonen, R. A. C. M.; Knipscheer, P. Recruitment and positioning determine the specific role of the XPF-ERCC1 endonuclease in interstrand crosslink repair. *The EMBO Journal* **2017**, 36, 2034-2046.
6. Yagi, T.; Katsuya, A.; Koyano, A.; Takebe, H. Sensitivity of group F xeroderma pigmentosum cells to UV and mitomycin C relative to levels of XPF and ERCC1 overexpression. *Mutagenesis* **1998**, 13, 595-599.
7. Gajjar, K. K.; Yadav, D. K.; Kobawala, T. P.; Trivedi, T. I.; Vora, H. H.; Ghosh, N. R. ERCC1 expression in patients with colorectal cancer: a pilot study. *Journal. of Cancer Metastasis and Treatment* **2016**, 2, 471-476.
8. McHugh, P. J.; Spanswick, V. J.; Hartley, J. A. Repair of DNA interstrand crosslinks: molecular mechanisms and clinical relevance. *The Lancet Oncology* **2001**, 2, 483-490.
9. Ahmad, A.; Robinson, A. R.; Duensing, A.; van Drunen, E.; Beverloo, H. B.; Weisberg, D. B.; Hastay, P.; Hoeijmakers, J. H. J.; Niedernhofer, L. J. ERCC1-XPF endonuclease facilitates DNA double-strand break repair. *Molecular and Cellular Biology* **2008**, 28, 5082-5092.
10. De Laat, W. L.; Appeldoorn, E.; Jaspers, N. G. J.; Hoeijmakers, J. H. J. DNA structural elements required for ERCC1-XPF endonuclease activity. *Journal of Biological Chemistry* **1998**, 273, 7835-7842.
11. Gaillard, P.-H. L.; Wood, R. D. Activity of individual ERCC1 and XPF subunits in DNA nucleotide excision repair. *Nucleic Acids Research* **2001**, 29, 872-879.
12. Gentile, F.; Tuszyński, J. A.; Barakat, K. H. New design of nucleotide excision repair (NER) inhibitors for combination cancer therapy. *Journal of Molecular Graphics and Modelling* **2016**, 65, 71-82.

13. Gentile, F.; Barakat, K. H.; Tuszynski, J. A. Computational Characterization of Small Molecules Binding to the Human XPF Active Site and Virtual Screening to Identify Potential New DNA Repair Inhibitors Targeting the ERCC1-XPF Endonuclease. *International Journal of Molecular Sciences* **2018**, *19*, 1328–1341 .
14. Gentile, F.; A Tuszynski, J.; H Barakat, K. Modelling DNA repair pathways: recent advances and future directions. *Current Pharmaceutical Design* **2016**, *22*, 3527-3546.
15. Ahmad, A.; Enzlin, J. H.; Bhagwat, N. R.; Wijgers, N.; Raams, A.; Appeldoorn, E.; Theil, A. F.; Hoeijmakers, J. H. J.; Vermeulen, W.; Jaspers, N. G. J. Mislocalization of XPF-ERCC1 nuclease contributes to reduced DNA repair in XP-F patients. *PLoS Genetics* **2010**, *6*, e1000871-e1000882.
16. De Laat, W. L.; Sijbers, A. M.; Odijk, H.; Jaspers, N. G. J.; Hoeijmakers, J. H. J. Mapping of interaction domains between human repair proteins ERCC1 and XPF. *Nucleic Acids Research* **1998**, *26*, 4146-4152.
17. Tripsianes, K.; Folkers, G.; Eiso, A. B.; Das, D.; Odijk, H.; Jaspers, N. G. J.; Hoeijmakers, J. H. J.; Kaptein, R.; Boelens, R. The structure of the human ERCC1/XPF interaction domains reveals a complementary role for the two proteins in nucleotide excision repair. *Structure* **2005**, *13*, 1849-1858.
18. Choi, Y.-J.; Ryu, K.-S.; Ko, Y.-M.; Chae, Y.-K.; Pelton, J. G.; Wemmer, D. E.; Choi, B.-S. Biophysical characterization of the interaction domains and mapping of the contact residues in the XPF-ERCC1 complex. *Journal of Biological Chemistry* **2005**, *280*, 28644-28652.
19. Tsodikov, O. V.; Enzlin, J. H.; Schärer, O. D.; Ellenberger, T. Crystal structure and DNA binding functions of ERCC1, a subunit of the DNA structure-specific endonuclease XPF–ERCC1. *Proceedings of the National Academy of Sciences of the United States of America* **2005**, *102*, 11236-11241.
20. McNeil, E. M.; Astell, K. R.; Ritchie, A.-M.; Shave, S.; Houston, D. R.; Bakrania, P.; Jones, H. M.; Khurana, P.; Wallace, C.; Chapman, T. Inhibition of the ERCC1–XPF structure-specific endonuclease to overcome cancer chemoresistance. *DNA Repair* **2015**, *31*, 19-28.
21. Chapman, T. M.; Gillen, K. J.; Wallace, C.; Lee, M. T.; Bakrania, P.; Khurana, P.; Coombs, P. J.; Stennett, L.; Fox, S.; Bureau, E. A. Catechols and 3-hydroxypyridones as inhibitors of the DNA repair complex ERCC1-XPF. *Bioorganic & Medicinal Chemistry Letters* **2015**, *25*, 4097-4103.
22. Chapman, T. M.; Wallace, C.; Gillen, K. J.; Bakrania, P.; Khurana, P.; Coombs, P. J.; Fox, S.; Bureau, E. A.; Brownlees, J.; Melton, D. W. N-Hydroxyimides and hydroxypyrimidinones as inhibitors of the DNA repair complex ERCC1–XPF. *Bioorganic & Medicinal Chemistry Letters* **2015**, *25*, 4104-4108.

23. Arora, S.; Heyza, J.; Zhang, H.; Kalman-Maltese, V.; Tillison, K.; Floyd, A. M.; Chalfin, E. M.; Bepler, G.; Patrick, S. M. Identification of small molecule inhibitors of ERCC1-XPF that inhibit DNA repair and potentiate cisplatin efficacy in cancer cells. *Oncotarget* **2016**, *7*, 75104-75117.
24. Yang, L.; Ritchie, A.-M.; Melton, D. W. Disruption of DNA repair in cancer cells by ubiquitination of a destabilising dimerization domain of nucleotide excision repair protein ERCC1. *Oncotarget* **2017**, *8*, 55246-55264.
25. Jordheim, L. P.; Barakat, K. H.; Heinrich-Balard, L.; Matera, E.-L.; Cros-Perrial, E.; Bouledrak, K.; El Sabeh, R.; Perez-Pineiro, R.; Wishart, D. S.; Cohen, R. Small molecule inhibitors of ERCC1-XPF protein-protein interaction synergize alkylating agents in cancer cells. *Molecular Pharmacology* **2013**, *84*, 12-24.
26. Chapman, T. M.; Gillen, K. J.; Wallace, C.; Lee, M. T.; Bakrania, P.; Khurana, P.; Coombs, P. J.; Stennett, L.; Fox, S.; Bureau, E. A.; Brownlees, J.; Melton, D. W.; Saxty, B. Catechols and 3-hydroxypyridones as inhibitors of the DNA repair complex ERCC1-XPF. *Bioorganic & Medicinal Chemistry Letters* **2015**, *25*, 4097-4103.
27. Arora, S.; Heyza, J.; Zhang, H.; Kalman-Maltese, V.; Tillison, K.; Floyd, A. M.; Chalfin, E. M.; Bepler, G.; Patrick, S. M. Identification of small molecule inhibitors of ERCC1-XPF that inhibit DNA repair and potentiate cisplatin efficacy in cancer cells. *Oncotarget* **2016**, *7*, 75104-75117.
28. Scurr, M.; Pembroke, T.; Bloom, A.; Roberts, D.; Thomson, A.; Smart, K.; Bridgeman, H.; Adams, R.; Brewster, A.; Jones, R.; Gwynne, S.; Blount, D.; Harrop, R.; Hills, R.; Gallimore, A.; Godkin, A. Low-Dose Cyclophosphamide Induces Antitumor T-Cell Responses, which Associate with Survival in Metastatic Colorectal Cancer. *Clinical Cancer Research : an Official Journal of the American Association for Cancer Research* **2017**, *23*, 6771-6780.
29. Bowles, M.; Lally, J.; Fadden, A. J.; Mouilleron, S.; Hammonds, T.; McDonald, N. Q. Fluorescence-based incision assay for human XPF-ERCC1 activity identifies important elements of DNA junction recognition. *Nucleic Acids Research* **2012**, *40*, e101-e101.
30. Mani, R. S.; Karimi-Busheri, F.; Fanta, M.; Caldecott, K. W.; Cass, C. E.; Weinfeld, M. Biophysical characterization of human XRCC1 and its binding to damaged and undamaged DNA. *Biochemistry* **2004**, *43*, 16505-16514.
31. Jerabek-Willemsen, M.; Wienken, C. J.; Braun, D.; Baaske, P.; Duhr, S. Molecular interaction studies using microscale thermophoresis. *Assay and Drug Development Technologies* **2011**, *9*, 342-353.
32. Wienken, C. J.; Baaske, P.; Rothbauer, U.; Braun, D.; Duhr, S. Protein-binding assays in biological liquids using microscale thermophoresis. *Nature communications* **2010**, *1*, 100-107.
33. Zillner, K.; Jerabek-Willemsen, M.; Duhr, S.; Braun, D.; Längst, G.; Baaske, P. Microscale thermophoresis as a sensitive method to quantify protein: nucleic acid interactions in solution. In *Functional Genomics*, Springer: 2012; pp 241-252.

34. Mirzayans, R.; Pollock, S.; Scott, A.; Gao, C. Q.; Murray, D. Metabolic labeling of human cells with tritiated nucleosides results in activation of the ATM-dependent p53 signaling pathway and acceleration of DNA repair. *Oncogene* **2003**, *22*, 5562-5571.
35. Philippopoulos, M.; Lim, C. Exploring the dynamic information content of a protein NMR structure: Comparison of a molecular dynamics simulation with the NMR and X-ray structures of Escherichia coli ribonuclease HI. *Proteins: Structure, Function, and Bioinformatics* **1999**, *36*, 87-110.
36. Ishima, R.; Torchia, D. A. Protein dynamics from NMR. *Nature Structural & Molecular Biology* **2000**, *7*, 740-743.
37. Berman, H. M.; Westbrook, J.; Feng, Z.; Gilliland, G.; Bhat, T. N.; Weissig, H.; Shindyalov, I. N.; Bourne, P. E. The Protein Data Bank. *Nucleic Acids Research* **2000**, *28*, 235-242.
38. Morris, G. M.; Goodsell, D. S.; Halliday, R. S.; Huey, R.; Hart, W. E.; Belew, R. K.; Olson, A. J. Automated docking using a Lamarckian genetic algorithm and an empirical binding free energy function. *Journal of Computational Chemistry* **1998**, *19*, 1639-1662.
39. Huey, R.; Morris, G. M.; Olson, A. J.; Goodsell, D. S. A semiempirical free energy force field with charge-based desolvation. *Journal of Computational Chemistry* **2007**, *28*, 1145-1152.
40. Morris, G. M.; Huey, R.; Lindstrom, W.; Sanner, M. F.; Belew, R. K.; Goodsell, D. S.; Olson, A. J. AutoDock4 and AutoDockTools4: Automated docking with selective receptor flexibility. *Journal of Computational Chemistry* **2009**, *30*, 2785-2791.
41. Chemical Computing Group, I. *Molecular Operating Environment (MOE)*, 2013.08; **2017**.
42. Lin, A. Overview of Pharmacophore Applications in MOE. In **2004**.
43. Schrödinger. LigPrep. In **2013**.
44. Labute, P. The generalized Born/volume integral implicit solvent model: estimation of the free energy of hydration using London dispersion instead of atomic surface area. *Journal of Computational Chemistry* **2008**, *29*, 1693-1698.
45. Wildman, S. A.; Crippen, G. M. Prediction of physicochemical parameters by atomic contributions. *Journal of Chemical Information and Computer Sciences* **1999**, *39*, 868-873.
46. Miller Iii, B. R.; McGee Jr, T. D.; Swails, J. M.; Homeyer, N.; Gohlke, H.; Roitberg, A. E. MMPBSA. py: an efficient program for end-state free energy calculations. *Journal of Chemical Theory and Computation* **2012**, *8*, 3314-3321.
47. Kassem, S.; Ahmed, M.; El-Sheikh, S.; Barakat, K. H. Entropy in bimolecular simulations: A comprehensive review of atomic fluctuations-based methods. *Journal of Molecular Graphics and Modelling* **2015**, *62*, 105-117.

## Chapter 3

1. López-Otín, C.; Blasco, M. A.; Partridge, L.; Serrano, M.; Kroemer, G. The hallmarks of aging. *Cell* **2013**, 153, 1194-1217.
2. Hanahan, D.; Weinberg, R. A. Hallmarks of cancer: the next generation. *Cell* **2011**, 144, 646-674.
3. Bukowska, B.; Karwowski, B. T. Actual state of knowledge in the field of diseases related with defective nucleotide excision repair. *Life Sciences* **2018**, 195, 6-18.
4. Cleaver, J. E.; Lam, E. T.; Revet, I. Disorders of nucleotide excision repair: the genetic and molecular basis of heterogeneity. *Nature Reviews Genetics* **2009**, 10, 756-768.
5. Helleday, T.; Petermann, E.; Lundin, C.; Hodgson, B.; Sharma, R. A. DNA repair pathways as targets for cancer therapy. *Nature Reviews Cancer* **2008**, 8, 193-204.
6. Ohmoto, A.; Yachida, S. Current status of poly (ADP-ribose) polymerase inhibitors and future directions. *OncoTargets and Therapy* **2017**, 10, 5195-5208.
7. Brown, J. S.; O'Carrigan, B.; Jackson, S. P.; Yap, T. A. Targeting DNA repair in cancer: beyond PARP inhibitors. *Cancer Discovery* **2017**, 7, 20-37.
8. McNeil, E. M.; Melton, D. W. DNA repair endonuclease ERCC1–XPF as a novel therapeutic target to overcome chemoresistance in cancer therapy. *Nucleic Acids Research* **2012**, 40, 9990-10004.
9. Faridounnia, M.; Folkers, G. E.; Boelens, R. Function and interactions of ERCC1-XPF in DNA damage response. *Molecules* **2018**, 23, 3205-323.
10. Gentile, F.; Elmenoufy, A. H.; Ciniero, G.; Jay, D.; Karimi-Busheri, F.; Barakat, K. H.; Weinfeld, M.; West, F. G.; Tuszynski, J. A. Computer-aided drug design of small molecule inhibitors of the ERCC1-XPF protein–protein interaction. *Chemical Biology & Drug Design* **2020**, 95, 460-471.
11. Arora, S.; Heyza, J.; Zhang, H.; Kalman-Maltese, V.; Tillison, K.; Floyd, A. M.; Chalfin, E. M.; Bepler, G.; Patrick, S. M. Identification of small molecule inhibitors of ERCC1-XPF that inhibit DNA repair and potentiate cisplatin efficacy in cancer cells. *Oncotarget* **2016**, 7, 75104-75117.
12. Mendoza, J.; Martínez, J.; Hernández, C.; Pérez-Montiel, D.; Castro, C.; Fabián-Morales, E.; Santibáñez, M.; González-Barrios, R.; Díaz-Chávez, J.; Andonegui, M. A. Association between ERCC1 and XPA expression and polymorphisms and the response to cisplatin in testicular germ cell tumours. *British Journal of Cancer* **2013**, 109, 68-75.
13. Gentile, F.; Tuszynski, J. A.; Barakat, K. H. New design of nucleotide excision repair (NER) inhibitors for combination cancer therapy. *Journal of Molecular Graphics and Modelling* **2016**, 65, 71-82.

14. Barakat, K. H.; Jordheim, L. P.; Perez-Pineiro, R.; Wishart, D.; Dumontet, C.; Tuszynski, J. A. Virtual screening and biological evaluation of inhibitors targeting the XPA-ERCC1 interaction. *PloS One* **2012**, *7*.
15. Chapman, T. M.; Wallace, C.; Gillen, K. J.; Bakrania, P.; Khurana, P.; Coombs, P. J.; Fox, S.; Bureau, E. A.; Brownlees, J.; Melton, D. W. N-Hydroxyimides and hydroxypyrimidinones as inhibitors of the DNA repair complex ERCC1–XPF. *Bioorganic & Medicinal Chemistry Letters* **2015**, *25*, 4104-4108.
16. Chapman, T. M.; Gillen, K. J.; Wallace, C.; Lee, M. T.; Bakrania, P.; Khurana, P.; Coombs, P. J.; Stennett, L.; Fox, S.; Bureau, E. A. Catechols and 3-hydroxypyridones as inhibitors of the DNA repair complex ERCC1-XPF. *Bioorganic & Medicinal Chemistry Letters* **2015**, *25*, 4097-4103.
17. McNeil, E. M.; Astell, K. R.; Ritchie, A.-M.; Shave, S.; Houston, D. R.; Bakrania, P.; Jones, H. M.; Khurana, P.; Wallace, C.; Chapman, T. Inhibition of the ERCC1–XPF structure-specific endonuclease to overcome cancer chemoresistance. *DNA Repair* **2015**, *31*, 19-28.
18. Gentile, F.; Barakat, K. H.; Tuszynski, J. A. Computational characterization of small molecules binding to the human XPF active site and virtual screening to identify potential new DNA repair inhibitors targeting the ERCC1-XPF endonuclease. *International Journal of Molecular Sciences* **2018**, *19*, 1328-1341.
19. Jordheim, L. P.; Barakat, K. H.; Heinrich-Balard, L.; Matera, E.-L.; Cros-Perrial, E.; Bouletrad, K.; El Sabeh, R.; Perez-Pineiro, R.; Wishart, D. S.; Cohen, R. Small molecule inhibitors of ERCC1-XPF protein-protein interaction synergize alkylating agents in cancer cells. *Molecular Pharmacology* **2013**, *84*, 12-24.
20. Elmenoufy, A. H.; Gentile, F.; Jay, D.; Karimi-Busheri, F.; Yang, X.; Soueidan, O. M.; Weilbeer, C.; Mani, R. S.; Barakat, K. H.; Tuszynski, J. A.; Weinfeld, M.; West, F. G. Targeting DNA Repair in Tumor Cells via Inhibition of ERCC1–XPF. *Journal of Medicinal Chemistry* **2019**, *62*, 7684-7696.
21. de Laat, W. L.; Sijbers, A. M.; Odijk, H.; Jaspers, N. G. J.; Hoeijmakers, J. H. J. Mapping of interaction domains between human repair proteins ERCC1 and XPF. *Nucleic Acids Research* **1998**, *26*, 4146-4152.
22. Sijbers, A. M.; van der Spek, P. J.; Odijk, H.; van den Berg, J.; van Duin, M.; Westerveld, A.; Jaspers, N. G. J.; Bootsma, D.; Hoeijmakers, J. H. J. Mutational analysis of the human nucleotide excision repair gene ERCC1. *Nucleic Acids Research* **1996**, *24*, 3370-3380.
23. Tripsianes, K.; Folkers, G.; Eiso, A. B.; Das, D.; Odijk, H.; Jaspers, N. G. J.; Hoeijmakers, J. H. J.; Kaptein, R.; Boelens, R. The structure of the human ERCC1/XPF interaction domains reveals a complementary role for the two proteins in nucleotide excision repair. *Structure* **2005**, *13*, 1849-1858.

24. Anandkrishnan, R.; Aguilar, B.; Onufriev, A. V. H++ 3.0: automating p K prediction and the preparation of biomolecular structures for atomistic molecular modeling and simulations. *Nucleic Acids Research* **2012**, *40*, W537-W541.
25. Case, D. A.; Babin, V.; Berryman, J.; Betz, R. M.; Cai, Q.; Cerutti, D. S.; Cheatham Iii, T. E.; Darden, T. A.; Duke, R. E.; Gohlke, H. AMBER 14, 2014. *University of California, San Francisco* **2014**.
26. Maier, J. A.; Martinez, C.; Kasavajhala, K.; Wickstrom, L.; Hauser, K. E.; Simmerling, C. ff14SB: improving the accuracy of protein side chain and backbone parameters from ff99SB. *Journal of Chemical Theory and Computation* **2015**, *11*, 3696-3713.
27. Li, P.; Roberts, B. P.; Chakravorty, D. K.; Merz Jr, K. M. Rational design of particle mesh Ewald compatible Lennard-Jones parameters for+ 2 metal cations in explicit solvent. *Journal of Chemical Theory and Computation* **2013**, *9*, 2733-2748.
28. Li, P.; Song, L. F.; Merz Jr, K. M. Systematic parameterization of monovalent ions employing the nonbonded model. *Journal of Chemical Theory and Computation* **2015**, *11*, 1645-1657.
29. Wang, J.; Wolf, R. M.; Caldwell, J. W.; Kollman, P. A.; Case, D. A. Development and testing of a general amber force field. *Journal of Computational Chemistry* **2004**, *25*, 1157-1174.
30. Jakalian, A.; Jack, D. B.; Bayly, C. I. Fast, efficient generation of high-quality atomic charges. AM1-BCC model: II. Parameterization and validation. *Journal of Computational Chemistry* **2002**, *23*, 1623-1641.
31. Jorgensen, W. L.; Chandrasekhar, J.; Madura, J. D.; Impey, R. W.; Klein, M. L. Comparison of simple potential functions for simulating liquid water. *The Journal of Chemical Physics* **1983**, *79*, 926-935.
32. Salomon-Ferrer, R.; Götz, A. W.; Poole, D.; Le Grand, S.; Walker, R. C. Routine microsecond molecular dynamics simulations with AMBER on GPUs. 2. Explicit solvent particle mesh Ewald. *Journal of Chemical Theory and Computation* **2013**, *9*, 3878-3888.
33. Kabsch, W.; Sander, C. Dictionary of protein secondary structure: pattern recognition of hydrogen-bonded and geometrical features. *Biopolymers: Original Research on Biomolecules* **1983**, *22*, 2577-2637.
34. Lin, A. Overview of Pharmacophore Applications in MOE. In 2004.
35. Inc., C. C. G. Molecular Operating Environment (MOE). *Chemical Computing Group Inc., Canada website: <http://www.chemcomp.com>* **2015**.
36. Groom, C. R.; Bruno, I. J.; Lightfoot, M. P.; Ward, S. C. The Cambridge structural database. *Acta Crystallographica Section B: Structural Science, Crystal Engineering and Materials* **2016**, *72*, 171-179.
37. Sterling, T.; Irwin, J. J. ZINC 15–ligand discovery for everyone. *Journal of Chemical Information and Modeling* **2015**, *55*, 2324-2337.

38. Labute, P. The generalized Born/volume integral implicit solvent model: estimation of the free energy of hydration using London dispersion instead of atomic surface area. *Journal of Computational Chemistry* **2008**, *29*, 1693-1698.
39. Wildman, S. A.; Crippen, G. M. Prediction of physicochemical parameters by atomic contributions. *Journal of Chemical Information and Computer Sciences* **1999**, *39*, 868-873.
40. Onufriev, A.; Bashford, D.; Case, D. A. Exploring protein native states and large-scale conformational changes with a modified generalized born model. *Proteins: Structure, Function, and Bioinformatics* **2004**, *55*, 383-394.
41. Miller III, B. R.; McGee Jr, T. D.; Swails, J. M.; Homeyer, N.; Gohlke, H.; Roitberg, A. E. MMPBSA. py: an efficient program for end-state free energy calculations. *Journal of Chemical Theory and Computation* **2012**, *8*, 3314-3321.
42. Genheden, S.; Ryde, U. The MM/PBSA and MM/GBSA methods to estimate ligand-binding affinities. *Expert Opinion on Drug Discovery* **2015**, *10*, 449-461.
43. Weiser, J.; Shenkin, P. S.; Still, W. C. Approximate atomic surfaces from linear combinations of pairwise overlaps (LCPO). *Journal of Computational Chemistry* **1999**, *20*, 217-230.
44. Kassem, S.; Ahmed, M.; El-Sheikh, S.; Barakat, K. H. Entropy in bimolecular simulations: A comprehensive review of atomic fluctuations-based methods. *Journal of Molecular Graphics and Modelling* **2015**, *62*, 105-117.
45. Carlson, W. W.; Cretcher, L. H. The Hydroxyethyl Analog of Quinacrine. *Journal of the American Chemical Society* **1948**, *70*, 597-599.
46. Sriram, D.; Devakaram, R. V.; Dinakaran, M.; Yogeewari, P. Aromatic amino analogues of artemisinin: synthesis and in vivo antimalarial activity. *Medicinal Chemistry Research* **2010**, *19*, 524-532.
47. Bowles, M.; Lally, J.; Fadden, A. J.; Mouilleron, S.; Hammonds, T.; McDonald, N. Q. Fluorescence-based incision assay for human XPF–ERCC1 activity identifies important elements of DNA junction recognition. *Nucleic Acids Research* **2012**, *40*, e101-e101.

## Chapter 4

1. Manandhar, M.; Boulware, K. S.; Wood, R. D. The ERCC1 and ERCC4 (XPF) genes and gene products. *Gene* **2015**, *569*, 153-161.
2. Staresinic, L.; Fagbemi, A. F.; Enzlin, J. H.; Gourdin, A. M.; Wijgers, N.; Dunand-Sauthier, I.; Giglia-Mari, G.; Clarkson, S. G.; Vermeulen, W.; Schärer, O. D. Coordination of dual incision and repair synthesis in human nucleotide excision repair. *The EMBO Journal* **2009**, *28*, 1111-1120.

3. Ahmad, A.; Robinson, A. R.; Duensing, A.; van Drunen, E.; Beverloo, H. B.; Weisberg, D. B.; Hasty, P.; Hoeijmakers, J. H. J.; Niedernhofer, L. J. ERCC1-XPF endonuclease facilitates DNA double-strand break repair. *Molecular and Cellular Biology* **2008**, *28*, 5082-5092.
4. McHugh, P. J.; Spanswick, V. J.; Hartley, J. A. Repair of DNA interstrand crosslinks: molecular mechanisms and clinical relevance. *The Lancet Oncology* **2001**, *2*, 483-490.
5. Yagi, T.; Katsuya, A.; Koyano, A.; Takebe, H. Sensitivity of group F xeroderma pigmentosum cells to UV and mitomycin C relative to levels of XPF and ERCC1 overexpression. *Mutagenesis* **1998**, *13*, 595-599.
6. Sijbers, A. M.; de Laat, W. L.; Ariza, R. R.; Biggerstaff, M.; Wei, Y.-F.; Moggs, J. G.; Carter, K. C.; Shell, B. K.; Evans, E.; de Jong, M. C. Xeroderma pigmentosum group F caused by a defect in a structure-specific DNA repair endonuclease. *Cell* **1996**, *86*, 811-822.
7. Gajjar, K. K.; Yadav, D. K.; Kobawala, T. P.; Trivedi, T. I.; Vora, H. H.; Ghosh, N. R. ERCC1 expression in patients with colorectal cancer: a pilot study. *Journal of Cancer Metastasis and Treatment* **2016**, *12*, 471-476.
8. Tripsianes, K.; Folkers, G.; Eiso, A. B.; Das, D.; Odijk, H.; Jaspers, N. G. J.; Hoeijmakers, J. H. J.; Kaptein, R.; Boelens, R. The structure of the human ERCC1/XPF interaction domains reveals a complementary role for the two proteins in nucleotide excision repair. *Structure* **2005**, *13*, 1849-1858.
9. McNeil, E. M.; Melton, D. W. DNA repair endonuclease ERCC1–XPF as a novel therapeutic target to overcome chemoresistance in cancer therapy. *Nucleic Acids Research* **2012**, *40*, 9990-10004.
10. Tsodikov, O. V.; Enzlin, J. H.; Schärer, O. D.; Ellenberger, T. Crystal structure and DNA binding functions of ERCC1, a subunit of the DNA structure-specific endonuclease XPF–ERCC1. *Proceedings of the National Academy of Sciences* **2005**, *102*, 11236-11241.
11. Choi, Y.-J.; Ryu, K.-S.; Ko, Y.-M.; Chae, Y.-K.; Pelton, J. G.; Wemmer, D. E.; Choi, B.-S. Biophysical characterization of the interaction domains and mapping of the contact residues in the XPF-ERCC1 complex. *Journal of Biological Chemistry* **2005**, *280*, 28644-28652.
12. Gentile, F.; Barakat, K. H.; Tuszynski, J. A. Computational Characterization of Small Molecules Binding to the Human XPF Active Site and Virtual Screening to Identify Potential New DNA Repair Inhibitors Targeting the ERCC1-XPF Endonuclease. *International Journal of Molecular Sciences* **2018**, *19*, 1328-1340.
13. Gentile, F.; Tuszynski, J. A.; Barakat, K. H. New design of nucleotide excision repair (NER) inhibitors for combination cancer therapy. *Journal of Molecular Graphics and Modelling* **2016**, *65*, 71-82.
14. Gentile, F.; Tuszynski, J.; Barakat, K. H. Modelling DNA repair pathways: recent advances and future directions. *Current Pharmaceutical Design* **2016**, *22*, 3527-3546.

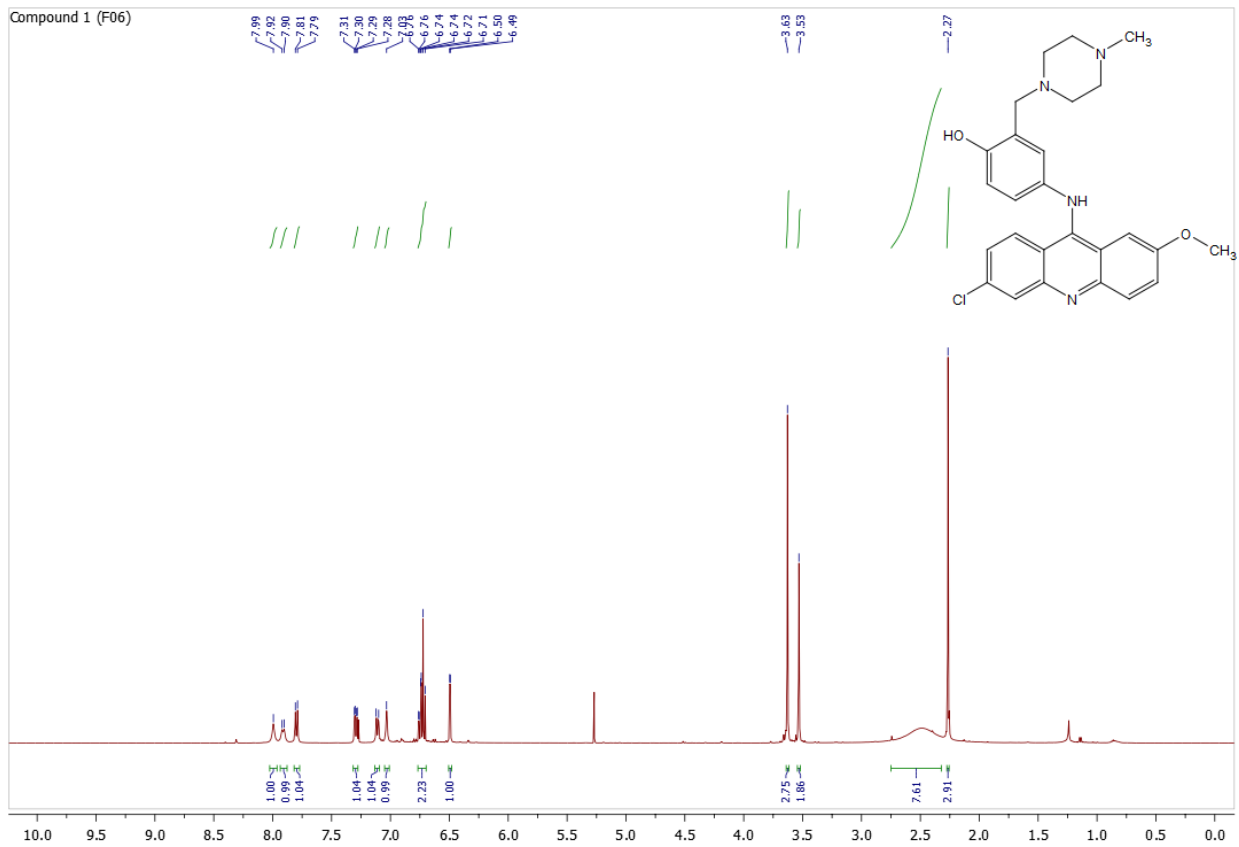
15. Yang, L.; Ritchie, A.-M.; Melton, D. W. Disruption of DNA repair in cancer cells by ubiquitination of a destabilising dimerization domain of nucleotide excision repair protein ERCC1. *Oncotarget* **2017**, *8*, 55246-55264.
16. Arora, S.; Heyza, J.; Zhang, H.; Kalman-Maltese, V.; Tillison, K.; Floyd, A. M.; Chalfin, E. M.; Bepler, G.; Patrick, S. M. Identification of small molecule inhibitors of ERCC1-XPF that inhibit DNA repair and potentiate cisplatin efficacy in cancer cells. *Oncotarget* **2016**, *7*, 75104-75117.
17. Chapman, T. M.; Wallace, C.; Gillen, K. J.; Bakrania, P.; Khurana, P.; Coombs, P. J.; Fox, S.; Bureau, E. A.; Brownlees, J.; Melton, D. W. N-Hydroxyimides and hydroxypyrimidinones as inhibitors of the DNA repair complex ERCC1-XPF. *Bioorganic & Medicinal Chemistry Letters* **2015**, *25*, 4104-4108.
18. Chapman, T. M.; Gillen, K. J.; Wallace, C.; Lee, M. T.; Bakrania, P.; Khurana, P.; Coombs, P. J.; Stennett, L.; Fox, S.; Bureau, E. A. Catechols and 3-hydroxypyridones as inhibitors of the DNA repair complex ERCC1-XPF. *Bioorganic & Medicinal Chemistry Letters* **2015**, *25*, 4097-4103.
19. McNeil, E. M.; Astell, K. R.; Ritchie, A.-M.; Shave, S.; Houston, D. R.; Bakrania, P.; Jones, H. M.; Khurana, P.; Wallace, C.; Chapman, T.; Wear, M. A.; Walkinshaw, M. D.; Saxty, B.; Melton, D. W. Inhibition of the ERCC1-XPF structure-specific endonuclease to overcome cancer chemoresistance. *DNA Repair* **2015**, *31*, 19-28.
20. Jordheim, L. P.; Barakat, K. H.; Heinrich-Balard, L.; Matera, E.-L.; Cros-Perrial, E.; Bouledrak, K.; El Sabeh, R.; Perez-Pineiro, R.; Wishart, D. S.; Cohen, R. Small molecule inhibitors of ERCC1-XPF protein-protein interaction synergize alkylating agents in cancer cells. *Molecular Pharmacology* **2013**, *84*, 12-24.
21. Arora, S.; Heyza, J.; Zhang, H.; Kalman-Maltese, V.; Tillison, K.; Floyd, A. M.; Chalfin, E. M.; Bepler, G.; Patrick, S. M. Identification of small molecule inhibitors of ERCC1-XPF that inhibit DNA repair and potentiate cisplatin efficacy in cancer cells. *Oncotarget* **2016**, *46*, 75104-75117.
22. Elmenoufy, A. H.; Gentile, F.; Jay, D.; Karimi-Busheri, F.; Yang, X.; Soueidan, O. M.; Weilbeer, C.; Mani, R. S.; Barakat, K. H.; Tuszynski, J. A.; Weinfeld, M.; West, F. G. Targeting DNA Repair in Tumor Cells via Inhibition of ERCC1-XPF. *Journal of Medicinal Chemistry* **2019**, *62*, 7684-7696.
23. Gentile, F.; Elmenoufy, A. H.; Ciniero, G.; Jay, D.; Karimi-Busheri, F.; Barakat, K. H.; Weinfeld, M.; West, F. G.; Tuszynski, J. A. Computer-Aided Drug Design of Small Molecule Inhibitors of the ERCC1-XPF Protein-Protein Interaction. *Chemical Biology & Drug Design* **2020**, *00*, 1-12.
24. Kelley, R. K.; Hwang, J.; Magbanua, M. J. M.; Watt, L.; Beumer, J. H.; Christner, S. M.; Baruchel, S.; Wu, B.; Fong, L.; Yeh, B. M.; Moore, A. P.; Ko, A. H.; Korn, W. M.; Rajpal, S.; Park, J. W.; Tempero, M. A.; Venook, A. P.; Bergsland, E. K. A phase 1 trial of imatinib,

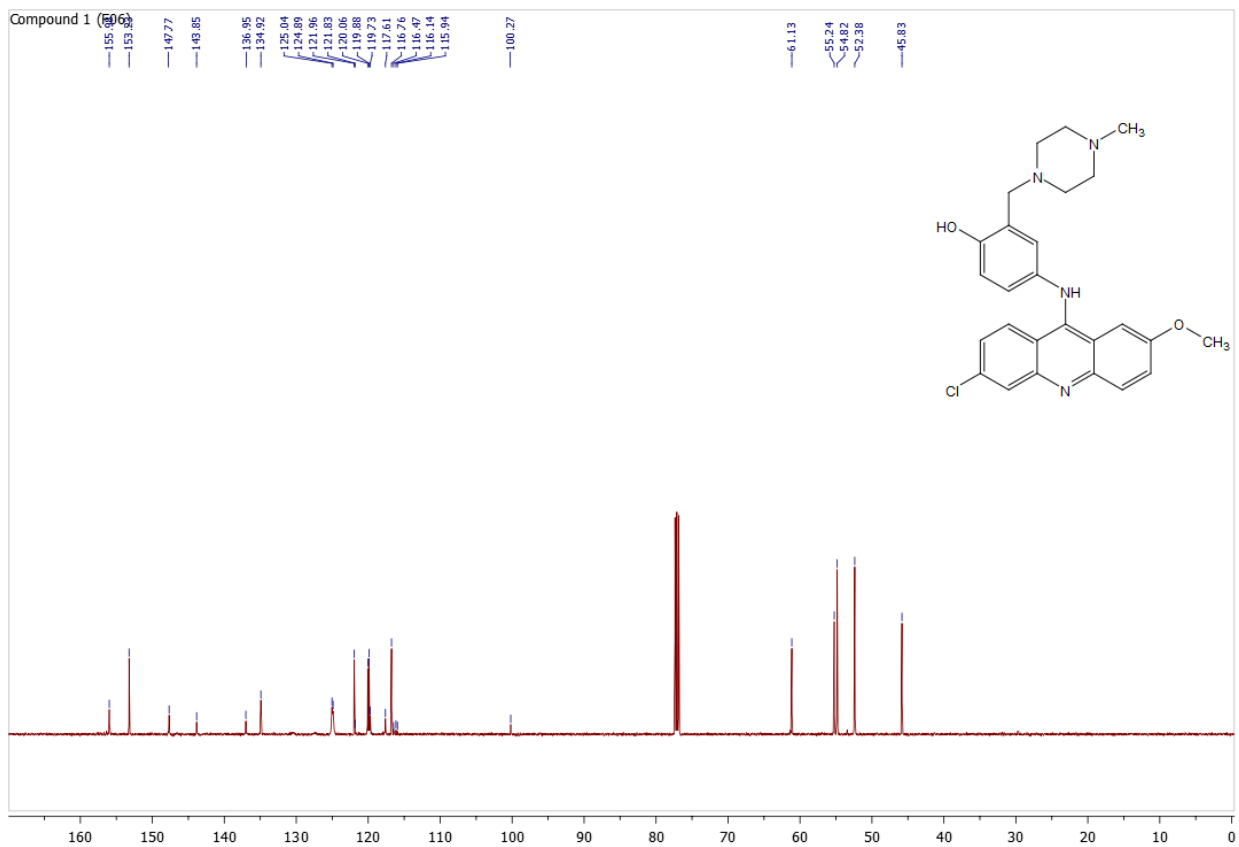
- bevacizumab, and metronomic cyclophosphamide in advanced colorectal cancer. *British Journal of Cancer* **2013**, 109, 1725-1734.
25. Cremolini, C.; Marmorino, F.; Bergamo, F.; Aprile, G.; Salvatore, L.; Masi, G.; Dell'Aquila, E.; Antoniotti, C.; Murgioni, S.; Allegrini, G. Phase II randomised study of maintenance treatment with bevacizumab or bevacizumab plus metronomic chemotherapy after first-line induction with FOLFOXIRI plus Bevacizumab for metastatic colorectal cancer patients: the MOMA trial. *European Journal of Cancer* **2019**, 109, 175-182.
26. Bowles, M.; Lally, J.; Fadden, A. J.; Mouilleron, S.; Hammonds, T.; McDonald, N. Q. Fluorescence-based incision assay for human XPF-ERCC1 activity identifies important elements of DNA junction recognition. *Nucleic Acids Research* **2012**, 40, 101-112.
27. Kourounakis, A. P.; Xanthopoulos, D.; Tzara, A. Morpholine as a privileged structure: A review on the medicinal chemistry and pharmacological activity of morpholine containing bioactive molecules. *Medicinal Research Reviews* **2019**, 1-44.
28. Mani, R. S.; Karimi-Busheri, F.; Fanta, M.; Caldecott, K. W.; Cass, C. E.; Weinfeld, M. Biophysical characterization of human XRCC1 and its binding to damaged and undamaged DNA. *Biochemistry* **2004**, 43, 16505-16514.
29. Carlson, W. W.; Cretcher, L. H. The Hydroxyethyl Analog of Quinacrine. *Journal of the American Chemical Society* **1948**, 70, 597-599.
30. Sriram, D.; Devakaram, R. V.; Dinakaran, M.; Yogeewari, P. Aromatic amino analogues of artemisinin: synthesis and *in-vivo* antimalarial activity. *Medicinal Chemistry Research* **2010**, 19, 524-532.
31. McNeil, E. M.; Astell, K. R.; Ritchie, A.-M.; Shave, S.; Houston, D. R.; Bakrania, P.; Jones, H. M.; Khurana, P.; Wallace, C.; Chapman, T. Inhibition of the ERCC1-XPF structure-specific endonuclease to overcome cancer chemoresistance. *DNA Repair* **2015**, 31, 19-28.
32. Mirzayans, R.; Pollock, S.; Scott, A.; Gao, C. Q.; Murray, D. Metabolic labeling of human cells with tritiated nucleosides results in activation of the ATM-dependent p53 signaling pathway and acceleration of DNA repair. *Oncogene* **2003**, 22, 5562-5571.
33. Feoktistova, M.; Geserick, P.; Leverkus, M. Crystal violet assay for determining viability of cultured cells. *Cold Spring Harbor Protocols* **2016**, 4, pdb-prot087379.
34. WuXi AppTech Inc., <https://www.wuxiapptec.com>

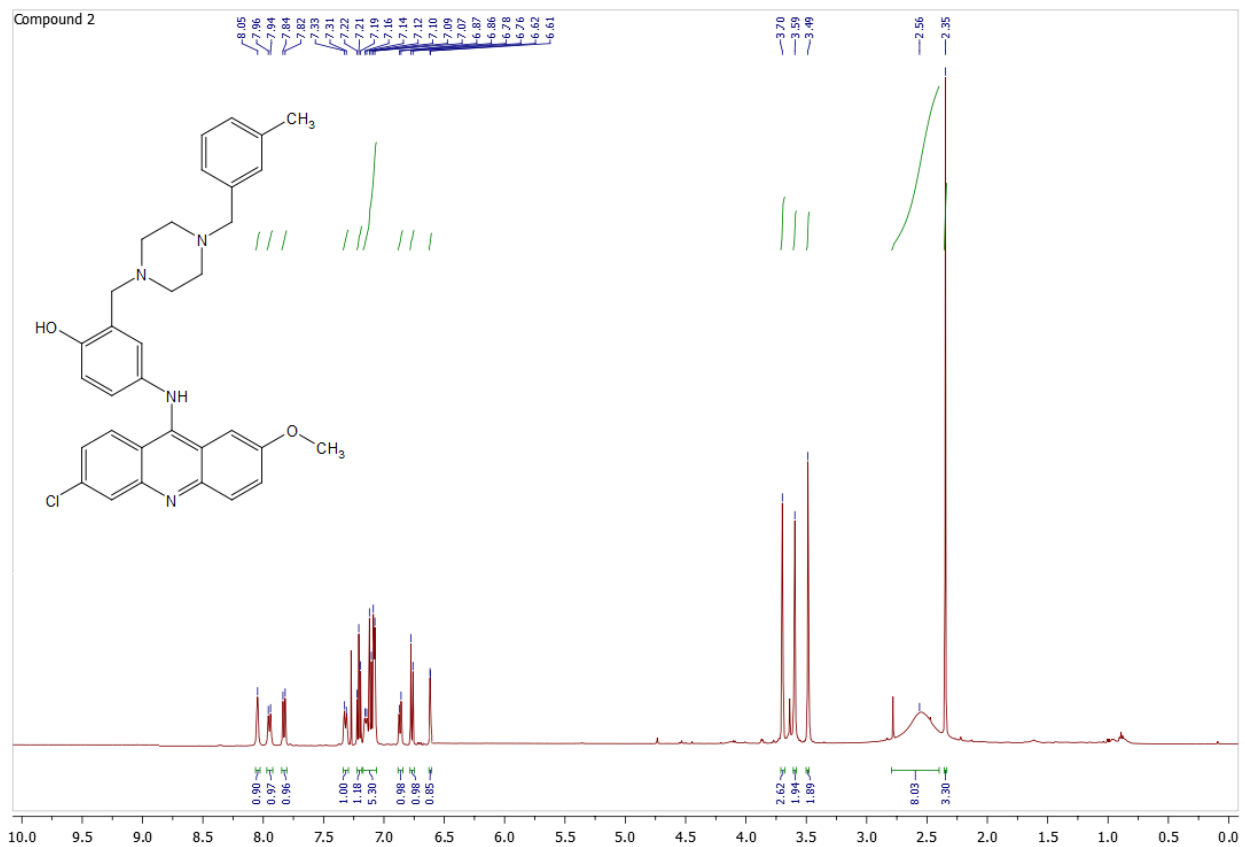
## Chapter 5

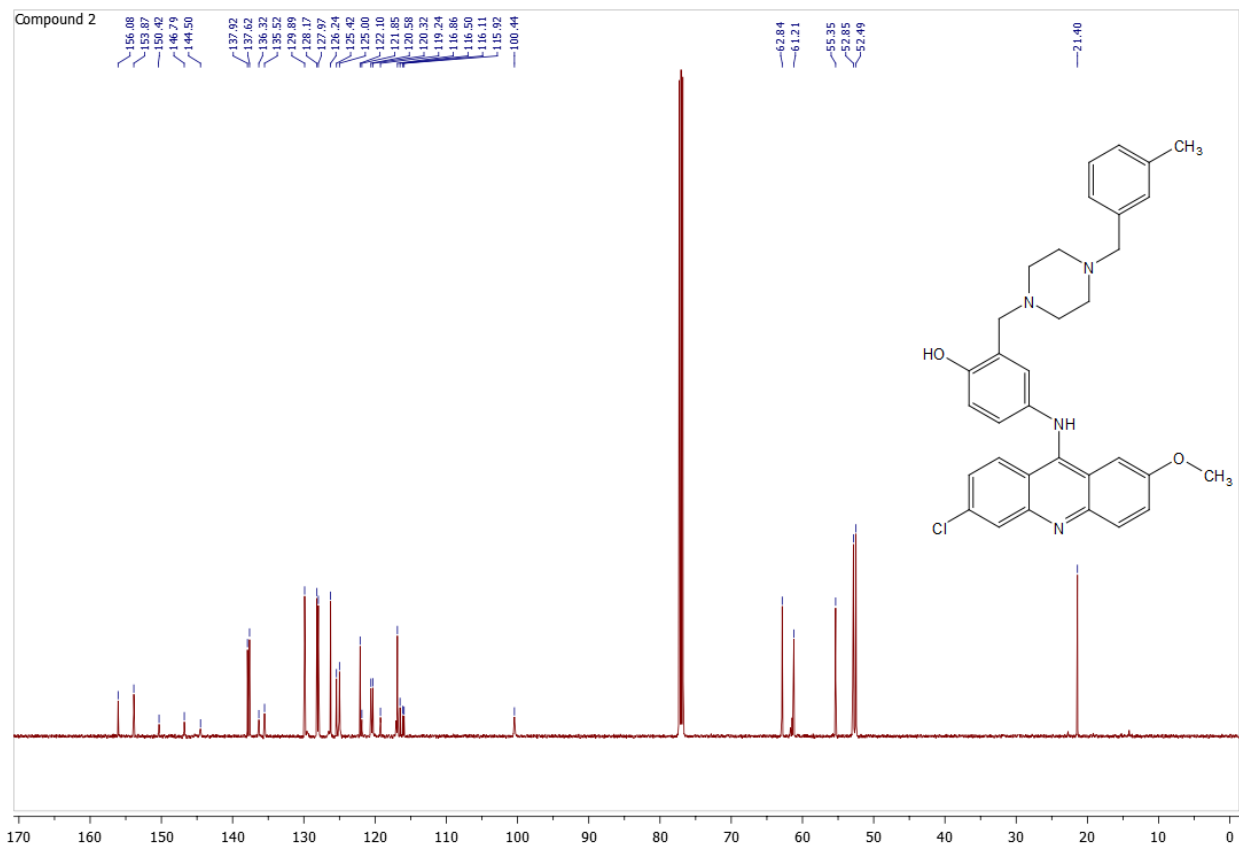
1. Fransson, Å.; Glaessgen, D.; Alfredsson, J.; Wiman, K. G.; Bajalica-Lagercrantz, S.; Mohell, N. Strong synergy with APR-246 and DNA-damaging drugs in primary cancer cells from patients with TP53 mutant High-Grade Serous ovarian cancer. *Journal of Ovarian Research* 2016, 9, 27-37.
2. Paiva, I.; Mattingly, S.; Wuest, M.; Leier, S.; Vakili, M. R.; Weinfeld, M.; Lavasanifar, A.; Wuest, F. Synthesis and analysis of <sup>64</sup>Cu-labeled GE11-modified polymeric micellar nanoparticles for EGFR-targeted molecular imaging in a colorectal cancer model. *Molecular Pharmaceutics* 2020, Just Accpeted.

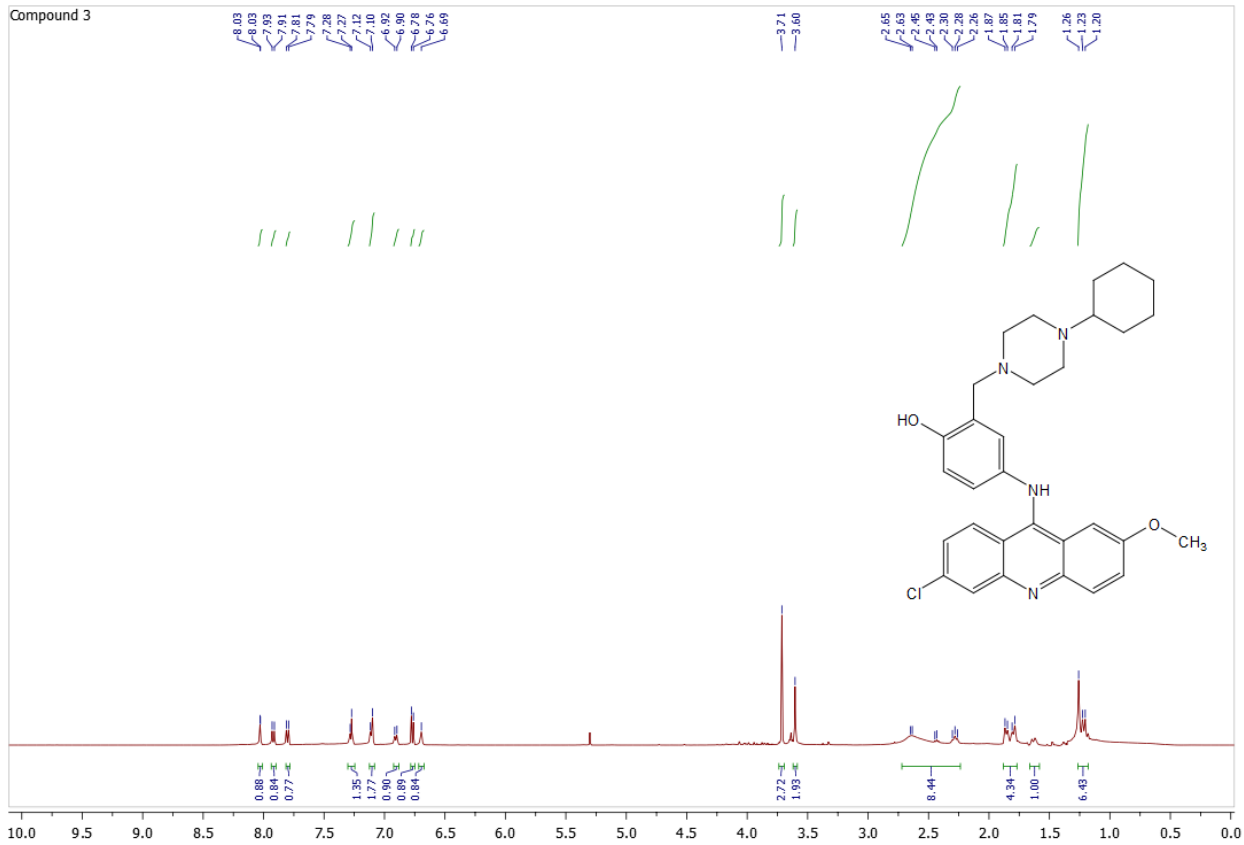
**Appendix I: Selected NMR Spectra**  
**(Chapter 2)**

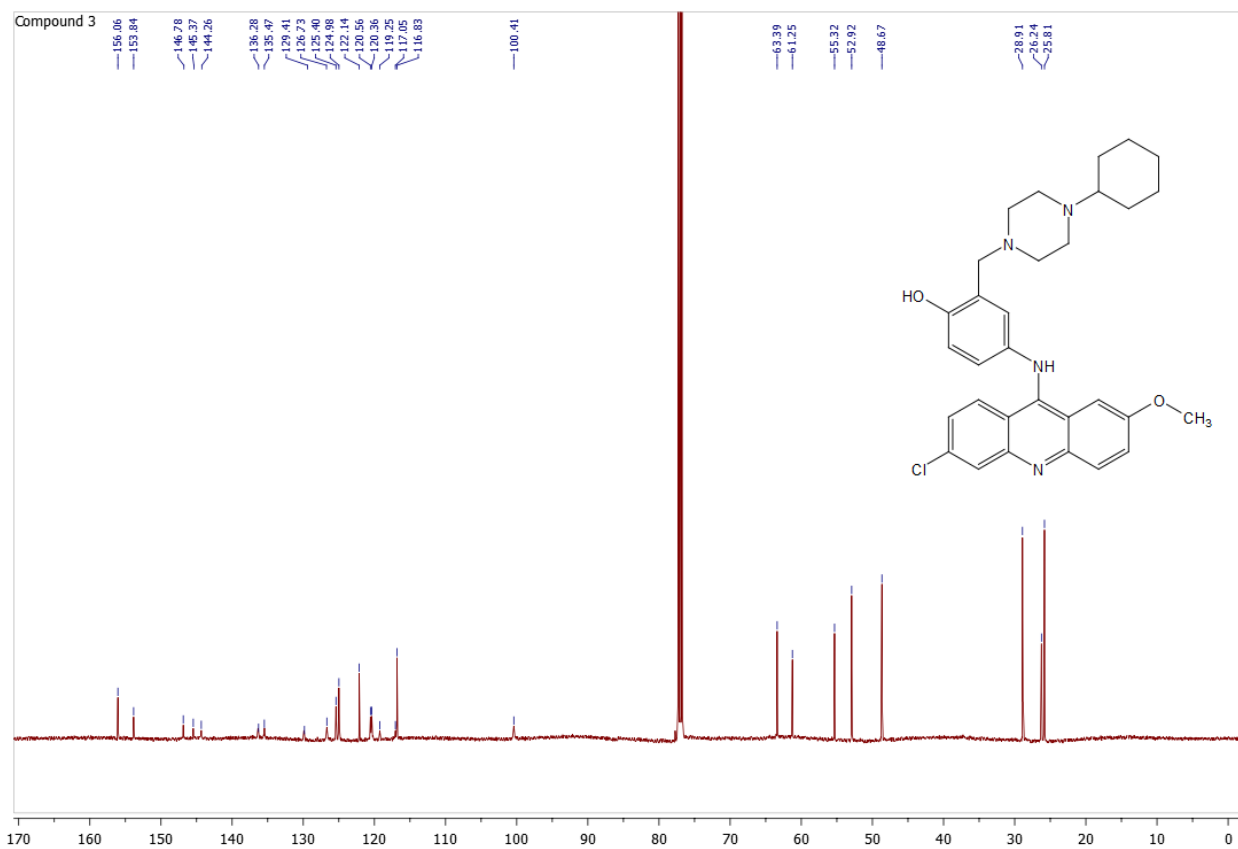


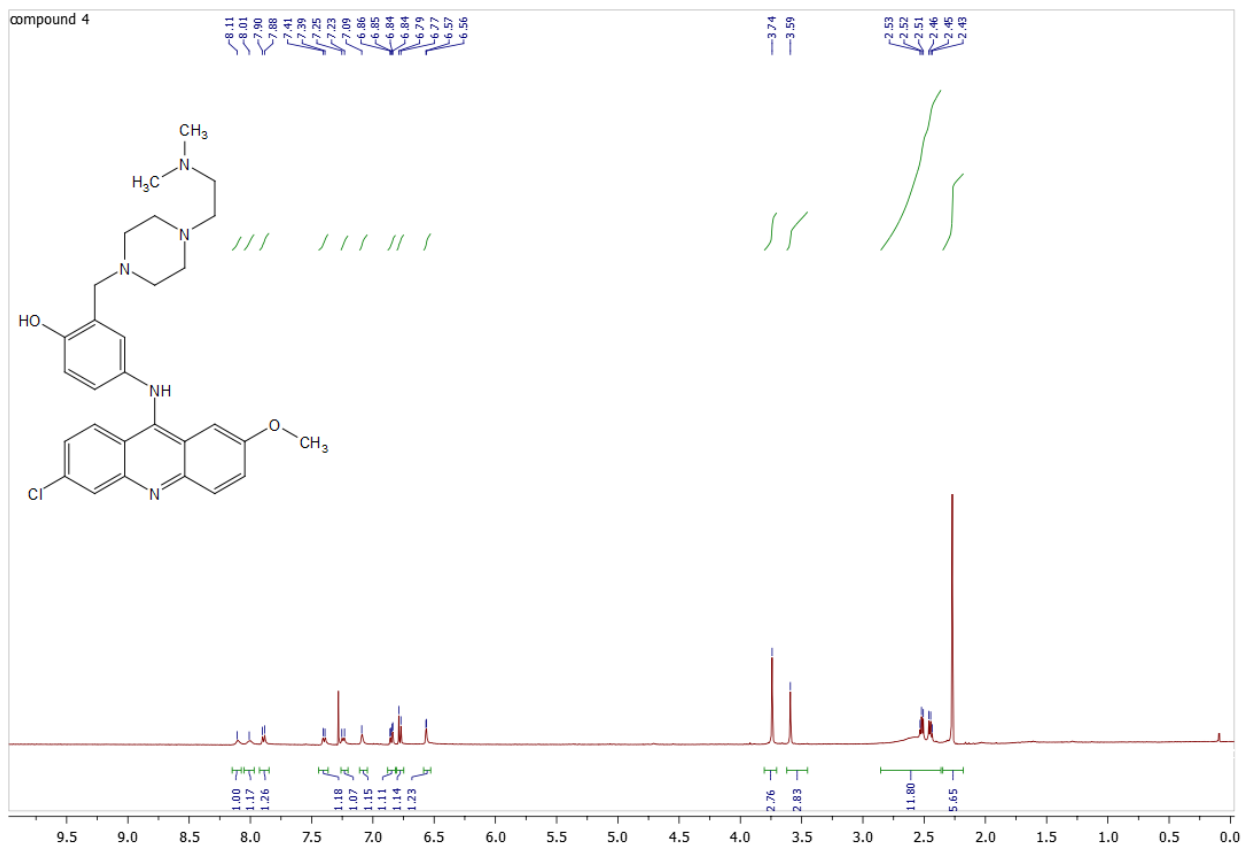


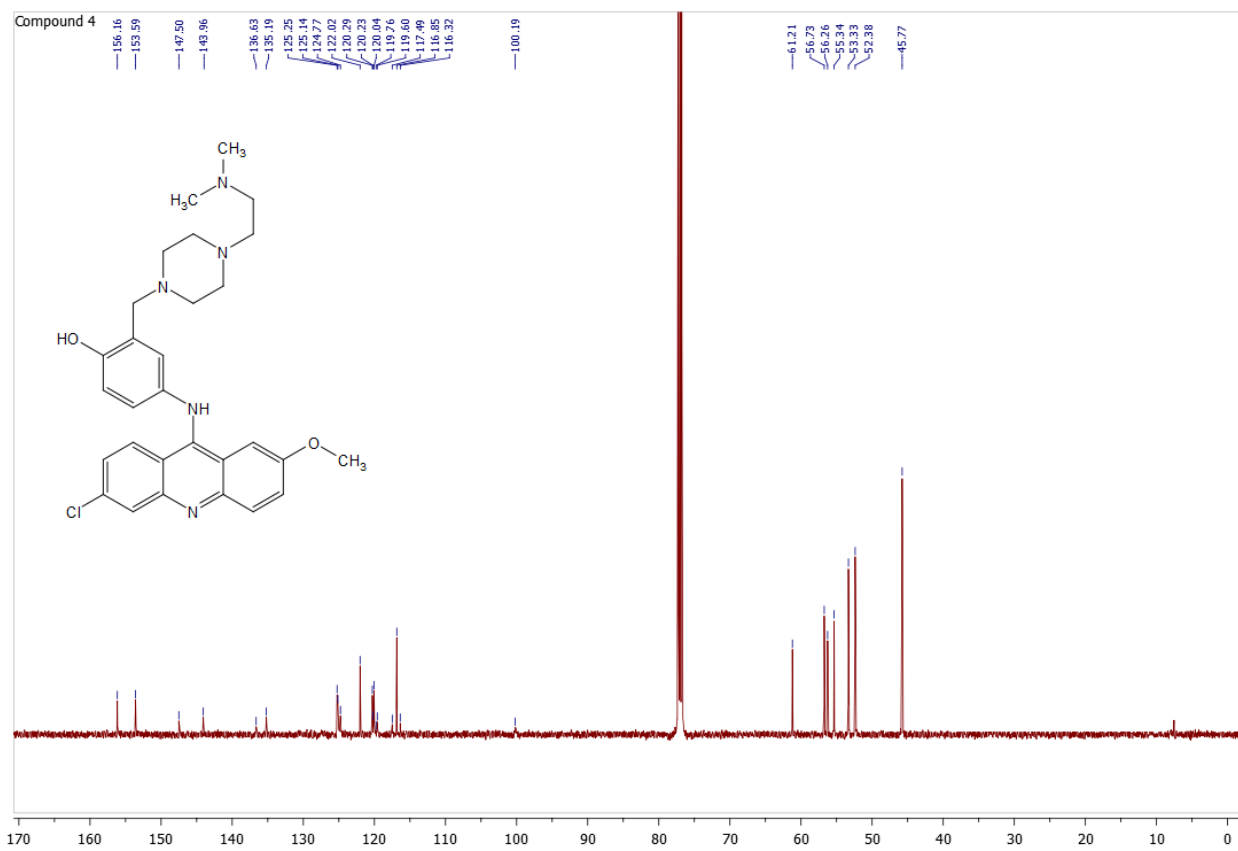


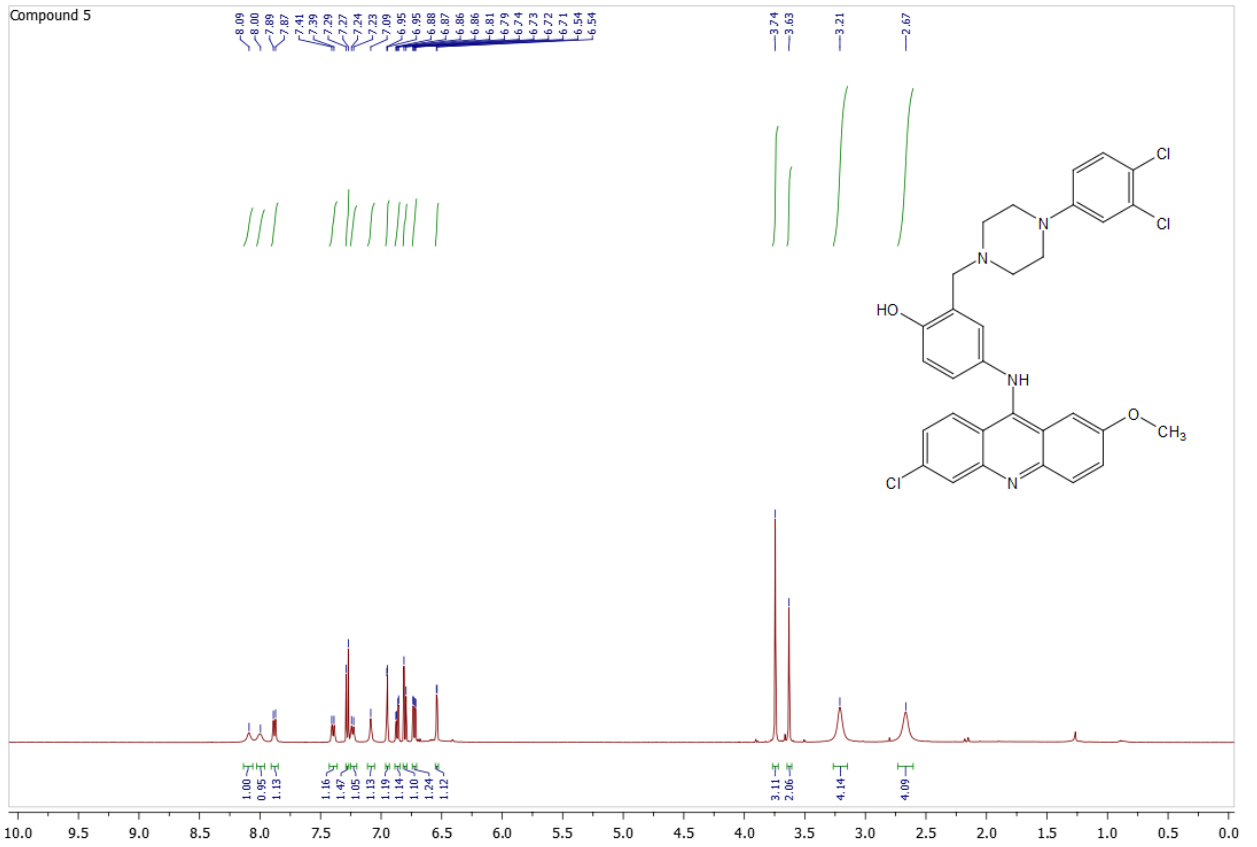


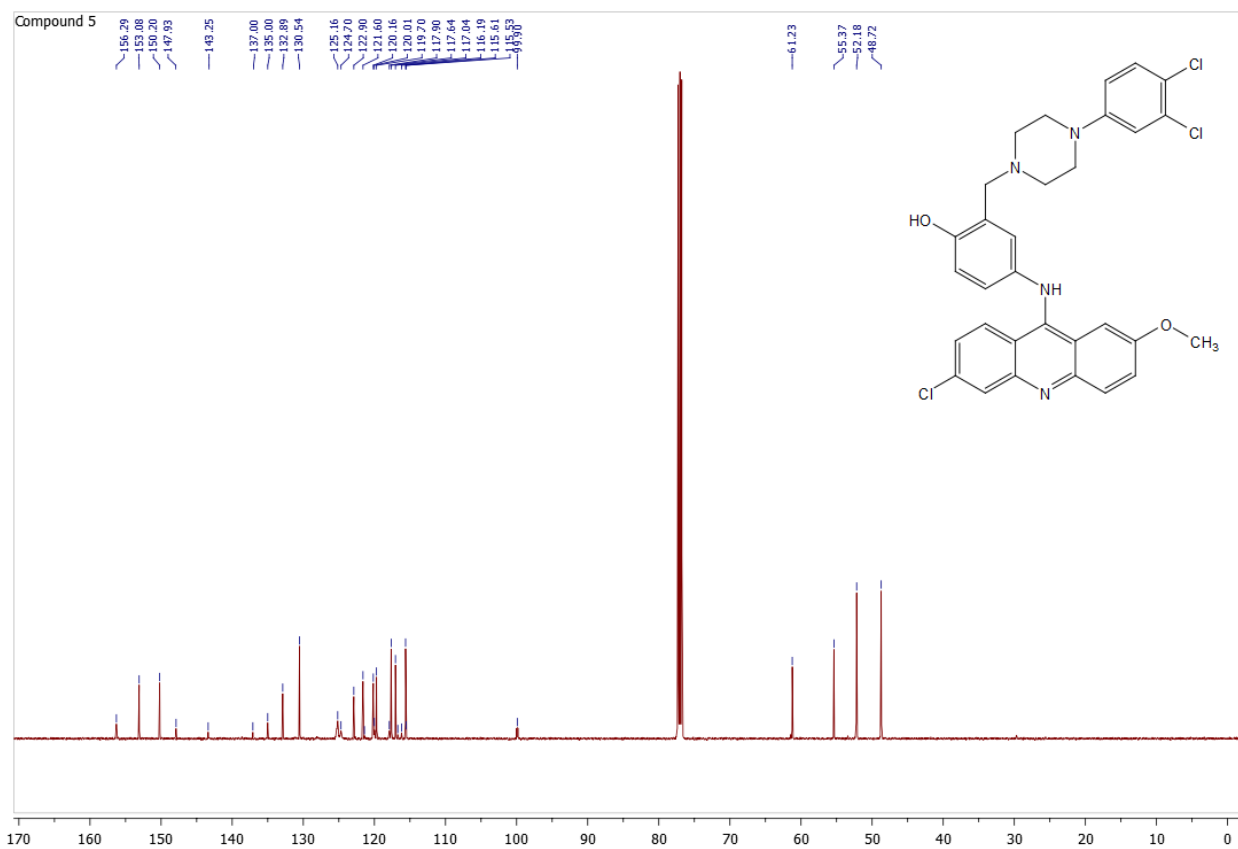


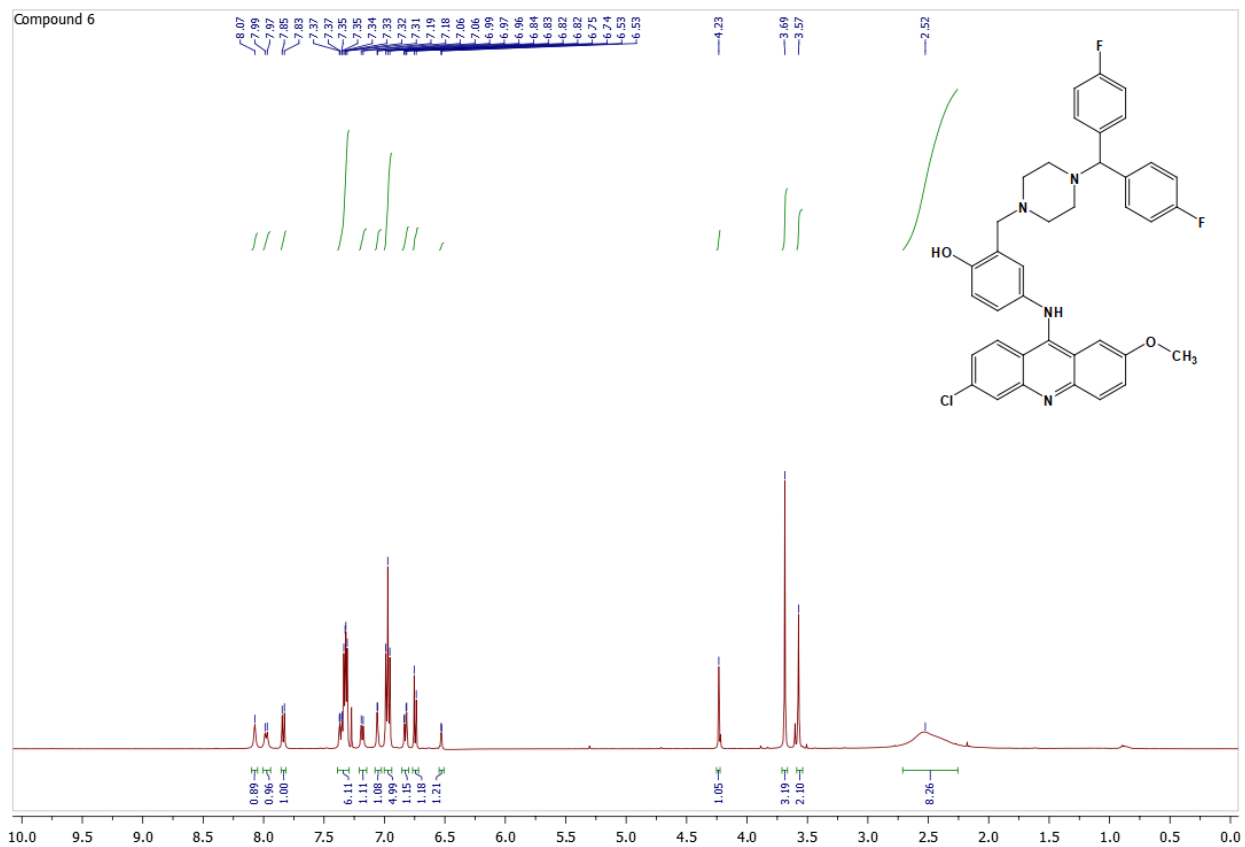


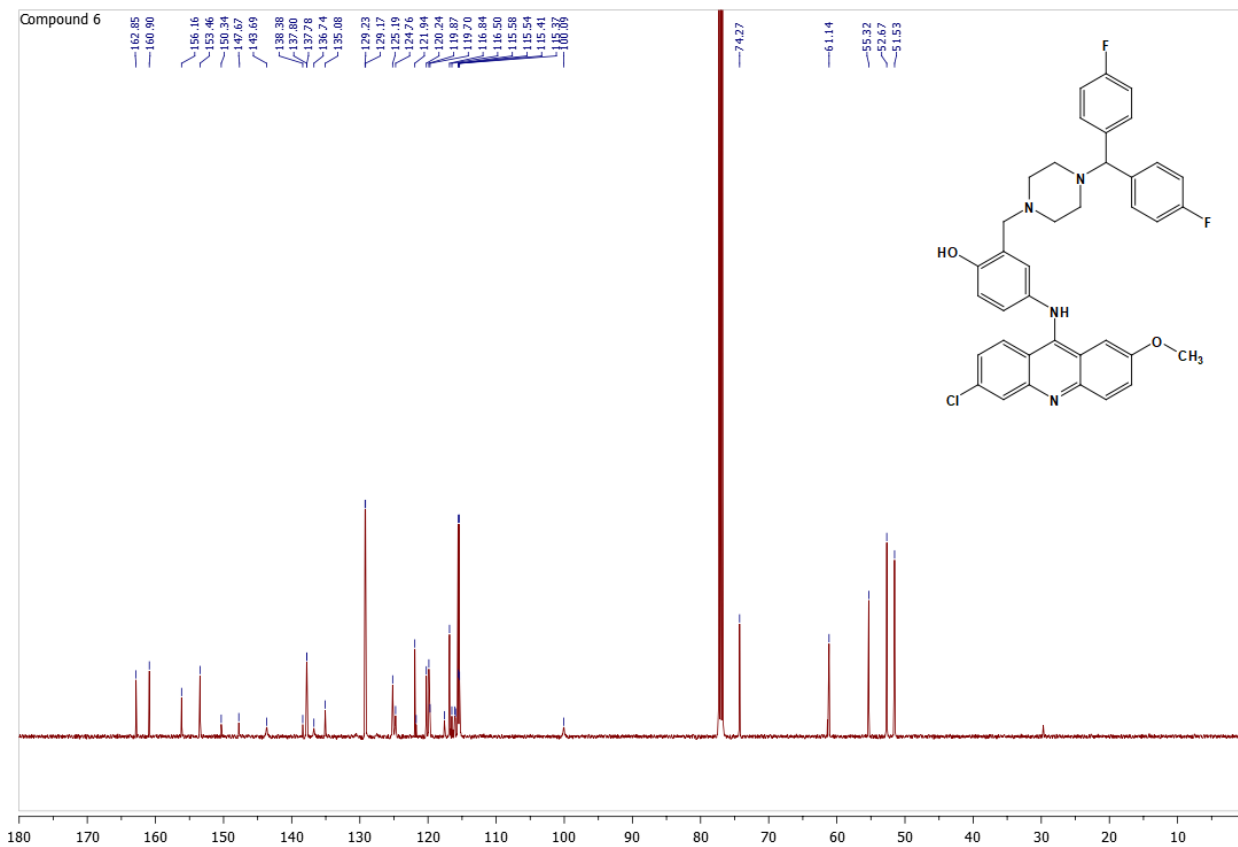


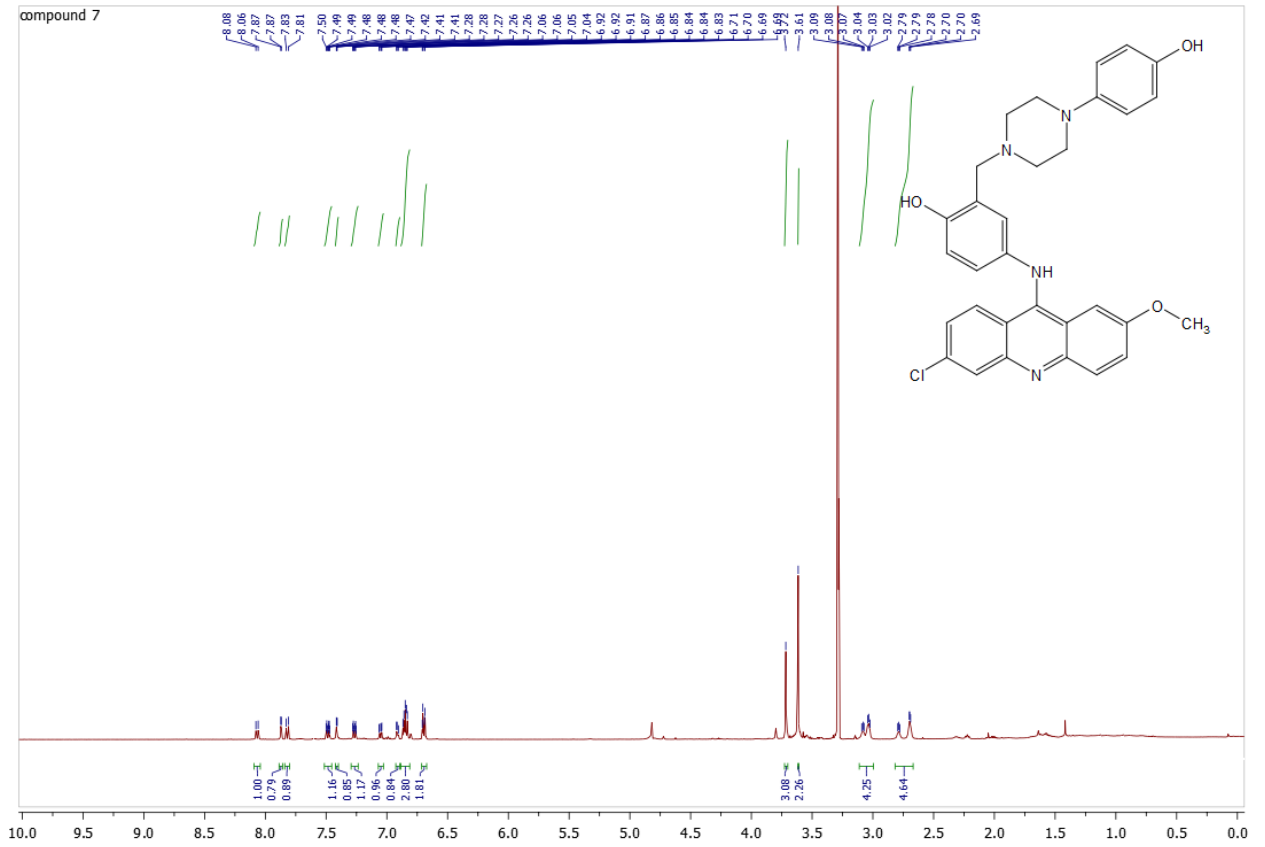


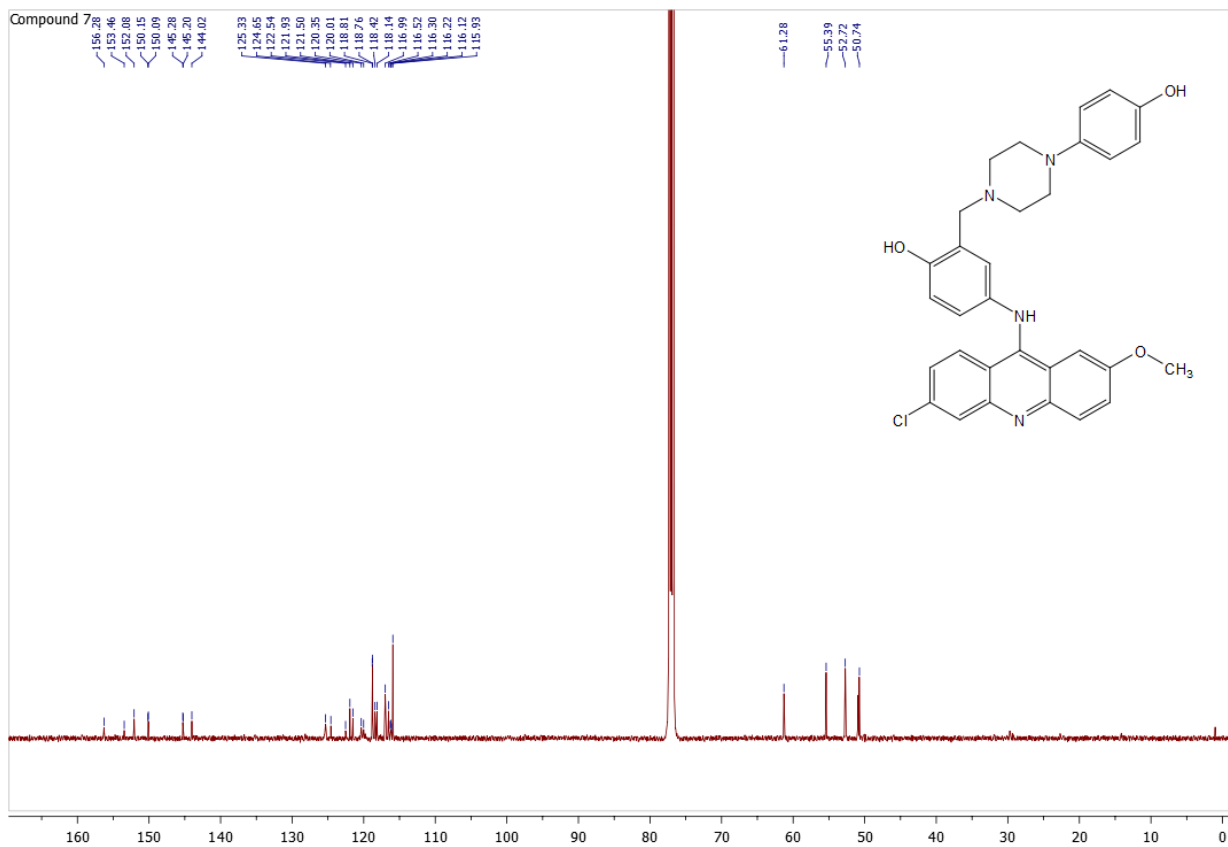


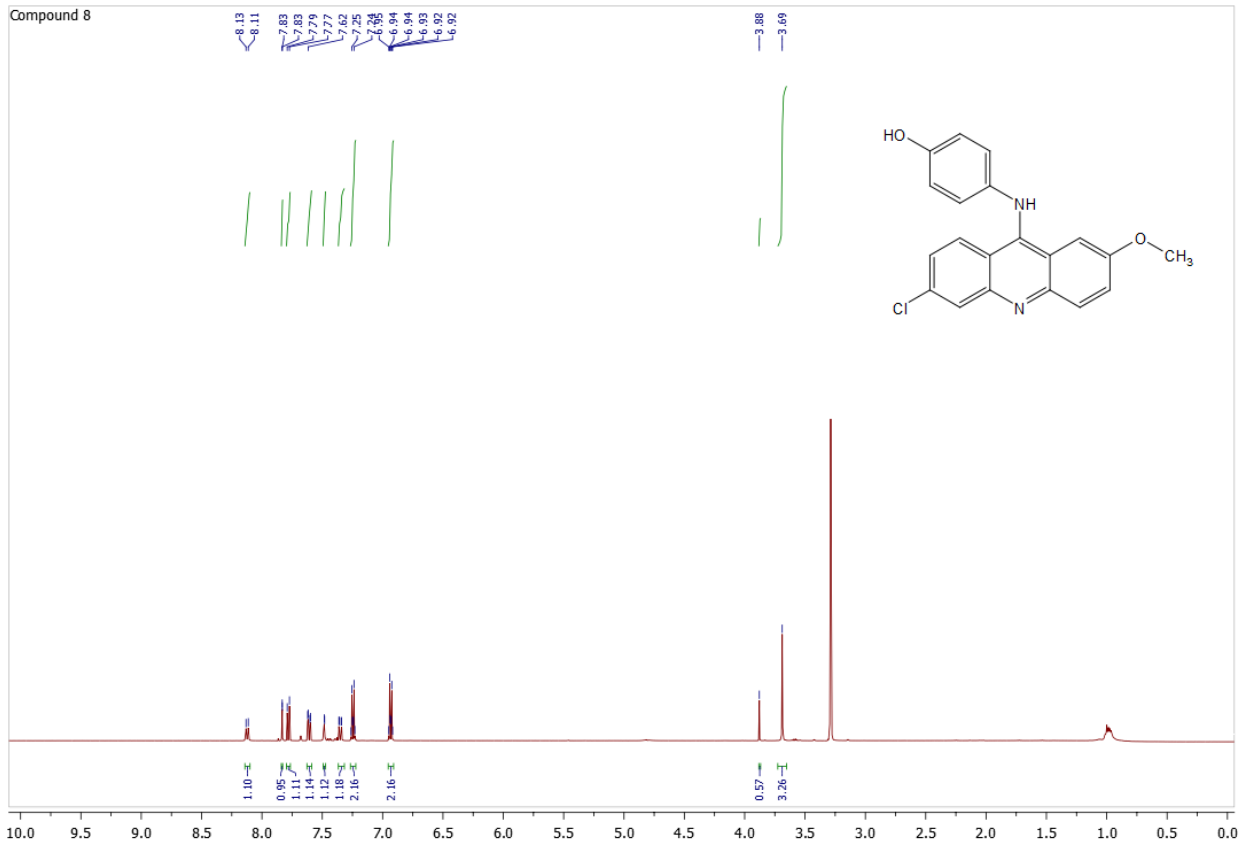


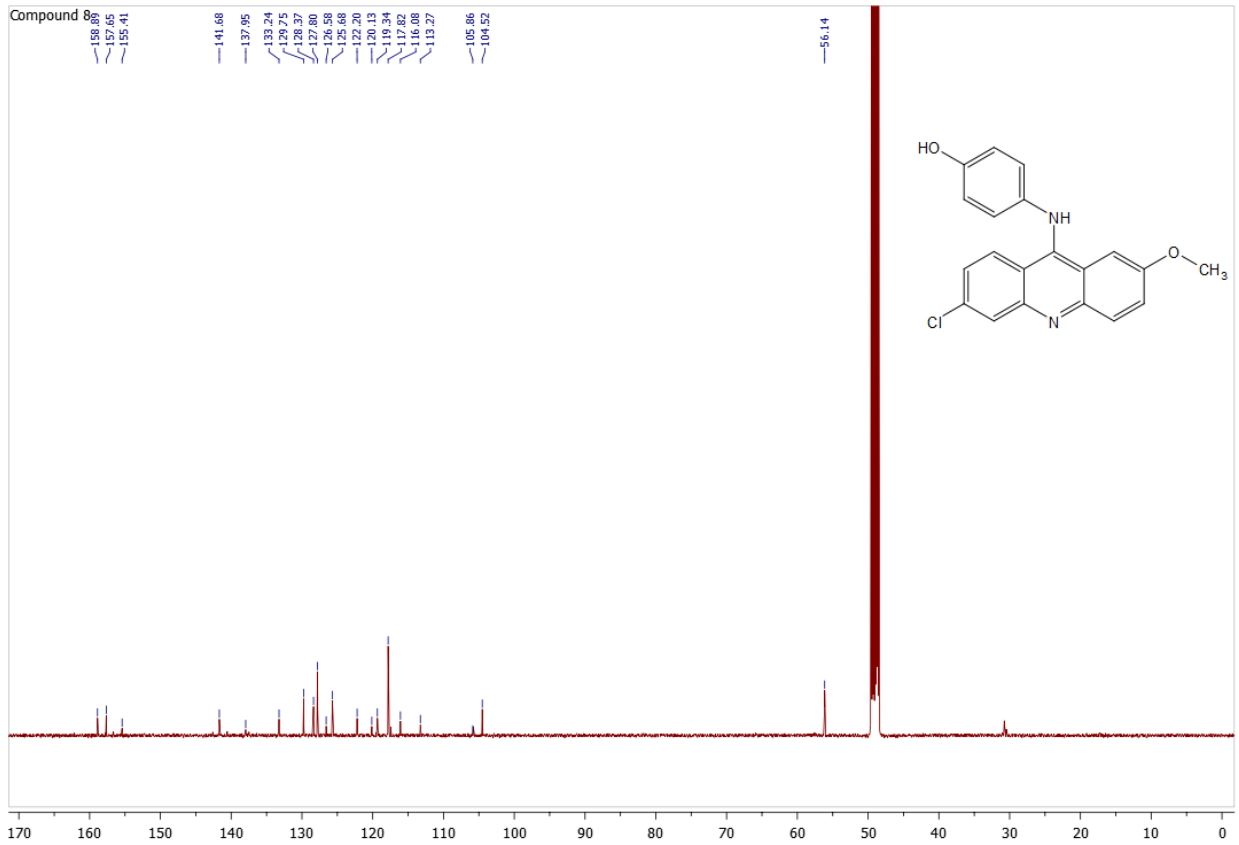




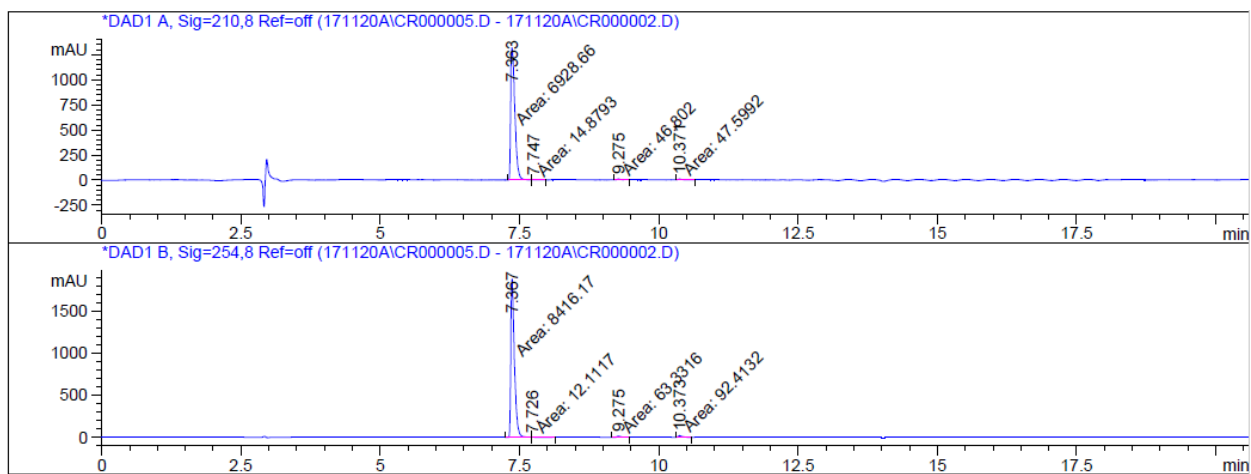








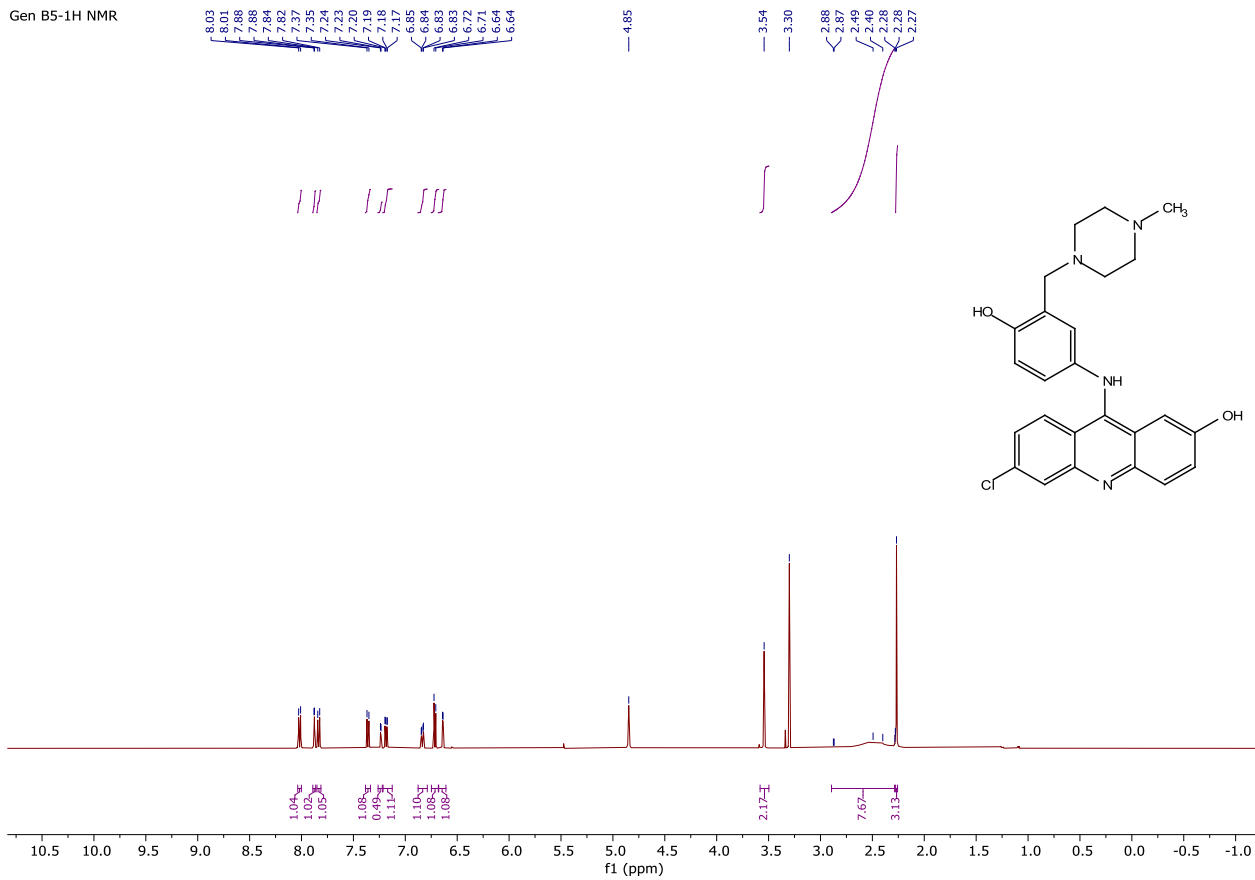
**Appendix II: HPLC chromatogram of  
Compound 4  
(Chapter 2)**



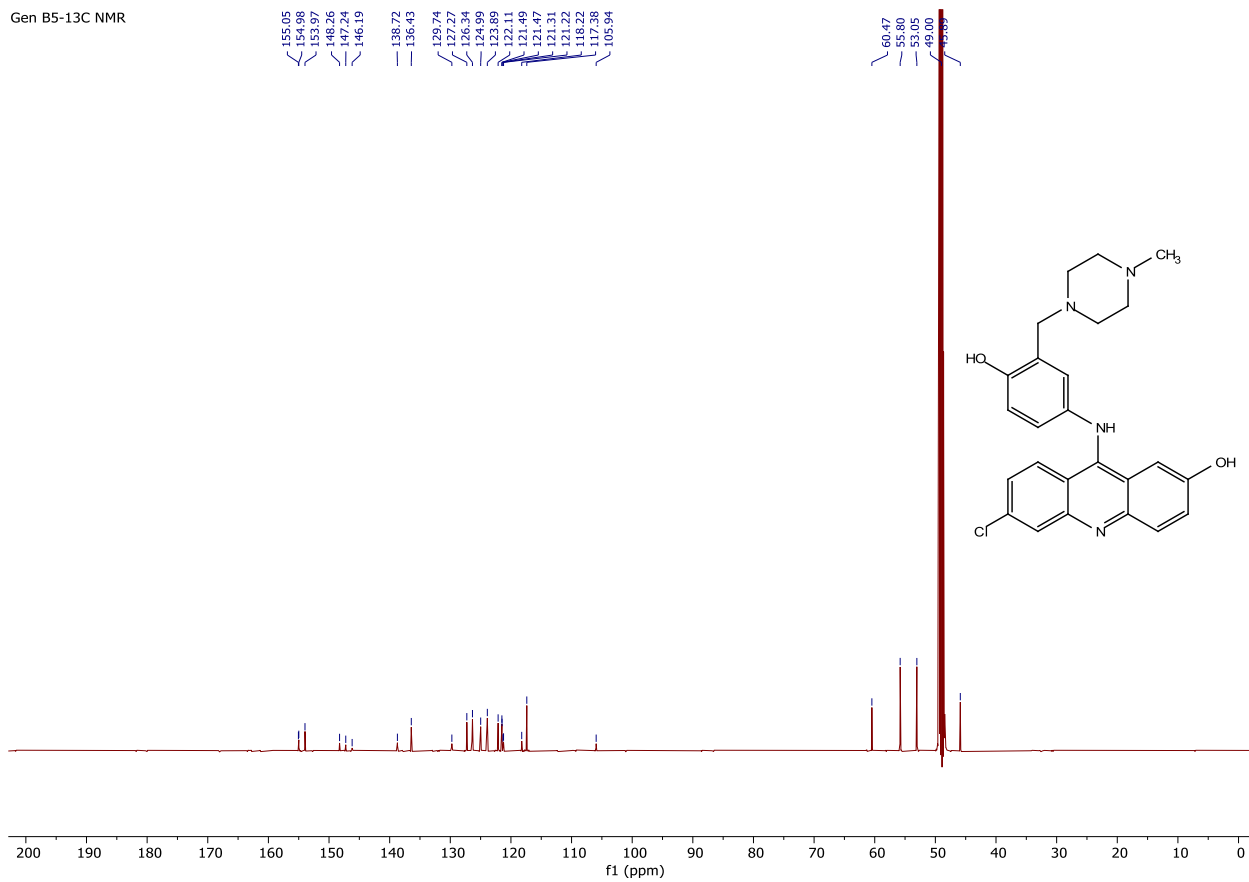
HPLC chromatogram of **A4**, yielded a purity of 98%.

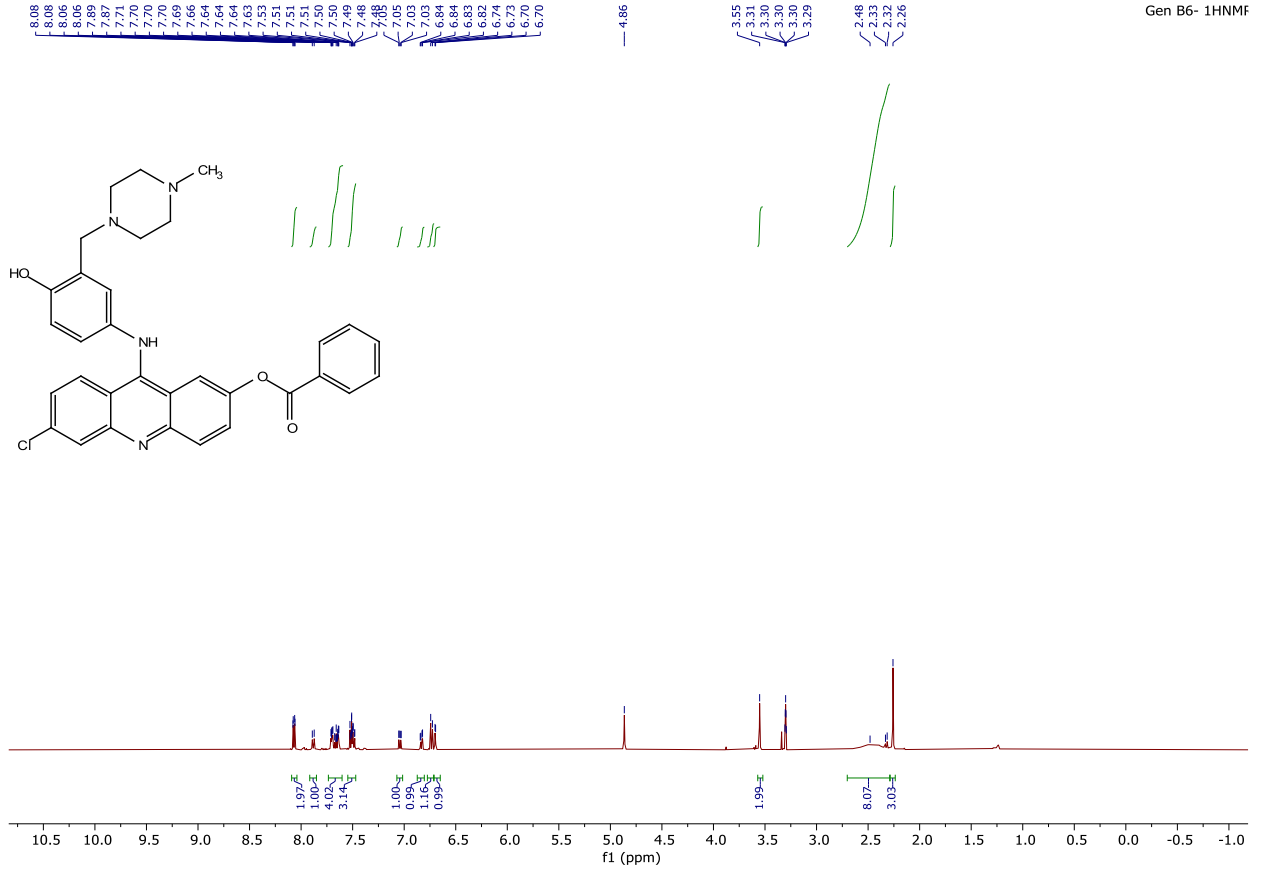
**Appendix III: Selected NMR Spectra**  
**(Chapter 3)**

Gen B5-1H NMR

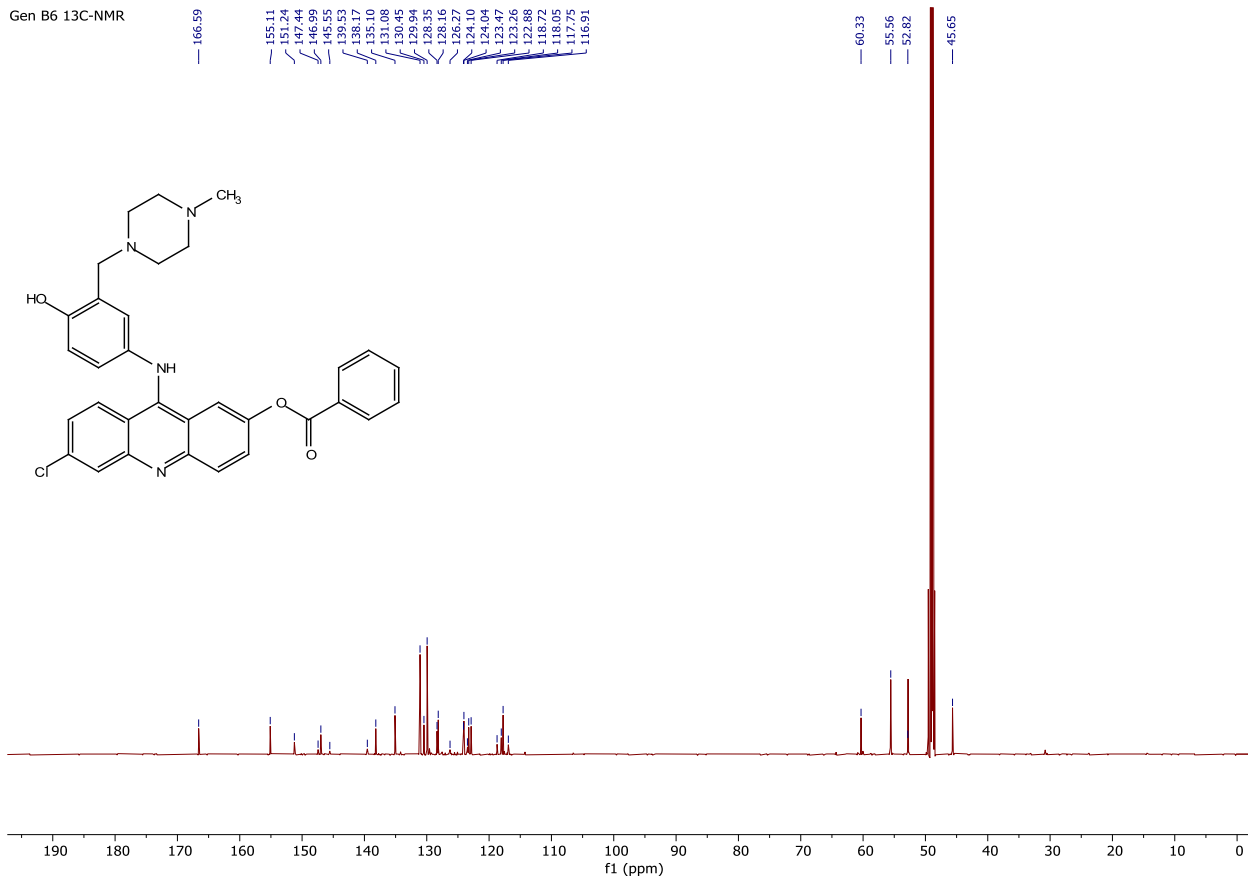


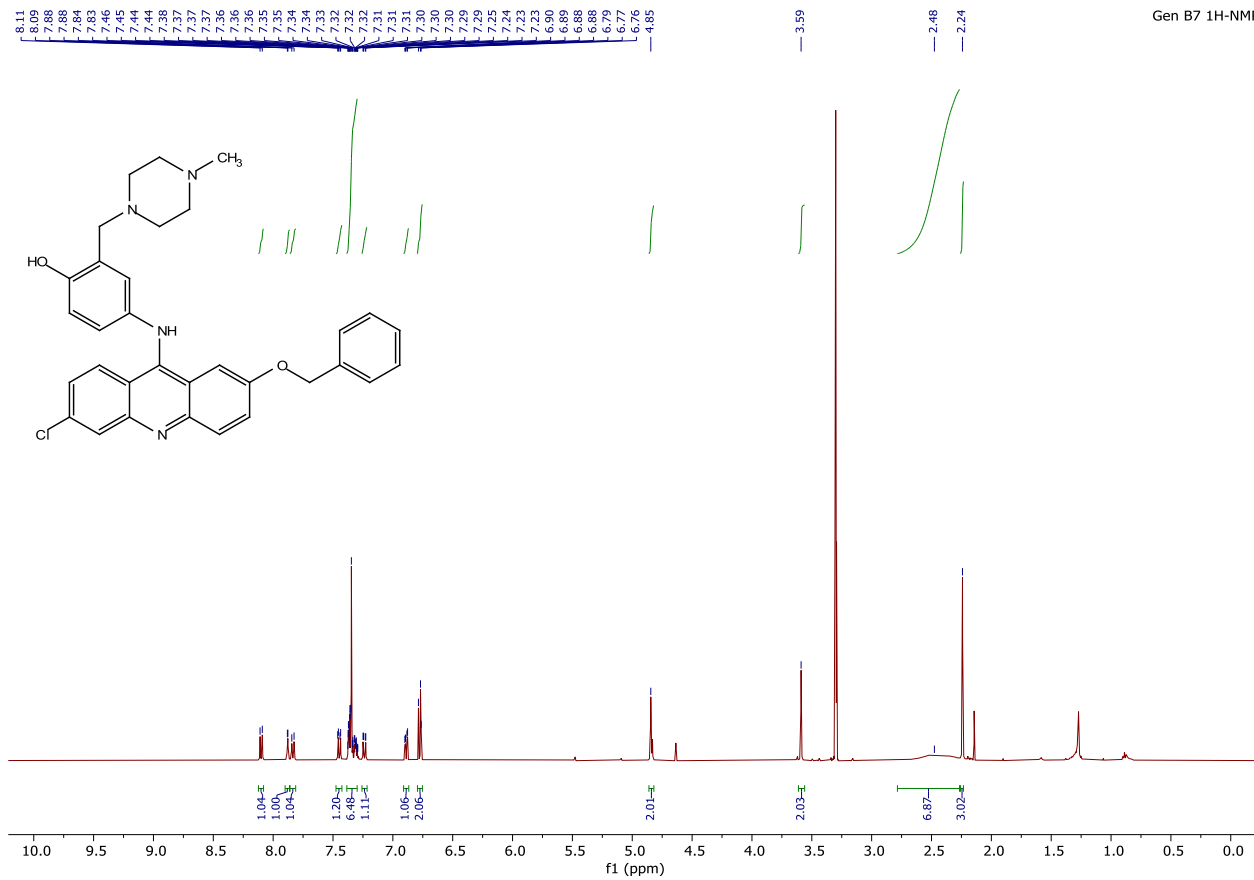
Gen B5-13C NMR

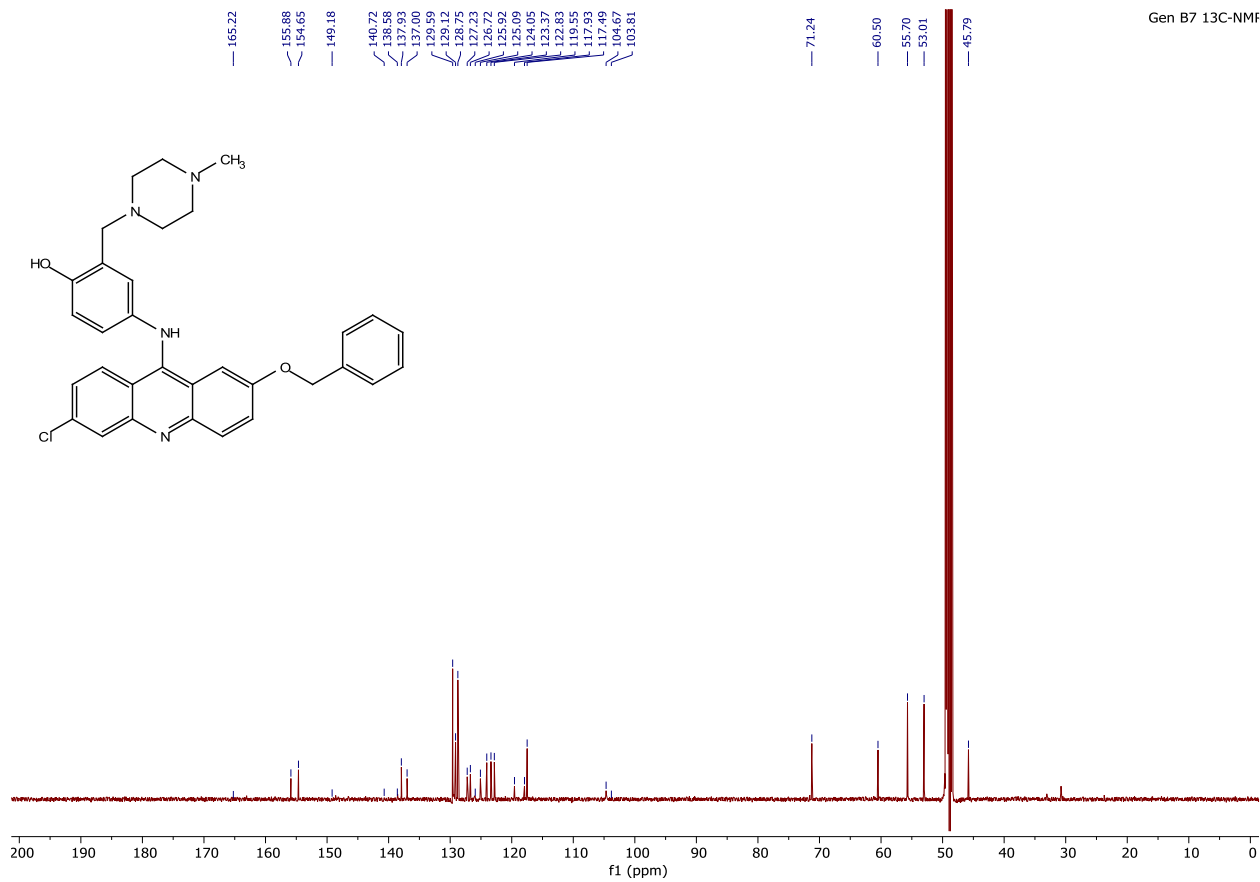


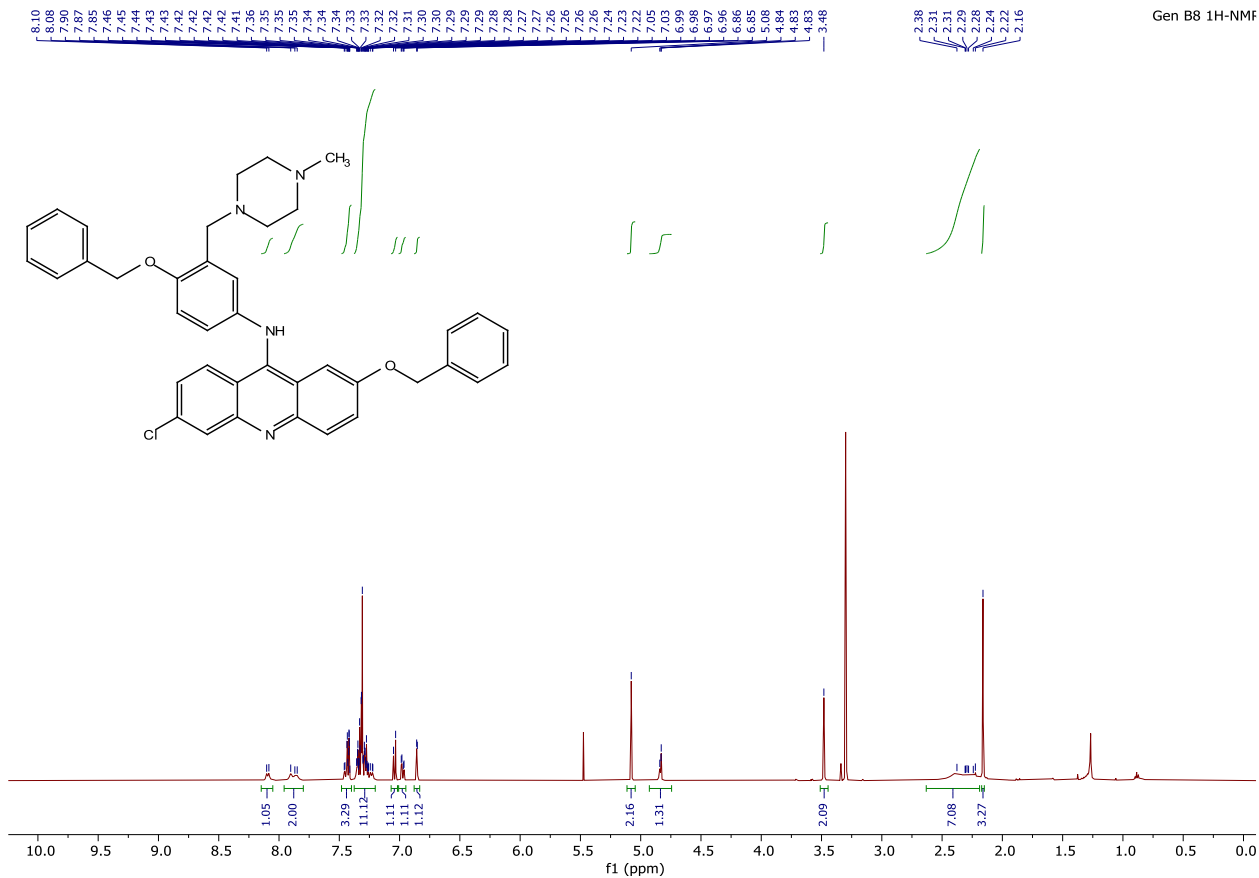


Gen B6 13C-NMR

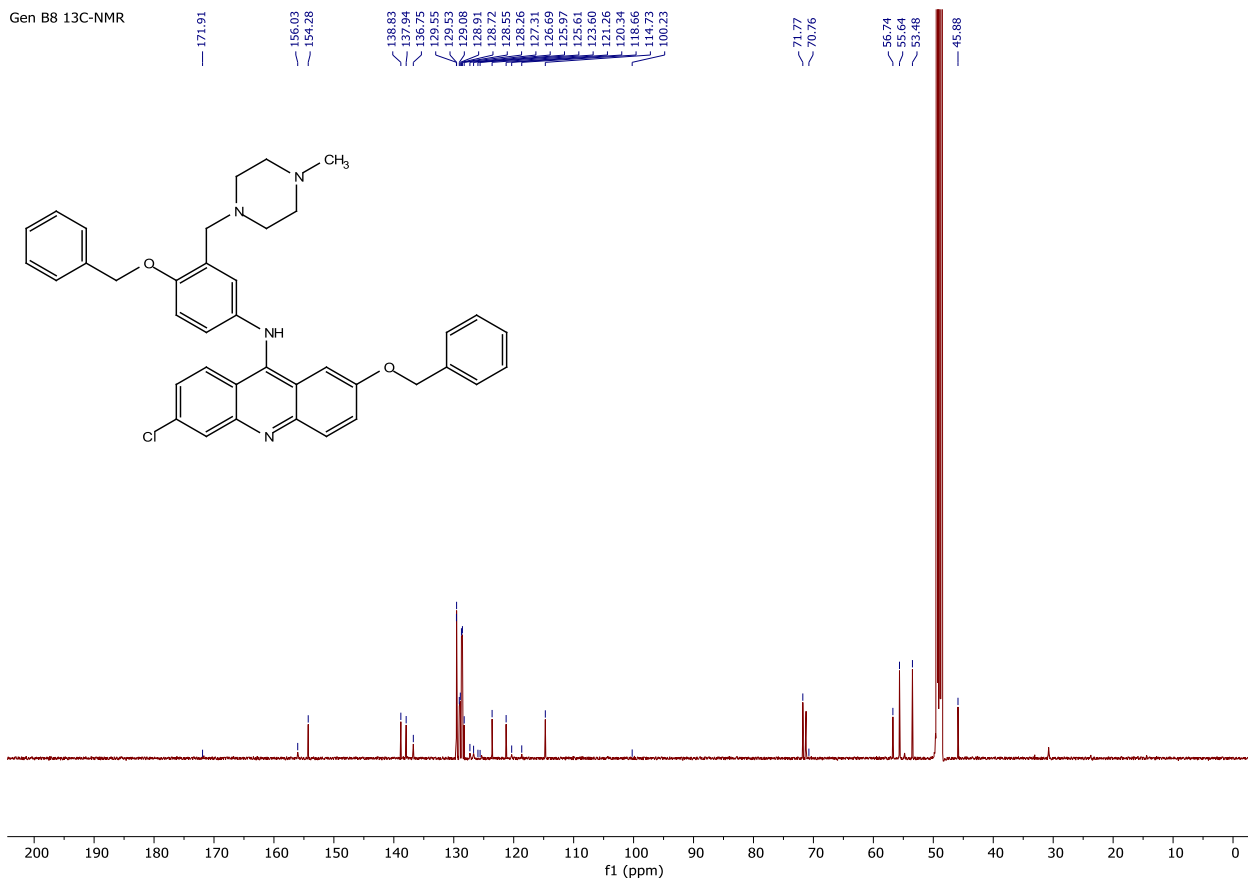


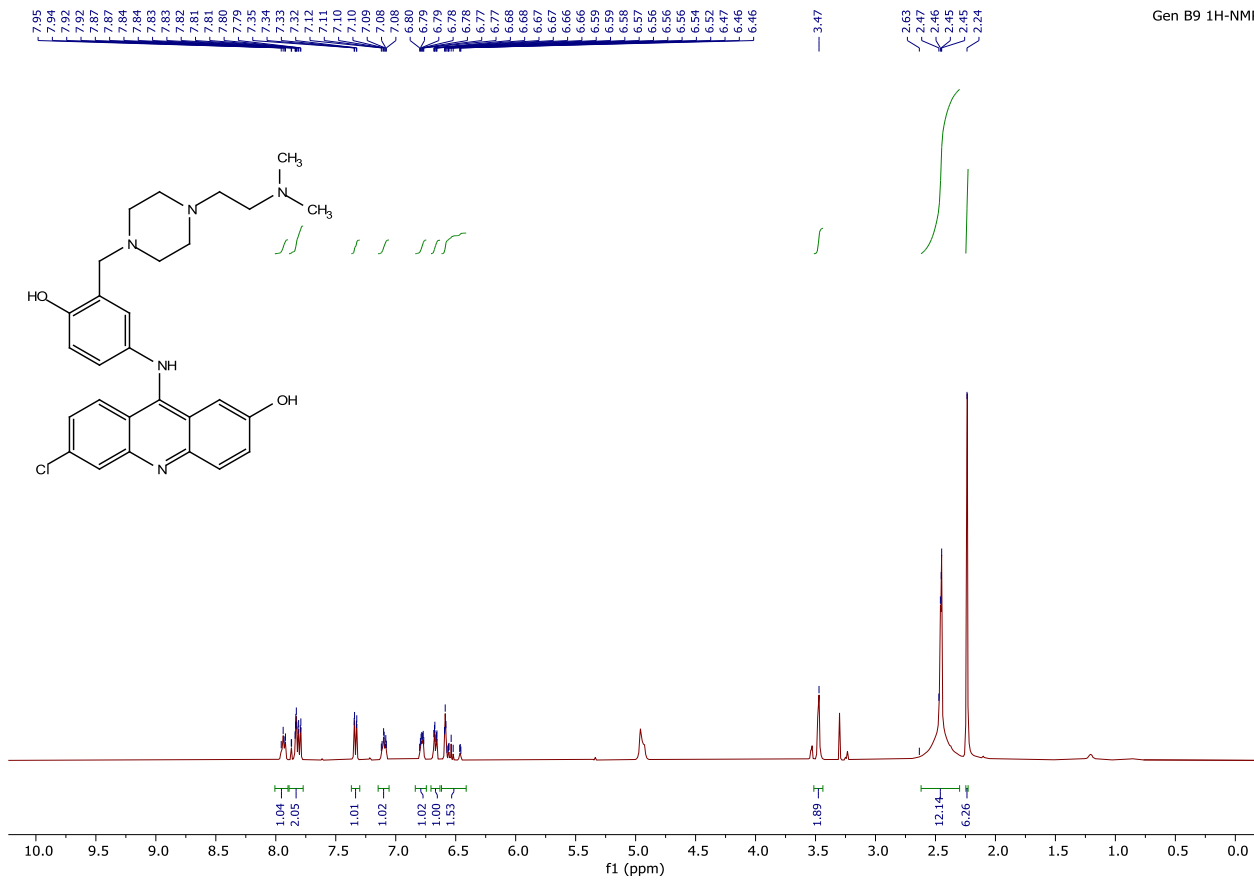






Gen B8 13C-NMR

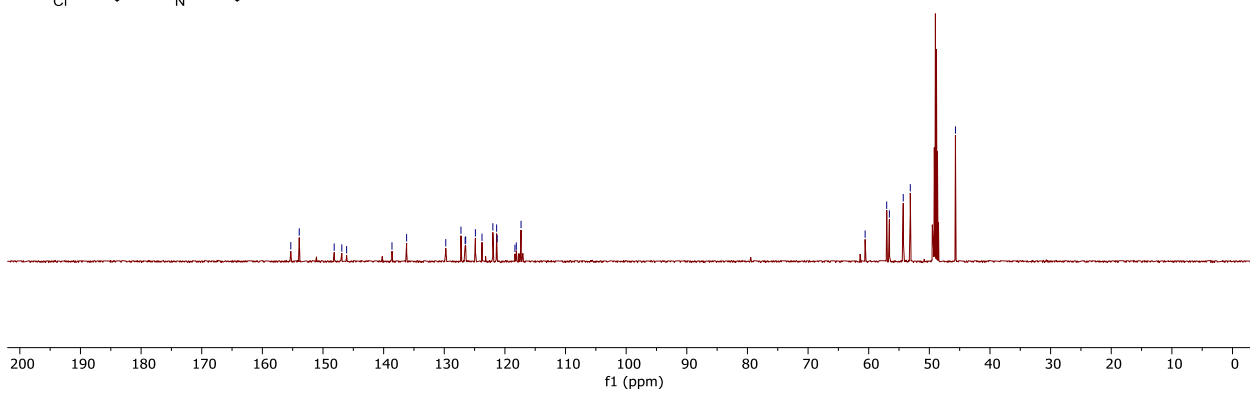
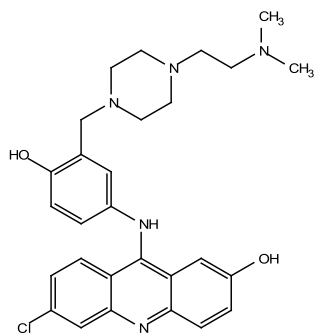




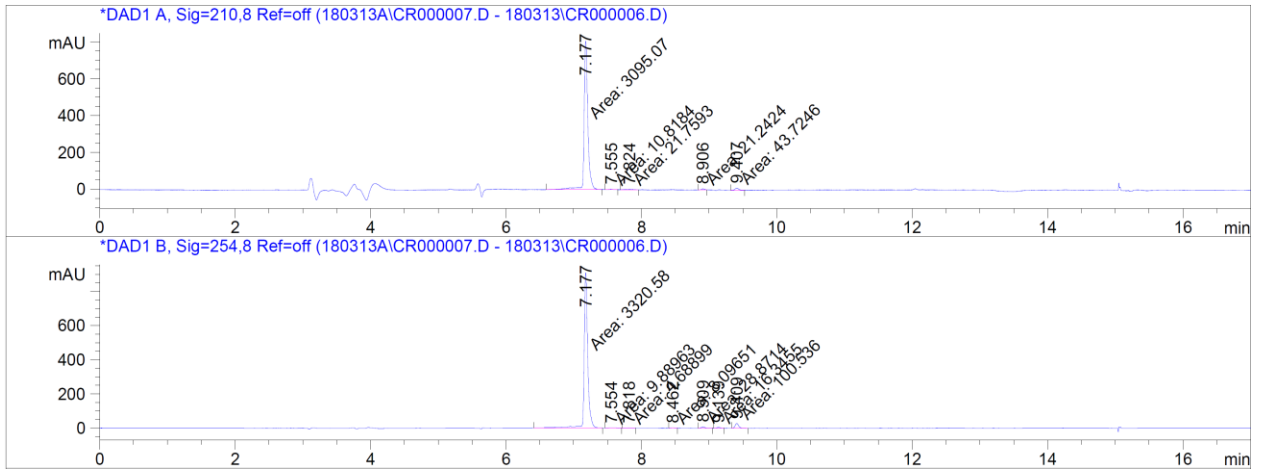
Gen B9 13C-NMR

155.31  
153.92  
148.16  
146.90  
146.10  
138.63  
136.21  
129.75  
127.25  
126.56  
126.47  
124.87  
123.77  
121.99  
121.58  
121.38  
118.34  
118.12  
117.34

60.59  
57.03  
56.53  
54.31  
53.14  
45.70



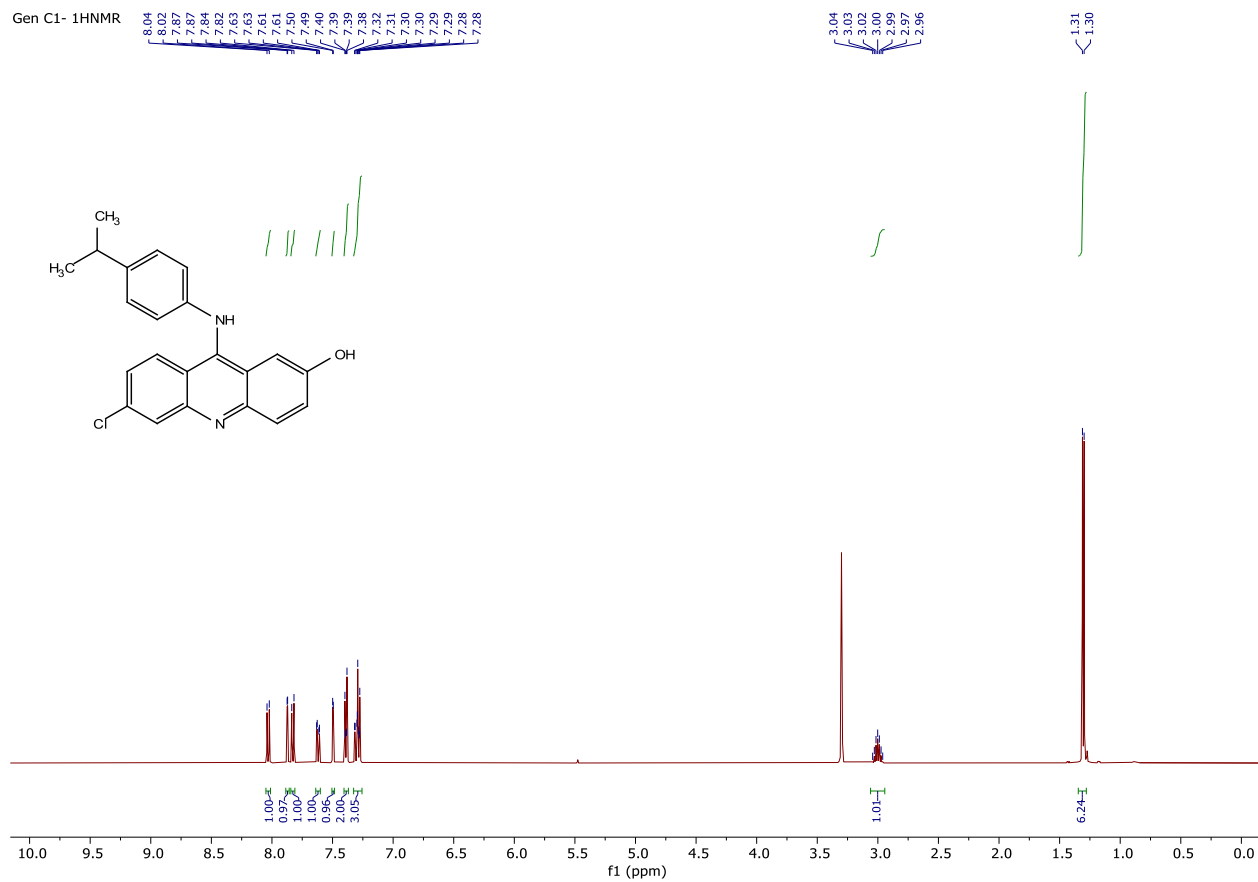
**Appendix IV: HPLC chromatogram of B9**  
**(Chapter 3)**



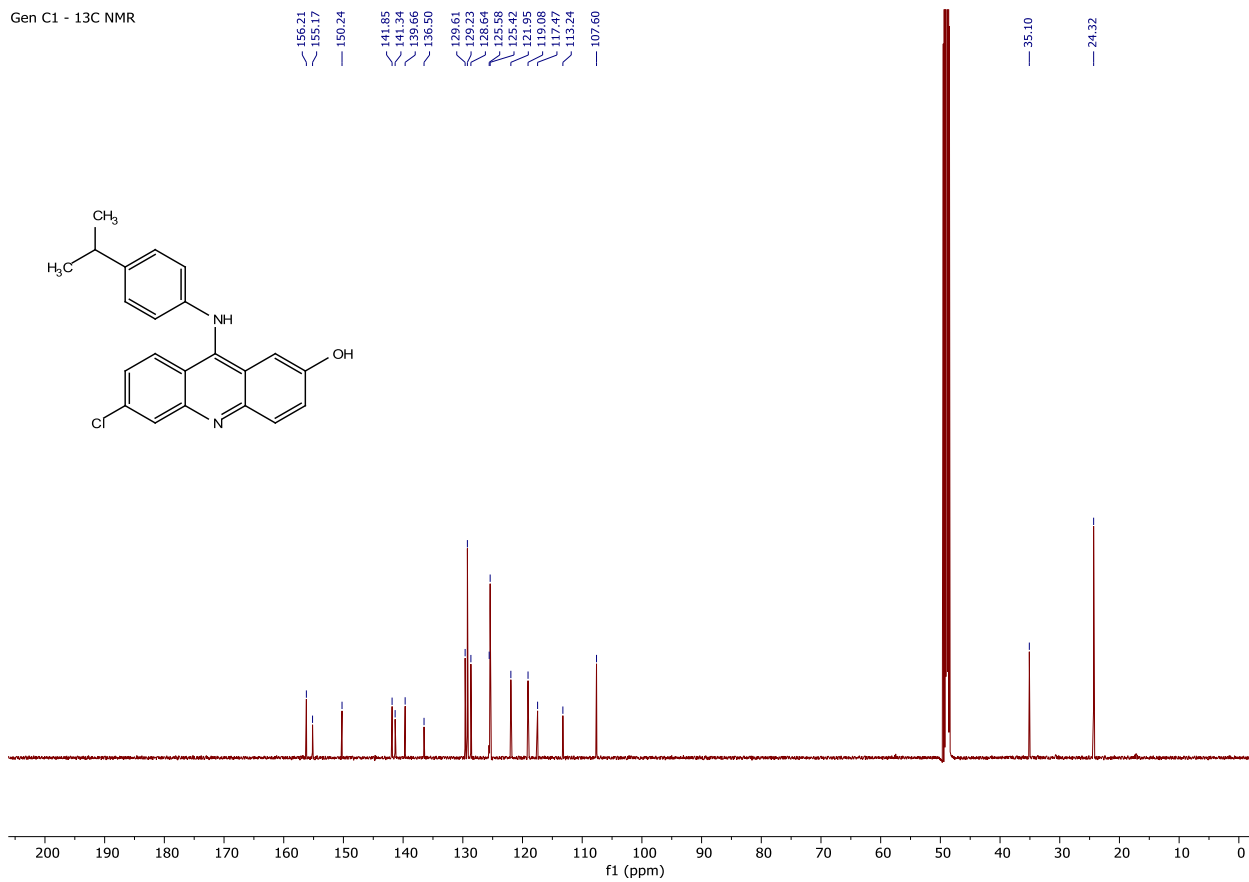
HPLC chromatogram of **B9**, yielded a purity of 96.9%.

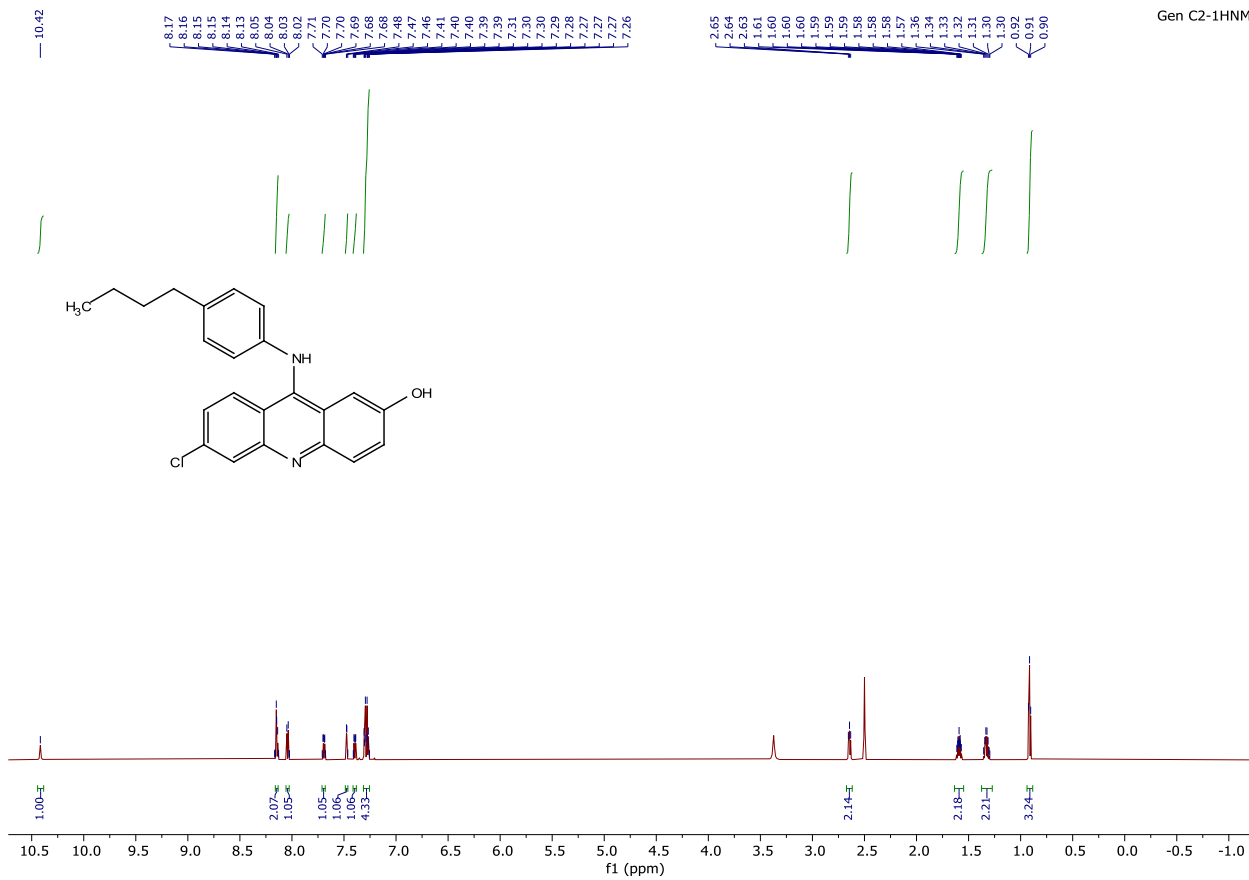
**Appendix V: Selected NMR Spectra**  
**(Chapter 4)**

# $^1\text{H}/^{13}\text{C}$ NMR spectra of Gen C compounds

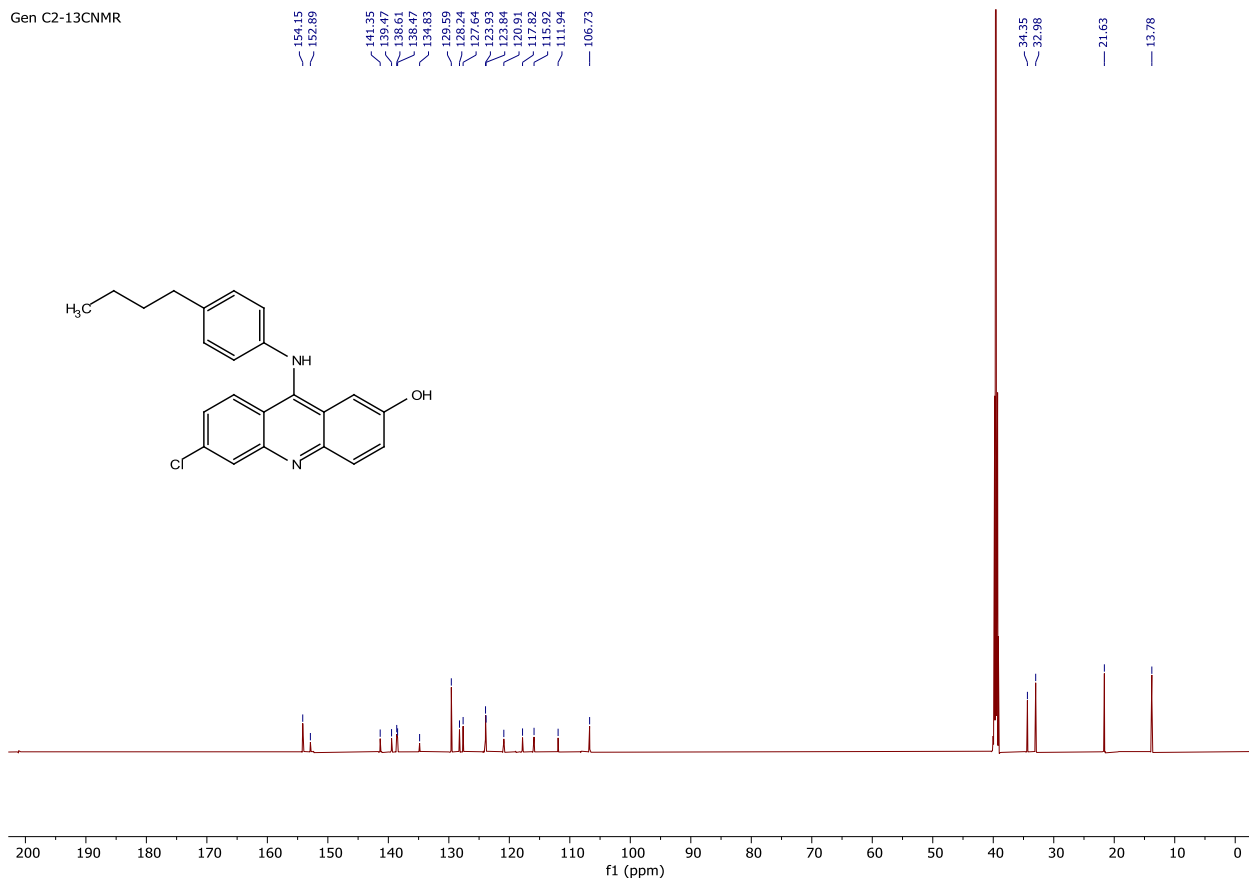


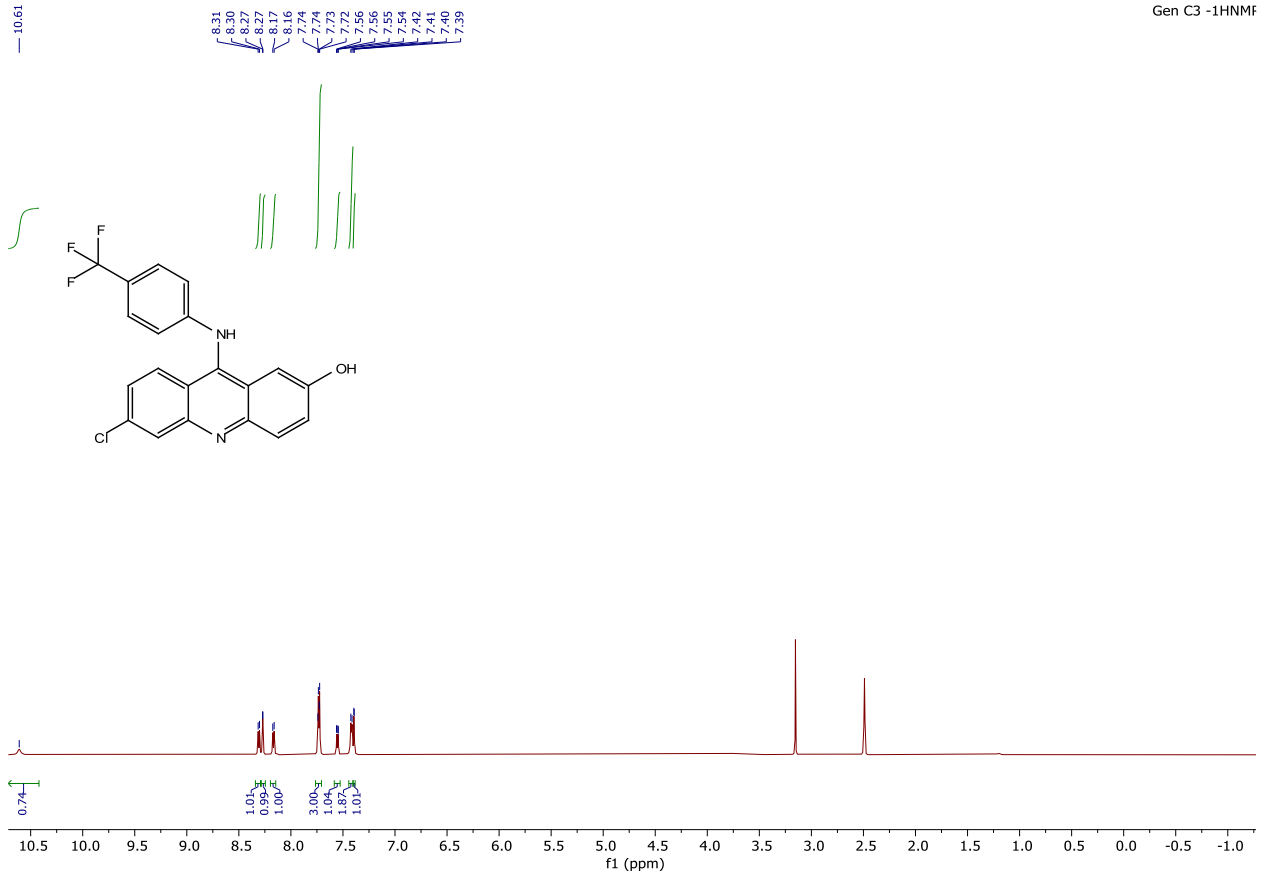
Gen C1 - 13C NMR



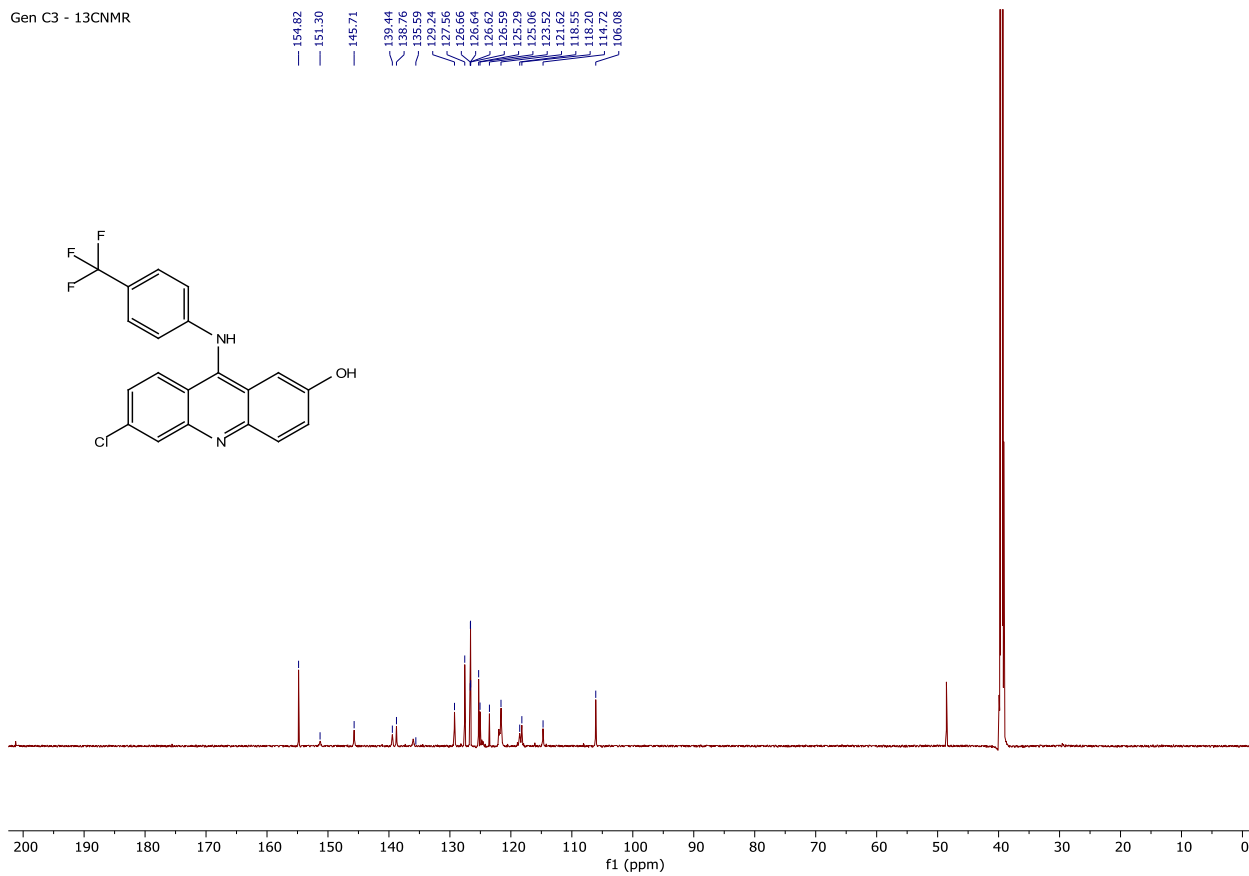


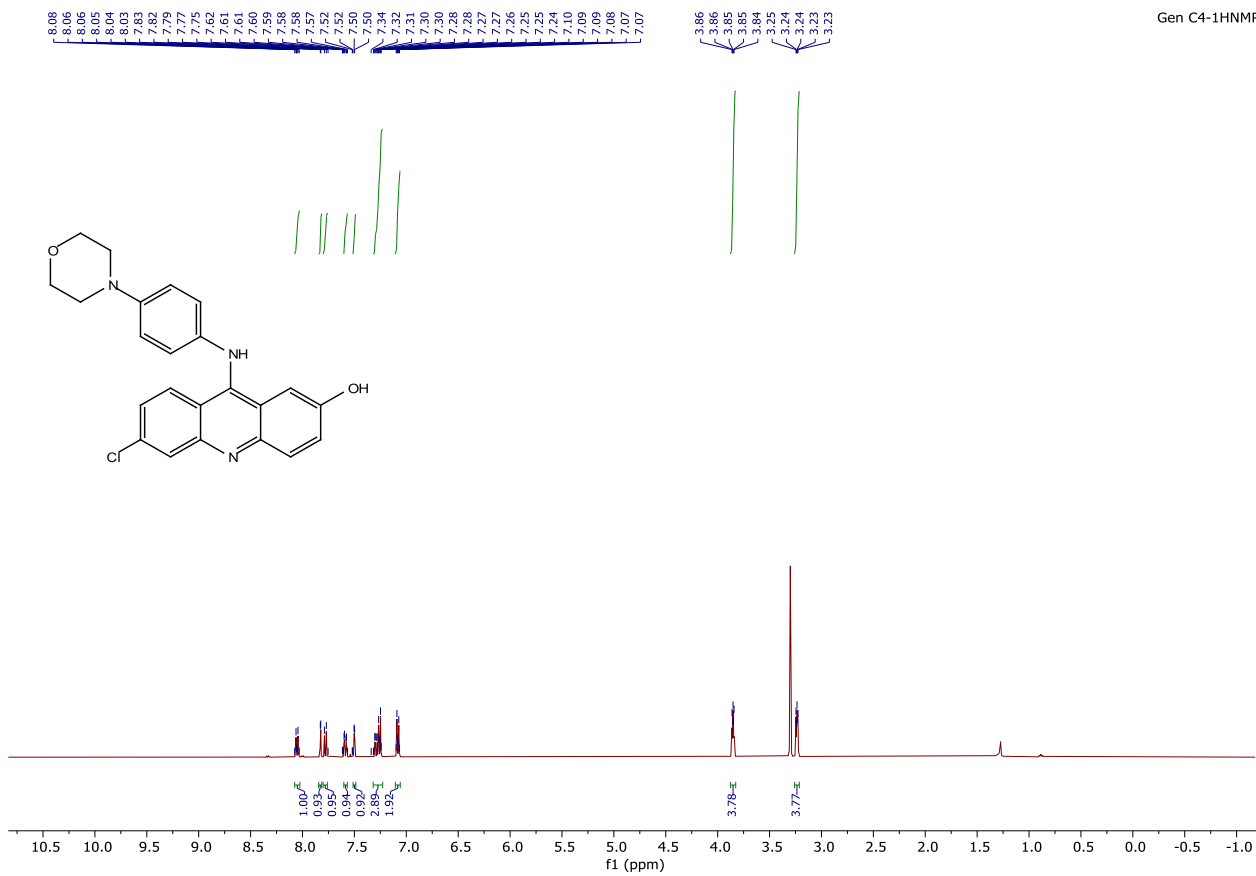
Gen C2-13CNMR





Gen C3 - <sup>13</sup>CNMR



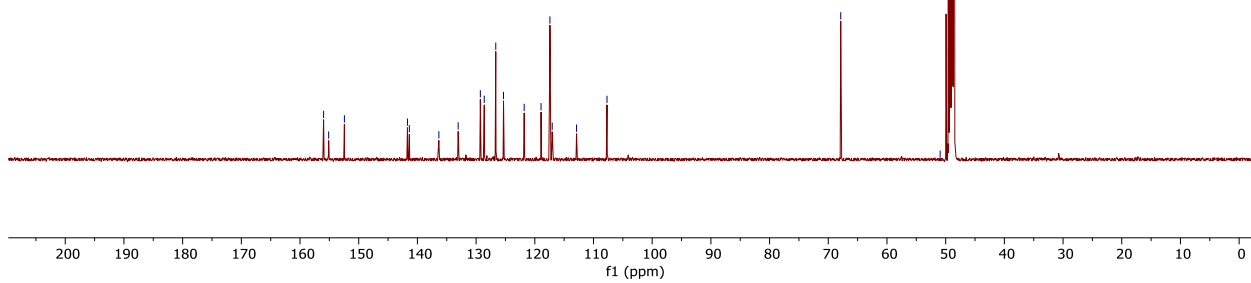
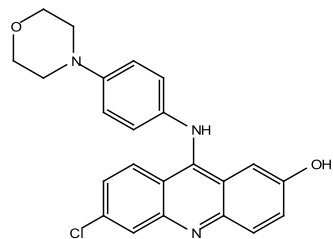


Gen C4-13CNMR

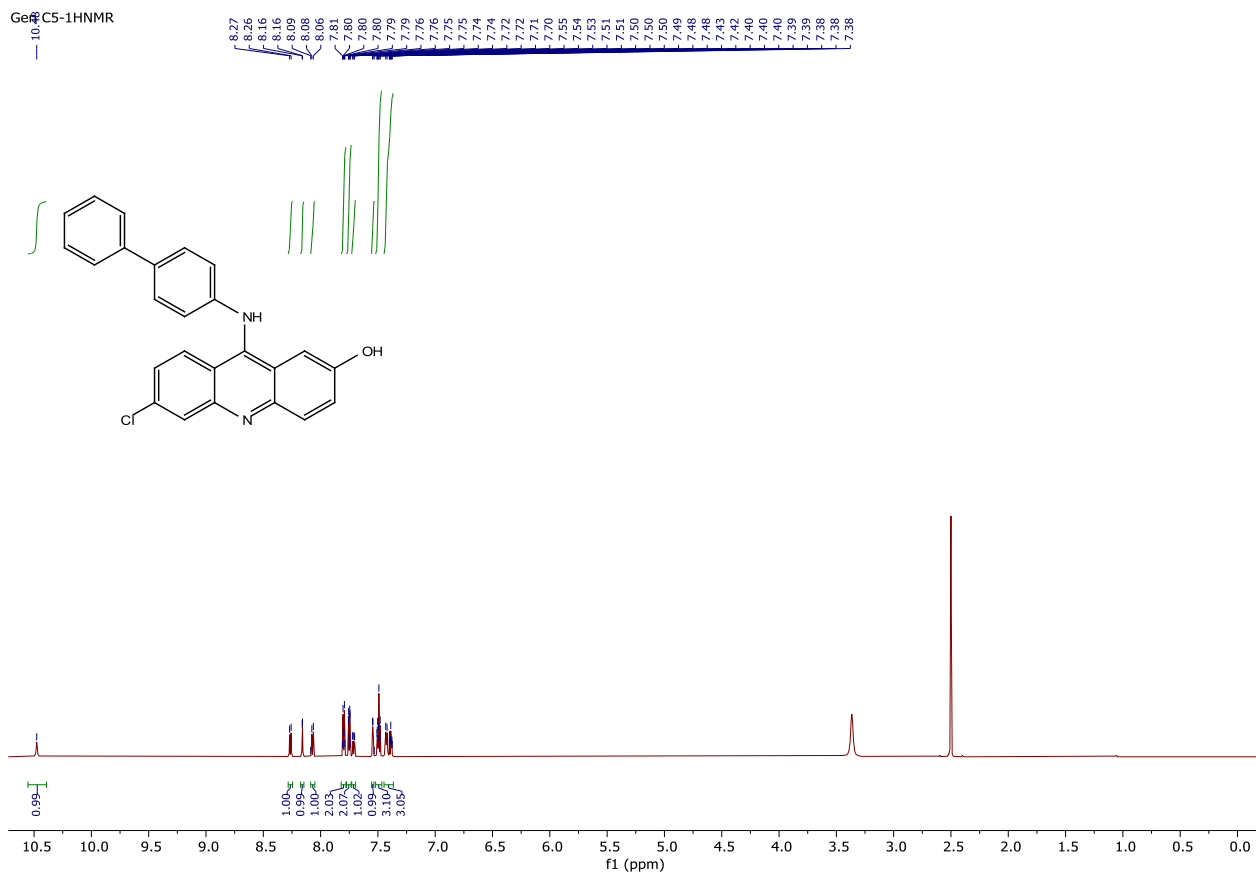
155.99  
155.12  
152.44  
141.69  
141.37  
136.35  
133.06  
129.28  
128.61  
126.65  
125.33  
118.84  
118.94  
117.42  
117.03  
112.89  
107.70

67.88

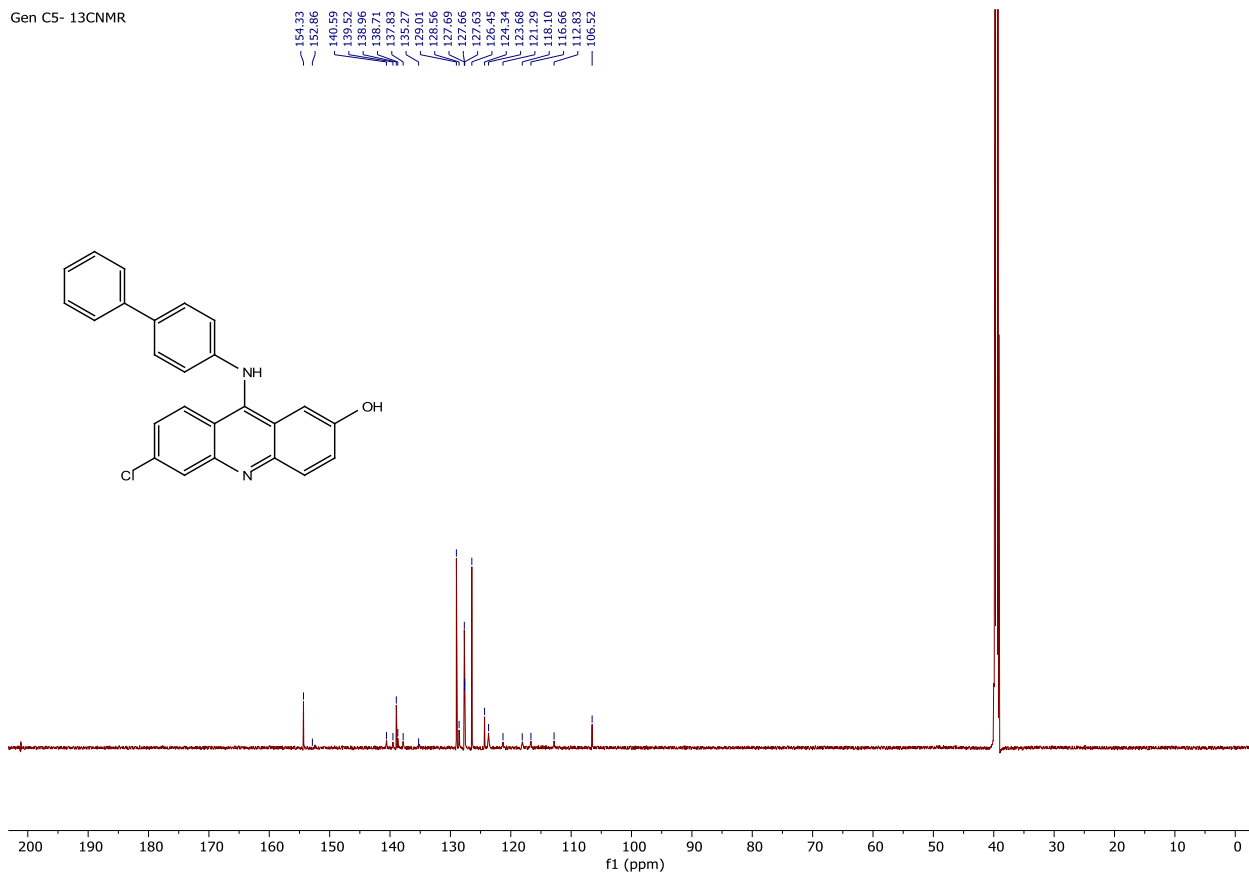
50.94



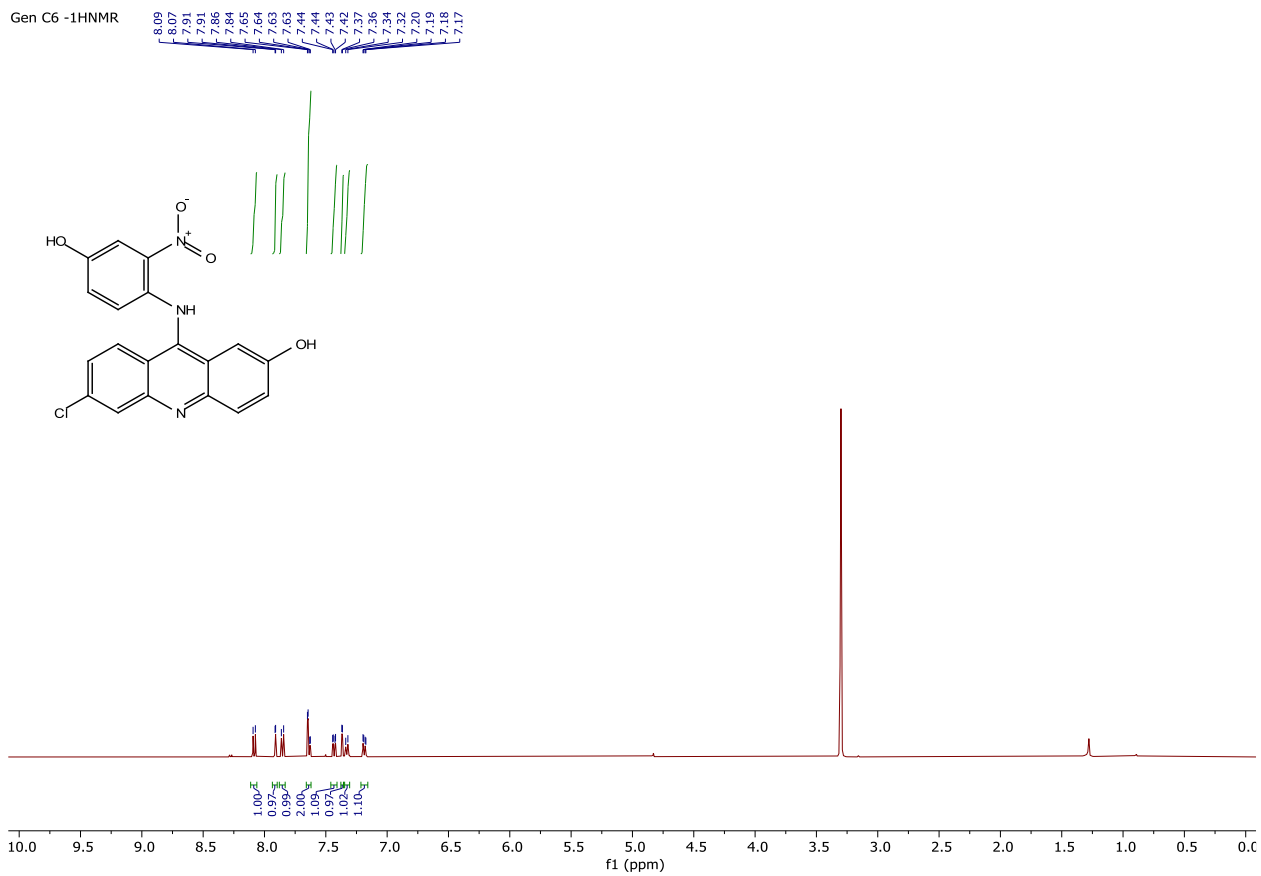
Ge-C5-1HNMR



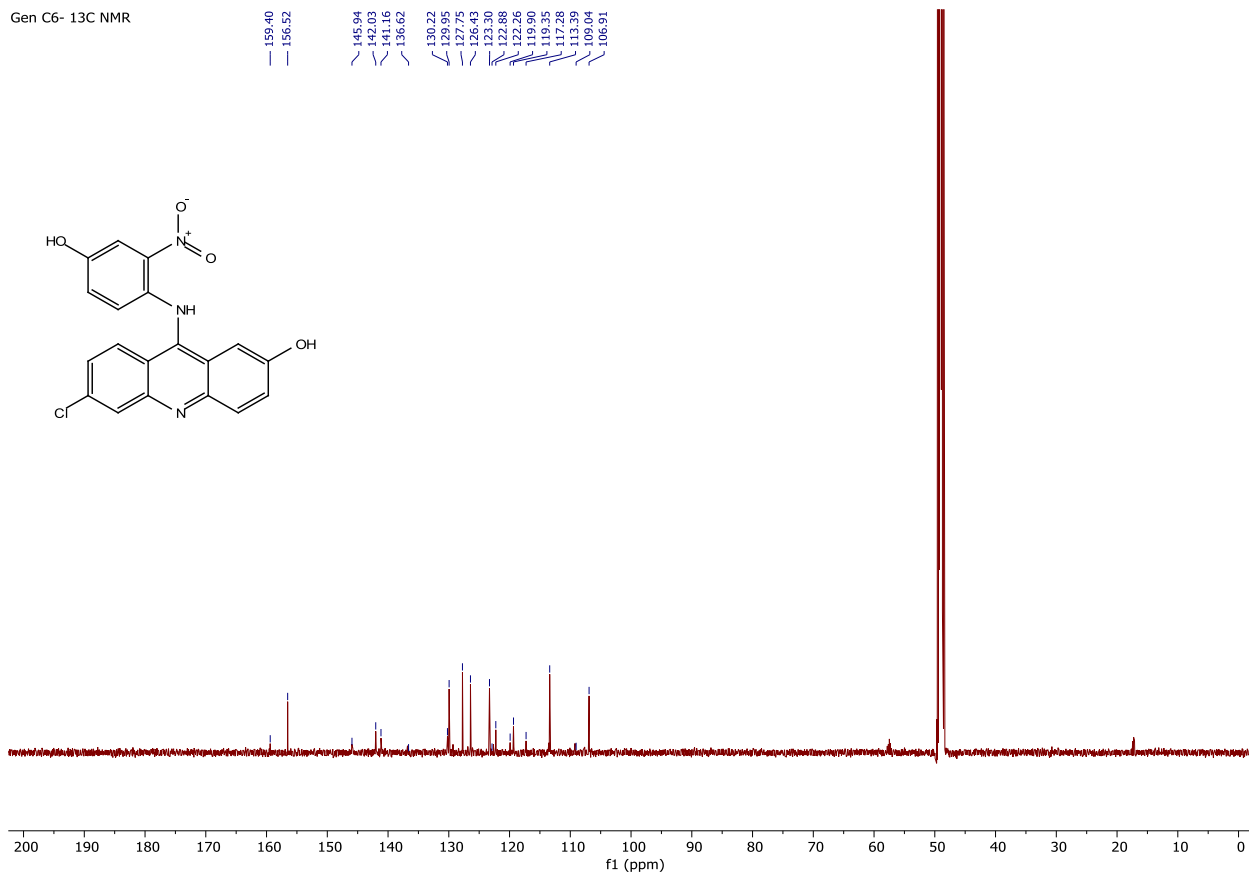
Gen C5- 13CNMR



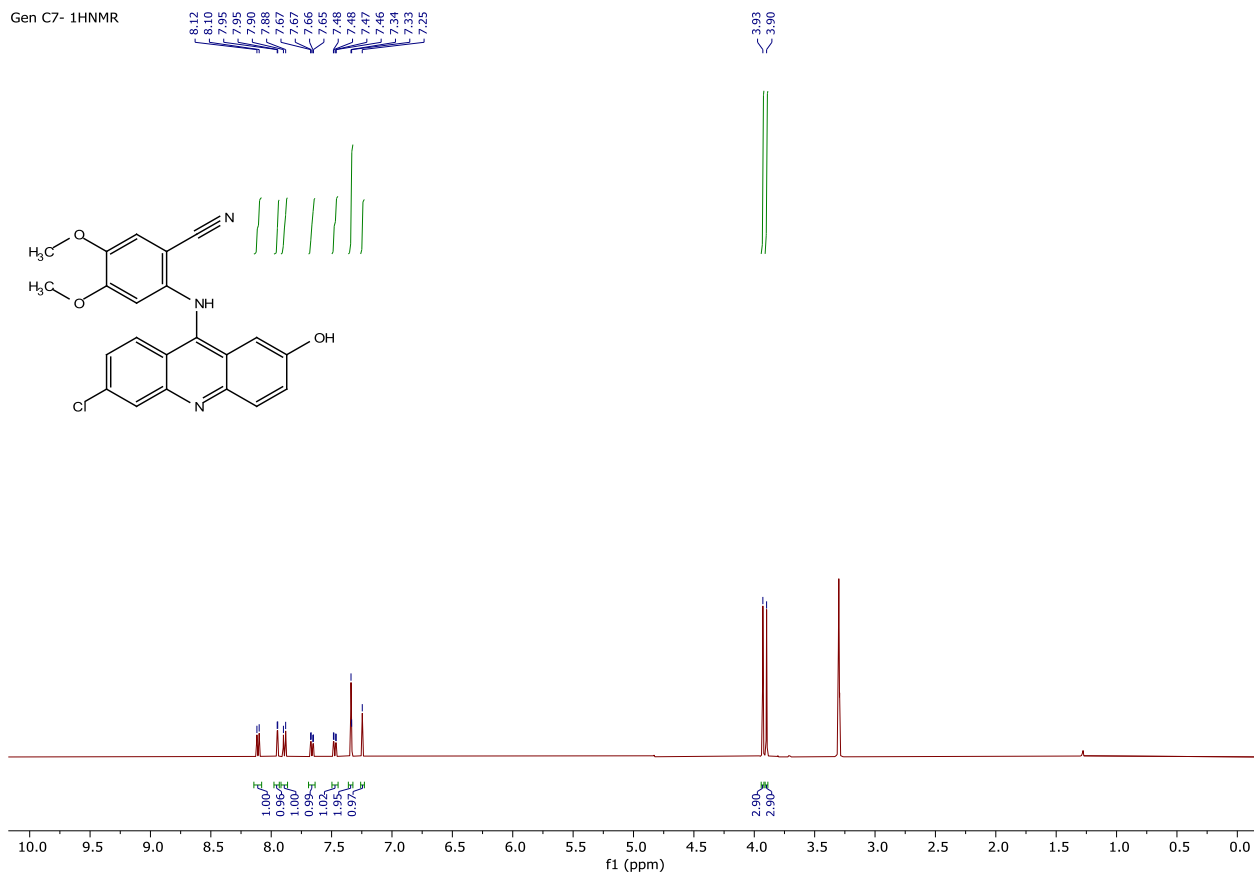
Gen C6 -1HNMR



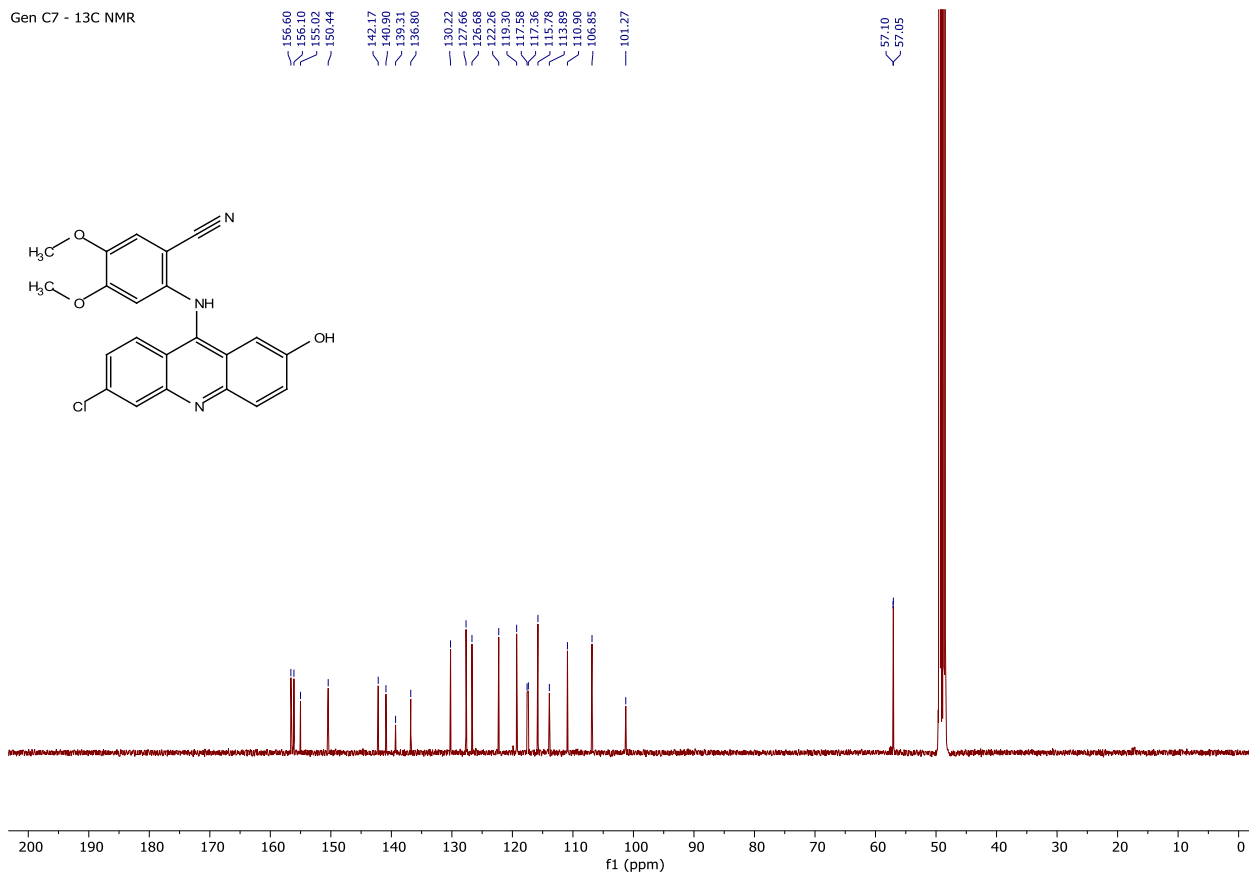
Gen C6- 13C NMR

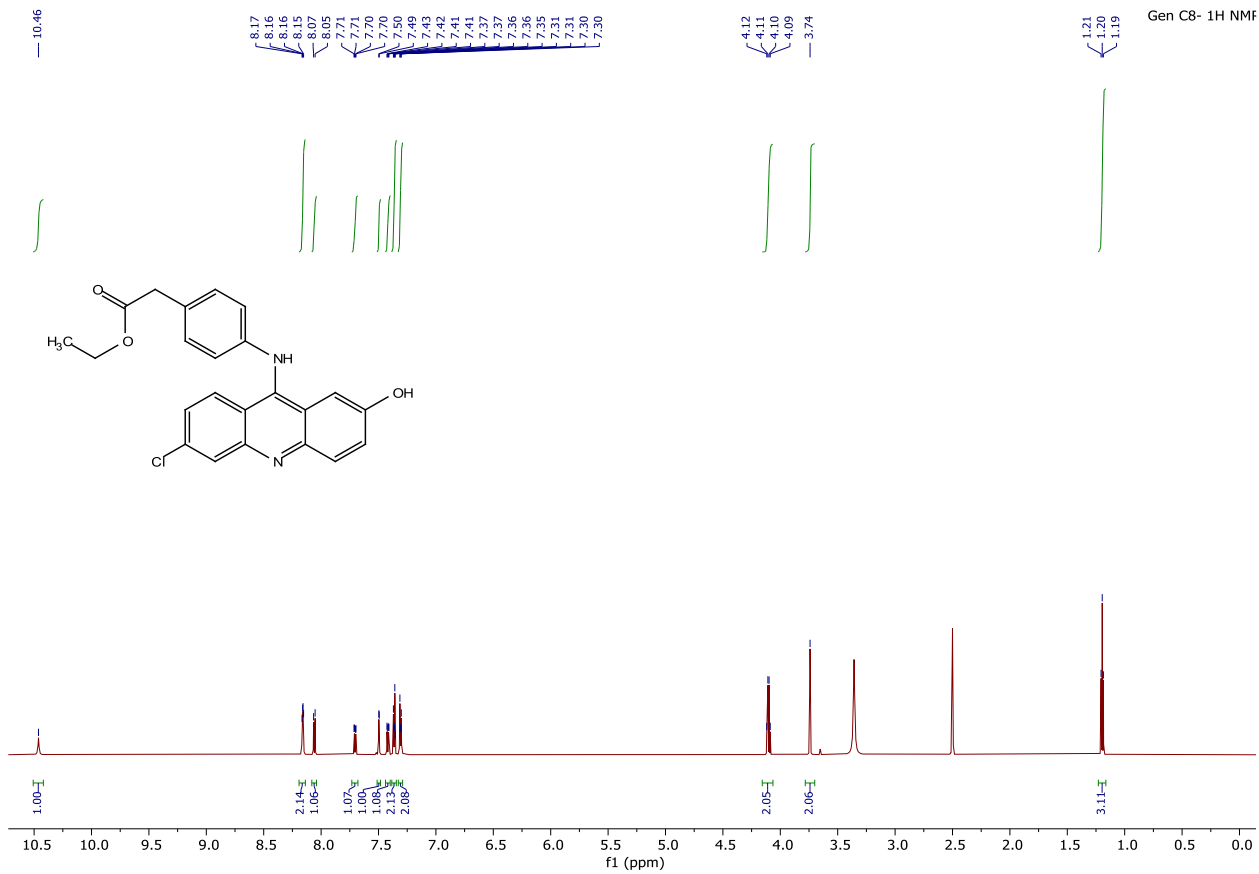


Gen C7- 1HNMR

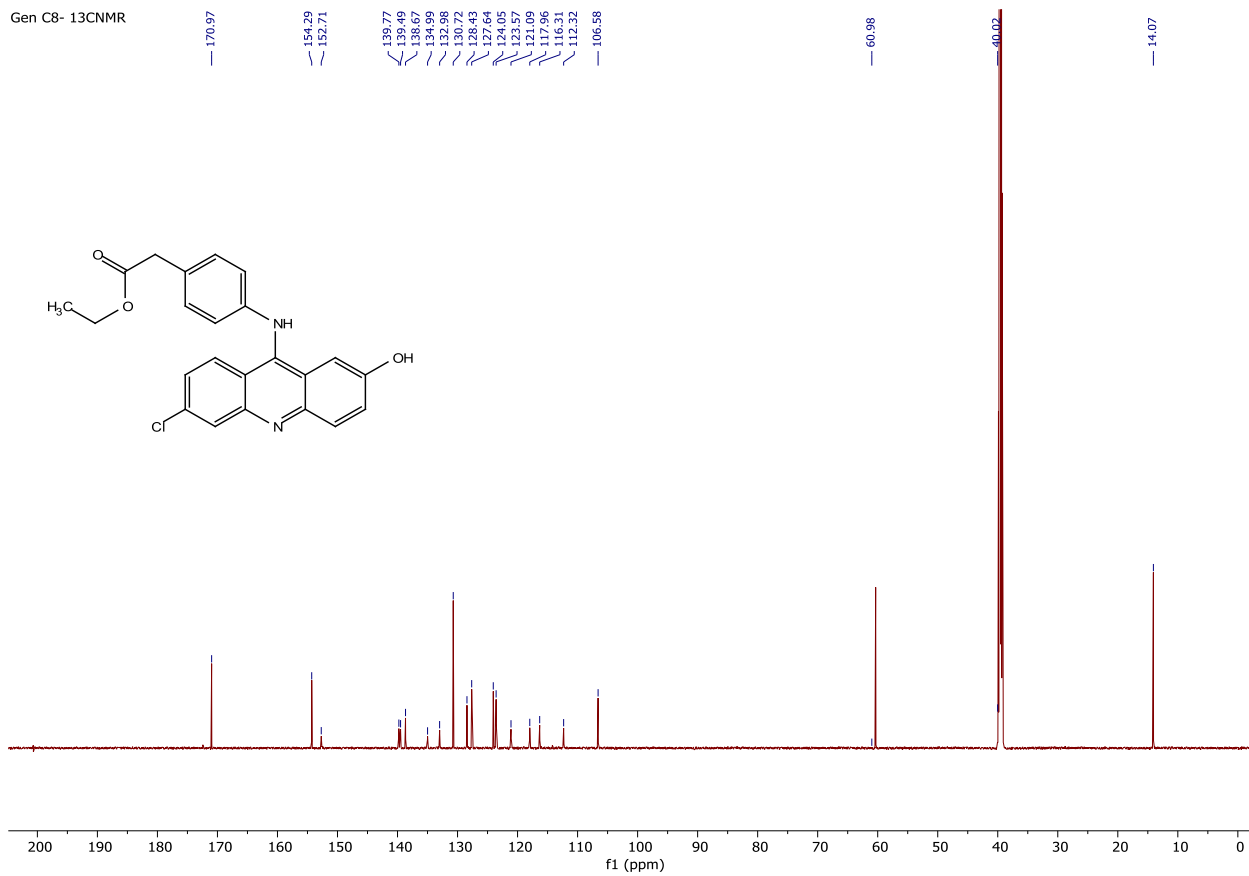


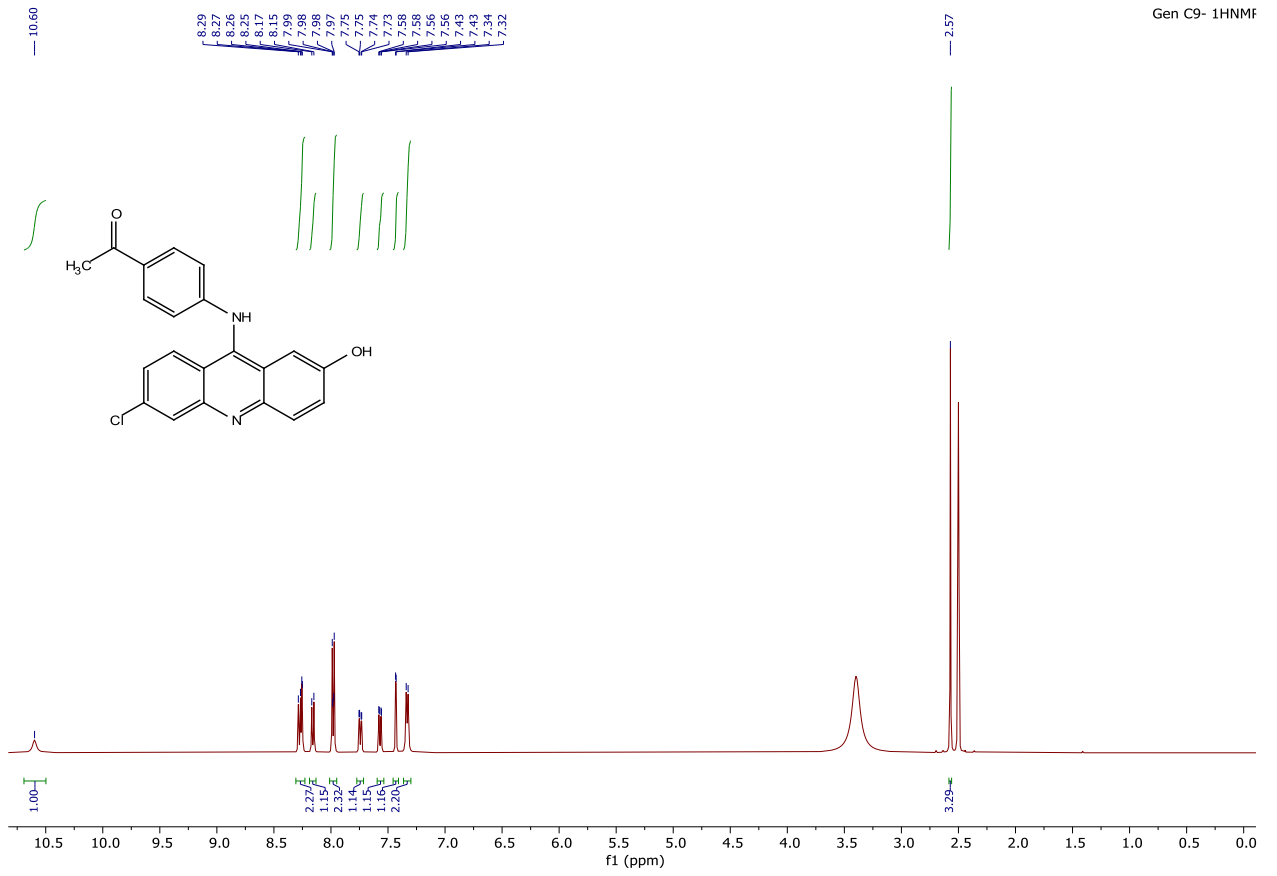
Gen C7 - 13C NMR



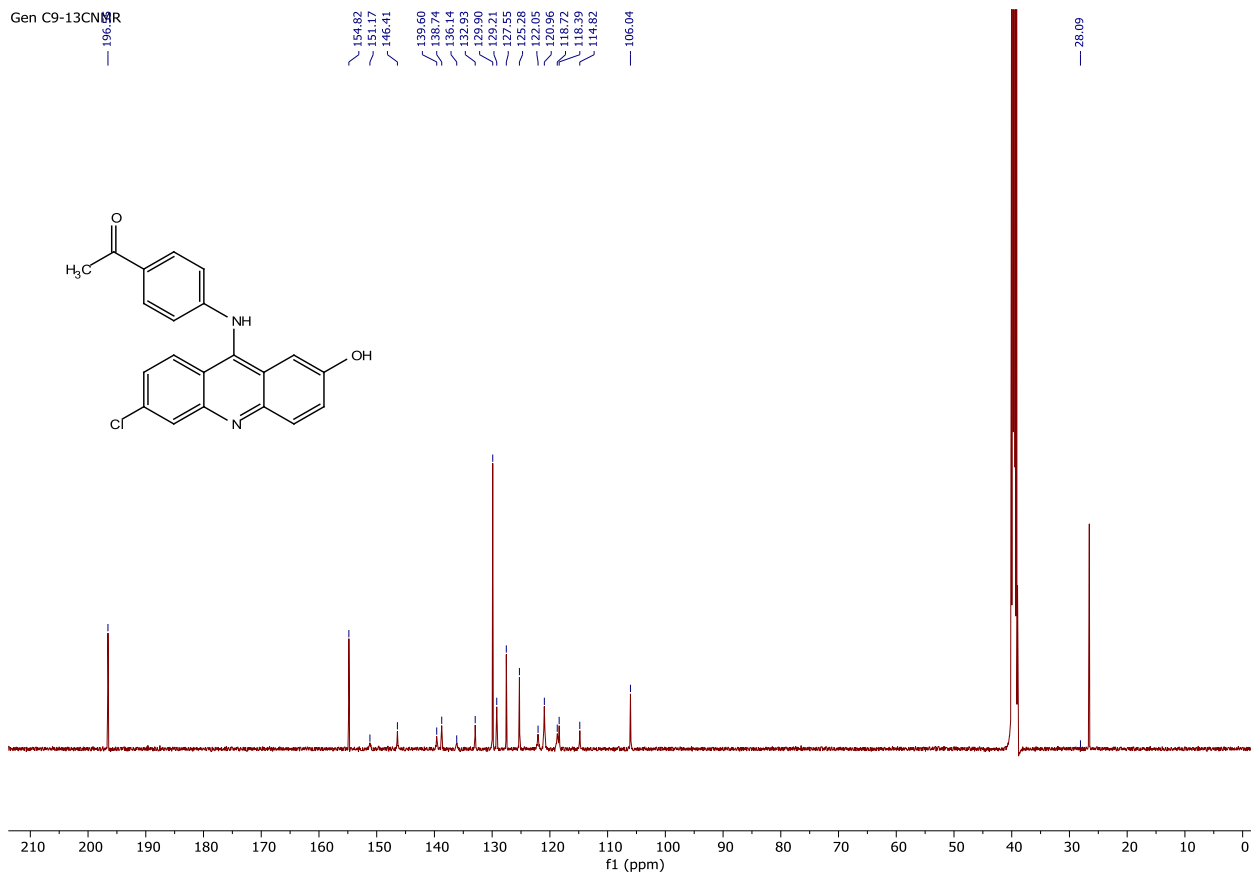


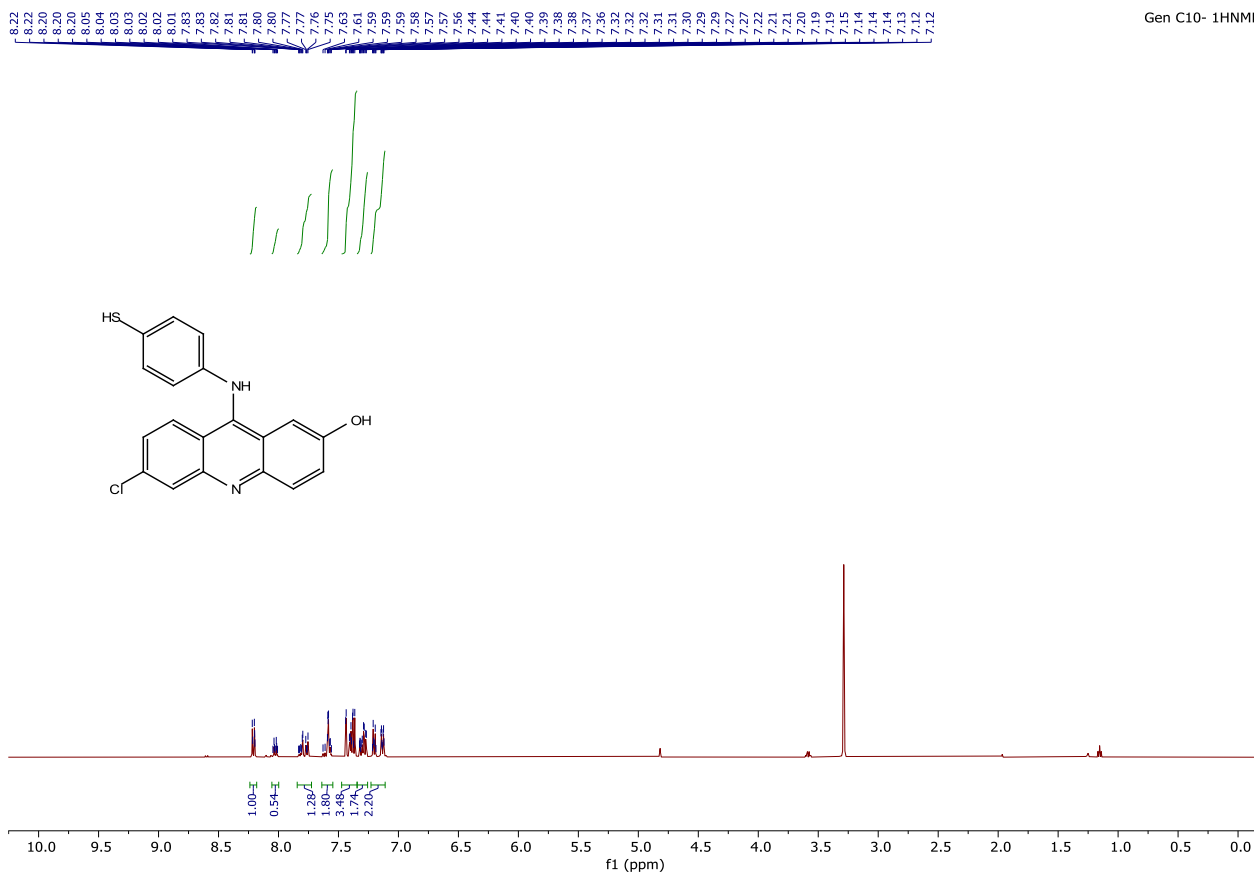
Gen C8- 13CNMR

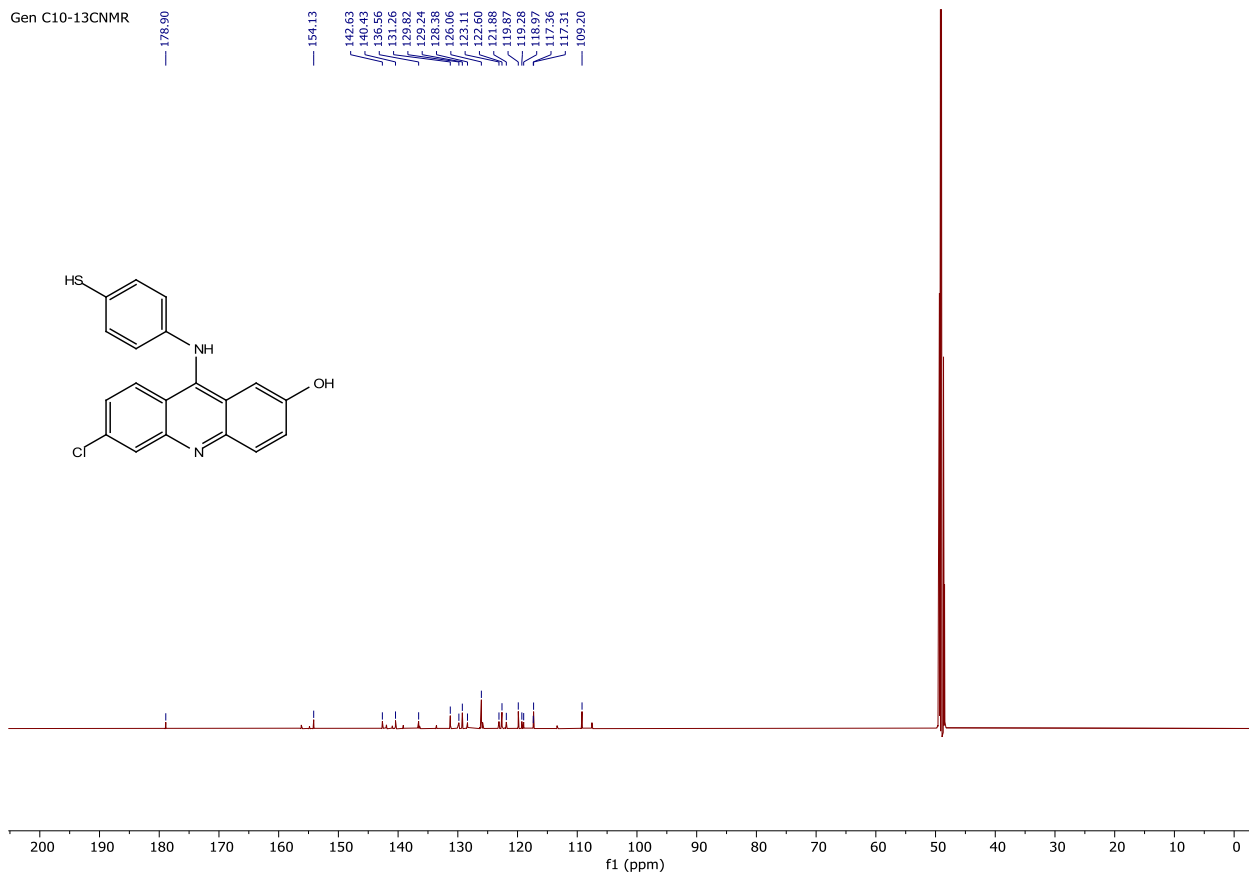




Gen C9-13CNMR

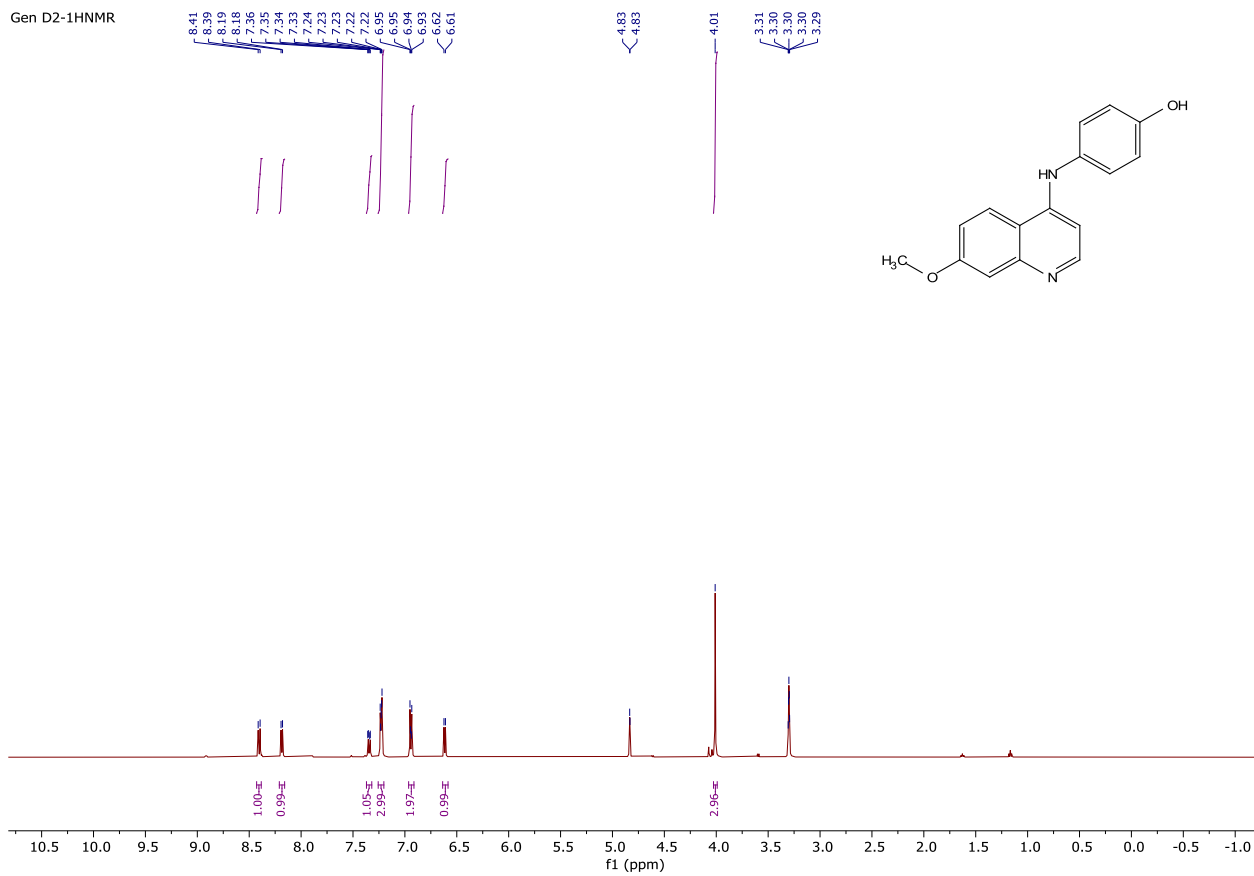




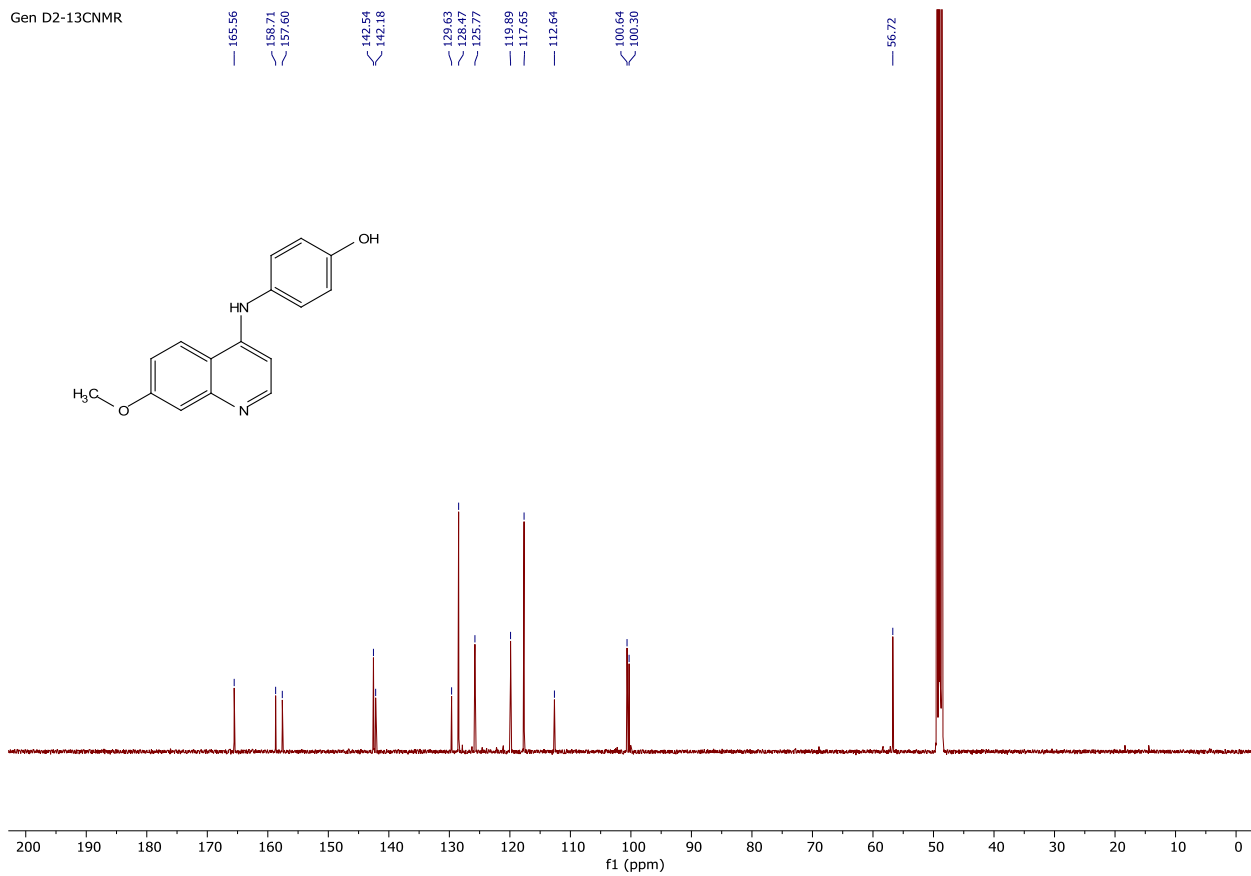
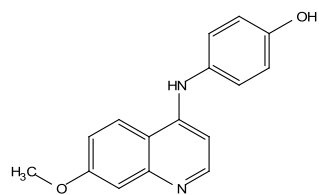


$^1\text{H}/^{13}\text{C}$  NMR spectra of Gen D compounds

Gen D2-1HNMR



Gen D2-13CNMR



Gen D5-1HNMR

